Nano-scale imaging and spectroscopy of plasmonic systems, thermal near-fields, and phase separation in complex oxides.

Andrew C. Jones

A dissertation submitted in partial fulfillment of
the requirements for the degree of

Doctor of Philosophy

University of Washington

2012

Reading Committee:
Markus B. Raschke, Chair
David H. Cobden
Xiaodong Xu

Program Authorized to Offer Degree:
Department of Physics

University of Washington

Abstract

Nano-scale imaging and spectroscopy of plasmonic systems, thermal near-fields, and phase separation in complex oxides.

Andrew C. Jones

Chair of the Supervisory Committee:
Professor Markus B. Raschke
Department of Physics

Optical spectroscopy represents a powerful characterization technique with the ability to directly interact with the electronic, spin, and lattice excitations in matter. In addition, through implementation of ultrafast techniques, further insight into the real-time dynamics of elementary interactions can be gained. However, the resolution of far-field microscopy techniques is restricted by the diffraction limit setting a spatial resolution limit in the 100s nm to micron range for visible and IR light, respectively. This resolution is too coarse for the characterization of mesoscopic phenomena in condensed matter physics.

The development of experimental techniques with nanoscale resolution and sensitivity to optical fields has been a long standing obstacle to the characterization of condensed matter systems on their natural length scales. This dissertation focuses on the fundamental near-field optical properties of surfaces and nanoscale systems as well as the utilization of nano-optical techniques, specifically apertureless *scattering*-type Scanning Near-field Optical Microscopy (*s*-SNOM), to characterize said optical properties with nanometer scale resolution.

First, the *s*-SNOM characterization of the field enhancement associated with the localized surface plasmon resonances on metallic structures is discussed. With their ability to localize light, plasmonic nano-structures are promising candidate systems to serve as molecular sensors and nano-photonic devices; however, it is well known that particle morphology

and the plasmon resonance alone do not uniquely reflect the details of the local field distribution. Here, I demonstrate the use interferometric *s*-SNOM for imaging of the near-fields associated with plasmonic resonances of crystalline triangular silver nano-prisms in the visible spectral range. I subsequently show the extension of the concept of a localized plasmon into the mid-IR spectral range with the characterization of near-fields of silver nano-rods. Strong spatial field variation on lengths scales as short as 20 nm is observed associated with the dipolar and quadrupolar modes of both systems with details sensitively depending on the nanoparticle structure and environment.

In light of recent publications predicting distinct spectral characteristics of thermal electromagnetic near-fields, I demonstrate the extension of *s*-SNOM techniques through the implementation of a heated atomic force microscope (AFM) tip acting as its own intrinsic light source for the characterization of thermal near-fields. Here, I detail the spectrally distinct and orders of magnitude enhanced resonant spectral near-field energy density associated with vibrational, phonon, and phonon-polariton modes. Modeling the thermal light scattering by the AFM, the scattering cross-section for thermal light may be related to the electromagnetic local density of states (EM-LDOS) above a surface.

Lastly, the unique capability of *s*-SNOM techniques to characterize phase separation phenomena in correlated electron systems is discussed. This measurement capability provides new microscopic insight into the underlying mechanisms of the rich phase transition behavior exhibited by these materials. As a specific example, the infrared *s*-SNOM mapping of the metal-insulator transition and the associated nano-domain formation in individual VO_2 micro-crystals subject to substrate stress is presented. Our results have important implications for the interpretation of the investigations of conventional polycrystalline thin films where the mutual interaction of constituent crystallites may affect the nature of phase separation processes.

TABLE OF CONTENTS

LIST OF FIGURES

ACKNOWLEDGMENTS

In no specific order, I gratefully acknowledge many of the people in my life whom have helped and encouraged me on the way to this milestone. Without the support of my co-workers, friends, and family, I never would have made it this far and most certainly would not have had such a fufilling time along the way.

I first would first like to thank those teachers and advisors from elementary school through my undergraduate degree who helped inspire my interest in science and mathematics. While this is by no means a comprehensive list, I would like to acknowledge Bonnie Imburgia and Jerry Behrens from my time in Cody, and Prof. Phillip Duxbury from my time at Michigan State University who was instrumental in my desire to pursue condensed matter physics.

I would like to recognize some of my fellow members of the Raschke lab both at the University of Washington and the University of Colorado over the past several years: Alexandria Anderson, Kseniya Deryckx, Ryan Murdick, Joanna Atkin, Xiaoji Xu, Honhua Yang, Brian O'Callahan, Emily Chavez, and Stephanie Crabtree. I thank both Matthias Rang and Catalin Neacsu from whom I learned very much as a new graduate student and show particular gratitude to the two students with whom I joined the group, Robert Olmon and Samuel Berweger, for being great co-workers and better friends.

I further wish to recognize my advisor Markus Raschke for investing the time and effort into ensuring the success of our research and my education.

Finally, and most importantly, I would like recognize with deepest thanks my friends and family for being my foundation through the past several years. I thank my Mom, whom has been ever supportive of my goals in life and particularly my dad, whom has provided for and encouraged my continued studies. Lastly, I would like to thank Maggi who has kept me grounded since the very beginning of this journey. I love you very much.

DEDICATION

To my friends and family

Chapter 1

INTRODUCTION TO NANO-OPTICS

1.1 An introduction to the nano-scale and nano-optics.

In a visionary lecture given by Nobel laureate Richard Feynman at an American Physical Society meeting on Dec. 29, 1959 at the California Institute of Technology entitled *"There's Plenty of Room at the Bottom"*, Feynman considered the ramifications of manipulating matter at short length scales [1]. While the concept of the atom was well developed, at the time the idea of manipulating matter on such short length scales was foreign. Still, it was recognized that the understanding of the behavior of matter at dimension sizes comparable to that of the natural of molecular, electronic, or lattice correlations held great promise for innovation across several fields including physical machinery, electronics, communications, and medicine.

Traditionally, the "everyday world" in which we live and interact lies in the macroscopic regime and is described by classical physics. As we study the behavior of objects at smaller and smaller length scales, the relative strength of the forces changes. At the micro-scale, gravity becomes a weak effect while electromagnetic forces such as Coulomb repulsion/attraction and the Van der Waals interactions become dominant [2]. Moving far down to the atomic scale, the fundamental physics of atoms is governed by quantum mechanics, which accounts for both the particle like-and wave-like behavior of matter. It is on mesoscopic length scales, lying in the transition regime between the macroscopic and atomic realms, that new, exciting, and complex physics arises from the interplay of classical and quantum effects (Fig. 1.1).

For homogeneous crystalline materials with bulk dimensions, the electrical, optical, thermal, and acoustic properties result from the periodic organization of the constituent atoms or molecules. At mesoscopic length scales, however, the combination of the ordering and bonding of atoms and the interplay of long range/classical physics with short range/quantum

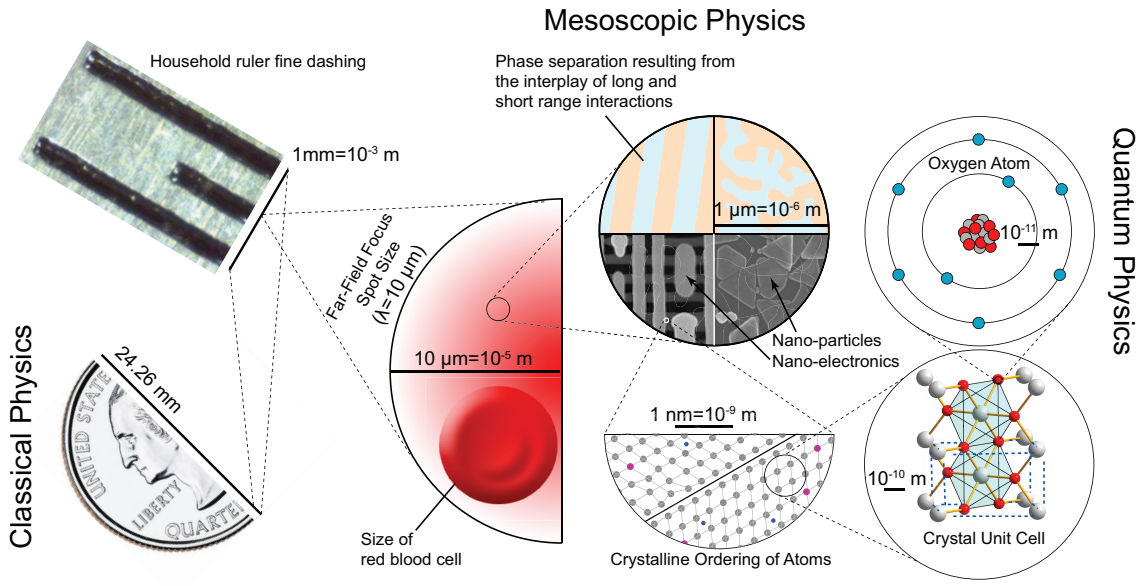

Figure 1.1: A diagram of the relationship of length scales transitioning from the macroscale through the microscale on down to the nanoscale is represented above illustrating where differing physical descriptions are valid.

mechanical physics can result in a diverse array of of physical properties and behaviors. One of the primary goals of nanoscience and nanotechnology has been the development of new materials with nanoscopic dimensions which take advantage of the novel properties which occur at these length scales.

As we progress towards engineering smaller devices and structures in the mesoscale regime, and as we discover new materials with unique properties (e.g. phase separation/domain formation) on these length scales, discovery of the underlying physics is essential to the development of our understanding of these systems. One of the primary challenges for condensed matter physics in the description of nanoscale phenomena is the development of experimental techniques precise enough to characterize the physical properties of these systems on short length scales. Such spatial sensitivity is vital in describing systems which exhibit heterogeneous properties on mesoscopic length scales (1 nm - 10 μm). A primary example of such heterogeneous behavior is the phase separation of domains of differing

crystallographic or electronic properties (Fig. 1.1) resulting from the mutual interplay of long and short range forces. Through the implementation of experimental techniques which enable the measurement of the characteristic size and spatial ordering of phase separated domains, we can gain further understanding into the fundamental mechanisms underlying domain formation.

However, while many experimental techniques provide valuable information on the properties on nanoscale systems, they are unable to access the energy scales in which many fundamental solid state excitations occur (0.01-5 eV). These energies typically correlate with the infrared and visible optical frequency ranges. As a consequence, in order to further understand mesoscopic/nanoscale systems, a technique with both high spatial resolution and sensitivity to optical properties is highly desirable. The field research of known as nano-optics thus focuses on the understanding of optical material properties on nanometer length scales. In the following chapters, I will discuss the development and application of an experimental technique to characterize the optical properties of materials with nano-scale resolution.

1.1.1 Introduction to nano-optical characterization.

By definition, optics is the study of the physical properties and characteristics of light. The use and understanding of the properties of light extends back to Newton, Galileo, and the very origins of physical science. Despite the fact that it has been studied for hundreds of years, optics remains at the forefront of current scientific research [3, 4]. One facet of current research effort is the field of nano-optics: the investigation of the properties of light matter interactions on length scales below the wavelength of light. As structural dimensions become smaller than the wavelength of light, new optical properties arise as translational invariance is broken yielding new scattering and resonance phenomena. Nanoscopic materials not only exhibit intrinsic optical properties inherent to the material, but also extrinsic properties dependent on the details of the structure geometry and size.

The implementation of far-field optics for the investigation of solid state materials is an invaluable tool in understanding fundamental electronic, spin, and vibrational excitations.

This characterization is possible as the energies of photons in the visible through the infrared spectral range directly correspond to the energy of electronic and vibrational excitations in these solid states systems. As a result, optical spectroscopic investigation into the manner in which light is generated, emitted, reflected, transported, transmitted, and amplified reveals vital information on the linear and non-linear optical responses and their associated physical properties within these systems.

In addition to the investigation of the relevant energy scales of solid state materials, optics further allows for the characterization of the optical response of these materials on their natural time-scales ($\sim$ 1 fs - 1 ns). This sensitivity to the temporal response of the elementary electronic and vibrational excitations in these systems is achieved through the generation/implementation of ultrafast optical pulses. Ultrafast optical pulses in the visible range, with durations down to several fs, are among the shortest events made by mankind and can be generated with relative ease in a small table-top experiment [5]. As a result, ultrafast spectroscopic characterization of has become a routine scientific technique in the efforts to understand the physics of solid media.

While use of conventional far-field optics provides access to the relevant energy scales of solid state excitations, for the characterization of systems with nanometer resolution there is a fundamental limitation on the achievable resolution. This restriction is known as the diffraction limit. Here, light converging on a focal point with a cone half-angle θ will make a spot whose radius r is given by [4]

$$r = \frac{1.22\lambda}{2n\sin[\theta]} = \frac{0.61\lambda}{\text{N.A.}}, \tag{1.1}$$

with the wavelength λ and index of refraction of the medium n. The size of this focal spot defines the resolution limit of conventional optical microscopy techniques. Unfortunately, even for large numerical apertures this resolution limit is several hundreds of nanometers for visible light up to several μm for infrared light, far too large to map material properties on the nanoscale.

Currently several alternative, non-optical, experimental techniques have been implemented to characterize nano-scale systems with high-spatial resolution. These include electron microscopy methods [6, 7] such as scanning electron microscopy (SEM), transmission

electron microscopy (TEM), photo-emission electron microscopy (PEEM), and electron energy loss spectroscopy (EELS). These electron microscopy methods are standard techniques and are able to provide structural and limited chemical information at very high resolution ($\sim 10^{-10}$ m for TEM); however, they are limited to vacuum environments and are not typically sensitive to electronic and vibrational excitations.

A second experimental strategy to increase resolution is the use of light of very short wavelengths. Here, X-ray microscopes have been implemented with high $20 - 100$ nm spatial resolution. This technique however, requires a synchnotron X-ray source such as the Advanced Light Source at Berkeley National Laboratory, and only is able to provide limited chemical information [8].

Finally, scanning probe microscopic techniques such as scanning tunneling microscopy (STM) and atomic force microscopy (AFM) have the ability to measure the topographic features of a surface with nanometer precision [9,10]. These techniques typically characterize a surface by maintaining a very sharp tip ($\sim$ 10 nm) in close proximity to the surface being studied through feedback via a tunneling current or atomic force interaction. These measurement methods have the advantage that they are are easily implemented in ambient conditions and, in combination with external magnetic or electric fields, are able to provide information about the DC conductivity, the electric polarizability, and magnetization.

Due to the limitations imposed by the diffraction limit (Eqn. 1.1), in order to characterize the optical properties of materials with nanometer spatial resolution, a new experimental method had to be devised. These methods came with the aforementioned invent and development of scanning probe microscopy technology introduced above throughout the 1980s and 1990s [11–13]. Here, nanometer scale optical resolution may be achieved through the implementation of microscopy utilizing optical *near-fields* [14]. This resolution is achieved by optically illuminating a sharp atomic force microscope (AFM) probe and measuring the scattered light resulting from the near-field enhancement of the electric field resulting from the mutual coupling of the AFM tip and the material surface [15]. As a result, we take advantage of the optical antenna properties of the nanoscopic tip which allows for a new combination of optical spectroscopy with scanning probe techniques.

This method of using an ultrasharp scanning probe tip to scatter the optical near-

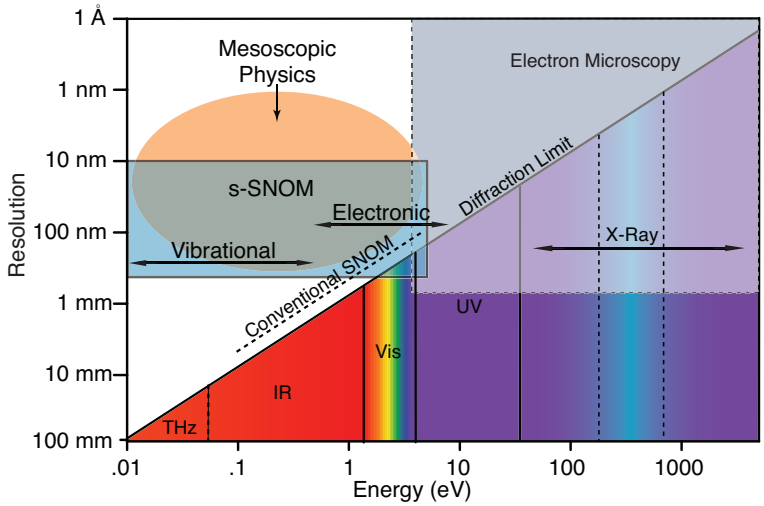

Figure 1.2: The shaded areas above represent the energy and spatial resolution and measurement range limits of current experimental characterization techniques. As *s*-SNOM characterization is sensitive the optical properties of the materials, it is capable of providing both high spatial and temporal resolution. This enables the characterization of mesoscopic physics on the intrinsic energy scales of solid state excitations.

fields above a surface is known as aperturless *scattering*-type Scanning Near-field Optical Microscopy (*s*-SNOM). Through this process, the field enhancement resulting from the mutual interaction of the probe tip with the surface is highly localized yielding a resolution down to the tip apex size. Fig. 1.2 displays a schematic comparing spatial and energy resolution achievable with conventional experimental techniques in comparison to *s*-SNOM characterization.

s-SNOM is unique in its ability to both characterize solid state systems with both high temporal and spatial resolution. Furthermore, these methods are applicable under ambient conditions which allows for the optical investigation of microscopic composition, electronic phase, and chemical functionality of nanoscale materials which have thus far been difficult to access.

1.2 Dissertation outline.

In the following chapters I will discuss the fundamentals and applications of *s*-SNOM measurement techniques across several fields of nano-optics.

To establish a foundation for the near-field optical properties of materials to which *s*-SNOM measurements are sensitive, Chapter 2 provides a brief theoretical description of the optical properties and electrodynamics of solid state materials with a focus on plasmonic and phononic surface wave phenomena. The Drude-model description for the free-electron model for the electrons in metals is discussed and related to the optical properties of metals over a wide frequency range; the optical response of dielectric media is similarly covered. Under the framework of the optical properties of these materials, a derivation for the conditions necessary for the generation of surface polariton waves will be discussed.

In Chapter 3 the historical development and modern implementation of *s*-SNOM characterization techniques is covered. Beginning with a discussion of the fundamental physics of the diffraction limit and the first proposals for sub-diffraction limit imaging by E.H. Synge, a historical overview of the development of nano-scale near-field optical characterization and strategies will be provided. The basics of non-contact atomic force microscopy are presented as a basis for *s*-SNOM characterization. Finally, the measurement principles and detection/contrast mechanisms of *s*-SNOM measurement techniques will be discussed with a particular focus on the field enhancement mechanisms and the spectral response of *s*-SNOM signals.

The utilization of *s*-SNOM techniques for the mapping of the spatial distribution of field enhancement associated with the localized plasmonic response of metallic nano-particles will be discussed in Chapter 4. Here, the concept of a localized surface plasmon resonance (LSPR) will be introduced and its dependence on size, shape, and material composition discussed with a focus on how the fine details of the structural properties of a nano-structure can drastically affect the spatial distribution of its optical field response. The experimental *s*-SNOM characterization of the spatial field distribution of the plasmonic response of Ag nano-prisms in the visible spectral range as well as the response Ag nano-rods in the mid-IR spectral range will be demonstrated. Corresponding theory modeling the LSPR response

for both nano-particle systems will also be presented.

In Chapter 5 the characterization of surfaces using Thermal Infrared Near-field Spectroscopy (TINS) will be discussed. Here, we present, for the first time, characterization of the magnitude and spectral distribution of near-field thermal near-field radiation. Using the description of conventional far-field thermal radiation as a basis, the development of new theoretical models for the behavior of thermal near-fields incorporating the presence of surface polariton waves will be developed. The experimental apparatus used to perform TINS measurements, implementing a heated AFM probe acting as its own intrinsic light source will be shown and discussed. The results of TINS measurements on molecular polytetrafluoroethylene, and crystalline SiC and SiO_2 surfaces are presented in the context of a theoretical model for the *s*-SNOM scattering of thermal near-field light and its relationship to the fundamental electromagnetic local density of states (EM-LDOS) above the surface.

Lastly, Chapter 6 details the implementation of *s*-SNOM measurement methods in the characterization of correlated electron systems with an emphasis on the mapping of the phase separation. Here, I discuss how utilization of *s*-SNOM can further enable the study of competing phases and nano-domain formation in complex systems addressing the fundamental physics behind their rich behavior. The physics behind the formation of heterogeneous phase separation and domain formation will be discussed with a focus on metal-insulator phase transitions (MIT). As a specific example, the mapping of domain formation and phase separation present in the MIT of VO_2 micro-crystals with *s*-SNOM is presented. With a focus on the underlying physical mechanisms involved with the MIT in VO_2, the information gained through optical characterization will be presented. Our results have important implications for the interpretation of the investigations of conventional polycrystalline thin films where the mutual interaction of constituent crystallites may affect the nature of phase separation processes.

Chapter 2

AN INTRODUCTION TO THE ELECTRODYNAMICS OF SOLID MATERIALS AND SURFACE WAVES.

2.1 Introduction.

The work in this thesis details the characterization of light-matter interactions in the near-field and on the nano-scale. Based upon the general physics of light-matter interactions in solid state systems, a semi-classical description is appropriate. In this semiclassical description, the propagation of light is modeled in terms of a wave obeying Maxwell's equations. The processes by which objects emit or absorb light are described in terms of quantized units, e.g. photons. The understanding of optical properties of nano-structures and nanoscale systems requires both a knowledge of electromagnetism and solid state theory. In the following section, I briefly introduce Maxwell's equations for electromagnetic waves and discuss how they relate to the fundamental optical properties of solid state systems. These concepts will be used as a basis for the derivation and description of the conditions necessary for electromagnetic surface waves such as surface plasmon polaritons (SPP) and surface phonon polaritons (SPhP). These surface waves play an important role in the observed near-field phenomena discussed in the subsequent chapters of this dissertation.

2.2 Maxwell's equations and the definition of important experimental parameters for the description of solid state systems.

The study of electrodynamics is the investigation of moving electric charges and their interaction with magnetic $\vec{B}[\vec{\mathbf{x}}, t]$ and electric fields $\vec{E}[\vec{\mathbf{x}}, t]$. Maxwell's equations express the relationship between electromagnetic fields and their sources, the charge density ρ and current density $\vec{J}$ in the medium. These equations are valid for both time-dependent and static systems and lay the foundation for classical electrodynamics, optics, and electric circuitry. The study of optics involves the description of propagating electromagnetic fields through both free-space and material systems.

Maxwell's equations for a medium with bound ρ_b and free ρ_f charges can be given as [16, 17]

$$\nabla \cdot \vec{D} = \rho_f \quad \text{(Gauss' Law)} \tag{2.1}$$

$$\nabla \cdot \vec{B} = 0 \quad \text{(Gauss' Law for magnetism)} \tag{2.2}$$

$$\nabla \times \vec{E} = -\frac{\partial \vec{B}}{\partial t} \quad \text{(Faraday's Law)} \tag{2.3}$$

$$\nabla \times \vec{H} = \vec{J}_f + \frac{\partial \vec{D}}{\partial t}. \quad \text{(Ampere's Law)} \tag{2.4}$$

This set of equations (together with the appropriate boundary conditions and the conservation of charge and energy) are sufficient to solve the time and spatial evolution of electromagnetic fields in the presence of matter.

The extension of Maxwell's laws to solid media involves linkage of the four basic fields in presence of matter: the external electric field $\vec{E}$, the dielectric displacement field $\vec{D}$, the external magnetic field $\vec{B}$, and the magnetic vector field $\vec{H}$. Here, $\vec{D}$ and $\vec{H}$ represent the additional field response due to the reaction of bound and free charges within a material due to the presence of the external $\vec{E}$ and $\vec{B}$ fields respectively.

$\vec{D}$ and $\vec{H}$ may be related to the external fields through the polarizability $\vec{P}$ and magnetization $\vec{M}$, respectively, through the following relation [16, 17]

$$\vec{D} = \epsilon_0 \vec{E} + \vec{P} \tag{2.5}$$

$$\vec{H} = \frac{1}{\mu_0}\vec{B} - \vec{M}. \tag{2.6}$$

The quantities ϵ_0 and μ_0 represent the vacuum dielectric permittivity and the magnetic permeability respectively. $\vec{P}$ describes the mean electric dipole moment per unit volume inside the material, caused by the alignment of microscopic dipoles with the electric field. In order to analyze dielectric systems, it is often useful to note that the total charge density ρ may be expressed as the sum of two contributions, bound charge density ρ_b and free charge density ρ_f

$$\rho = \rho_\mathrm{b} + \rho_\mathrm{f}. \tag{2.7}$$

One important bounding condition for Maxwell's equations given above is that charge conservation requires that [16, 17],

$$\nabla \cdot \vec{P} = -\rho_{\mathrm{b}} \tag{2.8}$$

$$\nabla \cdot \vec{D} = \nabla \cdot (\epsilon_0 \vec{E} + \vec{P}) = \rho_{\mathrm{f}}. \tag{2.9}$$

Similar to the charge density distribution within materials, the total current $\vec{J}$ can be expressed as a sum of bound $\vec{J}_{\mathrm{b}}$ and free $\vec{J}_{\mathrm{f}}$ currents

$$\vec{J} = \vec{J}_{\mathrm{b}} + \vec{J}_{\mathrm{f}}. \tag{2.10}$$

The requirement that electric charge is conserved throughout space further sets the following continuity equations [16, 17],

$$\nabla \cdot \vec{J} = -\frac{\partial \rho}{\partial t} \tag{2.11}$$

$$\vec{J}_b = \vec{\nabla} \times \vec{M} + \frac{\partial \vec{P}}{\partial t}. \tag{2.12}$$

The bound current above is expressed as the sum of current contributions stemming from the effective current density equivalent to the atomic magnetic dipoles from the magnetization and the polarization current $\vec{J}_P = \frac{\partial \vec{P}}{\partial t}$ resulting from the change of the electric polarization.

If the electromagnetic response of materials is linear, constitutive relations relating the total current density $\vec{J}$ and polarizability $\vec{P}$ to $\vec{E}$ and the magnetic permeability μ to $\vec{H}$ can be expressed as [16, 17]:

$$\vec{J} = \sigma \vec{E} \tag{2.13}$$

$$\vec{P} = \epsilon_0 \chi_e \vec{E} \tag{2.14}$$

$$\vec{M} = \chi_m \vec{H}. \tag{2.15}$$

Here, σ represents the conductivity of the material while χ_e and χ_m represent the electric and magnetic susceptibilities respectively. The relations above define the dielectric permittivity ϵ and magnetic permeability μ of *linear* materials as [16, 17]

$$\vec{D} = \epsilon_0(1 + \chi_e)\vec{E} = \epsilon_0 \epsilon \vec{E} \tag{2.16}$$

$$\vec{B} = \mu_0(1 + \chi_m)\vec{H} = \mu_0 \mu \vec{H}. \tag{2.17}$$

The quantities ϵ and μ enter the description of the behavior of electromagnetic waves in materials as characteristic input parameters specific to the material. It is important to note that Eqns. 2.16 and 2.17, in addition to Eqn. 2.13, are only valid for linear media which do not exhibit temporal or spatial dispersion. The reason why ϵ and μ are defined at a particular value need not be explained for the classical electromagnetic description to be correct. To describe the behavior of ϵ and μ, a microscopic picture of the light matter interaction for the specific material must be developed.

It should also be noted that ϵ is a frequency dependent quantity which results in temporal dispersion as light propagates through the medium. This frequency dependence reflects the causal nature of the induced material response arising after the application of an applied field with a resulting phase difference. ϵ must correspondingly be treated as a complex quantity to incorporate both the magnitude and phase of the material response. Here, Re$[\epsilon]$ is related to the amount of energy the material is able to store, while Im$[\epsilon]$ is related the dissipation of the medium.

The permittivity for a material has several well defined relationships between important experimental parameters. One such parameter is the conductivity σ which can be related to the permittivity by expressing the current density and displacement field in the Fourier domain to account for the frequency dependence of $\epsilon[\omega]$.

Rather than express in terms of real space vectors and time ($\vec{r}$ and t), through a Fourier transform the displacement field/electric field (Eqn. 2.16) and current density-electric field relationship (Eqn. 2.13) can be expressed in terms of a wavevector $\vec{K}$ and frequency ω as [18]

$$\vec{D}[\vec{K},\omega] = \epsilon_0\epsilon[\vec{K},\omega]\vec{E}[\vec{K},\omega] \tag{2.18}$$

$$\vec{J}[\vec{K},\omega] = \sigma[\vec{K},\omega]\vec{E}[\vec{K},\omega]. \tag{2.19}$$

Combining Eqn. 2.12 with Eqns. 2.18 and 2.19, a relationship between permittivity and conductivity can be derived [18],

$$\vec{J}[\vec{K},\omega] = \sigma[\vec{K},\omega]\vec{E} = \frac{\partial}{\partial t}\vec{P}[\vec{K},\omega] \tag{2.20}$$

$$= \frac{\partial}{\partial t}(\vec{D}[\vec{K},\omega] - \epsilon_0\vec{E}[\vec{K},\omega]) \tag{2.21}$$

$$= \frac{\partial}{\partial t}(\epsilon_0\epsilon[\vec{K},\omega]\vec{E}[\vec{K},\omega] - \epsilon_0\vec{E}[\vec{K},\omega]) \tag{2.22}$$

$$= -i\omega\epsilon_0(\epsilon[\vec{K},\omega]\vec{E}[\vec{K},\omega] - \vec{E}[\vec{K},\omega]) \tag{2.23}$$

$$\rightarrow \sigma[\vec{K},\omega] = -i\omega\epsilon_0(\epsilon[\vec{K},\omega] - 1). \tag{2.24}$$

In general, whether σ or ϵ represents the physically relevant physical parameter depends on the material in question. For dielectric materials at low-frequencies, ϵ is usually used for the description of the response of bound charges to a driving field, leading to an electric polarization. Not surprisingly, for conductive materials, the σ relates the amount of free current density induced by application of an external field. These distinctions become less clear at higher frequencies, where for example, metals are characterized by higher losses and cannot be treated as perfect conductors.

Finally, the permittivity can also be linked to the optical constants of a medium, the real n and imaginary κ parts of the index of refraction via the following relation [4, 19]

$$\mathrm{Re}[\epsilon] = n^2 - \kappa^2 \tag{2.25}$$

$$\mathrm{Im}[\epsilon] = 2n\kappa. \tag{2.26}$$

Indeed, the permittivity at optical frequencies is commonly derived through measurement of both n and κ. Note that both the real and imaginary parts of the index of fraction relate to specific observables for light in a medium. The real part n defines the size of the wavevector for propagating light $k = \frac{n\omega}{c} = \frac{2\pi n}{\lambda_0}$. Meanwhile the imaginary part κ determines the value absorption coefficient for the material $\alpha = \frac{2\omega\kappa}{c} = \frac{4\pi\kappa}{\lambda_0}$ following the Beer-Lambert law.

2.3 Drude model description for the optical properties of noble metals.

While proposed at the turn of the 20th century [20] only three years after the discovery of the electron by J.J. Thompson, the Drude model for the conduction of electrons in metals

has been surprisingly successful at describing the optical properties of noble metals over a frequency range spanning several orders of magnitude. From the low frequency radio waves to the optical regime, the Drude model accurately describes the electrical conductivity of noble metals through the simple application of the kinetic theory of gases to the electrons within the metal. The Drude model makes several assumptions in providing a description for the conductivity of noble metals, and while some of the assumptions may seem drastic, the Drude model works well in encompassing much of the electrodynamics of noble metal systems.

First, it is assumed that the electrons within the metal feel no interactive forces except for the forces coming into play over a short duration during scattering events. Consequently ballistic electrons are free to move throughout a metallic body, maintaining a linear flight trajectory until experiencing a scattering event. Collisions are inelastic in nature and are considered to be instantaneous events which abruptly alter the velocity of an electron. Each collision leads to a complete loss of directional information and results in a random orientation of the electron velocity.

For the Drude model, the microscopic nature of the scattering events is left undefined. In real metallic systems scattering events include electron-lattice, electron-phonon, electron-defect, and electron-electron collisions. As elastic scattering events are considered to be equivalent in the Drude model, the only important parameter which needs to be defined/determined is the mean time between collision events τ.

It is unique that such a drastic simplification of all scattering events into one characteristic parameter τ, the relaxation time of the metal, so effectively captures the physics of the system. Even more amazing is that τ, measured simply from the DC ($\tau = (m_e \sigma_{DC}/n_e e^2)$ at 0 Hz) conductivity of the material, effectively describes the physics across such a broad frequency range. The electron mass, charge, and density are represented by the symbols m_e, e, and n_e respectively while the σ_{DC} denotes the DC conductivity.

It should be noted that small adjustments to the Drude parameters may be required for certain materials at large optical frequencies. These adjustments may be required due to the additional contributions of scattering processes at high frequencies. While the scattering rate derived from the DC conductivity provides the correct qualitative values, accurate

Parameter	Cu	Ag	Au
n_e [m$^-$3]	$8.47 \cdot 10^{28}$	$5.86 \cdot 10^{28}$	$5.9 \cdot 10^{28}$
σ_{DC} [Ω^{-1}m^{-1}]	$6.41 \cdot 10^7$	$6.62 \cdot 10^7$	$4.9 \cdot 10^7$
m^*/m_e	(1.49)	(0.96)	(0.99)
$\hbar\omega_p$ [eV]	8.85	9.17	9.07
τ [fs]	40 (6.9 ± 0.7)	40 (31 ± 12)	29 (9.3 ± 0.9)
ϵ_∞	1.6	3.7	9.84

Figure 2.1: Typical parameters at room temperature (273 K) for the Drude model for the three noble metals are as follows [22, 24, 25]. The scattering rates derived from the Johnson and Christy [22] fits for optical frequencies are given in parentheses.

models of the permittivity of noble metals in the visible/IR frequency range may have slightly lower τ which may be derived from ellipsometry measurements [21–23]

What may complicate matters even further is the fact that several differing measurements of optical constants exist [21–23]. Variations in these parameters can lead to large deviations in the predicted optical properties (skin depth, plasmon propagation length, ect...) of structures composed of these noble metals. It is important when modeling noble metal systems, that careful thought is put into which optical constants are used to model the system.

While Ag is closely described by the DC scattering rate, in Au and Cu additional scattering effects reduce the scattering rate. In the table of Drude parameters below (Fig. 2.1), the parameters at optical frequencies corresponding to the Johnson and Christy data are included in parentheses [22].

Writing the equation of motion for an electron in a metal, and with the assumption of a solutions of the form $\vec{x}[t] = x_0 \exp[-i\omega t]$, it can be shown that

$$m_e\ddot{\vec{x}}[t] + m_e\gamma\dot{\vec{x}}[t] = -e\vec{E}[t] \tag{2.27}$$

$$-m_e(i\gamma\omega + \omega^2)\vec{x}[t] = -e\vec{E}[t] \tag{2.28}$$

$$\rightarrow \vec{x}[t] = \frac{e}{m_e(\omega^2 + i\gamma\omega)}\vec{E}[t]. \tag{2.29}$$

As displaced electrons contribute to the macroscopic polarization via the relation $\vec{P} = -ne\vec{x}$ the polarization may be expressed as

$$\vec{P} = -\frac{ne^2}{m_e(\omega^2 + i\gamma\omega)}\vec{E}. \tag{2.30}$$

Following from Eqn. 2.16, the expression for the dielectric permittivity of a Drude metal can be derived to be [24]

$$\vec{D} = \epsilon_0 \left(1 - \frac{\omega_p^2}{\omega(\omega + i\gamma_0)}\right)\vec{E} \quad \text{where,} \tag{2.31}$$

$$\rightarrow \epsilon[\omega] = \left(1 - \frac{\omega_p^2}{\omega(\omega + i\gamma_0)}\right). \tag{2.32}$$

Here, the $\gamma_0 = \tau^{-1}$ represents the scattering rate and ω_p the plasma frequency. The plasma frequency may be defined in terms of the effective mass $m^*$of the electrons and the electron density n_e to be

$$\omega_p = \sqrt{\left(\frac{n_e e^2}{\epsilon_0 m^*}\right)}. \tag{2.33}$$

While to this point ideal free electron behavior has been assumed, for higher optical frequencies $\omega \simeq \omega_p$ the filled d-orbital band in proximity to the Fermi surface leaves a residual polarization due to the positive background of the ion cores which can be described through the addition of an offset permittivity term ϵ_∞ to Eqn. 2.32.

$$\epsilon[\omega] = \left(\epsilon_\infty - \frac{\omega_p^2}{\omega(\omega + i\gamma_0)}\right). \tag{2.34}$$

Fig. 2.2 displays the relevant optical parameters for Ag, both derived from the Drude model and physically measured, over a broad frequency range. It is clear that there are several regimes where noble metals exhibit starkly differing properties. In the low frequency regime, also known as the Hagens-Rubens regime [18] ($\omega \ll \gamma$), the optical properties are largely determined by the flat DC conductivity. The real part of the permittivity Re[ϵ] is constant and large while the imaginary component scales $\propto 1/\omega$. In this case, both optical constants n and κ are equal. As noble metals are good DC conductors, σ_{Re} is large while σ_{Im} remains low.

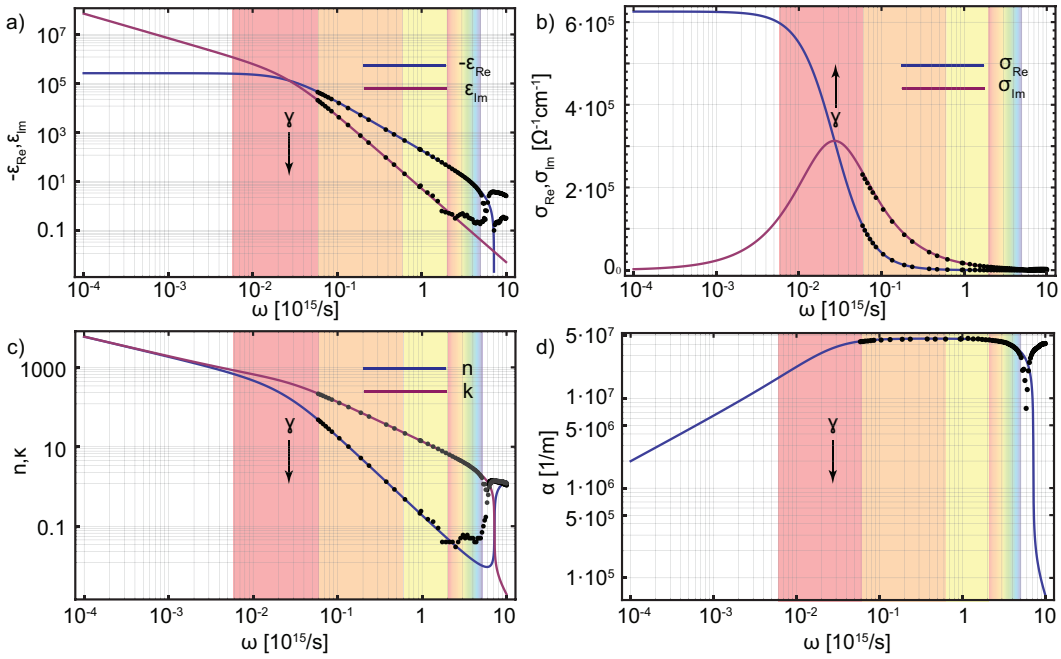

Figure 2.2: Parameters for the Drude model for Ag over a large frequency range spanning from the low-frequency range through visible range to the onset of the interband/transparency regime ($\omega \simeq \omega_p$) where the Drude model begins to break down. The real and imaginary parts of the dielectric permittivity a) and optical conductivity b) are displayed along with the index of refraction values (n and κ) c) and the absorption coefficient d). Wavelength regimes representing the visible (400-800 nm), near-infrared (800-3000 nm), mid-infrared (3-30 μm), and far-infrared (30-300 μm) are represented by the rainbow, yellow, orange, and red shaded areas respectively.

As ω approaches the scattering rate of the electrons, the $\omega \simeq \gamma$ system enters the relaxation regime. Here, a cross-over occurs for the optical conductivity as the imaginary part of the optical conductivity now becomes greater than the real part. Both the real and imaginary parts of the ϵ decrease in magnitude with increasing frequency. Meanwhile the values for the optical constants n and κ diverge from one another [18].

Finally, in the relaxation regime $\omega \gg \gamma$ noble metals are characterized by an imaginary conductivity which is much greater than the real component ($\mathrm{Im}[\sigma] \gg \mathrm{Re}[\sigma]$). Both the real and imaginary parts of the permittivity decrease with increasing frequency scaling as $\mathrm{Re}[\epsilon] \approx 1 - \frac{\omega_p^2}{\omega^2}$ and $\mathrm{Im}[\epsilon] \approx 1 - \frac{\omega_p^2 \gamma}{\omega^3}$. Here the absorption coefficient is large and constant with respect

to frequency. This means that unlike the DC regime, noble metals are characteristically lossy materials at optical frequencies.

2.4 Optical properties of dielectric media.

In nonconducting, isotropic media the electrons are statically bound to the atomic sites in the material. It can be assumed that the electrons are bound to their atomic sites in a harmonic potential defined by a force constant K_e. In a time varying electric field the electronic motion can be described by the damped-driven harmonic oscillator problem as

$$m_e \frac{d^2\vec{r}}{dt^2} + m_e\gamma\frac{d\vec{r}}{dt} + K_e\vec{r} = -e\vec{E}\exp[-i\omega t], \tag{2.35}$$

and assuming a harmonic solution $\propto \exp[-i\omega t]$ the equation of motion may be re-expressed as

$$(-m_e\omega^2 - im_e\gamma\omega + K_e)\vec{r} = -e\vec{E}. \tag{2.36}$$

This yields a solution to the polarizability $\vec{P}$ of

$$\vec{P} = Ne\vec{r} = \frac{n_e e^2}{(-m_e\omega^2 - im_e\gamma\omega + K_e)}\vec{E} \tag{2.37}$$

$$= \frac{n_e e^2/m_e}{(\omega_0^2 - \omega^2 - i\gamma\omega)}\vec{E}, \tag{2.38}$$

where here n_e represents the valence electron density, $\omega_0 = \sqrt{K_e/m}$, and γ defines the damping parameter.

Following from the definition of the displacement field in Eqn 2.6 the dielectric permittivity for a dielectric media can be defined as

$$\epsilon[\omega] = \left(1 + \frac{n_e e^2}{m_e\epsilon_0}\frac{1}{(\omega_0^2 - \omega^2 - i\gamma\omega)}\right). \tag{2.39}$$

The description above implicitly assumes that all the electrons within the media were identically bound. This is certainly not the case as there are large differences in the behavior of core and valence bound electrons. To account for the fact that electrons are bound in states with differing resonant frequencies, a sum over all electronic resonance and a fraction factor accounting for the number of electrons sensitive to the resonance may be introduced in the equation for the permittivity. This can be written in the form of

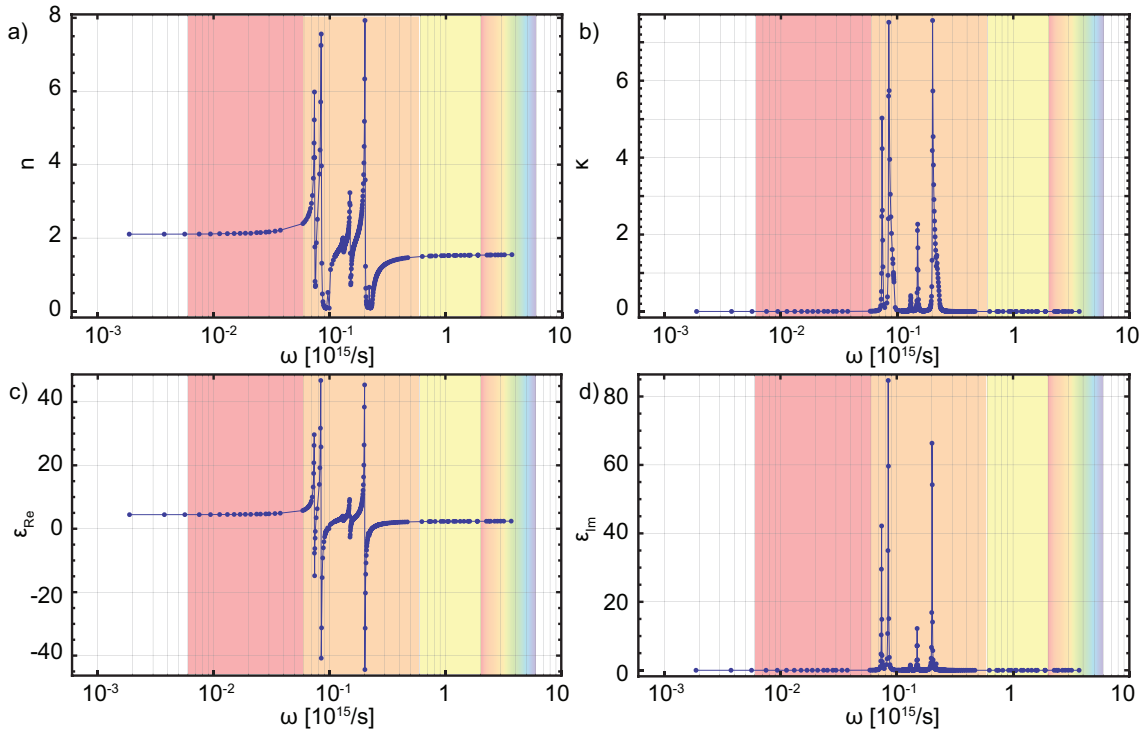

Figure 2.3: The optical constants for the ordinary index of α cut quartz crystal are displayed above over a large frequency range as a demonstration of the typical optical behavior of a dielectric medium. Panels a) and b) display the real n and imaginary κ parts of the index of refraction. Panels c) and d) display the corresponding real and imaginary components of the permittivity, Re[ϵ] and Im[ϵ]. The visible (400-800nm), near-IR (800 nm-3 μm), mid-IR (3- 30 μm), and far-IR (30 -300 μm) spectral ranges are displayed by the rainbow, yellow, orange, and red shading respectively. The characteristic phonon resonances for quartz are clearly evident in the mid-IR spectral range.

$$\epsilon[\omega] = \left(1 + \frac{ne^2}{m_e \epsilon_0} \sum_j \frac{f_j}{(\omega_0^2 - \omega^2 - i\gamma\omega)}\right). \tag{2.40}$$

The interaction of electromagnetic waves with a dielectric media (either a molecule or crystal unit cell) may be described by considering the total dipole moment of the molecule or crystal unit cell,

$$\vec{p} = \vec{p}_{\rm p} + \boldsymbol{\alpha} \cdot \vec{E}_0, \tag{2.41}$$

where $\vec{p}_{\mathrm{p}}$ represents permanent dipole moment (if present), α the polarizability tensor, and $\vec{E}_0$ the incident electric field at frequency $\omega = 2\pi\nu$.

The charges which constitute the structure may oscillate about their equilibrium positions x_E along their normal coordinates q_N at resonant frequencies nu_N determined by the bond strengths/lengths. Implementing a harmonic approximation for small oscillation amplitudes, the variation along the normal coordinate directions may be expressed as

$$q_N[t] = q_{N0}\cos[\omega_N t]. \tag{2.42}$$

For the IR regime, the electric field is constant over range of the oscillation motion. As the structure vibrates, changes in the polarizability and the associated dipole moment are induced which may be approximated in the form of a Taylor expansion as

$$\alpha_{ij}[q] = \alpha_{ij}[x_E] + \sum_N \left(\frac{\partial \alpha_{ij}}{\partial q_N}\right)_{x_E} q_N + \cdots \tag{2.43}$$

Similarly the dipole moment may be expressed as

$$\vec{p}[q] = \vec{p}[x_E] + \sum_N \left(\frac{\partial \vec{p}}{\partial q_N}\right)_{x_E} q_N + \cdots \tag{2.44}$$

In combining Eqns. 2.42, 2.43, and 2.44 the time-dependent dipole moment may be expressed as

$$\vec{p}[q] = \vec{p}[x_E] + \underbrace{\sum_N \left(\frac{\partial \vec{p}}{\partial q_N}\right)_{X_E} q_{N0}\cos[\omega_N t]}_{\text{IR}} \tag{2.45}$$

$$+ \underbrace{\boldsymbol{\alpha}[x_E]\cdot\vec{E}_0\cos[\omega t]}_{\text{Elastic}} \tag{2.46}$$

$$+ \underbrace{\left(\sum_N \left(\frac{\partial \boldsymbol{\alpha}}{\partial q_N}\right)_{X_E} q_{N0}\cos[(\omega \pm \omega_N)t]\right)\frac{\vec{E}_0}{2}}_{\text{Raman}} + ... \tag{2.47}$$

Here, the permanent dipole moment is represented by the first term and the IR active vibrational modes are represented by the second term. The third and fourth terms encapsulate scattering effects. Elastic Rayleigh scattering is described by the third term while

the fourth term represents the Raman effect and inelastic scattering. Implementation Raman spectroscopy characterization techniques may be employed to yield information on the vibrational modes and orientation of a material allowing insight into the symmetry of the system being studied.

2.5 Surface polariton waves.

As scattering-Scanning Near-field Optical Microscopy techniques map the optical fields related to surfaces, it is important to understand the role of surface waves in solid media in order to interpret how the presence of such waves may affect the *s*-SNOM signal. Surface waves exist at an interface between two differing media and propagate in the direction of the surface interface, decaying exponentially in the normal direction to the surface. The coupling of the electromagnetic field of the surface wave to a resonant polarization oscillation in the material results in the formation of what is known as a surface polariton. For metals, this can arise through coupling to the plasmon oscillation of the metal resulting in a surface plasmon polariton (SPP). Correspondingly for dielectric materials, this coupling to the resonant vibrational modes of the material can result in the formation of surface phonon polaritons (SPhP).

The geometry defining surface polariton waves is depicted in Fig. 2.4a). Medium 1, generally defined by frequency dependent permittivity $\epsilon_1[\omega]$ and magnetic permeability $\mu_1[\omega]$ occupies upper half space $z > 0$ whilst medium 2 similarly occupies the lower half space ($\epsilon_2[\omega]$, $\mu_2[\omega]$, $z < 0$). The three unit vectors $\hat{x}$, $\hat{y}$, and $\hat{z}$ define a point in space as $\vec{r} = x\hat{x} + y\hat{y} + z\hat{z}$ and wavevectors as $\vec{k} = k_x\hat{x} + k_y\hat{y} + k_z\hat{z}$. It is simpler to further express these vectors in terms of the in and out-of-plane contributions as $\vec{r} = \vec{R} + \vec{z}$ and $\vec{k} = \vec{k}_{\|} + \vec{k}_{\perp}$ where $\vec{R} = x\hat{x} + y\hat{y}$, $\vec{k}_{\|} = k_x\hat{x} + k_y\hat{y}$, and $\vec{k}_{\perp,i} = k_z\hat{z}$. Fig. 2.4a) shows the relationship of the wavevectors between both the upper and lower media. This geometry is depicted in Fig. 2.4a.

The form of a surface wave with translational invariance decaying exponentially from the interface can be expressed in the following forms in medium 1 and 2 respectively [26],

$$\vec{E}_1(\vec{r},\omega) = \begin{pmatrix} E_{x,1} \\ E_{y,1} \\ E_{z,1} \end{pmatrix} \exp[i(\vec{k_\parallel} \cdot \vec{R} + k_{\perp,1} z)] \tag{2.48}$$

$$\vec{E}_2(\vec{r},\omega) = \begin{pmatrix} E_{x,2} \\ E_{y,2} \\ E_{z,2} \end{pmatrix} \exp[i(\vec{k_\parallel} \cdot \vec{R} - k_{\perp,2} z)]. \tag{2.49}$$

Momentum conservation requires that the sum of the in- and out-of-plane wavevector components add up to the free space wavevector ($k_{\perp,i}^2 + k_{\parallel,i}^2 = \epsilon_i \mu_i k_0^2$). The exponential decay component in the $\hat{z}$ direction in both media are thus defined as

$$k_{\perp,1}^2 = \epsilon_1 \mu_1 k_0^2 - k_\parallel^2 \text{ for } \mathrm{Im}[k_{\perp,1}] > 0 \tag{2.50}$$

$$k_{\perp,2}^2 = \epsilon_2 \mu_2 k_0^2 - k_\parallel^2 \text{ for } \mathrm{Im}[k_{\perp,2}] > 0. \tag{2.51}$$

In the following sections we shall cover the existence of surface waves for both *s*- and *p*-polarized waves.

2.5.1 Surface waves with s-Polarization.

For *s*-polarized light the electric field is parallel to the x-direction. It should be noted that *s*-polarized waves occur solely in magnetic media which are not covered in the scope of this thesis, but for completeness of the description of surface wave physics, the derivation of their dispersion relation is included here [26].

With the field oriented in the $\hat{x}$ direction, the field equations from Eqn. 2.48 and 2.49 can be expressed as

$$\vec{E}_1(\vec{r},\omega) = E_{x,1}\hat{x} \exp[i(\vec{k_\parallel} \cdot \vec{R} + k_{\perp,1} z)] \tag{2.52}$$

$$\vec{E}_2(\vec{r},\omega) = E_{x,2}\hat{x} \exp[i(\vec{k_\parallel} \cdot \vec{R} - k_{\perp,2} z)]. \tag{2.53}$$

The boundary conditions at the surface interface require continuity of both the $\vec{E}$ and $\vec{H}$ fields.

$$E_{x,1} - E_{x,2} = 0 \tag{2.54}$$

$$\frac{k_{\perp,1}}{\mu_1[\omega]} E_{x,1} + \frac{k_{\perp,2}}{\mu_2[\omega]} E_{x,2} = 0. \tag{2.55}$$

We arrive at the second term by expressing $\vec{H}$ in terms of $\vec{E}$ via Faraday's law $\vec{H} = -i\nabla \times \vec{E}/\mu[\omega]\omega$. Solving Eqns. 2.54 and 2.55 to remove $E_{x,1}$ and $E_{x,2}$ the condition for a homogeneous solution is

$$\mu_2[\omega]k_{\perp,1} + \mu_1[\omega]k_{\perp,2} = 0. \tag{2.56}$$

Finally, combining Eqns. 2.50 and 2.51 with Eqn. 2.56, the dispersion relationship for an s-polarized surface wave is derived

$$k_{\parallel}^2 = \frac{\omega^2}{c^2} \cdot \frac{\mu_1[\omega]\mu_2[\omega](\mu_2[\omega]\epsilon_1 - \mu_1[\omega]\epsilon_2)}{\mu_2^2[\omega] - \mu_1^2[\omega]}. \tag{2.57}$$

This relation can be further simplified for the case that $\epsilon_1 = \epsilon_2 = \epsilon$ to

$$k_{\parallel}^2 = \frac{\omega^2}{c^2}\epsilon\frac{\mu_1[\omega]\mu_2[\omega]}{\mu_1[\omega] + \mu_2[\omega]}. \tag{2.58}$$

2.5.2 Surface waves with p-Polarization.

The p-polarized or Transverse Magnetic (TM) solution for the surface wave is the solution of interest for optical excitations. Here the equations for the field of the surface wave in both upper and lower half-space may be expressed as [26]

$$\vec{E}_1(\vec{r},\omega) = \begin{pmatrix} 0 \\ E_{y,1} \\ E_{z,1} \end{pmatrix} \exp[i(\vec{k_{\parallel}} \cdot \vec{R} + k_{\perp,2}z)] \tag{2.59}$$

$$\vec{E}_2(\vec{r},\omega) = \begin{pmatrix} 0 \\ E_{y,2} \\ E_{z,2} \end{pmatrix} \exp[i(\vec{k_{\parallel}} \cdot \vec{R} - k_{\perp,2}z)]. \tag{2.60}$$

Continuity of the tangential field requires that

$$E_{y,1} - E_{y,2} = 0. \tag{2.61}$$

Gauss' Law further requires that $\nabla \cdot \vec{E} = 0$, which imposes a relation between the two

components of the electric field

$$k_{\|}E_{y,2} - k_{\perp,2}E_{z,2} = 0 \tag{2.62}$$

$$k_{\|}E_{y,1} - k_{\perp,1}E_{z,1} = 0. \tag{2.63}$$

Continuity of the z-component of $\vec{D}$ finally requires

$$\epsilon_1[\omega]E_{z,1} = \epsilon_2[\omega]E_{z,2}. \tag{2.64}$$

Solving the four boundary condition equations from Eqns. 2.61, 2.62, 2.63, and 2.64, one arrives at the condition for a homogeneous solution,

$$\epsilon_1[\omega]k_{\perp,2} + \epsilon_2[\omega]k_{\perp,1} = 0. \tag{2.65}$$

Through combination of Eqns. 2.50 and 2.51 with Eqn. 2.65, the dispersion relationship for p-polarized surface wave can be expressed as

$$k_{\|}^2 = \frac{\omega^2}{c^2} \cdot \frac{\epsilon_1[\omega]\epsilon_2[\omega](\epsilon_1[\omega]\mu_1 - \epsilon_2[\omega]\mu_2)}{\epsilon_2^2[\omega] - \epsilon_1^2[\omega]}. \tag{2.66}$$

for the case that $\mu_1 = \mu_2 = \mu$, this relation further simplifies to

$$k_{\|}^2 = \frac{\omega^2}{c^2}\mu\frac{\epsilon_1[\omega]\epsilon_2[\omega]}{\epsilon_1[\omega] + \epsilon_2[\omega]}. \tag{2.67}$$

For the specific case of a material-vacuum interface $\epsilon_1 = \mu_1 = 1$, the dispersion relation for the surface polariton is

$$k_{\|}^2 = \frac{\omega^2}{c^2}\frac{\epsilon_2[\omega]}{1 + \epsilon_2[\omega]}. \tag{2.68}$$

This surface wave dispersion relationship is shown for surface plasmons in the visible for an Ag surface in Fig. 2.4b and for surface phonon polaritons in quartz in Fig. 2.4c.

2.6 Properties and visualization of surface waves.

It is interesting to note that in the presence of losses, the dispersion relation yields two equations; however, both frequency and wavevector can be complex yielding four parameters. Two cases are of practical interest: (1) a real frequency and a complex wavevector and (2) a complex frequency and a real wavevector. These two choices lead to different shapes

of the dispersion relation, as discussed in [27–29]. The imaginary part of ω describes the finite lifetime of the mode due to losses. Conversely, for a given real ω, the imaginary part of $k_{\|}$ yields a finite propagation length along the interface.

Fig. 2.4 displays visualizations of the geometry (a), dispersion relationships (b,c), and spatial field distribution (d-i) of the surfaces waves discussed in the previous sections. In particular, the correspondence between the proximity of the surface wave dispersion solution to the light-line and the degree of localization of the surface wave fields to the surface is depicted in panels d-i). For the Ag surface-wave dispersion relationship shown in Fig. 2.4b, surface waves in the IR occur near the light-line (purple star). Correspondingly, the solution for the surface wave is "light"-like in that the field is contained primarily outside the surface medium (panels d,e). As the frequency approaches the surface wave resonance frequency (green star), the momentum of the surface-wave becomes bigger with respect to the free-space wavevector of light resulting in a higher degree of localization (panels f,g). Finally, near the resonance frequency, the momentum of the surface wave is large, resulting in a high degree of localization to the surface with the field contained in- and out of the surface medium (panels h,i).

Surface waves may be typically categorized into four types: Fano, Evanescent, Brewster, and Zenneck modes. Fano and evanescent modes are identified with surface polariton waves. The Brewster case is known to far-field optics as the case in which p-polarized light is incident at an interface at angle θ_1 and refracted at angle θ_2, that there is no reflected light when $\theta_1 + \theta_2 = 90°$. When damping is present, a solution for Maxwell's equations exists such that the amplitudes of the two rays decay exponentially from the interface. Zenneck modes are identical to electromagnetic waves which propagate at a conducting surface. Fig. 2.5 shows the relationship between the dielectric conditions necessary for each type of surface wave.

The location and relationship with these surface modes with the dispersion relationship is visualized in Fig. 2.6. Here, the real and imaginary parts of the dielectric permittivity are plotted for an hypothetical dielectric medium a) and a Ag surface c). The permittivity of the dielectric medium shown in panel a) follows the functional form following ref [30],

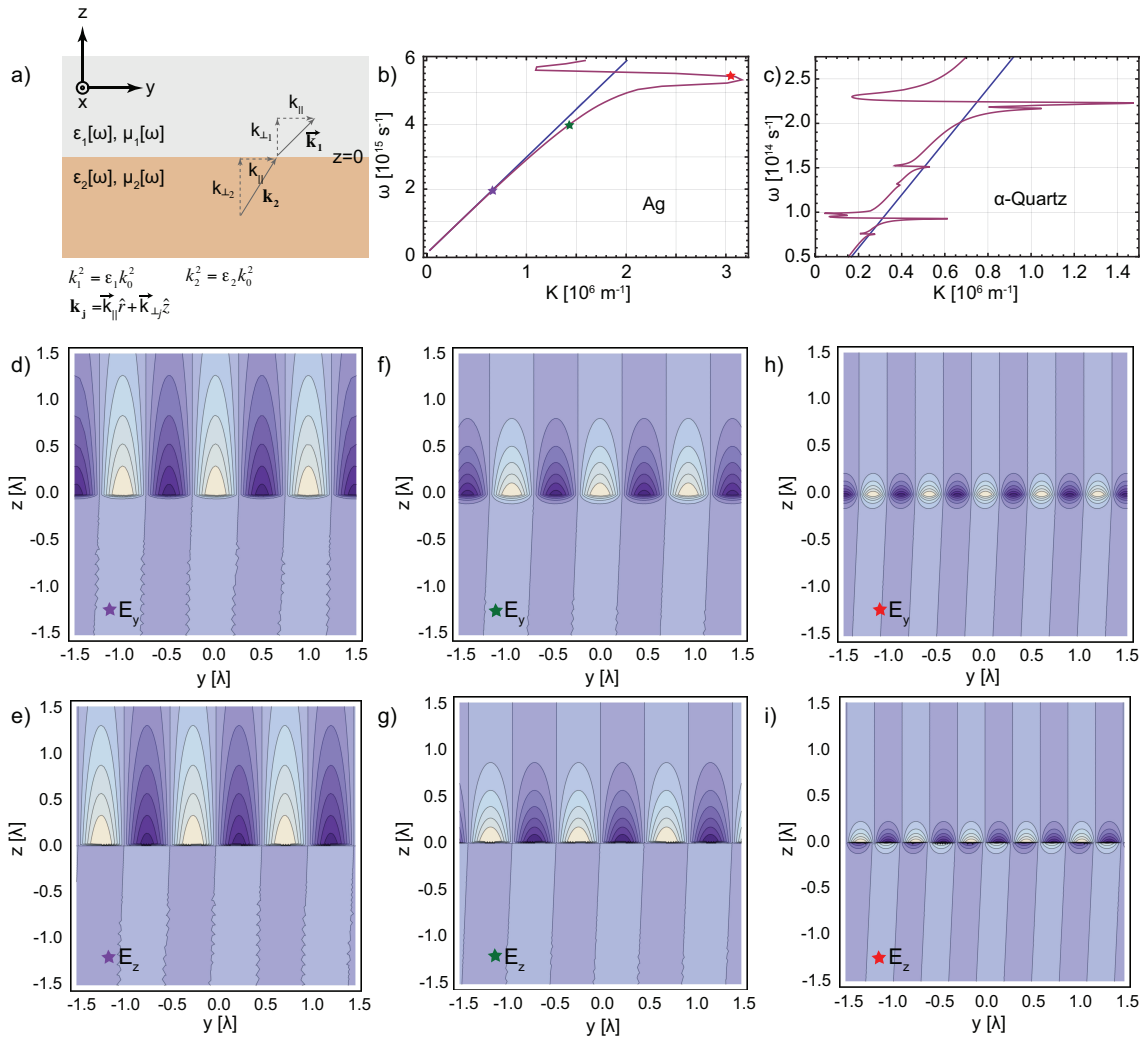

Figure 2.4: The geometry and relevant parameters for surface waves are displayed in panel a). As an example of the formation of both surface plasmon polaritons and surface phonon polaritons, the dispersion relationship where surface waves exist is shown for Ag in the IR-to visible range (b) and quartz in the mid-IR spectral range (c). Panels d-i) represent the visualization of the spatial distribution of the electric field for different points along the dispersion curve of Ag (denoted by the colored stars in panel b). Here spatial distributions of the E_y and E_z field components are shown for $\omega = 2 \cdot 10^{15}$ (purple star, panels d) and e), $\omega = 4 \cdot 10^{15}$ (green star, panels f) and g), and $\omega = 2 \cdot 10^{15}$ (red star, panels h) and i).

Mode	Dielectric function	Wavevector component	Phase velocity	comment
Fano	$\mathrm{Re}[\epsilon] \leq -1$ $\mathrm{Im}[\epsilon] \ll \lvert\mathrm{Re}[\epsilon]\rvert$	$\mathrm{Re}[k_\parallel] \gg \mathrm{Im}[k_\parallel]$ $\mathrm{Re}[k_\perp] \ll \mathrm{Im}[k_\perp]$	$< c$	True surface mode
Evanescent	$-1 \leq \mathrm{Re}[\epsilon] \leq 0$ $\mathrm{Im}[\epsilon] \simeq \lvert\mathrm{Re}[\epsilon]\rvert$	$\mathrm{Re}[k_\parallel] \simeq \mathrm{Im}[k_\parallel]$ $\mathrm{Re}[k_\perp] \simeq \mathrm{Im}[k_\perp]$		Rapidly attenuating
Brewster	$\mathrm{Re}[\epsilon] > 0$ $\mathrm{Im}[\epsilon] \ll \mathrm{Re}[\epsilon]$	$\mathrm{Re}[k_\parallel] \gg \mathrm{Im}[k_\parallel]$ $\mathrm{Re}[k_\perp] \gg \mathrm{Im}[k_\perp]$	$> c$	Bound to surf. in pres. of damping
Zenneck	$\mathrm{Re}[\epsilon] \ll -1$ $\mathrm{Im}[\epsilon] \gg \lvert\mathrm{Re}[\epsilon]\rvert$	$\mathrm{Re}[k_\parallel] \gg \mathrm{Im}[k_\parallel]$ $\mathrm{Re}[k_\perp] \simeq \mathrm{Im}[k_\perp]$	$\gtrsim c$	prop in conductive media

Figure 2.5: Summary of surface electromagnetic modes following ref [28].

$$\epsilon[\omega] = 1 + \epsilon_\infty \cdot \left(\frac{\omega_{T,1}^2 - \omega_{L,1}^2}{\omega(\omega + i\Gamma_1) - \omega_{T,1}^2} \right) + \frac{\omega_{T,2}^2 - \omega_{L,2}^2}{\omega(\omega + i\Gamma_2) - \omega_{T,2}^2}, \tag{2.69}$$

where $\epsilon_\infty = 6$, $\omega_{T,1} = \omega_{T,1}$, $\omega_{T,2} = 5\omega_{T,1}$, $\omega_{L,1} = 2\omega_{T,1}$, $\omega_{L,2} = 6\omega_{T,1}$, $\Gamma_1 = 0.05\omega_{T,1}$, and $\Gamma_2 = 0.05\omega_{T,1}$. The areas where Fano (red), Evanescent (orange), Brewster (blue), and Zenneck (green) waves occur are denoted on the graphs. It is interesting to note that Zenneck waves may occur for dielectric media, but only at localized frequencies. Zenneck waves in conductors, in contrast, span the entire low frequency regime.

2.7 Outlook.

The surface waves discussed above play an important role in nano-scale optical physics as they act as a mechanism to achieve highly confined fields. These waves take the form of surface plasmon polaritons and surface phonon polaritons which represent the collective coherent electron/polarizatability oscillations which exist at the interface between any two materials where the real part of the dielectric function changes sign across the interface (e.g. a metal-dielectric interface). The localization of the optical fields enabled by these types of surface waves are highly desirable by many photonic and molecular sensing applications.

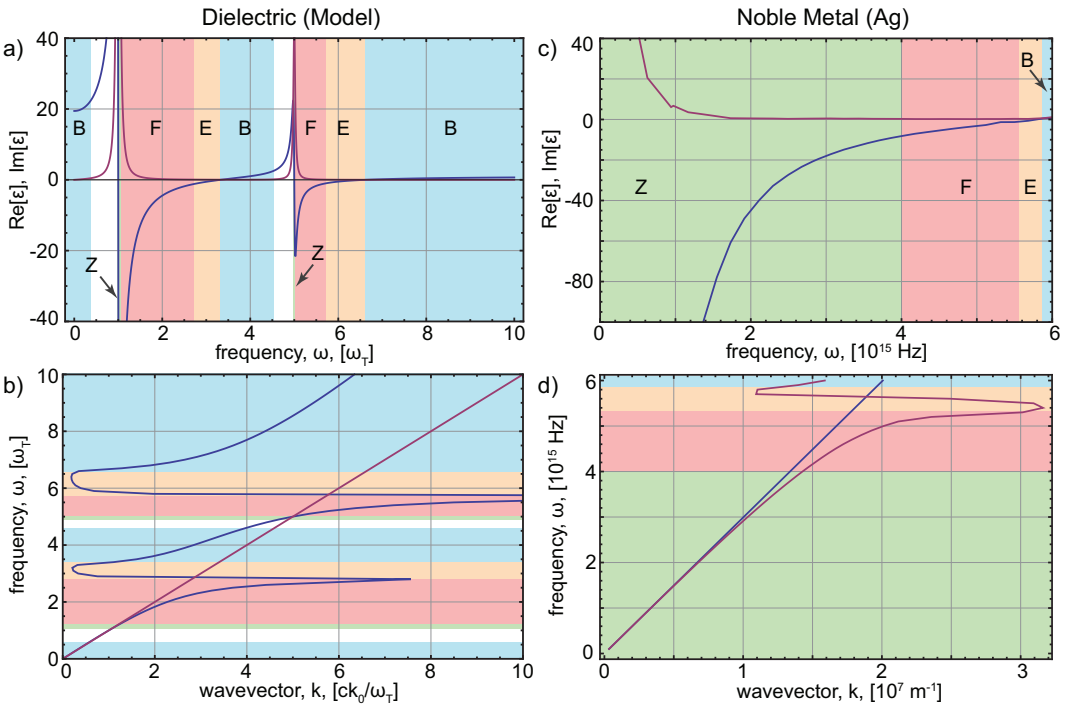

Figure 2.6: The real (blue) and imaginary (magenta) parts of the dielectric permittivity for a model dielectric (following ref [30]) a) and an Ag c) surface are displayed. The corresponding surface wave dispersion relation is displayed in panels b) and d) respectively. The colored regions denote the frequency range in which Fano (red), Evanescent (orange), Brewster (blue), and Zenneck (green) type solutions occur.

One such application is the extension of the concept of a surface wave to a finite-sized nano-structure where coherent optical resonances are known as localized surface plasmon resonances (LSPR). In the following chapters, the role of surface waves in *s*-SNOM characterization will be discussed with a special emphasis on how surface waves affect the LSPR in metallic nano-structures and the intrinsic thermal electromagnetic local density of states above surfaces.

Chapter 3

SCATTERING-TYPE SCANNING NEAR-FIELD OPTICAL MICROSCOPY TECHNIQUES.

scattering- type Scanning Near-field Optical Microscopy (*s*-SNOM) represents the unification of two distinct lines of experimental characterization techniques: optical characterization and scanning probe microscopy. Here, taking advantage of the optical antenna properties of a nanoscopic atomic force microscope tip allows the combination of the sensitivity of optical characterization to the solid state excitations with the high spatial resolution of scanning probe microscopy techniques. In the following chapter, the origin and historical development of the concept of near-field, sub-diffraction, optical imaging will be discussed. The physical principles of the optical contrast in *s*-SNOM characterization techniques will be detailed with a specific focus on current methods of signal amplification and background filtering. These concepts are motivated by the desire to extract specific information about the properties of near-fields/surfaces while minimally perturbing the intrinsic fields and avoiding the presence of unrelated background signals.

3.1 Introduction to optical microscopy and the diffraction limit.

Optical microscopy has long been a useful technique for the scientific characterization of material properties. For short length-scale resolution, conventional microscopy techniques typically implement lens/mirror systems in order to collect and focus far-field radiation to form a magnified image of the specimen or sample in question. Fig. 3.1a) schematically displays this concept for an infinity corrected microscope lens system illustrating the inversion and magnification of an image of the sample.

In terms of spatial resolution, the limit of any far-field microscopy technique is defined by both the aberration and diffraction of the optics in the imaging system. While aberration effects can in principle be corrected for through modification of the geometric properties of the optics, the diffractive limits on the resolution cannot be corrected. This is a consequence

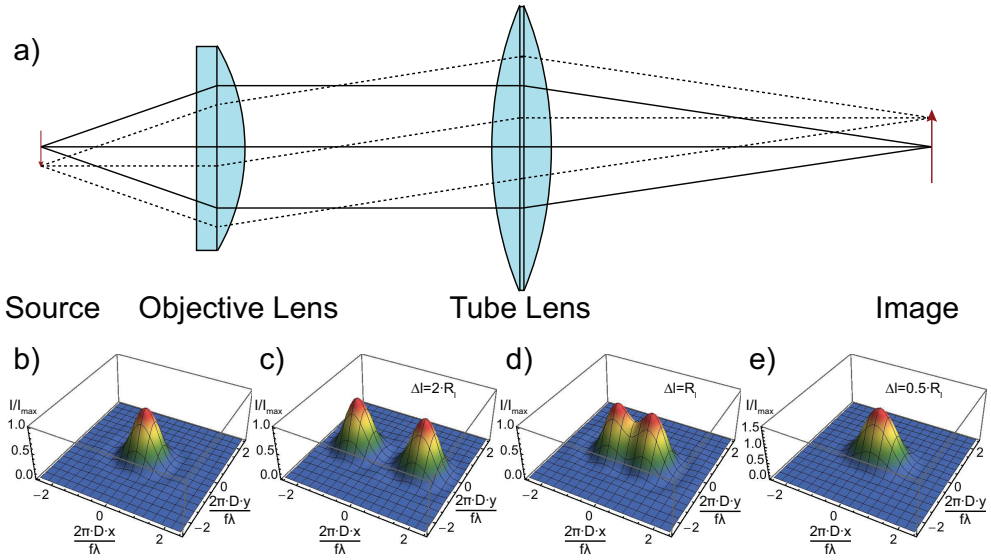

Figure 3.1: a) A simple beam diagram for an infinity corrected microscope. b) The Airy disk distribution for a point source scatterer for NA=0.5 lens system. Panels c-e) demonstrate the diffraction limit for two point scatters with separations of multiples of 2, 1, and 0.5 the Rayleigh limit R_l respectively.

of the wave-like nature of light as it passes through the finite sized apertures of optical imaging elements [4].

The resolution of any optical system may be defined by it point spread function. Consider a point source radiator; as the source is infinitely small in size, it is characterized by an infinite spectrum of spatial frequencies k_x and k_y. Via the propagation of light from the image to the source, frequency contributions corresponding to evanescent waves ($(k_x^2+k_y^2) > k_0^2$, where $k_0 = 2\pi/\lambda$) are filtered out. In addition, not all of the propagating waves emitted by the point source radiator can be collected leading to further reductions in bandwidth. As a result, a complete image of the point source may not be constructed and thus will have finite size [14].

The image of any point source formed via a focusing lens forms an Airy disk spatial distribution through diffraction due to the finite aperture D of the lens (Fig. 3.1b). The description for the ultimate resolution attainable through an optical microscope was realized

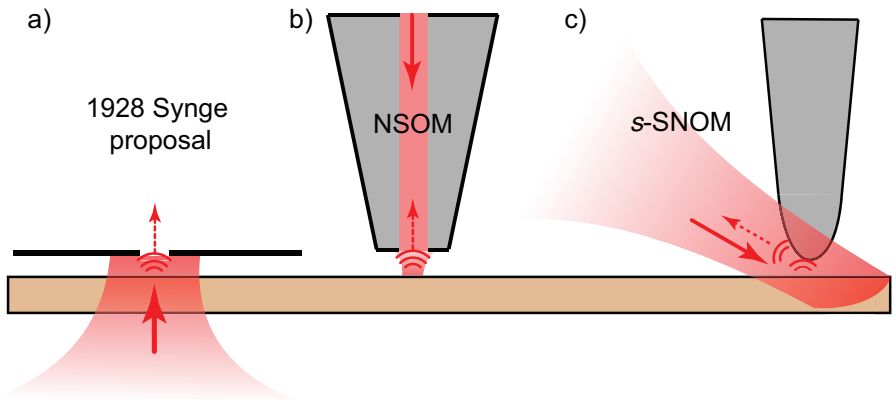

Figure 3.2: a) The experimental schematic for Synge's original 1928 proposal for sub-diffraction imaging on biological samples. Simple sketches of the conceptual experimental geometry for modern NSOM and *s*-SNOM measurements are displayed in panels b) and c) respectively.

early on in the development of the modern microscope; here, the most widely accepted form of the diffraction limit on the resolution of a lens was given by Rayleigh in 1896 [31]. The Rayleigh limit on spatial resolution R_l, i.e., the distance Δl at which two point sources can be separated and distinguished from one another, is determined by the distance at which the maxima of the Airy distribution of one point source overlaps the minima of the Airy distribution of the second point source. This can be expressed through the following relation,

$$R_l \simeq \frac{1.22 f \lambda}{D} = \frac{0.61 \lambda}{\mathrm{NA}}, \tag{3.1}$$

where λ represents the wavelength of light, f the focal distance of the lens, D the aperture diameter of the lens, and NA the numerical aperture of the lens. This diffraction limit to resolution is displayed in Fig. 3.1c-e) where the image formed by two point sources separated by distances of $2R_l$, R_l, and $0.5R_l$ is given in panels c), d), and e) respectively.

3.2 Towards breaking the diffraction limit: the development of scanning probe techniques.

The concept of an experimental apparatus with the ability to optically characterize samples with resolution below the diffraction limit dates back to a proposal by E.H. Synge in the late 1920s. Although limited by the technology of the era, Synge foresaw a means of imaging below the diffraction limit by virtue of the transmission of light through a small aperture (a proposed 10 nm) which he suggested be placed above a biological sample. The difficulty at the time of the Synge's proposal was four-fold: 1) a source of illumination which was suitably intense needed to be found, 2) nanometer scale precision positioning of the sample was required, 3) the sample surface needed to be suitably flat, and 4) the construction of an opaque plate or film with the small hole would be needed [32].

With the evolution of advanced scientific instrumentation and measurement techniques, each experimental obstacle above would eventually be overcome. First, the requirement of a strong illumination source is today satisfied through the implementation of high fluence laser sources. The second challenge, a mechanism for sub-nanometer control of spatial movement, is met through the use of piezo-electric scanner-positioners. Finally, both the third and fourth obstacles would be overcome through the development of scanning probe microscopy, which began in the early 1980s with the development of instrumentation to utilize a sharpened probe in order to scan sample surfaces.

An initial demonstration of Synge's proposed measurement for sub-diffraction resolution was demonstrated in 1983 [33]. The technique, initially dubbed "optical stethoscopy," utilized a gold-coated quartz crystal with a sharp tip apex where the gold was removed to create a small aperture through which laser light could transmit to the sample. It was, however, the demonstration of a new technique in 1983 that would set the stage for the development of modern sub-diffraction imaging methods.

The advent of Scanning Tunneling Microscopy (STM) [11] and subsequently Atomic Force Microscopy (AFM) [12, 13] techniques enabled the fine control of the height position of an experimental probe above a surface via implementation of either tunneling current (STM) or atomic force (AFM) feedback. This represented a major advance in nanoscale

characterization techniques and was soon combined with sub-diffraction imaging efforts to yield the first spatial characterization of evanescent fields at optical frequencies [34].

A further advance came in the following years with the creation of aperture probes made by metal coating thermally pulled quartz optical fibers [35–37], initiating the technique now widely known as Near-field Scanning Optical Microscopy (NSOM) (Fig. 3.3b). Here, the small aperture in the metal of the fiber tip acts as the modern realization of Synge's proposed aperture in an opaque slide with the further advantage that it may be paired with an intense light source via the optical fiber.

NSOM measurement techniques have subsequently been applied towards the characterization of a wide variety of experimental systems. The technique, however, has a limited the spectral range as the optical fiber restricts wavelengths to the visible to near-infrared regimes. Furthermore, the transmission of light through the probe aperture limits the resolution attainable via NSOM. As described by Bethe in 1944, the total power of transmission P_{trans} through a small aperture of radius a in a metallic film scales $\propto (1/\lambda)^4$ as given below [38],

$$P_{\text{trans}}(\lambda, a, E_{\text{inc}}) = \underbrace{\frac{64}{27\pi}\left(\frac{2\pi a}{\lambda}\right)^4 a^2}_{\sigma_{\text{eff}}} \cdot \underbrace{\frac{c}{2}\varepsilon_0 E_{\text{inc}}^2}_{\text{incident flux}} , \tag{3.2}$$

where $c/2 \cdot \varepsilon_0 E_{\text{inc}}^2$ represents the the incident flux on the aperture and the σ_{eff} term represents the effective transmission cross-section of the aperture.

As a consequence of the aperture transmission, resolution of NSOM measurements comes at the cost of severe depletion of its signal magnitude; for $\lambda/10$ spatial resolution, the illumination is depleted by a factor of over 10^{-5}. In most practical measurements, this limits the resolution of NSOM techniques to $\simeq 50 - 100$ nm. In order to access a larger spectral range and to achieve higher spatial resolutions, a near-field optical technique which does not utilize optical fibers or apertures is required. As will be presented in the following sections, this is achieved through the realization of a sharp ($\simeq$ 10 nm) AFM probe as a near-field scattering/field enhancement source.

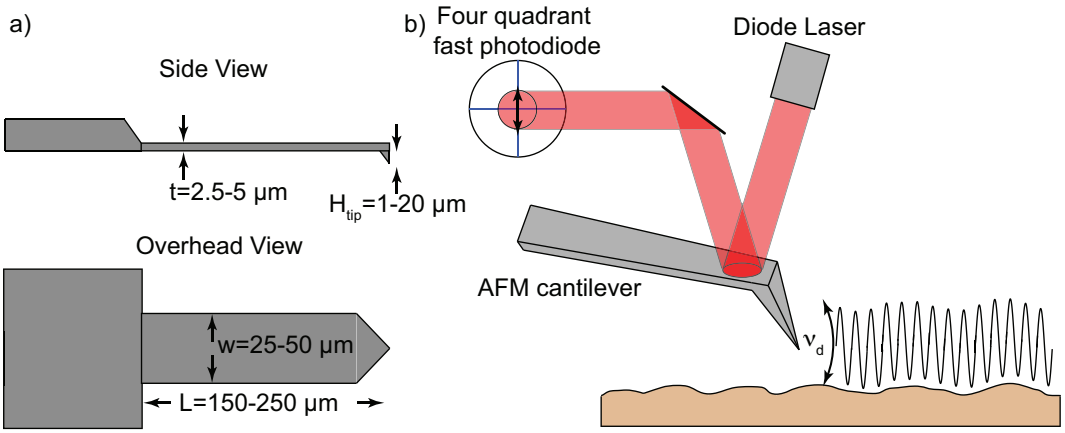

Figure 3.3: a) the geometric layout of typical and size ranges for typical commercially available AFM probes. b) Schematic for non-contact/tapping mode AFM measurements where the magnitude of the vertical oscillation of the tip is monitored, for example here with a diode laser and four-quadrant photodiode, and used to maintain dynamic feedback with a sample surface.

3.3 Non-contact AFM probes as mechanism for a localized near-field scattering source.

Rather than use an aperture for sub-diffraction imaging, a more simple approach of utilizing the localized electric field enhancement between an extremely sharp AFM probe ($\simeq 10$ nm) and the surface may be implemented. This concept of an apertureless near-field optical microscope was developed throughout the 1990s first through use of STM probes [39,40] and eventually AFM techniques as feedback mechanisms [40–42]. These initial measurements utilizing an AFM to demonstrate that a sharp tip scatterer could provide high spatial resolution would lay the groundwork for the technique of *scattering*-Scanning Near-field Optical Microscopy (*s*-SNOM).

The advantage of AFM techniques is that the sharp probe of an AFM tip may be in close proximity with a wide variety of surfaces (unlike STM which requires a conductive substrate). This is accomplished by the transduction of surface forces experienced by the sharp AFM probe tip into a measurable quantity. In AFM microscopy, a sharp probe is attached to the end of a soft cantilever beam. Subsequent observation of the deflection

of the cantilever from its equilibrium position yields information about the forces exerted on the tip. Small changes in the deflection of the cantilever can be sensed by shining a diode laser onto the back of the cantilever; its reflection is directed onto a four-quadrant photodetector (Fig. 3.3).

In dynamic non-contact/tapping mode atomic force microscopy, the cantilever beam is resonantly driven via a dither piezo such that it oscillates with amplitude A_0. The geometric dimensions of commercially available tapping mode cantilever beams are displayed in Fig. 3.3a). In a typical measurement, displayed in Fig. 3.3b), vertical motion of the AFM tip is excited through driving of the dither piezo. As the AFM approaches the surface, the cantilever motion is damped through interaction with the surface resulting in a decrease in cantilever oscillation amplitude. A reduced cantilever oscillation amplitude A can be utilized via PID control setpoint/feedback mechanisms to maintain the tip in close dynamic feedback with the surface. Values for the ratio of the feedback setpoint to amplitude of free oscillation usually fall in the range of $A/A_0 = 0.7 - 0.9$.

For a specific cantilever beam, the spring constant k_c and the associated free-space resonance frequency ω_{c0} is dependent on both the cantilever geometry and size and can be expressed as [43]

$$k_c = \frac{Ywt^3}{4L^3}, \tag{3.3}$$

and

$$\omega_{c0} = 0.162 \cdot \frac{2\pi t}{L^2}\sqrt{\frac{Y}{\rho}} = \sqrt{\frac{k_c}{m^*}}. \tag{3.4}$$

where t is the beam thickness, w the width, L the length, Y the Young's modulus of the material, and ρ the mass density of the beam material. The quantity m^* represents the "effective mass" of the cantilever beam system.

Since most measurements are performed in ambient conditions, the primary contribution to the damping on the cantilever motion is viscous drag through the air. This damping force is linear in velocity, which allows for the motion of the tip of the AFM cantilever to be modeled as a damped harmonic oscillator driven by a harmonic force.

$$\ddot{z}(t) + 2\gamma\dot{z}(t) + \omega_{c0}^2 z(t) = \frac{F\exp[i\omega t]}{m^*} \tag{3.5}$$

Here the decay constant γ is related to the viscous drag coefficient b and quality factor Q of the cantilever by the relation

$$\gamma = \frac{\omega_{c0}}{2Q}. \tag{3.6}$$

The general solution to Eqn. 3.5 can be expressed as

$$z(t) = \alpha\exp[-\gamma t + i(\omega' t + \theta)] + A_c\exp[i(\omega t + \phi)]. \tag{3.7}$$

The first term in Eqn. 3.7 represents the transient decay of the initial conditions of the oscillator specified by α and θ, where $\omega' = \sqrt{\omega_{c0}^2 - \gamma^2}$. For example, for a typical cantilever beam resonance in ambient conditions as depicted in Fig. 3.4, ω'^{-1} defines a response time of the cantilever system inversely proportional to Q and approximately 1 ms. It is important to note that the response time of the cantilever is governed by this parameter limiting the ultimate scanning rate of the cantilever.

The second term in Eqn. 3.7 represents the steady state solution which yields a harmonic time-dependent z motion of the tip as well as solutions for the cantilever oscillation amplitude $A_c(\omega)$ and the cantilever phase ϕ. For long t,

$$z(t) = A_c\exp[i(\omega t + \phi)] \tag{3.8}$$

$$A_c(\omega) = \frac{(F/m^*)}{\sqrt{(\omega_{c0}^2 - \omega^2)^2 + \omega^2\omega_{c0}^2/Q^2}} = \frac{(F/m^*)}{\sqrt{(\omega_{c0}^2 - \omega^2)^2 + 4\omega^2\gamma^2}} \tag{3.9}$$

$$\phi = -\arctan\left[\frac{\omega\omega_{c0}}{Q\cdot(\omega_{c0}^2 - \omega^2))}\right] = -\arctan\left[\frac{2\omega\gamma}{(\omega_{c0}^2 - \omega^2))}\right]. \tag{3.10}$$

The peak cantilever oscillation amplitude here occurs at $\omega_{peak} = \sqrt{\omega_{c0}^2 - \omega_{c0}^2/2Q^2} = \sqrt{\omega_{c0}^2 - 2\gamma^2}$ and may be expressed as

$$A_c(\omega_{peak}) = \frac{F}{m^*}\cdot\frac{2Q^2}{\omega_{c0}^2\sqrt{-1+4Q^2}} = \frac{F}{m^*}\cdot\frac{1}{2\gamma\left(-1+\frac{\omega_{c0}^2}{\gamma^2}\right)}. \tag{3.11}$$

The phase lag ϕ between the cantilever and the driving piezo is zero for driving frequencies far below ω_{peak}, $\pi/2$ on resonance, and π for driving frequencies much greater than

ω_{peak}. In certain circumstances, the measurement of variations in the cantilever phase can provide useful information about the damping properties of the surface. Driving at a constant, near-resonance frequency the absolute phase is $\simeq 0$. While the driving frequency from the dither piezo remains constant, variations in the damping properties as the tip tracks the surface will affect the Q factor of the system, thus varying the resonance frequency of the cantilever system ($\omega_{peak} \propto Q$). The variation in resonance frequency when driving at a fixed resonant dither frequency can be measured by tracking the phase shift from zero via the following expression,

$$\phi(\Delta\omega) = -\arctan\left[\frac{1+\frac{\Delta\omega}{\omega_{c0}}}{Q(1-(1+\frac{\Delta\omega}{\omega_{c0}}))}\right]. \tag{3.12}$$

Using the identity that $-\arctan[x] = \mathrm{arccot[x]} - \pi/2$, we can define a shifted phase variable $\psi = \phi - \pi/2$ such that,

$$\psi(\Delta\omega) = \mathrm{arccot}\left[\frac{1+\frac{\Delta\omega}{\omega_{c0}}}{Q(1-(1+\frac{\Delta\omega}{\omega_{c0}}))}\right]. \tag{3.13}$$

Expressing in terms of an arctan function and expanding to first order in a Taylor series around $\Delta\omega/\omega_{c0}$, it can be shown that for small $\Delta\omega$,

$$\psi(\Delta\omega) = \arctan\left[\frac{Q(1-(1+\frac{\Delta\omega}{\omega_{c0}}))}{1+\frac{\Delta\omega}{\omega_{c0}}}\right] \simeq \mathrm{arccot}\left[-\frac{2Q\Delta\omega}{\omega_{c0}}\right] \simeq -2Q\Delta\omega/\omega_{c0}. \tag{3.14}$$

This relation of observable quantities to the small changes in interaction forces between the tip and the surface illustrates the strong transduction sensitivity of the cantilever system.

3.4 The principle of scattering-Scanning Near-field Optical Microscopy.

The operating principle of *scattering*-type Scanning Near-field Optical Microscopy (*s*-SNOM) is that the sharp tip of the cantilever (generally 5-15 nm radius of curvature) acts as a localized scattering source for electric fields induced between the tip and the surface. The origin of the induced electric field may come from a variety of sources including coherent continuous-wave lasers, pulsed lasers, incoherent external broadband thermal sources [44], as well as the intrinsic thermal light produced by the tip/substrate system as will be discussed in chapter 5.

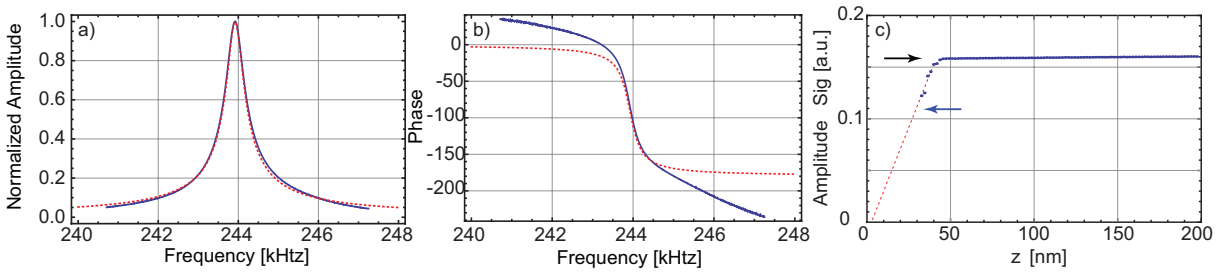

Figure 3.4: The panels above illustrate the measured (blue solid line) and corresponding fitted model (red dotted line) for a) the amplitude of oscillation and b) phase for a typical AFM probe (Arrow NC-pt, resonance frequency = 239.92 kHz, $Q \simeq 600$). A typical approach curve is displayed in panel c) which illustrates the reduction of the AFM oscillation amplitude as the tip begins interacting with the surface. The free-space oscillation amplitude (black arrow) and a typical feedback set-point value (blue arrow) are displayed.

Fig. 3.5 illustrates the experimental layout of a typical s-SNOM measurement. The defining characteristic of all s-SNOM measurements is the utilization of a non-contact/tapping mode AFM tip held fixed within the focus of a collective objective/parabolic mirror as a mechanism for generating a sub-diffraction sized scattering center whose scattering contribution may be differentiated from the total optical signal collected from the entire focal region. The requirement that the tip position remain fixed and centered in the focus of the collection objective necessitates that AFM scanning be performed via sample scanning (as opposed to tip-scanning).

Separation of the tip-apex scattered light from the large background signal occurs via filtering the total detected optical signal using a lock-in amplifier to extract the component of the total signal that varies at the harmonics of the tip-dither frequency (ν_d, $2\nu_d$, ..., $n\nu_d$). While the component of the signal at ν_d generally contains large background contributions attributable to scattering from the tip shaft regions away from the surface, the signal components at higher harmonics ($2\nu_d$, ..., $n\nu_d$) are associated with the enhancement of the field between the tip-apex and the surface. As will be explicitly derived in the following sections, measurement of these signal contributions directly relates information on the magnitude of the near-fields associated with the surface.

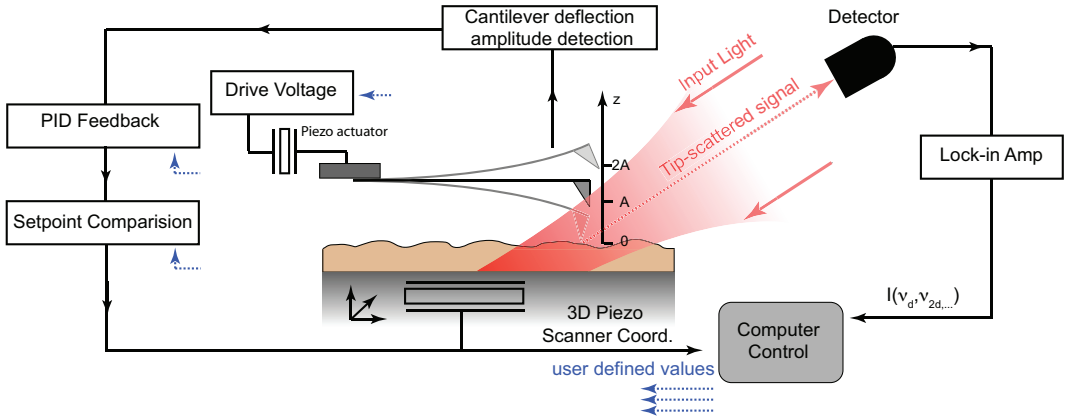

Figure 3.5: A general schematic of a *s*-SNOM measurement illustrating the combination of dynamic feedback of the AFM with the surface topography, correlated with the detection of the contribution of optical signal varying at the harmonics of the tip-dither frequency (ν_d, $2\nu_d$, ..., $n\nu_d$)

As shown schematically in Fig. 3.5, in typical measurements a control computer simultaneously controls/records the topographic position of the AFM probe above the surface while recording the optical near-field scattering contribution to create correlated topography and optical scattering maps of a given surface.

In this implementation, the advantages of *s*-SNOM measurements are two-fold. First, the free-space illumination of the AFM tip allows for a wide frequency range of optical excitation extending from the UV to the far-infrared. Second, the enhancement of fields between the AFM-tip and the surface occurs in a highly localized area in the tip-sample gap region. An example of the highly localized field enhancement is displayed in Fig. 3.6b), which shows a 2D map of the field intensity between an Au tip and an Au surface with an excitation wavelength of $\lambda = 800$ nm. Here, the enhancement of the field distribution in both the z and x directions can be modeled (Fig. 3.6c and d) by describing the AFM tip in the electrostatic limit as a hyperboloidal structure [45]. As the field distribution is highly localized, the ultimate resolution limit to *s*-SNOM characterization is typically restricted to the diameter of the AFM tip-apex (5-15 nm).

3.5 Origin of optical near-field signal: the coupled dipole model for tip-sample optical interaction.

As discussed previously, the total optical field incident on the detector $\vec{E}_{\mathrm{det}}$ can be viewed as having several components including background, near-field, and an optional reference field contribution. The background signal $\vec{E}_{\mathrm{bg}}$ originates from scattering processes attributable to spurious optical reflections from components in the optical beam-line as well as backscattering from the large focus area on the tip-shaft/surface. $\vec{E}_{\mathrm{bg}}$ is typically orders of magnitude larger than the near-field contribution $\vec{E}_{\mathrm{nf}}$ and is experimentally undesirable because it contains no information on the surface near-fields of interest.

The intrinsic difference between the background and near-field signal contributions which allows for their separation in detection is that the near-field signal strength greatly increases as the AFM probe approaches the surface. While $\vec{E}_{\mathrm{bg}}$ is large, it does not significantly vary with the vertical position of the AFM tip apex as it modulates with frequency ν_d and amplitude A in dynamic force feedback above the surface. This means that the detected background signal is largely contained in either the DC or ν_d frequencies.

Conversely, $\vec{E}_{\mathrm{nf}}$ is enhanced through the tip-sample interaction as the AFM tip-apex nears the surface. This enhancement occurs through the mutual interaction of the polarized AFM probe with its own image dipole in the surface. The formation of an image dipole results from the redistribution of surface charges as a response to the fields associated with the AFM tip and can be derived as a simple consequence of Maxwell's equations for a surface interface in the electrostatic limit (for heights above the surface $z \ll \lambda$). Fig. 3.6a) schematically depicts the geometry of the tip-dipole with its own image below the surface.

The effective polarizability of the tip can be defined as the polarizability of the AFM tip under the influence of both the external electric field and the field of its own image dipole in the surface. This effective polarizability of the tip can be simply modeled by approximating the AFM tip as a simple polarizable sphere above a planar surface [15, 46]. While more complex models have been put forth incorporating, for example, the elongated structure of the AFM probe [47, 48], the approximation of a tip as a polarizable sphere qualitatively describes the correct enhancement behavior and to first order correctly

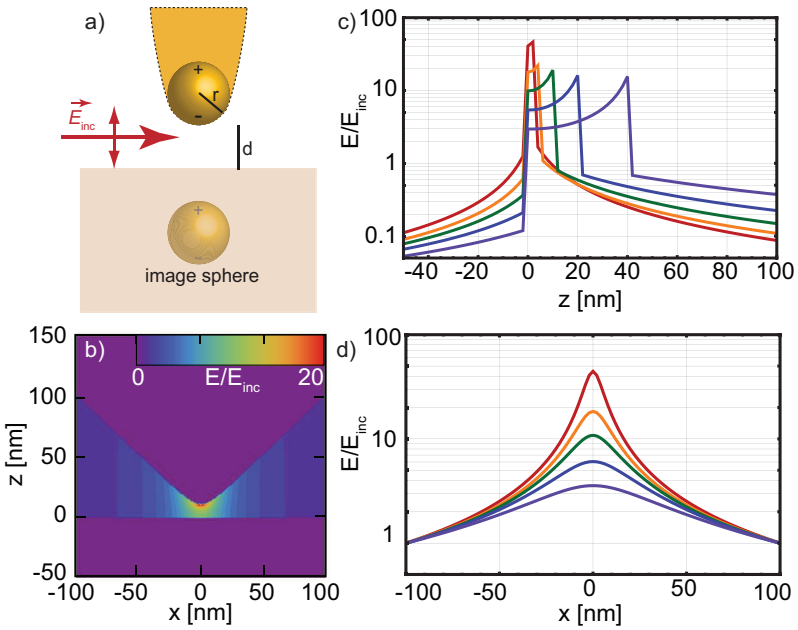

Figure 3.6: a) a polarizable AFM probe and its corresponding induced image dipole within the surface. Panels b-d) represent calculation of the field enhancement between the AFM tip and a gold substrate by modeling the tip as a hyperboloid structure [45]. b) Spatial distribution and variation of field enhancement (E/E_{inc}) with tip-sample separation for Au tip and substrate with apex radius $r = 10$ nm, height above the surface $d = 10$ nm, and optical excitation wavelength $\lambda = 800$ nm. c) the variation of E/E_{inc} along the axial direction across the Au tip-Au sample gap region ($x = 0$ nm) for different distances $d = 2$ (red), 5 (orange), 10 (green), 20 (blue), and 40 nm (purple) demonstrate the high enhancement of the tip-related fields as the AFM tip nears the surface. d) Lateral cross-sections in the center of the tip-sample gap for the equivalent tip-sample separation distances given in (c).

quantitatively predicts the degree of field enhancement.

Describing the total dipole moment of the tip sphere $\vec{p}_{\text{sph}}$ via the Clausius-Mosetti expression for the polarizability of a dielectric sphere $\boldsymbol{\alpha}_{\text{sph}}$ of radius r we find,

$$\vec{p}_{\text{sph}} = \boldsymbol{\alpha}_{\text{sph}} \vec{E}_{\text{inc}}, \tag{3.15}$$

where

$$\boldsymbol{\alpha}_{\text{sph},ij} = 4\pi\epsilon_0 r^3 \left(\frac{\epsilon_{\text{sph}} - 1}{\epsilon_{\text{sph}} + 2} \right) \delta_{ij}. \tag{3.16}$$

It should be noted that the polarizability of the tip should be represented as a matrix. While the polarizability of a sphere is isotropic, this is not technically true in the case of an extended tip structure optically coupled with the surface. Here, the polarizability will differ depending on whether the tip sphere is polarized parallel or perpendicular to the surface plane.

When a charge distribution is in the presence of a dielectric substrate surface charges move, arranging themselves to satisfy the boundary conditions of Maxwell's equations at the surface interface. The distribution of these charges results in a field distribution which is equivalent to the scenario where a hypothetical image charge is embedded within the surface medium. The relative magnitude of the image charge necessary to satisfy the Maxwell's equations boundary conditions of the surface of the dielectric is defined to be

$$\beta = \left(\frac{\epsilon_2 - 1}{\epsilon_2 + 1} \right). \tag{3.17}$$

Consequently, when a polarized sphere is brought in proximity to a surface, the dipole moment of the sphere initiates the formation of image charges in the surface. Calculation of the total strength of the dipole moment must then take into account the external applied field as well as the field the sphere experiences from its own image in the surface.

Let us first consider the case that the polarization of the incident field lies in the out-of-plane direction, $\vec{E}_{\text{inc}} = (0 \cdot \hat{\mathbf{x}}, 0 \cdot \hat{\mathbf{y}}, E_{\text{inc}} \cdot \hat{\mathbf{z}})$. Here, the image dipole within the surface forms aligned in the same direction as the tip-sphere dipole. This may be expressed in the following form as a function of distance d above the surface,

$$p_{\mathrm{eff,z}} = \alpha_{\mathrm{eff,z}} E_{\mathrm{inc,z}} = \alpha_{\mathrm{sph,z}} \left(1 + \frac{\alpha_{\mathrm{eff,z}}\beta}{2\pi\epsilon_0(2(r+d))^3}\right) E_{\mathrm{inc,z}}. \tag{3.18}$$

The recursion relation for $\alpha_{\mathrm{eff,z}}$ given by Eqn. 3.18 can be solved to yield the effective polarizability for a sphere above a surface.

$$\alpha_{\mathrm{eff,z}} = \alpha_{\mathrm{sph,z}} \left(1 - \frac{\alpha_{\mathrm{sph,z}}\beta}{16\pi\epsilon_0(r+d)^3}\right)^{-1} \tag{3.19}$$

For a dipole oriented parallel to the surface plane, $\vec{E}_{\mathrm{inc}} = (E_{\mathrm{inc}} \cdot \hat{\mathbf{x}}, 0 \cdot \hat{\mathbf{y}}, 0 \cdot \hat{\mathbf{z}})$ the image dipole is oriented in the opposite direction of the tip-sphere dipole.

Here, the total dipole of the tip-sphere may be expressed as

$$p_{\mathrm{eff,x}} = \alpha_{\mathrm{eff,x}} E_{\mathrm{inc,x}} = \alpha_{\mathrm{sph,x}} \left(1 + \frac{\alpha_{\mathrm{eff,x}}\beta}{4\pi\epsilon_0(2(r+d))^3}\right) E_{\mathrm{inc,x}}. \tag{3.20}$$

Note that the coupling between the tip-sphere and its image in the surface is here reduced by a factor of two compared to the p polarized example (p denotes polarization parallel to tip, while s denotes polarization perpendicular to the tip axis). This is a result of the fact that the dipole field strength for a displacement perpendicular to the dipole orientation is half of that when the displacement occurs parallel to the dipole orientation.

Again, solving the recursion relation for the self-interaction for the effective polarizability we find for the in-plane polarizability,

$$\alpha_{\mathrm{eff,x}} = \alpha_{\mathrm{sph,x}} \left(1 - \frac{\alpha_{\mathrm{sph,x}}\beta}{32\pi\epsilon_0(r+d)^3}\right)^{-1}. \tag{3.21}$$

3.6 Extraction of near-field signal.

As discussed in the previous section, the origin of the near-field signal component may be described by modeling the tip-sample coupling as a polarizable sphere coupled with its image within the surface. The scattering cross section of a sphere in the quasi-static limit ($r \ll \lambda$) may be expressed as [49]

$$C_{\mathrm{scat,i}} = \frac{k^4}{6\pi} |\alpha_{\mathrm{sph,i}}|^2. \tag{3.22}$$

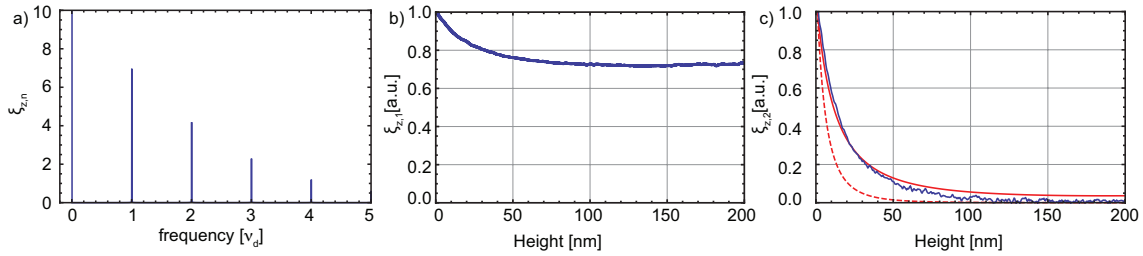

Figure 3.7: a) due to the AFM tip oscillation at frequency $f = \nu_d$ the scattered field of the tip varies at the series of harmonics of ν_d. As the near-field contribution is strongly localized to the surface it is generally contained in the higher harmonic contributions ($n \geq 2$). Panels b) and c), display approach curve data from an Pt tip, $r = 20$ over an Au surface. As seen in panel b), while $\xi_{z,1}$ contains a near-field component, it also contains significant contributions from background scattering from the tip which are uncontrolled and not localized to the surface. Panel c) shows the strong increase of signal related to the near-field contribution along with tip-dipole (dashed line) and monopole models (solid line) for the approach scaling. See the following sections for a comparison/discussion of both the dipole and monopole models.

As the cross section is defined for the scattered intensity, the simplest approximation which can be made for an estimation of the total scattered field $\vec{E}_{\text{scat}}$ can be made by noting that the field scattering cross section C_{scat} is proportional to α_{eff},

$$E_{\text{scat,i}} \propto \boldsymbol{\alpha}_{\text{eff,i}} \cdot E_{\text{inc}}. \tag{3.23}$$

A complete description of the collected signal accounts for the fact that the AFM tip is illuminated by the incident field both directly and indirectly due to its reflection at the sample surface. Typically the light-cone of illumination from the focusing element has an approximate numerical aperture of NA$= 0.5$ with the center optic axis forming a 30 degree angle with the surface. The tip scattering field may also emerge directly from the tip or reflect of the sample surface [48].

For the case of p polarized illumination, the effective polarizability of the tip is generally much stronger in the out-of-plane direction. As a result the enhancement contributions of the field for polarizations parallel to the surface are typically neglected. Hence, the total scattering field of the tip can be approximated as

$$E_{\text{scat,z}} = f_{\text{scat,z}} \left(1 + r_p\right)^2 \alpha_{\text{eff,z}} E_{\text{inc,z}}, \tag{3.24}$$

where r_p is the Fresnel reflection coefficient for p-polarized light. The constant $f_{\text{scat,z}}$ represents a proportionality constant dependent on the experimental parameters of the system including the wavelength scaling of the tip-scattering (see Eqn. 3.22), the illumination angle of the AFM tip, and the numerical aperture of the focusing element. The $(1 + r_p)^2$ term accounts for the direct and surface reflected illumination of the AFM tip, as well as the direct and surface reflected signal pathways. The $(1 + r_p)^2$ term in Eqn. 3.24 accounts for both the direct and surface reflection external illumination of the AFM tip as well as the direct and surface reflected signal contributions of the light scattered by the AFM tip.

For typical s-SNOM measurements the AFM tip is dynamically oscillating in the z direction in feedback with the sample surface. This motion can be approximated to be sinusoidal in nature and defined by an oscillation amplitude A and distance of closest approach to the surface h ($h = 0$ when in contact with the surface).

$$z_{\text{tip}}[t] = A(1 + \cos[\nu_d \cdot t]) + h \tag{3.25}$$

The periodic motion of the AFM tip allows for the near-field scattering signal to be expressed as a sum of harmonics of the tip-motion frequency $(\nu_d, 2\nu_d, ..., n\nu_d)$.

$$E_{\text{scat,z}}[t] = \sum_{-\infty}^{\infty} \xi_{z,n} \cdot \exp[i \cdot n\nu_d t] \tag{3.26}$$

Furthermore, as Eqn. 3.19 shows, the effective polarizability of the AFM tip and thus the total scattered field is highly dependent on the height above the sample surface. This enhancement of the scattered field as the AFM tip periodically nears the surface results in the allocation of part of the near-field scattering to the higher harmonics of ν_d (see Fig 3.7a).

The magnitude of the scattering field at a given harmonic $\xi_{z,n}$ $(n = 0, 1, 2, ...)$ incident on the detector can be expressed as the Fourier component of the total signal at said harmonic frequency.

$$\xi_{z,n} = \frac{1}{T} \int_{-T/2}^{T/2} E_{\text{scat,z}}(t) \cdot \exp[-i \cdot n\nu_d t] \tag{3.27}$$

The quantity ξ_n is a complex value, whose absolute value represents the magnitude of the scattered field and whose real and imaginary parts define the phase of the scattered light.

$$\phi = \arctan\left[\frac{\mathrm{Im}[\xi_n]}{\mathrm{Re}[\xi_n]}\right] \tag{3.28}$$

It is important to emphasize that the background signal contributions occur primarily at the DC (n=0) and first harmonic (n=1) frequencies. Conversely, the sharp field enhancement as the tip approaches the surface results in the distribution of the near-field signal contributions across the higher harmonics of the ν_d, i.e. $n \geq 2$. This is illustrated schematically in Fig. 3.7.

3.7 Spectral variation of s-SNOM signal.

The sensitivity of near-field optical signals to variations in the optical properties of materials is one of the unique advantages of *s*-SNOM measurements. Variations in the associated optical constants n and κ, and thus the real and imaginary parts of the dielectric permittivity of the surface material, result in contrast in the magnitude of the scattered *s*-SNOM near-field signal component. Variations in $\xi_{i,n}$ (i here denotes polarization of scattering) occur through a variety of mechanisms as the effective polarizability (Eqn. 3.19 and Eqn. 3.21) depends on several different parameters including the tip-sample separation, the tip material, as well as the surface material. As a result, enhancement of $\xi_{i,n}$ may occur either through sample or tip related resonances.

Fig. 3.8 displays simulated resonant contrast-enhancement of the optical signal scattering at the second harmonic $\xi_{z,2}/f_{\mathrm{scat,z}}$ using the tip-dipole model for an Au tip above differing sample surfaces with dither amplitude $A = r$. Here, "contrast" implies that the spectral scaling of *s*-SNOM signal resulting from the $k^4 = (2\pi/\lambda)^4$ scaling of the scattering-intensity efficiency in Eqn. 3.22 has been normalized. This normalization $k^4 = (2\pi/\lambda)^4$ scaling makes sense when comparing the signal contrast observed for excitation at a single wavelength, but would need to be accounted for in the signal observed in, for example, broadband spectrally resolved measurements. The upper panels in Fig. 3.8 represent the spectral dependence of the contrast enhancement of $\xi_{z,2}$ as the tip approaches the surface while the lower panels

display line-traces for heights of $h = 0$ (red), $h = r/4$ (orange), $h = r/2$ (green), $h = r$(blue), and $h = 2r$ (purple).

Panel a) represents the effect of a tip resonance on the magnitude of the s-SNOM signal. Here, the dipolar resonance for a spherical gold particle in the quasi-static limit ($r \ll \lambda$) gives a particle resonance in the visible spectral range. This resonant polarizability of the tip-sphere is enhanced and slightly red-shifted as the AFM tip moves closer to the surface. This red-shift is attributable to the shift in resonance frequency of the coupled sphere-surface system as the AFM tip sphere experiences increased interaction with its image dipole within the surface [50, 51].

Conversely, for panels b-e) in the IR range, the Au sphere is far off-resonance and acts simply as a good conductor. In these panels resonances occur through the surface material resonances. These resonances can occur through the presence of surface phonon polaritons as is the case for SiC and quartz SiO_2 in b) and c). They may also occur through molecular resonances of the surface material as seen in for the case of polytetrafluoroethylene (PTFE) and Poly(methyl methacrylate) (PMMA) in panels d) and d).

Note that the s-SNOM signal enhancement and variation for the surface phonon related signals occurs at much stronger intensities than the signal associated with molecular resonances. This is a result of the strong-evanescent fields associated with surface polariton waves at a dielectric interface. As can be seen in the lower panels of Fig. 3.8, as the AFM tip approaches the surface, the signal component $\xi_{z,2}$ tends to red-shift in the presence of either AFM tip (a) or surface phonon polariton resonances (b-c) due to the large variation of the real part of the dielectric permittivity through the resonance condition ($\epsilon_r = -2$ for sphere resonance, $\epsilon_r = -1$ for surface polariton resonance).

3.8 Beyond the tip-dipole approximation.

While the coupled dipole/tip-sphere model of $\alpha_{\text{eff,i}}$ qualitatively describes the enhancement above a surface, it is clear simply from the geometric perspective that the tip is, in reality, a more extended object and that a more detailed model of the surface related enhancement of the polarizability may be necessary. To this end, several models have been presented which incorporate the AFM tip's more extended geometry into the enhancement model

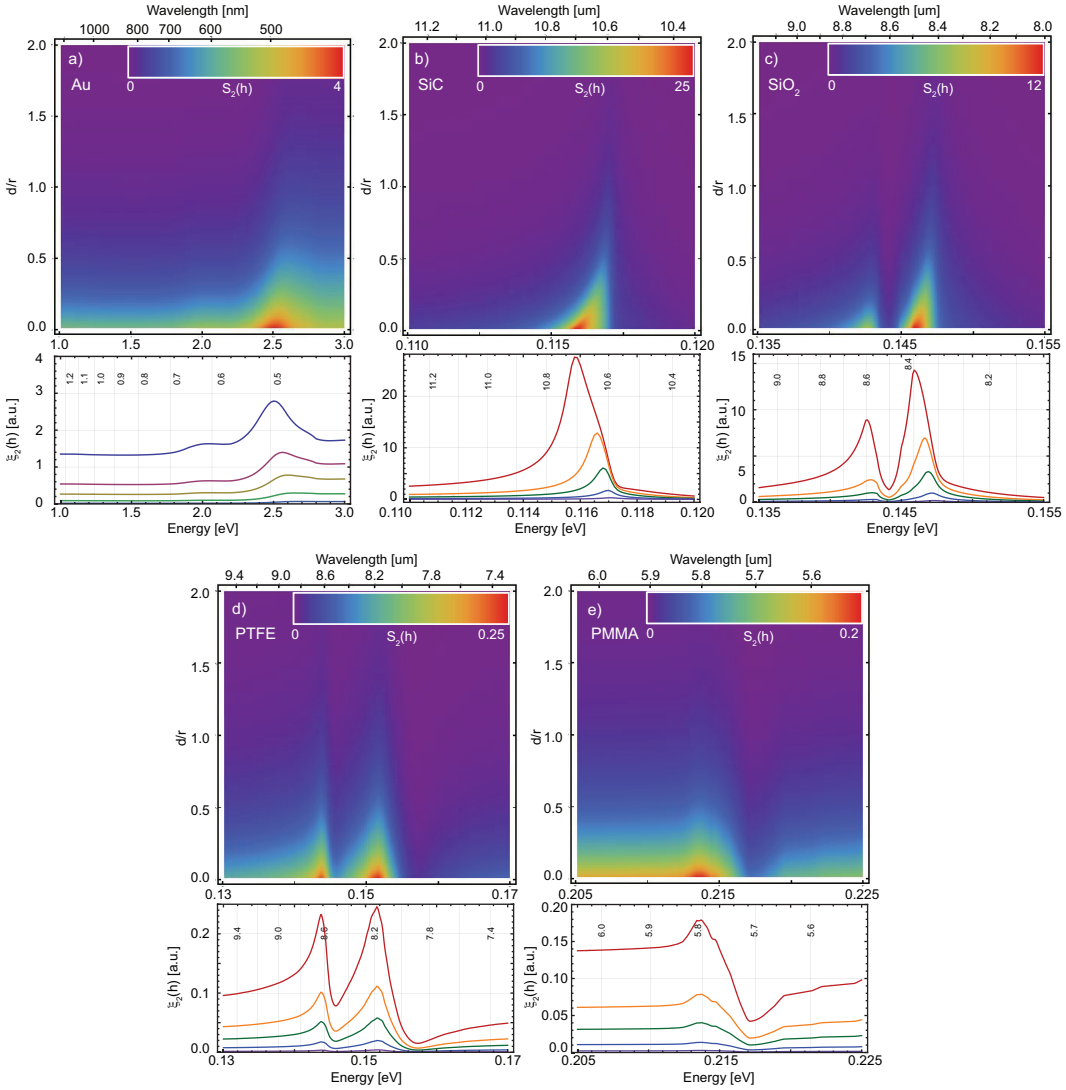

Figure 3.8: Modeling of the spectral enhancement of s-SNOM signal; $|\xi_2|$ is displayed for several example materials. Approximating the AFM-tip as an Au sphere, the panels display simulated s-SNOM signal for an AFM oscillation amplitude of $A = r$ at varying distances of closest approach h above the surface. a) the signal above an Au surface in the visual range, b) above SiC, c) above SiO_2, d) above PTFE, e) above PMMA in the IR range where resonances occur.

[45, 47, 52, 53]. Many of these models, however, require extended numerical simulations in order to reconstruct the E-field distribution associated with the AFM tip. This requirement for extended numeric simulation makes it difficult to analyze the behavior of the scattering of the tip as it periodically moves above the surface.

In order to provide an analytic expression for observed s-SNOM signal, a model was put forth by A. Cvitkovic, et al [48] which approximated the tip as an extended spheroidal structure. In the following section the monopole approximation of the fields of this prolate spheroid will be covered following reference [48], as well as its differences from the spherical model will be discussed.

The prolate spheroidal structure in reference [48] is characterized by a radius of curvature of the tip R and the length of the spheroid L. Here, the field at the tip of a prolate spheroid, illuminated by an external field E_{inc} and polarized along the longitudinal axis of the spheroid may be modeled as [48, 54],

$$E_{\text{psph}}[D] = \gamma E_{\text{inc}} = \left(\frac{\frac{2F(L+D)}{D^2+L(2D+R)} + \ln\left[\frac{L-F-D}{L+F+D}\right]}{2\frac{F(L-\epsilon R)}{LR(\epsilon-1)} - \ln\left[\frac{L-F}{L+F}\right]} + 1 \right) E_{\text{inc}}, \tag{3.29}$$

where F is the half distance between the spheroid focii, $F = (L(L-R))^{1/2}$ and D is the distance from the tip of the spheroid. Setting $D = 0$, we find the total field at the tip to be

$$E_{\text{psph}}[0] = \gamma_0 E_{\text{inc}} = \left(\frac{\frac{2F}{R} + \ln\left[\frac{L-F}{L+F}\right]}{2\frac{F(L-\epsilon R)}{LR(\epsilon-1)} - \ln\left[\frac{L-F}{L+F}\right]} + 1 \right) E_{\text{inc}}. \tag{3.30}$$

While the distance dependence of the field moving along the spheroid axis is complex, Cvitkovic et al. make the assumption that the field induced for an isolated spheroidal structure can be approximated by two point charges (Q_0 and $-Q_0$) placed at a distance W_0 from the ends of the spheroid [48]. The magnitude of these of approximation charges induced by the external field can be determined by matching the monopolar field magnitude to the induced field of the prolate spheroid,

$$E_{\text{mp}}[D] = \frac{Q_0}{(W_0+D)^2} = \frac{W_0^2(E_{\text{psph}}[0] - E_{\text{inc}})}{(W_0+D)^2}. \tag{3.31}$$

This leads to an estimated monopole strength of

$$Q_0 = W_0^2(\gamma_0 - 1)E_{\text{inc}}, \tag{3.32}$$

where $W_0 \simeq \frac{1.31RL}{L+2R}$ is the position of the approximation for the point charge within the spheroid for values of $R/L < 0.3$.

Bringing the surface close to the spheroid, an image charge $Q_0' = \beta Q_0$ forms due to the presence of Q_0 close to the surface which in turn results in the formation of a second set of charges within the spheroid (Q_i and $-Q_i$). The charge distribution picture is completed by the final location of a final image charge Q_i' in the surface. Through estimation of the magnitude of the charge induced at the end of the tip due to the presence of the surface Q_i, an estimation of the near-field polarization contribution $p_{\text{nf}} \simeq Q_i \cdot L$ may be made in comparison to the far-field polarization $p_{\text{ff}} \simeq Q_0 \cdot 2L$.

Following some derivation and taken explicitly from [48] analytic expressions for the magnitude of the image charges induced in the spheroid can then be derived,

$$Q_i = \frac{\beta f_0}{1 - \beta f_1} Q_0 \text{ where,} \tag{3.33}$$

$$f_0 = (g - \frac{2H + W_0 + R}{2L}) \frac{\ln\left[\frac{4L}{4H+2W_0+R}\right]}{\ln\left[\frac{4L}{R}\right]} \tag{3.34}$$

$$f_1 = (g - \frac{2H + W_i + R}{2L}) \frac{\ln\left[\frac{4L}{4H+2R}\right]}{\ln\left[\frac{4L}{R}\right]}. \tag{3.35}$$

Here R, H, and L correspond to the distance of the monopole charge Q_0 from the end of the sphere, the spheroid surface separation, and the total length of the spheroid. The quantity g represents a scaling parameter necessary for the approximation of the spheroid field to that of a monopole field for charge Q_0 and is typically $\simeq 0.7 \pm 0.1$ [48]. The final expression for the near-field enhancement factor can be expressed as

$$\eta(H) = \frac{p_i}{p_0} = \frac{Q_i \cdot L}{Q_0 \cdot 2L} = \frac{\beta(2Lg - 2H - W_0 - R)\ln\left[\frac{4L}{4H+2W_0+R}\right]}{4L\ln\left[\frac{4L}{R}\right] - \beta(4Lg - 4H - 3R)\ln\left[\frac{4L}{4H+2R}\right]}. \tag{3.36}$$

Finally the effective polarization p_{eff} of the spheroid system may be expressed in term

of the two constituent dipoles induced in the spheroid,

$$p_{\text{eff}} = p_0 + p_i = 2Q_0 \cdot L(1+\eta). \tag{3.37}$$

This implies that the effective polarizability for the system can be expressed as

$$\alpha_{\text{eff,z}} = 2(\gamma_0 - 1)W_0^2 L(1+\eta). \tag{3.38}$$

The approximations made in the monopole model should be stressed. First, the prolate spheroid is approximated to be in the electrostatic limit ($L \ll \lambda$). Second, the field induced on the prolate spheroid near the surface is approximated to that of a mono-polar point charge. Furthermore, the equations for the effective polarizability are only accurate for large aspect ratio ellipsoids, $R/L < 0.3$, for distances below $\simeq 3R$. The only adjustable parameter in the model is g, the constant approximating the amount of the induced charge participating in the near-field interaction. Typically g can be assigned a value of 0.7 ± 0.1 based on the tip-geometry, but can also be given a small imaginary part to account for the finite conductivity/radiation resistance for the probe.

If the above approximations apply, it has been shown that the monopolar approximation can successfully model the magnitude of s-SNOM signal observed above materials which exhibit polaritonic surface resonances. Specifically, the incorporation of an extended tip-geometry into the model more correctly models the red-shift and spectral broadening of the s-SNOM signal [48] which the coupled dipole/tip-sphere model does not correctly predict.

Fig. 3.9b-f) exhibits the primary differences between the monopole model and the coupled dipole/tip-sphere model. For the monopole approximation, a tip curvature to length ratio of $R/L = 0.1$ was taken. Panel b displays the differences in the s-SNOM signal expected for an Au probe above a SiC surface. Most notably the spectrum of the monopole model is broadened and red-shifted in comparison to the coupled dipole/tip-sphere model due to its incorporation of an elongated scatterer.

Panels c and d display the simulated s-SNOM contrast normalized against that of a perfect conductor as a function of the real part of the substrate material. The differing lines represent the s-SNOM signal associated with different values of the imaginary part of the substrate material. It is clear here that the extended dipole model predicts much larger s-SNOM contrast in the presence of surface polaritons occurring when $\text{Re}[\epsilon] = -1$.

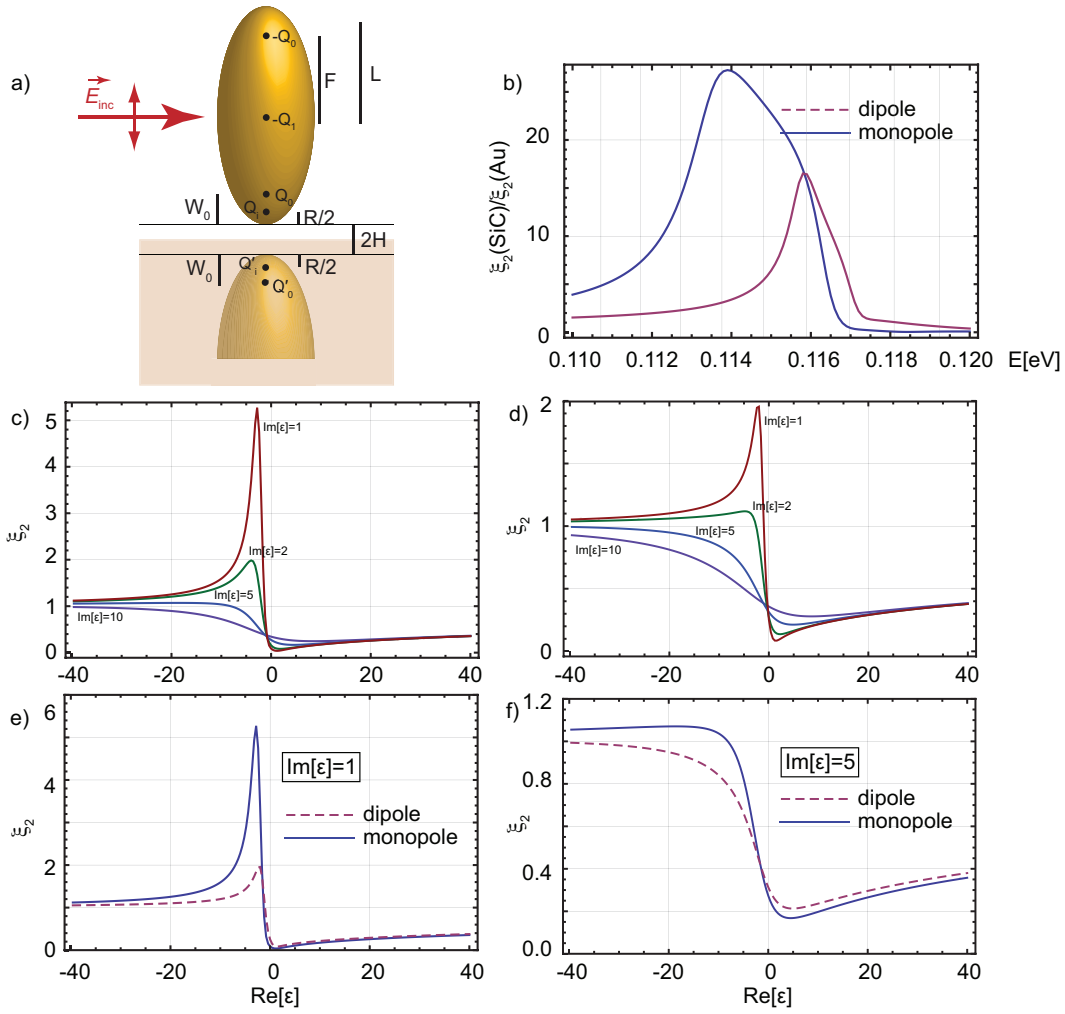

Figure 3.9: A comparison of the tip-sphere dipole model with the model of an AFM tip as a more extended spheroid using the monopole approximation. The geometry of the spheroidal approximation description is depicted in panel a. Panel b illustrates the normalized scattering field spectra of SiC for both the dipole and monopole models. The signal dependence of both the monopole and dipole models on the dielectric properties of the surface are provided in c and d for fixed values of Im[ϵ]. Panels e and f represent a comparison of the dipole and monopole models for fixed Im[ϵ] = 1 and Im[ϵ] = 5 respectively.

Panels e and f give a side-by-side comparison of the monopolar and coupled dipole/tip-sphere models for specified values of the imaginary part of the surface ϵ. As shown in panel e, it can be seen that the magnitude of the *s*-SNOM contrast varies significantly when $\mathrm{Re}[\epsilon] \simeq -1$ and $\mathrm{Im}[\epsilon]$ is small, corresponding to a strong polaritonic resonance. However, when $\mathrm{Re}[\epsilon]$ is far from -1 and/or the $\mathrm{Im}[\epsilon] > 2$ there is only a slight difference between the two models. This has important consequences for how spectroscopic *s*-SNOM data are analyzed. If the material studied exhibits polaritonic surface resonances, the monopolar model should more accurately describe the *s*-SNOM contrast. In all other cases, simple modeling of the contrast using the coupled dipole/tip-sphere model should be as accurate.

3.9 Non-interferometric s-SNOM Signal Analysis.

For the following section, the nature of the detected *s*-SNOM signal without any source of interferometric amplification will be considered. Here, it will be assumed that the incident electric field upon the AFM probe will be polarized parallel to the tip axis (*p*-polarization). As the tip scattering coefficient is much larger for *p*-polarized light, the *s*-polarized signal contribution will here be neglected. Still, it should be emphasized that the field incident on the detector can, in certain cases, have polarization dependence which can affect the nature of the relationship of the detected signal with the background and near-fields. Specifically, this is the case when illuminating the AFM tip with *s*-polarized light, which will be covered in the following section. For this reason the vector notation for the electric fields is maintained.

For *p*-polarized illumination and detection, the light collected by the focusing optics in an *s*-SNOM experimental setup is composed of a small near-field scattering contribution $\vec{E}_{\mathrm{nf}}$ from the region of interest at the tip-sample gap region, as well as a much stronger background signal contribution $\vec{E}_{\mathrm{bg}}$ related to various backscattering processes from the extended tip/sample region. The near-field contribution may be viewed as equivalent to the scattering-field $\vec{E}_{\mathrm{scat,i}}$ discussed in the previous sections.

Under this description, the field incident upon the detector can be expressed in terms of the sum of these two field contributions, each with their own characteristic temporal phase,

$\phi_{\rm nf}$ and $\phi_{\rm bf}$, respectively.

$$\vec{E}_{\rm det}[t] = \vec{E}_{\rm nf}[t] \cdot \exp[i(\omega t - \phi_{\rm nf})] + \vec{E}_{\rm bg}[t] \cdot \exp[i(\omega t - \phi_{\rm bg})] \tag{3.39}$$

$\vec{E}_{\rm nf}$ may be related to the scattering coefficient derived in section 3.6 as described via the relation with the strength of the incident driving field $\vec{E}_{\rm inc}$. Here, $\mathbf{S}_{\rm nf,n}$ represents the scattering matrix of the AFM tip-substrate system, although for this example the only the p-polarized scattering from p-polarized incident fields is considered.

$$\vec{E}_{\rm nf}[t] = \sum_{-\infty}^{\infty} \mathbf{S}_{\rm nf,n} \vec{E}_{\rm inc} \exp[in\nu_d t] \tag{3.40}$$

In Eqn. 3.24 for example, the term $\left(f_{\rm scat,z}\left(1+r_p\right)^2 \alpha_{\rm eff,z}\right)$ would represent the scattering matrix for p-polarized excitation and detection defining both the amplitude and phase of the s-SNOM signal with respect to the external optical excitation.

As a result, the near- and background field contributions may also be described in terms of an expansion of the harmonics of the tip-dither frequency.

$$\vec{E}_{\rm nf}[t] \cdot \exp[i(\omega t - \phi_{\rm nf})] = \left(\sum_{n=-\infty}^{\infty} \vec{E}_{\rm nf,n} \exp[in\omega_d t] \right) \cdot \exp[i(\omega t - \phi_{\rm nf})] \tag{3.41}$$

$$\vec{E}_{\rm bg}[t] \cdot \exp[i(\omega t - \phi_{\rm bg})] = \left(\sum_{n=-\infty}^{\infty} \vec{E}_{\rm bg,n} \exp[in\omega_d t] \right) \cdot \exp[i(\omega t - \phi_{\rm bg})] \tag{3.42}$$

The total intensity incident upon the detector can thus be expressed as

$$I_{\rm det}[t] = \vec{E}_{\rm det}[t] \cdot \vec{E}^*_{\rm det}[t] \tag{3.43}$$

$$= |\vec{E}_{\rm bg}[t]|^2 + |\vec{E}_{\rm nf}[t]|^2 + 2\vec{E}_{\rm bg}[t] \cdot \vec{E}_{\rm nf}[t] \cos[\Delta\Phi]. \tag{3.44}$$

Where $\Delta\Phi = \phi_{\rm bg} - \phi_{\rm nf}$ represents the phase difference between the background and near-field signals.

We can break down each of the field contributions even further. The background is contained extensively in the DC ($n = 0$) frequency ($|E_{\rm bg,0}| \gg |E_{\rm bg,1}| \gg |E_{\rm bg,n}|$). Conversely, the near-field signal contribution is spread over many of the higher harmonics. For the $n = 0$ and $n = 1$ harmonics of ν_d, the magnitude of the background signal is much greater than or comparable to the near-field signal ($|E_{bg,0}| \gg |E_{nf,0}|$, $|E_{bg,1}| \simeq |E_{nf,1}|$). At higher harmonics

greater $n > 2$ however, the near-field contribution is much larger than the background ($|E_{\mathrm{bg,n}\geq 2}| \ll |E_{\mathrm{nf,n}\geq 2}|$).

As a result, Eqn. 3.44 may be expressed in terms of the main background contributions.

$$I_{\mathrm{det}}[t] = |E_{\mathrm{bg},0}|^2 + |E_{\mathrm{nf}}[t]|^2 + 2\vec{E}_{\mathrm{bg},0} \cdot \vec{E}_{\mathrm{nf}}[t] \cos[\Delta\Phi] \tag{3.45}$$

With C_{det} representing the detector responsivity for a given wavelength and intensity of light, the total observable detector voltage for a given harmonic signal n can be expressed as

$$U_{\mathrm{det,n}} = C_{\mathrm{det}} \left(2E_{\mathrm{bg},0}E_{\mathrm{nf,n}} \cos[\Delta\Phi]\right). \tag{3.46}$$

The intrinsic disadvantage in non-interferometric detection can be seen in Eqn. 3.46; the magnitude of the signal is directly proportional to the both the magnitude and phase difference of the background signal. Both of these aspects of the background signal are uncontrolled by the user and can vary as the sample moves beneath the tip. This uncontrolled "self-homodyne" amplification of the near-field signal can result in a modulation of the observed near-field signal in the form of interference fringes as the near-field phase component moves between being in and out of phase with the background field. For small s-SNOM scans, this effect may not be an issue if the near-field signal is clearly observed and the scan size is much smaller than the wavelength of light.

However, for larger scans it is necessary to implement the use of a reference field with well defined and controllable amplitude and phase. This is achieved through homodyne amplification of the near-field signal.

3.10 Homodyne s-SNOM signal analysis.

Implementation of homodyne amplification involves the addition of the field from a reference arm with an adjustable delay length as a means of controlling the reference phase. The basic experimental layout of an s-SNOM optical path is displayed in Fig. 3.10 ,with the reference beam shown as the left arm of the interferometer. The total field incident upon the detector can consequently be expressed as

$$\vec{E}_{\mathrm{det}}[t] = \vec{E}_{\mathrm{nf}}[t] \cdot \exp[i(\omega t - \phi_{\mathrm{nf}})] + \vec{E}_{\mathrm{bg}}[t] \cdot \exp[i(\omega t - \phi_{\mathrm{bg}})] + \vec{E}_{\mathrm{ref}}[t] \cdot \exp[i(\omega t - \phi_{\mathrm{ref}})]. \tag{3.47}$$

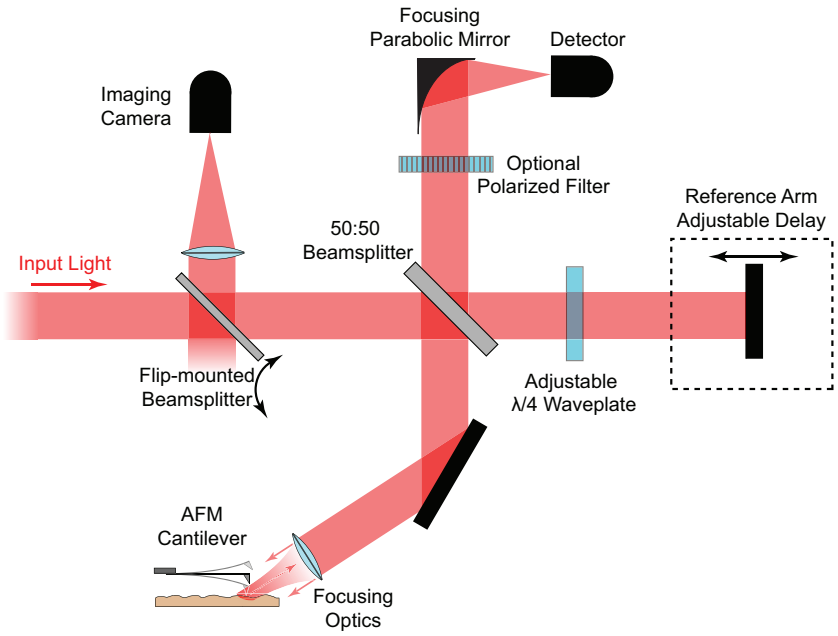

Figure 3.10: The optical beam-path for a basic *s*-SNOM measurement with application of a homodyne reference field.

For most measurements, we shall make the approximation that the homodyne field is very strong compared to the other signal contributions, $\vec{E}_{\mathrm{ref}} \gg \vec{E}_{\mathrm{bg}} \gg \vec{E}_{\mathrm{nf}}$. It follows from Eqn. 3.47 that the intensity at the detector may be written as the sum of six terms,

$$\begin{aligned} I_{\mathrm{det}}[t] =& |E_{\mathrm{ref}}[t]|^2 + |E_{\mathrm{bg}}[t]|^2 + |E_{\mathrm{nf}}[t]|^2 + 2\vec{E}_{\mathrm{ref}}[t] \cdot \vec{E}_{\mathrm{bg}}[t] \cos[\phi_{\mathrm{ref}} - \phi_{\mathrm{bg}}] \\ &+ 2\vec{E}_{\mathrm{bg}}[t] \cdot \vec{E}_{\mathrm{nf}}[t] \cos[\phi_{\mathrm{bg}} - \phi_{\mathrm{nf}}] + 2\vec{E}_{\mathrm{ref}}[t] \cdot \vec{E}_{\mathrm{nf}}[t] \cos[\phi_{\mathrm{ref}} - \phi_{\mathrm{nf}}]. \end{aligned} \tag{3.48}$$

By applying lock-in filtering on $n\nu_d$, terms 1, 2, and 4 in Eqn. 3.48 are removed from the detector signal. In addition, under the assumption that the reference field is large compared to the background and near-fields, it may be assumed that the magnitude of term 6 in Eqn. 3.48 is the dominant term in the detectable signal. The resulting detector voltage thus can be expressed as

$$U_{\mathrm{det,n}} = C_{\mathrm{det}} \left(2E_{\mathrm{ref},0} E_{\mathrm{nf,n}} \cos[\Delta\Phi]\right). \tag{3.49}$$

Here, $\Delta\Phi$ represents the phase difference between the reference and near-field signal contributions, and while Eqn 3.49 looks similar to Eqn. 3.46, both the magnitude and phase of the homodyne arm now represent controllable parameters. This allows for the determination of the phase of the near-field scattered light through two-phase interferometry. This requires that two measurements of the signal magnitude be made with the reference phase shifted by $\pi/2$ between the two measurements.

The arctangent of the signal magnitude of the two measured signal intensities yields the phase of the scattered signal with respect to the reference phase.

$$\Delta\Phi = \arctan\left[\frac{U_{\mathrm{det,n}}(\phi_{\mathrm{ref}} - \pi/2)}{U_{\mathrm{det,n}}(\phi_{\mathrm{ref}})}\right] \tag{3.50}$$

3.11 Pseudo-heterodyne s-SNOM signal amplification.

A recently developed novel technique was recently put forth by N. Ocelic et al whereby efficient background suppression as well as resolution of the phase of the near-field scattered light may be simultaneously measured in a single scan [55]. This technique, termed "pseudo-heterodyne" detection, involves periodically varying the delay of the reference arm while recording the near-field related signal in the detector.

Through the modulation of the length of the reference arm, the reference phase is varied with a phase modulation amplitude of γ at frequency M. Here, ϕ_{ref} represents the average phase offset of the reference arm.

$$E_{\mathrm{ref}}[t] \cdot \exp[i\omega t + \phi_{\mathrm{ref}}] = E_{\mathrm{R}} \exp[i\gamma \cos[Mt]] \cdot \exp[i\omega t + \phi_{\mathrm{ref}}] \tag{3.51}$$

For pseudo-heterodyne measurements, the mirror modulation frequency is required to be a much lower frequency than the dither frequency ($M \ll \nu_d$). Typical values for the frequency lie in the $M/2\pi \simeq 200$ Hz range. Decomposing the reference field into its Fourier expansion components for a phase-modulated field, the reference field can be expressed as

$$E_{\mathrm{ref}}[t] \cdot \exp[i\omega t + \phi_{\mathrm{ref}}] = \left(\sum_{m=-\infty}^{\infty} E_{\mathrm{ref,m}} \exp[imMt]\right) \cdot \exp[i\omega t + \phi_{\mathrm{ref}}]. \tag{3.52}$$

Where,

$$E_{\mathrm{ref,m}} = \frac{1}{T}\int_{-T/2}^{T/2} E_{\mathrm{ref}}[t]\exp[imMt] \tag{3.53}$$

$$= \frac{1}{T}\int_{-T/2}^{T/2} E_{\mathrm{R}}\exp[i\gamma\cos[Mt]]\exp[imMt] \tag{3.54}$$

$$= E_{\mathrm{R}}\cdot J_m[\gamma]\exp[i(\phi_{\mathrm{ref}}+\frac{m\pi}{2})]. \tag{3.55}$$

J_m here represents the spherical Bessel function. The total electric field at the detector takes the same form as the conventional homodyne interference measurement shown in Eqn. 3.48. The distinguishing difference for pseudo-heterodyne detection is that unlike a conventional homodyne measurement in which the reference field is entirely encompassed by a static term $E_{\mathrm{ref},0}$, the reference field in pseudo-heterodyne detection measurements is spread across several harmonics of the reference arm modulation frequency M.

The interference of the reference and near-field signal consequently results in the splitting of the near-field signal into sideband frequencies, $\nu_{\mathrm{nm}} = n\nu_d + mM$. As a result the detected signal at a given sum frequency of the harmonics can be expressed as

$$U_{\mathrm{det,n,m}} = C_{\mathrm{det}}\left(2E_{\mathrm{R}}\cdot J_m[\gamma]E_{\mathrm{nf,n}}\cos[\phi_{\mathrm{nf}}-\phi_{\mathrm{ref}}-\frac{m\pi}{2}]\right). \tag{3.56}$$

As can be seen that from Eqn. 3.56 above, measurement of an even sideband (m =even) gives the in phase real part of the near-field signal, while for m =odd, the sideband measures the out-of-phase imaginary component of the Fourier component. Through the measurement of two sidebands the magnitude of the near-field component can be found to be

$$E_{\mathrm{nf,n}} = \frac{1}{2C_{\mathrm{det}}E_{\mathrm{R}}}\left(\frac{U_{\mathrm{det,n,m}}}{J_m[\gamma]}+i\frac{U_{\mathrm{det,n,l}}}{J_l[\gamma]}\right). \tag{3.57}$$

For the the special case in which $J_m[\gamma]$ is equal to $J_l[\gamma]$, which occurs when the modulation depth $\gamma_{12} = 2.63$, the expression for the magnitude of the near-field can be further simplified to

$$E_{\mathrm{nf,n}} = \frac{1}{2C_{\mathrm{det}}E_{\mathrm{R}}J_1[\gamma_{12}]}\left(U_{\mathrm{det,n,2}}+iU_{\mathrm{det,n,1}}\right). \tag{3.58}$$

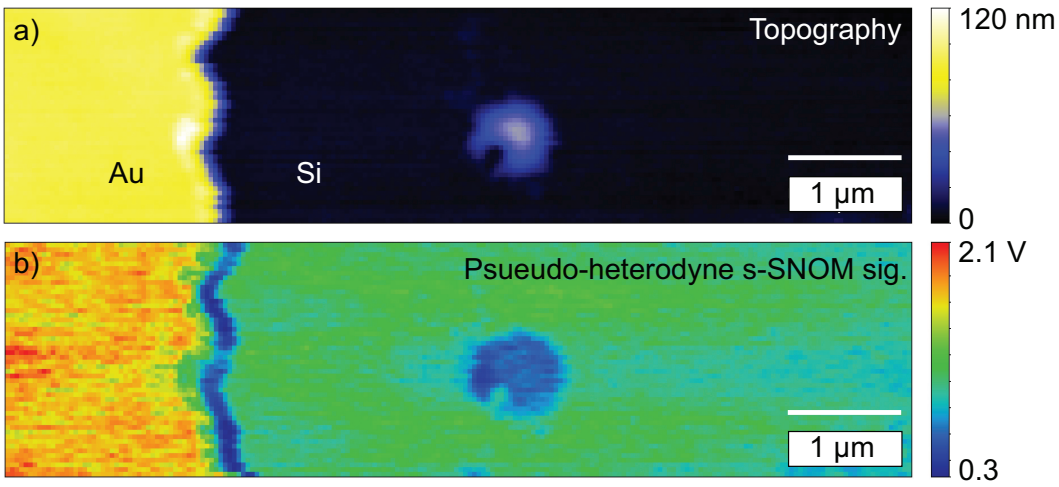

Figure 3.11: The panels above display the topography and associated s-SNOM optical signal measured using pseudo-heterodyne signal filtering techniques for an Au-Si interface using optical excitation from a CO_2 laser ($\lambda = 10.6$ μm). A clear correlation of the measured optical signal b) with the substrate material is observed with no background effects from the uncontrolled self-homodyne component of the signal.

The modulation depth which corresponds to this phase modulation amplitude is $\Delta l = \frac{\gamma_{12} \cdot \lambda}{2 \cdot 2\pi} \simeq 0.21\lambda$. Finally, the phase difference between the near-field and reference field can be derived from the arctangent of the two detected signal components,

$$\Delta\Phi = \arctan\left[\frac{U_{\mathrm{det,n,1}}}{U_{\mathrm{det,n,2}}}\right]. \tag{3.59}$$

Fig. 3.11 displays an example of the implementation of pseudo-heterodyne signal filtering techniques. Here, using mid-IR optical excitation from a CO_2 laser ($\lambda = 10.6$ μm) the variation in s-SNOM contrast is measured across a gold-silicon interface. As expected, a clear enhancement of the s-SNOM signal occurs over the gold as compared to the silicon substrate. It is further notable, that this measurement technique provides a near background free measurement of the near-field signal scattered by the tip as evidenced by the absence of signal fluctuations in the optical signal due to uncontrolled self-homodyne effects.

Chapter 4

MAPPING OF THE NEAR-FIELD DISTRIBUTIONS ASSOCIATED NANO-PLASMONIC STRUCTURES.

4.1 Introduction.

Surface plasmons in noble metal materials are electromagnetic surface waves which are composed of a coherent oscillation of the free-electron charge density. These oscillations can lead to a large near-field enhancement associated with the presence of surface waves in the IR-Vis spectral range. The ability of noble metal nano-structures to further confine light and enhance the electromagnetic fields associated with surface waves has made them the focus of much theoretical and experimental research interest. Specifically, the study of surface plasmon polariton (SPP) excitations in both surfaces and nano-structures has generated a great deal of scientific interest in recent years as these polaritonic excitations show great promise for the capture, confinement, and enhancement of electromagnetic fields. The unique optical properties of noble metal nanostructures, in particular, offer significant potential for diverse applications such as surface-enhanced Raman [56, 57] and fluorescence spectroscopies, [58, 59] molecular sensing [60], biomedical diagnostics [61, 62], tomography agents [63–65], cancer therapy [63, 66, 67], photonic circuits, [68, 69] and optical waveguides [70, 71].

The common characteristic of the role of noble metal nano-structures in the applications listed above is the implementation of the nano-structures for local optical electric field enhancement on nanometer length-scales. The primary challenge facing further progress in the development of advanced plasmonic systems is the design of structures with specific optical properties in the near-field regime has remained difficult. Creating a suitable set of selection criteria and pertinent properties which establish the relevant characteristics of the near-field of a plasmonic response is a necessary step in designing next-generation plasmonic systems/devices. In these efforts, it is well known that knowledge alone of the par-

ticle morphology and its related SPP spectral resonances is insufficient in understanding the distribution and magnitude of the field enhancement around the nano-structure. This understanding is due to the fact that the details of the local field distribution are not uniquely reflected in the spectrally broad SPP response due to the intrinsic ultrafast electronic dephasing [72]. Indeed, it is possible for fundamentally different near-field distributions to result from different nano-structures with nominally identical SPP spectral responses. The insight that can be gained from probing the near-field distribution is thus indispensable for the design of future plasmonic nano-structures with specific optical functionalities.

In this chapter, I will cover the basic principles of localized surface plasmon resonances and will discuss the implementation of *s*-SNOM measurement techniques as a means of characterizing the intrinsic plasmonic response of two systems, Ag nanoprisms exhibiting resonances in the visible regime and Ag nanorods with resonances in the mid-IR spectral range. Of the different geometries, plasmonic nanoprisms have emerged as a prototypical building block for nanoplasmonic applications in the visible due to the tunability of the plasmon resonance with size over a broad spectral range [73–75], the anticipated strong local-field enhancement associated with the particle tips [76, 77], and the prospect of pairs of nanoprisms to serve as optical antennas [78–80]. Ag nanorods, with their high aspect ratios, allow for the extension of the concept of a localized surface plasmon resonance from the visible to the infrared regime. In the following sections, I will review the observed field localization for these nano-rod structures via *s*-SNOM characterization and will discuss the characteristic differences in properties of localized plasmon resonances between the visible and infrared frequency regimes.

4.2 Localized Surface Plasmon Resonances.

As defined in section (2.5) a surface polariton is a solution to the conditions for an electromagnetic surface wave in the presence of a strong material resonance (for example, the bulk plasmon modes in metals or a phonon resonance in dielectric media). Through the surface wave dispersion relation, the condition for a resonant surface wave occurs when the real part of the dielectric permittivity for a surface is equal to -1 (Re[ϵ]=-1). The concept of a surface polariton resonance, i.e. a resonant solution to Maxwell's equations for the material and

surface geometry, can analogously be extended to describe optical resonances in nanoscale particles. Here, the solution for the particle polarizability for a given nano-structure exhibits resonances based upon the dielectric properties of the material and the details of the structure geometry. For example, in noble metal nano-structures the dielectric properties described by the Drude model allow for resonant oscillations of the free electrons confined to the particle. These resonant oscillations of the confined electron cloud are correspondingly defined as localized surface plasmon resonances (LSPR).

Unlike surface waves, which correspond to the well defined dispersion relation for the in-plane wavevector component (Fig. 4.1a, purple line), LSPR resonances are defined by a single characteristic resonance frequency across all wavevectors (Fig. 4.1a, black-dashed line). This concentration of allowable wavevector contributions is indicative of the high degree of field confinement in the localized plasmon response.

For nano-scale metallic structures several approximations may be made in describing the basic characteristics of localized surface plasmon resonances. First, in the Rayleigh approximation, the characteristic length scale of nano-structure l_{ns} is assumed to be much smaller than the wavelength of light $l_{\mathrm{ns}} \ll \lambda$. This approximation allows for the adoption of the quasi-static description which states that the magnitude and phase of the driving electric field may be considered to be constant throughout the entire nano-structure.

A further approximation for noble metal nano-structures is that the thickness t_{ns} is on the order of the skin depth δ of the metal $t_{\mathrm{ns}} \simeq \delta$. This relationship means that the electric fields incident upon the nano-structure are able to significantly penetrate into the nano-structure. As a result, external fields are able to collectively affect the conduction electrons of the entire particle as a whole with respect to the fixed positively charged lattice ions.

Through this forced motion of the collective electron cloud, a negative charge builds on the surface at one side of the particle while a positive charge builds on the opposite side via the remaining presence of positively charged lattice sites. The attraction of the negatively charged electron cloud to its own positively charged vacancy which it left behind at the opposite side of the nano-structure results in a restorative force. The characteristic strength of this restorative force, which results from the displacement of the electron cloud defines the resonance frequency of the LSPR for the nano-structure.

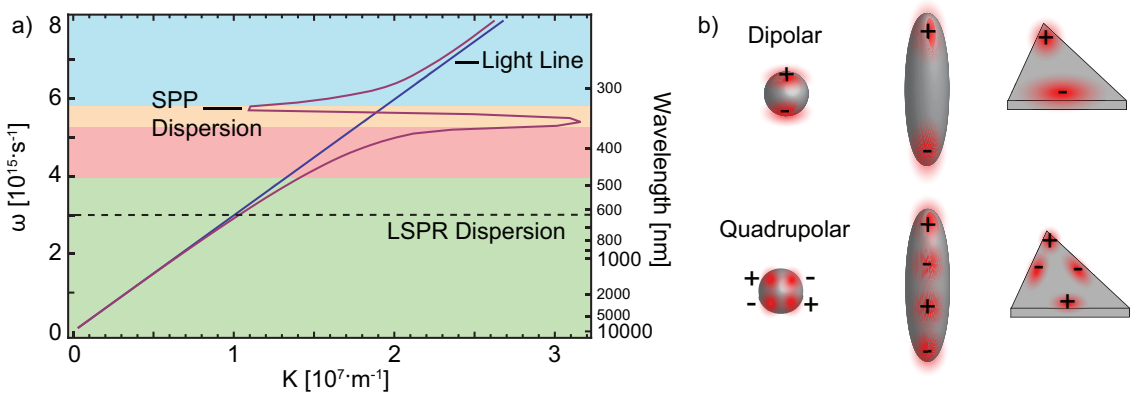

Figure 4.1: Panel a) displays the dispersion relation for the in-plane component of light in free space (blue), a surface wave on an Ag surface (purple), and for an example localized surface plasmon resonance (black dashed). The large distribution of allowed wavevectors for a localized plasmonic excitation allows for the efficient concentration of light. As discussed in Chapter 2, the background shading represents the nature of the surface wave with Zenneck, Fano, Evanescent, and Brewster waves represented by green, orange, red, and blue respectively. Panel b) displays simple qualitative examples of possible spatial distributions of the electric field for dipolar and quadrupolar excitations on spherical, ellipsoidal, and triangular nano-structures.

Fig. 4.1 a) depicts the variation of the spatial near-fields associated with both dipolar and quadrupolar resonances for sphere, elliptical, and triangular nano-structures. As shown, the spectral and spatial characteristics of the LSPR resonances may be manipulated through the variation of the nano-structure morphology.

4.2.1 The structural dependence of localized surface plasmon resonances.

The magnitude of the restorative force on a displaced electron cloud in a metallic nano-structure depends on several of the parameters including the size, shape, and particle material in addition to the dielectric properties of the medium in which the nano-structure is embedded. These attributes are all intricately tied to the polarizability of the electron cloud within the metallic nano-structure. For the case in which the excitation frequency of the external electric field matches the resonance frequency, the polarizability of the nano-particle is resonantly enhanced resulting in a drastic increase in the local strength of the

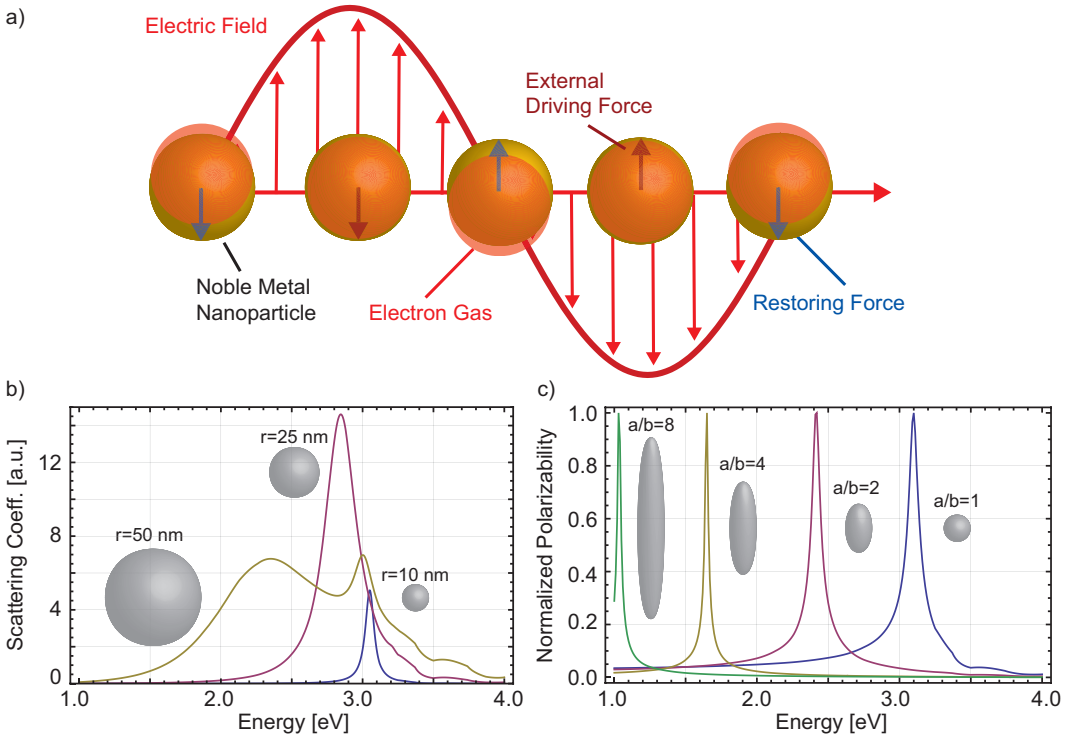

Figure 4.2: The schematic of the excitation of a localized surface plasmon for a small noble metal sphere is depicted in panel a). The external electric field, shown as the red sinusoidal wave, drives the oscillation of the electron cloud, whose oscillation is phase shifted by $\pi/2$ on resonance. Panel b) displays the spectral dependence of the scattering coefficient for differing sizes of Ag spheres as calculated by Mie theory. The strong dependence of the polarizability resonance on the aspect ratio of the nano-particle is displayed in panel c). Simulations for b) and c) were performed for particles embedded in a medium of refractive index $n = 1.5$.

electric fields associated with the nano-structure. Fig. 4.2a) displays a representation of the relationship between a spherical nano-particle, the driving external electric field, and the motion of the electron cloud for an on-resonance excitation frequency.

The dependence of the LSPR on differing geometric details is shown in Fig. 4.2b) (size) and c) (elongation ratio) for the specific case of Ag spheroidal structures embedded in a dielectric medium of $n = 1.5$. Panel b) displays the dependence of the scattering coefficient of Ag nano-spheres on the radius r of the sphere as modeled via Mie theory [49]. Here, it can be seen that small spheres fitting the Rayleigh approximation exhibit only a characteristic

dipolar response as exhibited by the resonance of the $r = 10$ nm particle. For nano-spheres of radii of $r = 25$ nm and $r = 50$ nm, as the radius increases the dipolar resonance broadens and redshifts while contributions from quadrupolar and other higher order modes begin to contribute to the extinction at higher energies.

Panel c) of Fig. 4.2 illustrates how the dipolar resonance in the longitudinal particle polarizability redshifts as a function of the ellipticity of a spheroidal Ag particle. Again operating under the Rayleigh approximation, spherical particles exhibit an LSPR spectral response which occurs at the blue end of the visible spectrum (4.2b and c, blue lines). As the aspect ratio of the particle is increased, the dipolar resonance linearly red-shifts to longer wavelengths. For example, for an aspect ratio of 8, the spheroidal nanostructure exhibits a longitudinal LSPR resonance which is already well into the near-infrared regime. This strategy of elongating the aspect ratio of a nano-structure to achieve LSPR resonances in the infrared regime and the associated properties as the resonance moves into the mid-IR spectral range will be discussed later in this chapter in section 4.4.

Adjustments to the Drude model description.

Typically model calculations like the ones presented in Fig. 4.2 are performed utilizing the bulk dielectric properties which for noble metals under the Drude model are characterized by an intrinsic free-electron scattering time τ_{scat}. This characteristic scattering time can be associated with the average distance an electron travels between scattering events by multiplying τ_{scat} by the Fermi velocity ($l_{\text{scat}} = v_F \cdot \tau_{\text{scat}}$). For example, for Ag the Fermi velocity and scattering times are $1.40 \cdot 10^6$ m/s [81] and 40 fs [24] respectively leading to a scattering length of $l_{\text{scat}} \simeq 50$ nm. Neglecting the effects of radiation damping, this means that for particles of size larger than the characteristic bulk scattering length, the spectral width of the localized plasmon resonance should primarily lie in agreement with the Rayleigh limit as characterized by the simple Drude model for bulk relaxation and should be independent of particle shape [72]. For particles of characteristic lengths smaller than the scattering length ($l_{\text{ns}} < l_{\text{scat}}$) a broadening of the plasmon should be observed corresponding to the increased contribution of surface related scattering to the total damping

of the plasmon excitation.

4.2.2 The effect of fine-scale structural details on localized surface plasmon resonances.

Noble metal nano-structures may be created by a variety of fabrication and lithography methods including electron-beam (E-beam) lithography [82] and chemical synthesis techniques. The advantage of E-beam lithography techniques lies in the high degree of control over the geometric arrangement of nano-structures. Through this fabrication technique arrays and specific arrangements of structures may be easily created allowing for the creation of extended complex geometric structures/patterns. However, E-beam lithography techniques and, in general, fabrication techniques which rely on evaporation of metal films onto a surface are limited to a spatial resolution of $\simeq 5 - 15$ nm. This resolution limitation is important in determining the characteristics of LSPR resonances, as the nature of the field distribution of localized plasmon resonant response is highly dependent on the fine-scale geometric features of the nano-structure. Defects caused through grain boundaries or inhomogeneous metal deposition can result in a poorly defined response of the LSPR in both the spatial and frequency domains.

In order to correlate a well-defined geometric structure with a characteristic LSPR electric field distribution, chemically synthesized metallic nano-structures have the advantage of a highly controllable geometric structure. Here, the development of novel chemical synthetic growth methods has led to creation of crystalline metal nanoparticles with structural control down to the nm range for a wide variety of sizes and shapes. Available geometries include cubes [83], prisms [73, 74, 84], rods [85], or spheroids [86] of several metals and their alloys which allows for the excitation of LSPR eigenmodes which are often stronger and better defined compared to those of polycrystalline structures produced by E-beam lithography techniques [87].

As revealed through dark-field spectroscopy techniques [75,88–94] and numerical simulations [76,77,95–98], the fine-structure geometric details of a nano-particle can have dramatic effects on the spectral distribution of the LSPR. Here, the local structural details of the nanoparticle affects how the electron cloud distributes itself across the particle as it is oscillates

through optical excitation. The high-crystal quality of chemically synthesized structures minimizes electron scattering from grain boundary defects thus reducing the mean electron scattering time τ_{scat} resulting in narrower sharper plasmons resonances [87]. Details such as sharpness of point features on nano-prisms or corners of nano-cubes can drastically affect the confinement of the electron cloud to constricted portions of the nano-structure both affecting the field strength and magnitude of the restoring force [76]. Furthermore, the nature of the local index of refraction can drastically alter the spectral location of the LSPR leading to the proposal of metallic nano-structures as sensing devices [90].

As most experimental characterization tools for the optical properties of metallic nano-structures operate in the far-field regime, little is known of the nature of the near-field distribution and strength related to these structures. This lack of understanding exists despite the fact that information on properties of the near-field distribution is vitally important both in confirming the predictions of numerical simulations and in implementing the many potential applications of nano-plasmonics which rely on the enhancement of the electric-field around the nano-structures. *s*-SNOM represents a unique technique which allows for the characterization of the spatial distribution and strength of the near-field distribution surrounding these nano-structures with high resolution. The results of *s*-SNOM mapping allow for a correlation between the far-field spectral behavior of the localized surface plasmon resonances both with the spatial distribution of the near-fields and how said near-fields relate to the fine structural details of the nano-particle geometry.

4.3 Near-field characterization of Ag triangular nanoprisms.

For characterization of the spatial distribution of near-fields associated with localized surface plasmon resonances, triangular nanoprisms hold several unique attributes which make them ideal candidates for *s*-SNOM characterization in the visible spectral range. It has been well established via previous dark-field spectroscopy measurements [75, 88, 99] and numerical simulations [76, 77] that Ag nanoprisms exhibit not only a strong LSPR response, but also a response whose spectral properties are highly dependent on the prism size and the specific details of the geometry. These far-field studies and analysis have further shown that in addition to the presence of dipolar LSPR resonances, an additional rich spectral struc-

ture also exists which includes higher order quadrupolar modes located at higher energies. While the spatial distribution of the electric fields associated with the dipolar resonances of these structures may seem trivial, the spatial distribution of the higher order quadrupolar excitations are complex. Indeed, previous to the measurements presented here, the field distribution of the quadrupole modes was only accessible via numeric simulation. Through implementation of *s*-SNOM mapping of the LSPR resonances, we are able to experimentally characterize the spatial near-field distributions associated with both the dipolar and more complex quadrupolar excitations of these triangular nanoprisms

4.3.1 Synthesis and far-field characterization.

For our studies, triangular nanoprisms with sizes ranging from 50 to 400 nm were synthesized from aqueous solution of silver nitrate ($AgNO_3$) and poly(vinyl pyrrolidone) (PVP) as discussed previously [74]. This method has been shown to produce triangular nanoprisms of controllable size with {111} triangular face and {100} side facets as determined by electron diffraction [100]. Samples were prepared by dispersing the nanoparticles on a silica substrate using a drop cast deposition technique. As the synthesis technique involves the presence of a PVP polymer solution , the samples were subsequently rinsed under deionized water in order to remove as much remaining PVP on the surface as possible. The resulting sample consists of an assortment of individual nanoprisms randomly distributed across the substrate surface. The LSPR response of the individual nanoprism shown is measured using standard white-light dark-field micro-spectroscopy.

The spectral width of the LSPR resonances in the Ag nanoprisms studied corresponded well with the Rayleigh limit discussed in section 4.2.2 implying that the bulk scattering contributions were still the primary damping mechanism of the plasmon excitations. Fig. 4.3a) displays an typical dark-field scattering spectrum for an Ag nanoprism with a length of 200 nm as estimated from the LSPR resonance location.

In general, it has been well established both experimentally [73–75] and theoretically [76,77,95] that for both Ag and Au nanoprisms the dipole resonance broadens and red-shifts with increasing particle size. As the size of the particle increases beyond the Rayleigh ap-

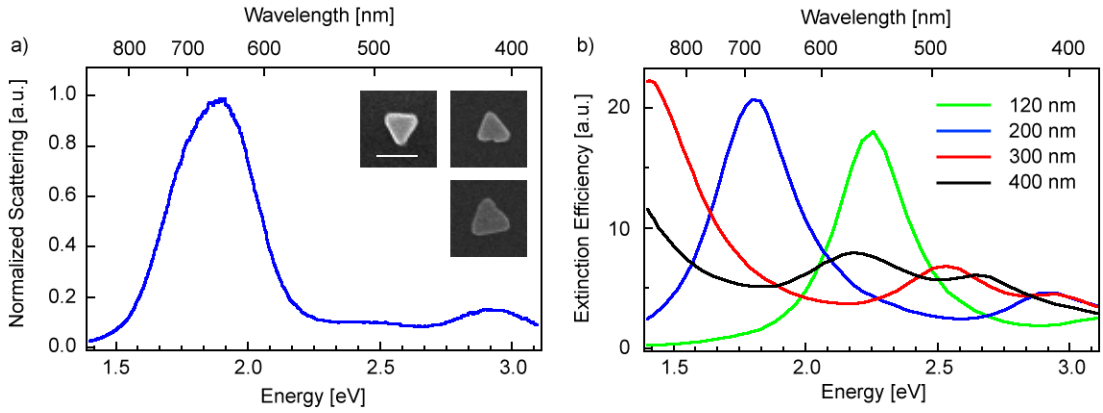

Figure 4.3: An example dark field LSPR scattering spectrum for an individual Ag nanoprism with a length of 200 nm as estimated from the LSPR resonance location is displayed in panel a). The insets display electron micrographs of typical nanoprism structures with the scale bar of length 200 nm. Panel b) displays the calculated optical extinction spectra for Ag nanoprism particles truncated tips and sizes corresponding to an edge length of 120, 200, 300, and 400 nm with under *s* polarized illuminating light. The calculated extinction spectra are characterized by a large dipolar excitation at lower energies with weaker spectrally separated multipolar modes at higher energies. As the edge length increases the LSPR resonances systematically shift to lower energies.

proximation scattering limit, quadrupole and higher order multipole modes begin to emerge leading the appearance of additional spectral features at higher energies [74, 75]. This is observed within Fig. 4.3a) by the peak corresponding to the quadrupolar resonance in the dark-field scattering spectra at $\simeq 415$ nm. Discrete Dipole Approximation (DDA) simulations of the relationship of the spectral positions of the dipole and quadrupolar modes with the edge length of the nanoprism are displayed in Fig. 4.3b). The clear spectral separation of the dipole and multipole modes and their systematic, near linear frequency shift to lower energies with increasing size allows for the investigation of the near-field distribution associated with these different LSPR modes by tuning the particle size for a fixed laser excitation frequency.

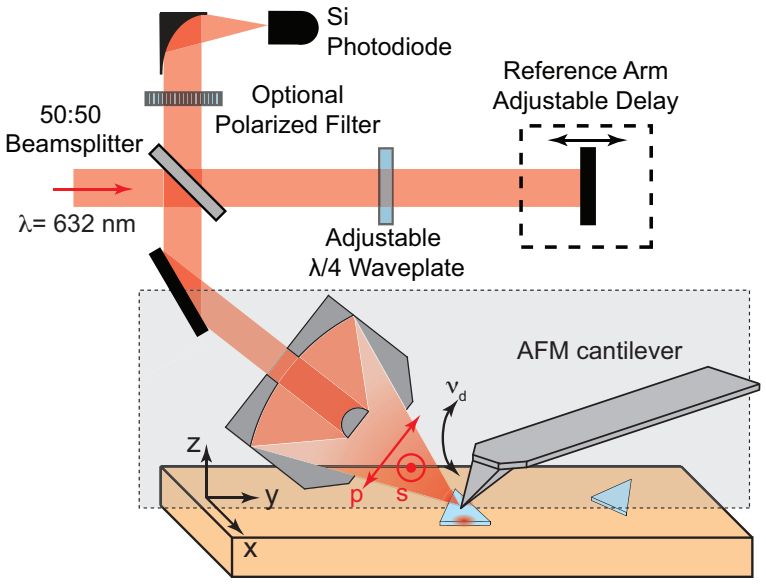

Figure 4.4: Schematic of experimental setup for mapping of the near-fields associated with localized surface plasmon resonances on noble metallic nano-structures. For the *s*-SNOM mapping of Ag nanoprisms, polarization selective excitation at $\lambda = 632$ nm was implemented for nanoprisms of varying size. The use of Si AFM probe tips ensures minimal perturbation of the intrinsic particle near-field distribution. Phase and polarization sensitive information is obtained by interferometric homodyne detection.

4.3.2 s-SNOM mapping of Ag nanoprisms.

In order to probe the plasmonic near-field of the Ag nanoprisms we utilize *s*-SNOM measurement techniques implementing the use of a dielectric AFM tip as a minimally perturbative scattering probe [101–103]. As discussed in chapter 3, this experimental approach towards characterizing evanescent fields associated with the nanoprisms provides enhanced sensitivity and superior spatial resolution down to ∼15 nm compared to conventional microscopy techniques [104–107]. Additionally, the projection of the near-field polarization and phase into the far-field of the tip-scattered signal uniquely allows for amplitude and phase sensitive probing of the nanoprism fields via the homodyne interferometric detection [55,108–110] techniques discussed in section 3.10.

The experimental setup as shown schematically in Fig. 4.4 is based on a modified atomic

force microscope (AFM, CP-Research, Veeco Inc.) with sample scanning and dynamic force control of the cantilever probe tip. For the measurements on Ag nanoprisms described here, monochromatic excitation from a HeNe laser ($\lambda = 632.8$ nm) was used for resonant excitation of the optical LSPR polarization of individual nanoprisms. In an epi-illumination and -detection geometry a Cassegrain objective (NA = 0.5, working distance =20 mm, f=13 mm, angle of incidence = 60° with respect to the surface normal) directs the light onto the tip apex region with elliptical focus size of $\sim$2 μm in width at a power of $\sim$5 mW. The incident and detected polarizations can be controlled by polarizing optics with s and p defined with respect to the plane formed by incidence/emission k-vector and the tip axis (see Fig. 4.4). For the scattering experiments, individual nanoprisms of desired size are located by AFM scanning. Under laser illumination the tip-scattered near-field response of the particle is then recorded simultaneously with the topography. With the s-SNOM acquisition times between 10 and 60 minutes small sample drifts result in minor image distortions as indicated by the slightly different shapes of the dashed image contours.

For the mapping of fields surrounding Ag nanoprisms silicon scanning probe tips (ATEC NC-20, Nanosensors) were used as near-field probes. While probing of the optical near-field is necessarily associated with a frustration of the evanescent field of the nanostructure through the presence of the AFM tip, silicon as a tip material ensures a small perturbation of the intrinsic particle near-field distribution albeit at the expense of a reduced signal intensity compared to the implementation of metallic AFM probe tips. Due to the lack of antenna or plasmon resonances at visible wavelengths for Si tips, the invasive effect of the probe is minimized especially with regard to the strong plasmon resonant polarization of the crystalline Ag nanoprisms. The tip scatters both s- and p-polarized light effectively, however, the magnitude of the scattering is dependent on the geometry-related tip scattering function [108, 109, 111]. While the tip scatters both s and p-polarizations, generally the magnitude of the scattering of the p-component is stronger. For a given measurement, the combination of the incident and detection polarizations will be denoted by the subscripts "in" and "det" respectively (i.e. a measurement with s incident polarization and p detection polarization would be denoted $s_{\mathrm{in}}p_{\mathrm{det}}$).

The tip-scattered near-field signal is directed onto a silicon photodiode (Model 1801, New

Focus). An optional interferometric detection with a reference beam of adjustable phase is used for homodyne amplification in order to extract the near-field phase information. Selection of the polarization of the reference field is performed through use of a $\lambda/4$ waveplate in the reference arm. As discussed in section 3.6, the near-field scattering response from the tip-sample gap region is discriminated from the far-field background by signal demodulation at the second and higher harmonics of the cantilever tip-sample dither frequency ν_d by lock-in detection [112].

4.3.3 Ag nanoprism s-SNOM characterization results.

Fig. 4.5 shows the near-field pattern resulting from s-SNOM characterization of a small rounded Ag prism exhibiting a resonant dipole excitation with an edge length of $l \approx 120$ nm and a height of $h \approx 35$ nm for different excitation and detection polarization combinations. Topography (a) and s-SNOM data of the second-harmonic demodulated optical signal (c) are shown for s-polarized resonant excitation and scanning in the xy plane as defined in Fig. 4.4. The corresponding out-of-plane field localization in the z direction is illustrated by a s-SNOM measurement in the yz plane shown in Fig. 4.5b) which was performed along the trajectory indicated by the white dashed line in the topography scan.

The observed field localization to within just several 10s of nm above the nanoprism confirms the evanescent near-field character of the signal detected in these experiments. As the Si AFM probe primarily scatters p polarized light, from polarization selective detection it can be demonstrated that the s-SNOM signal without interferometric detection predominantly probes the out of plane $|E_\mathrm{z}|$-component of the nanoprism (Fig. 4.5c).

For comparison, Fig. 4.5e) shows corresponding s-SNOM result of the same particle applying interferometric homodyne signal amplification for s-polarized excitation and s-polarized detection ($s_\mathrm{in}s_\mathrm{amp}$), amplifying the in-plane $|E_\mathrm{x}|$ field distribution. Similarly, for p-polarized excitation and detection ($p_\mathrm{in}p_\mathrm{amp}$) as shown in Fig. 4.5f) the $|E_\mathrm{z}|$ component is probed. As can be seen the optical field in the vicinity of the small nanoprism is characteristic of a simple in-plane resonant dipole excitation with its orientation determined by the input polarization. The two lobes of the s-SNOM intensity distribution, being proportional

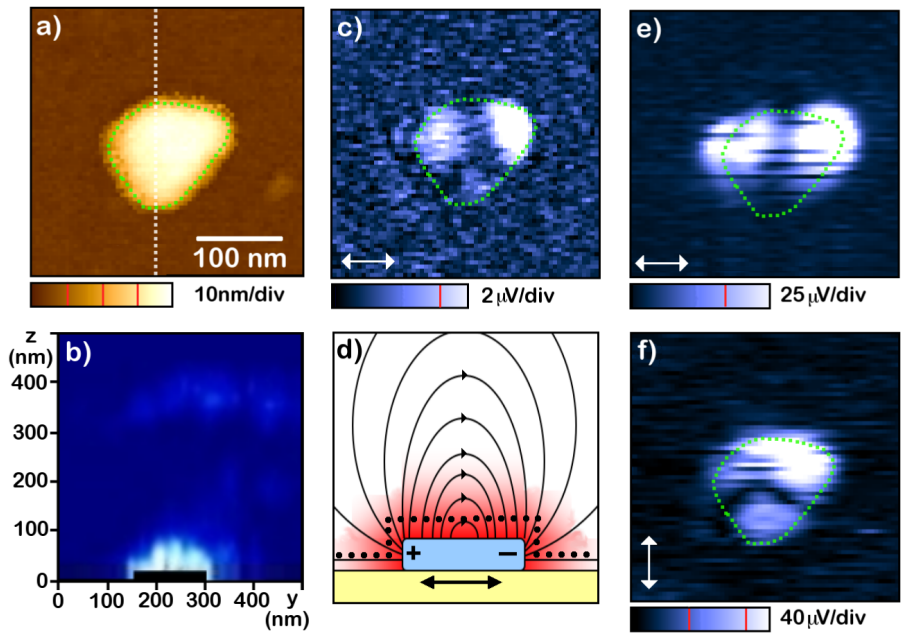

Figure 4.5: Topography (a) and corresponding near-field s-SNOM images for a rounded single crystal Ag nanoprism exhibiting a dipolar excitation. For s-polarized excitation and non-interferometric detection, (c), the signal is dominated by the out-of-plane z-component, $|E_z|$. The spatial 3D field localization to within 10's nm above the particle is seen from the xz-scan (b) for p-polarization excitation along the trajectory indicated by the dashed line in the topography (a). For comparison, in homodyne amplification detection in $s_{\rm in}s_{\rm amp}$ polarization configuration the in-plane field component $|E_x|$ is probed (e) as compared to $|E_z|$ for $p_{\rm in}p_{\rm amp}$, (f). Schematic (d) shows a corresponding model field distribution with tip scan line indicated (dotted). Arrows indicate incident polarization.

to the absolute value squared of the tip-scattered local evanescent field, thus represent the field enhancement near the two poles of the oscillating dipole. In contrast to the $|E_{\rm z}|$ field, which is predominantly concentrated at the near-edge regions confined within the boundaries of the particle (Fig. 4.5c, f), the in-plane $|E_{\rm x}|$ field exhibits significant intensity beyond the outer periphery of the nanostructure (Fig. 4.5e) consistent with the expected dipolar field distribution as shown schematically in Fig. 4.5d).

Fig. 4.6 shows corresponding s-SNOM results for a large nanoprism with an edge length of $l \approx 450$ nm. For 633 nm excitation wavelength the response is dominated by the higher order quadrupolar polarization response (Fig. 4.3) [74, 77, 113]. The s-SNOM images in

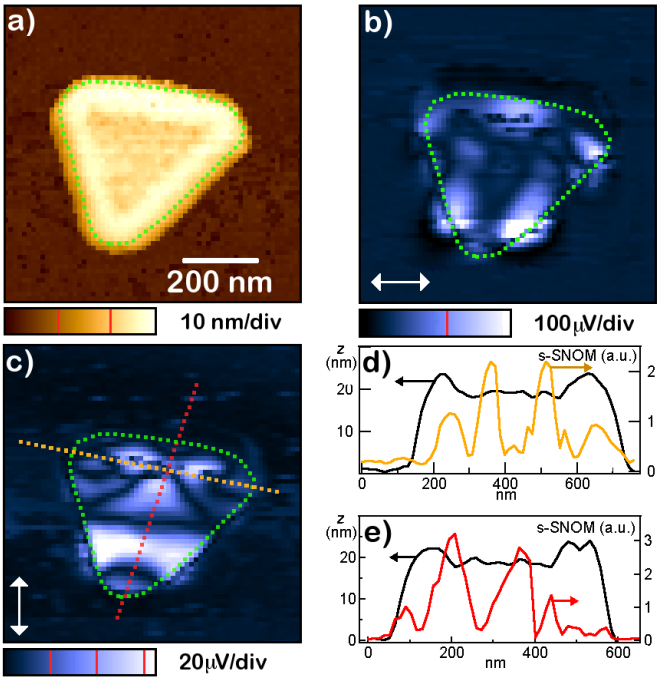

Figure 4.6: Topography (a) and corresponding tip-scattered near-field images at 633 nm for *p*- (c) and *s*-polarization (b), of a large single crystal Ag nanoprism exhibiting quadrupole excitation. The *s*-SNOM cross sections (d,e) indicate spatial field variations at lengths scales as short as 20 nm.

Fig. 4.6 are observed for *p*- (c) and *s*-(b) polarized excitation. They exhibit large spatial modulations on length scales as short as 20 nm as seen in the lateral signal cross sections (d,e). The dominant features of the near-field distribution observed can be identified with the quadrupolar spp excitation as discussed below in section 4.3.4. Finer details are likely due to slight asymmetries in particle shape, and possible spectral overlap of higher order excitations together with the possible effect of the retardation induced phase variation of the incident driving field.

4.3.4 Comparison Ag nanoprism measurements with numerical simulations.

Numerical calculations using the discrete dipole approximation (DDA) [114] provide insight into the origin of the spp mode structure and its variation with particle size. Fig. 4.7

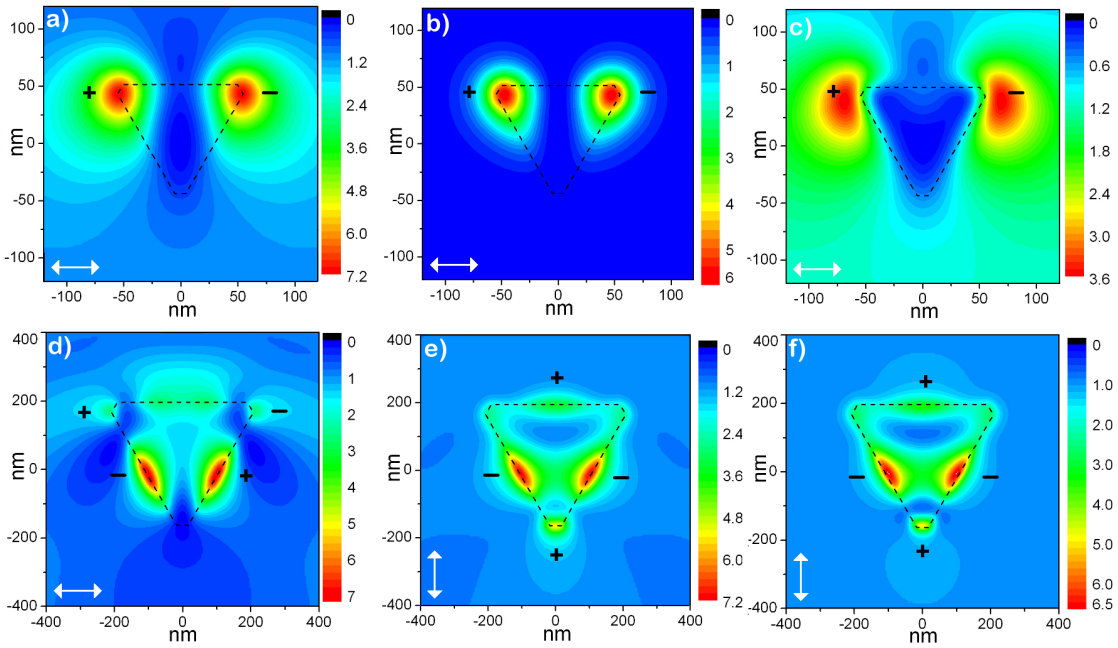

Figure 4.7: Calculated optical near-field distribution of Ag nanoprism for 633 nm excitation. Top row: dipolar mode for nanoprism with edge length 120 nm, thickness 35 nm, and 10nm truncated from each tip under s-polarized excitation, with total field $|E^2| = |E_x^2 + E_y^2 + E_z^2|$ (a), z-component $|E_z^2|$ (b), and in-plane field $|E^2| = |E_x^2 + E_y^2|$ (c). Bottom row: quadrupolar fields of nanoprism with edge length 450 nm, thickness 25 nm, and 35 nm truncated from each tip. Panel d) shows the total field $|E^2|$ under the s-polarized excitation. Panels e) and f) represent the total field $|E^2|$ and z-component $|E_z^2|$ under the p-polarized illumination respectively. Signs represent relative phase of quadrupoles

shows calculated near-field patterns expected under the experimental conditions with angle of incidence of 70° and both polarization excitations for 633 nm light, i.e., with the driving electric field parallel or perpendicular with respect to the top edge of the prism. For the dipole resonance of a small nanoprism with edge length of 120 nm the calculated near-field patterns at a vertical plane 20 nm above the triangular plate surface are displayed for the total field intensity ($|E^2| = |E_x^2 + E_y^2 + E_z^2|$) (a), the z-component field intensity ($|E_z^2|$) (b), and the in-plane component field intensity ($|E_x^2 + E_y^2|$) (c). The largest field and strongest confinement at the tips is found for E_z with the two poles being out of phase in accordance with the experimental observation. The weaker in-plane field exhibits a more

extended spatial distribution beyond the particle boundaries (see Fig. 4.5e) and Fig. 4.7c). For orthogonal polarization, i.e., driving the plasmon eigenmode between a prism tip and its opposite edge, the enhancement is spatially less confined not only at the edge as expected, but also at the prism tip as evident from the $|E_z|$ field distribution (Fig. 4.5f). This can be rationalized considering the induced free electron current being scattered by the tapering prism edges under an angle with respect to the driving optical laser field.

The calculated near-field patterns for a quadrupole resonance as associated with a large nanoprism particle are shown in Fig. 4.7d-f). Fig. 4.7d) represents the distribution of the total field intensity, $|E^2|$, under the *s*-polarized incidence. Fig. 4.7e) and f) represent the total field $|E^2|$ and its *z*-component $|E_z^2|$, respectively, under *p*-polarized excitation. Similar to the case of small prisms, the *z*-component dominates over the in-plane field. In *p*-polarized excitation, the spp near-field pattern shows a quadrupole response characterized by four field enhanced regions (+/- signs indicate their relative phases). These poles exhibit unequal field intensity and different shape as also observed in the experiment. In accordance with experiment both *s*- and *p*-polarization give rise to a large local field enhancement at the lower two adjacent edges which dominates over the corresponding fields found at the tips (Fig. 4.6b,c). For *s*-polarization, the other two weaker charge centers of the quadrupole can be discerned at the two tips located at either end of the top edge of the prism as seen in Fig. 4.6b)) (experiment) and Fig. 4.7d) (theory). Similarly, for the *p*-polarized case only one pole is located at a tip giving rise to a corresponding small field enhancement for the lower tip as seen in Fig. 4.6c) (experiment) and Fig. 4.7e,f) (theory). With an oblique angle of incidence and structure sizes up to several hundred nanometers, phase retardation can influence the spp excitation. Varying the angle of incident radiation, comparison of further calculations (data not shown) with the results shown in Fig. 4.7 indicates retardation of the excitation field has minimal effects on the quadrupolar modal distribution observed.

In agreement with the experimental observation, the calculations also predict the additional polarization density along the top edge of the prism. The quadrupole assignment for *s*-polarized excitation is furthermore consistent with the theoretically derived quadrupole vector field in [ref. [77]]. The interference of the quadrupole mode with dipole and higher order modes may give rise to the additional signal modulations at higher spatial frequencies

as observed in the experiments together with possible effects due to deviations from the ideal equilateral triangular shape and inhomogeneities in the illumination.

From the observed transition of the near-field distribution from a simple dipole to a complex quadrupole spp excitation with the size of the Ag nanoprisms a number of general conclusions can be drawn. For small particles with edge length of order $l < 50 - 100$ nm the emission is dominated by a single resonance due to pure dipole excitation [74, 77]. This characteristic size corresponds to the size limit for the validity of the Rayleigh approximation with the optical response becoming independent of the particle geometry in general [72].

Observed optical signal between separate scans of s- and p- polarization in Figs. 4.5 and 4.6 differ by less than a factor of 2 which is a good indication that the fields induced by each polarization excitation are of comparable strength as indicated by numerical simulations in Fig. 4.7. It should be noted however, that a quantitative comparison of the relative strength of the different polarization components of s-SNOM fields is difficult in general. Even with reference homodyne amplification, a polarization anisotropic self-homodyning background of uncontrolled phase orientation from the far field and tip scattering may still affect the magnitude of the detected signal.

The nature of the multipolar excitations has been of interest since the first experimental observations of spectral features at higher optical frequencies in Au or Ag nanoprisms [77,84, 115]. Our results provide the first identification of the corresponding near-field distribution with ultrahigh spatial resolution. The reduced dimensionality, resultant from the high aspect ratio in terms of edge length with respect to thickness, uniquely allows for the suppression of out-of-plane modes and the spectral separation of quadrupole and even higher order mode excitation for these effectively 2D structures [77]. This behavior is akin to elongated quasi-1D rods [89] where spectrally well-separated multipole resonances can be observed. This is in contrast to, e.g., spherical particles, where the multipolar resonances are not spectrally distinct from the broadening of the dipolar resonance.

It was noted theoretically that the multimode excitation in plasmonic nanoprisms becomes increasingly efficient with increasing size and decreasing thickness giving rise to a surprisingly strong surface plasmon polarization density across large areas of the nanoprism [77]. Our experiments seem to confirm this prediction: The tip-scattered intensities of the

multipole modes for large prisms are comparable to the signal obtained for the small dipolar nanoprisms under otherwise identical experimental conditions. This behavior can be interpreted with the prism thickness being comparable to or thinner than the skin depth of ~ 30 nm for Ag at the excitation wavelength of 633 nm. As a result, the optical field inside the prism experiences a low loss of the multimode field excitations that are otherwise strongly damped in the bulk due to the smaller wavevectors associated with them [77]. Note however, that the near-field intensities are not necessarily reflected in intense radiative far-field emission as seen by the comparably small scattering intensities of the multipoles. This is due to the in general larger wavevector mismatch of the multipole vs. the dipole excitation with the optical far-field as known form antenna theory [89].

Contrary to intuitive expectation, in cases of multipole excitation as seen in the data presented here and other data for different sized prisms (data not shown), the tips of the triangles in general do not represent regions of highest local field enhancement. While higher order modes are expected to penetrate more effectively into smaller geometrically confined regions due to their larger wavevector [113], these regions are not necessarily associated with the highest polarization density.

4.4 Extension of LSPR to mid-infrared regime.

As many noble metal nano-structures in the Rayleigh limit have aspect ratios $\simeq 1$, their characteristic LSPR response occurs in the visible or near-IR spectral regimes. This spectral response, however, does not mean that the concept of a resonant polarizability response cannot be extended to lower frequencies. In fact, it is well known that phenomena and applications involving electromagnetic surface waves on noble metals encompass a wide frequency range extending over many orders of magnitude only limited at high energies by the interband absorption typically in the blue/UV spectral range as determined by the electronic band structure of the metal.

In contrast to the visible spectral region, the intrinsic properties of surface waves in the mid-IR regime are less well understood. This is despite the general importance of mid-IR active nanostructures for surface enhanced IR absorption (SEIRA) [116–121], as optical antennas for IR emitters [122–124], IR and THz detectors [125], and thermal sensors [126,127].

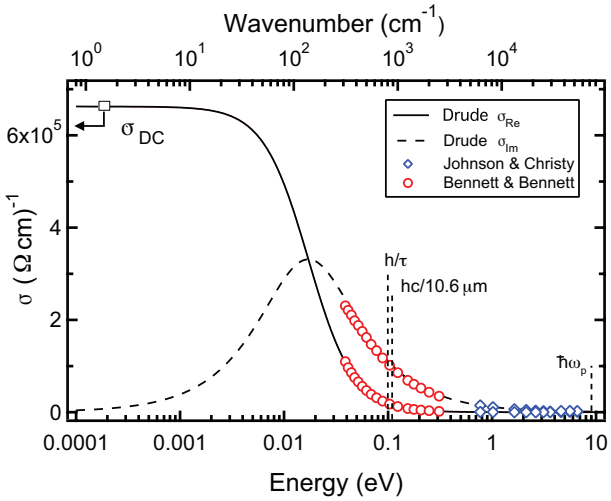

Figure 4.8: Drude model prediction of the frequency dependence of the real (solid line) and imaginary (dashed line) conductivity of silver. Selected data points up to the longest wavelength available from reference [132], derived from measured optical constants of silver, illustrate the close correspondence between Drude theory ($\tau = 40$ fs, $\hbar\omega_{\rm pl} = 9.17$ eV, and $\epsilon_{\rm DC} = 3.7$) as discussed in section 2.3 and experiment in the mid-IR and visible spectral ranges [21, 22, 132].

Due to the strong damping of the coherent electron oscillation at visible frequencies, the corresponding SPP propagation length is limited to several micrometers [128–130]. The damping is greatly reduced in the IR allowing propagation lengths into the millimeter range [131]. In addition, studying the mid-IR response of metal nanostructures provides microscopic insight into the underlying electron dynamics with the optical cycle period being comparable to the Drude electronic relaxation time $\tau_{\rm scat}$. This spectral range signifies the transition regime that links the low energy Hagen-Rubens regime describing classical antenna resonances ($\omega \ll \tau_{\rm scat}^{-1}$) with the relaxation regime ($\tau_{\rm scat}^{-1} < \omega < \omega_p$) of the surface plasmon, with ω_p being the plasma frequency of the metal [18].

Fig. 4.8 displays the experimentally measured values and Drude fit of the real and imaginary components of the optical conductivity of Ag across a frequency range several orders in magnitude spanning from the low frequency regime through the visible spectral range. Here, the mid-IR spectral range is distinguished from the visible by a both larger real

conductivity Re[σ] and imaginary conductivity Im[σ]. For conventional surface waves, this elevated conductivity manifests itself in less confined more "light-like" surface waves, with longer propagation distances than the visible regime (refer to Chapter 2). These "light-like" surface waves correspond to Zenneck-type surface waves. By utilizing structural resonances in low-dimensional/quasi-1D noble metal structures, the lack of confinement characteristic of the mid-IR 2D plasmonic excitations may be overcome through the concentration of intense fields within/around the nano-particle.

4.4.1 The concept of dipolar optical antennas in the form of rod-like nanostructures.

As shown in Fig. 4.8, there are several characteristic regimes for the conductivity of noble metals (for further details refer to Chapter 2). The low frequency limit is characterized by a high real part of the conductivity and a low imaginary component related to the loss. It is in this radio frequency/microwave frequency regime where the traditional understanding of an antenna structure is defined. Several assumptions are made as to the nature of relation of the wavelength of light generated/captured to the antenna. Specifically, for a simple dipole antenna, it is a simple first order assumption that the antenna material is a perfect conductor ($\sigma = \infty$), that radius of the antenna structure is negligible ($r \ll \lambda_{\text{exc}}$), and that penetration of the electric field inside the antenna structure is small ($r \gg \delta$). These assumptions imply that, for an incoming excitation wavelength λ_{exc}, the resonant length for a dipolar antenna excitation L_d should occur approximately at half the excitation wavelength $L_d = \lambda_{\text{exc}}/2$.

The above assumptions, however, break down and do not extend to localized surface plasmon resonances at optical frequencies. At these high frequencies for conventional rod-like nano-structures the noble metals exhibit significant loss (Im[σ] > Re[σ]), the ratio of the radius of the nanorod to the resonance wavelength is finite ($r/\lambda \neq 0$), and the electric field may significantly penetrate into the nano-rod structure ($\delta/r \neq 0$). This means that the traditional scaling of low-frequency dipolar resonances breaks down, and that a new model which incorporates the above parameters into the determination of the resonant length must be found.

One method of modeling the LSPR resonances in cylindrical particles is by describing

the nano-structure in terms of a cylindrical waveguide. Here, a light traveling along the waveguide is defined in terms of an on-axis wavevector γ and an off-axis wavevector inside κ_1 and outside κ_2 the cylinder. As the size of the waveguide is reduced, it is well known that the corresponding propagating wavevector γ is also reduced. The relationship of γ to the radius of the cylindrical structure is given by the solution for TM_0 modes for a cylindrical waveguide [133, 134],

$$\frac{\epsilon_{\text{rod}}[\lambda]}{\kappa_1 r}\frac{J_1[\kappa_1 r]}{J_0[\kappa_1 r]} - \frac{\epsilon_{\text{surr}}[\lambda]}{\kappa_2 r}\frac{H_1^{(1)}[\kappa_2 r]}{H_0^{(1)}[\kappa_2 r]} = 0 \tag{4.1}$$

where,

$$\kappa_1 = k_0\left(\epsilon_{\text{rod}} - \left(\frac{\gamma}{k_0}\right)^2\right)^{1/2} \tag{4.2}$$

$$\kappa_2 = k_0\left(\epsilon_{\text{surr}} - \left(\frac{\gamma}{k_0}\right)^2\right)^{1/2}. \tag{4.3}$$

Given a excitation wavelength λ and radius r and with defined values for the dielectric permittivity of the rod ϵ_{rod} and the surrounding medium ϵ_{surr}, we may solve for the propagation constant γ which satisfies Eqn. 4.1. The quantity γ defines an effective wavelength for light in the waveguide $\lambda_{\text{eff}} = 2\pi/\gamma$. The effective dipole resonant length, can to first order then be defined as $L_d = \lambda_{\text{eff}}/2$. Recently theoretical work has further incorporated an additional modification to account for the apparent increase in antenna length due to the reactance of the nano-rod end resulting the following expression for the dipole resonance length [135],

$$L_d = \frac{1}{2}\left(\lambda\frac{k_0}{\gamma} - 4r\right). \tag{4.4}$$

The dependence on the L_d on both the radius of the cylindrical nanostructure and the wavelength of light is displayed in Fig. 4.9. Panel a) exhibits scaling of the effective dipole length as a function of r. It is noteworthy here that deviation from the classical resonance length occurs for radii below the nominal skin depth of the rod material. The linear scaling of the dipolar resonance with wavelength is exhibited in panel b) for the visible spectral range and panel c) for the infrared for rods of varying radii.

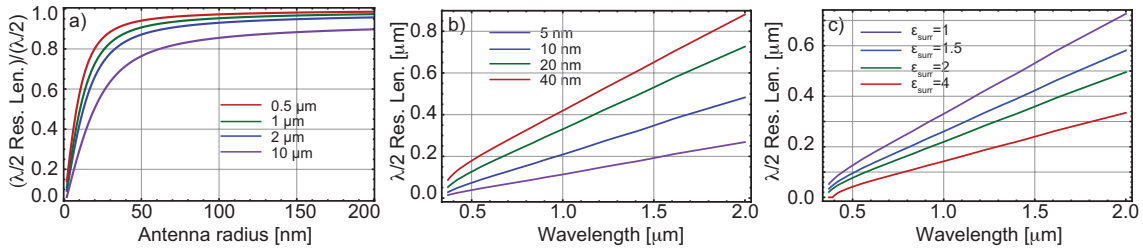

Figure 4.9: The characteristics of the dipolar resonance length for rod-like Ag plasmonic structures are depicted above. Several factors play important roles in determining the dipolar resonance length including the effective index of refraction in which the nanorod is embedded and the radius of the rod. Panel a) displays the relation of the resonance dipolar resonance length as a function of the nanorod radius for an antenna composed of Ag and excitation wavelengths of $\lambda = 0.5$, 1, 2 and 10 μm. Panel b) displays the near-linear scaling of the dipolar resonance length of Ag nanorods as a function of excitation wavelength for nanorod radii of 5, 10, 20, and 40 nm in a surrounding medium of permittivity $\epsilon = 1$. Finally, panel c) demonstrates the sensitive dependence of the dipolar resonance length/excitation wavelength relationship on the index of refraction of the surrounding medium. For a rod of radius $r = 20$ nm, the $\lambda/2$ resonant length is plotted for surrounding media of dielectric constant ϵ_{surr} =1, 1.5, 2, and 4.

The synthesis of high aspect ratio silver nanowires/rods with lengths up to tens of micrometers (synthesis discussed below) enables the extension of structural plasmon resonances into the mid-IR range. With previous work having been limited to the study of the far-field properties of these crystalline structures, little is yet known as to the nature of the underlying resonant modes and associated spatial field distribution and local field enhancements resulting from plasmonic excitations in the mid-IR range. To address these questions, *s*-SNOM measurement techniques can be employed to study the resonant dipole and higher order modes at the low energy limit of the coherent plasmon polariton regime of these Ag nanowires. Phase sensitive optical vector near-field mapping at an excitation wavelength of $\lambda = 10.6$ μm provides a direct image of the nanometer scale spatial field distribution of the surface standing waves and their dependence on microscopic structural parameters. *s*-SNOM can be further utilized to establish the scaling of the dipolar resonance with wavelength in order to compare with classically understood antenna resonances. Here, deviation from the classical prediction is expected as the skin-depth δ and rod radius r are

similar in size [135–137].

4.4.2 Synthesis of Ag nanorods and s-SNOM measurement procedure for mid-IR characterization.

High aspect ratio crystalline Ag rods can be grown with high yield by reducing silver nitrate with ethylene glycol in the presence of poly(vinyl pyrrolidone) (PVP). A homogeneous diameter even for high aspect ratios (1:10 to 1:200), an atomically smooth surface, and reduced electron scattering with the absence of grain boundaries due to the crystalline structure enables an improvement of the optical properties relative to rough, polycrystalline wires made from electrothermal deposition thus providing an ideal material for mid-IR plasmonics. The Ag nanowires measured were synthesized as described in detail previously [138]. 5 mL of ethylene glycol (EG) were stirred in a glass vial, suspended in an oil bath (150°C). After heating for 1 hour under stirring at 260 rpm, 40 μL of a 4 mM copper(II) chloride solution ($CuCl_2$) in EG were added. After an additional 15 minutes, 1.5 mL of a 0.147 M poly(vinyl pyrrolidone) (PVP, Molecular weight Mw $\approx$ 55,000, concentration expressed in terms of monomer) solution in EG were added followed immediately by 1.5 mL of a 0.094 M silver nitrate ($AgNO_3$) solution in EG. The reaction was quenched after another 1 hour. Finally, the reaction products were washed with acetone, collected by centrifugation, and subsequently dispersed in water. The silver nanorods obtained were characterized by scanning and transmission electron microscopy (SEM/TEM) as shown in Fig. 4.10b-d). They exhibit a pentagonal cross-section due to fivefold twinning consistent with silver nanowires grown from decahedral seeds in which the (100) surfaces of the wire have been stabilized with PVP [93, 139].

4.4.3 Results/Discussion of mid-IR s-SNOM mapping of Ag rods.

Fig. 4.11 displays topography and non-phase resolved s-SNOM scans corresponding to $|E_z|^2$ of different Ag wires under the $s_{\text{in}}p_{\text{out}}$ illumination and detection configuration. Panels a), c), and e) display the topography data of Ag nanorods of lengths ranging between from $L \approx 1$ μm to $L \approx 12.3$ μm. For lengths up to approximately 4 μm, dipolar mode

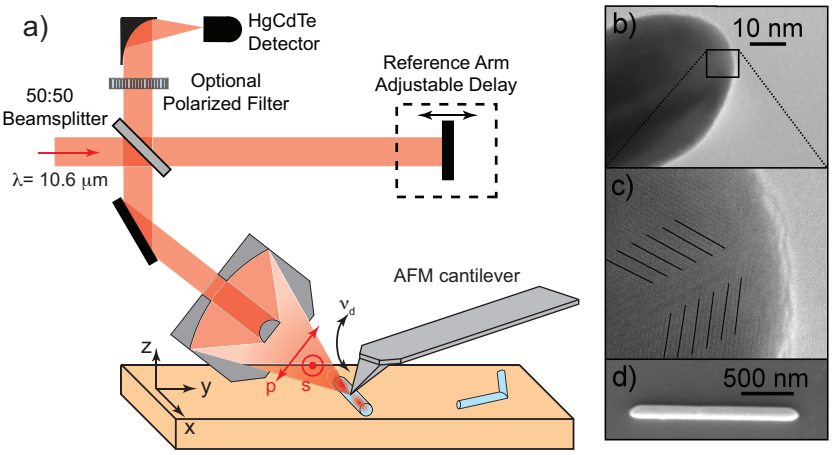

Figure 4.10: Scattering-scanning near-field optical microscopy (s-SNOM) (a) with polarization selective excitation and interferometric homodyne detection to probe specific near-field vector components of IR plasmon modes of Ag nanowires. Transmission electron microscope images (TEM) confirm the crystalline nature and pentagonal twinning of the nanowires (b, c). Solid lines parallel to the atomic planes have been added as a guide to the eye. Scanning electron microscope (SEM) image of a representative Ag nanowire with typical aspect ratio studied (d).

patterns are observed (Fig. 4.11b) and d) with one lobe at either end of the wire. For longer wires, $L \approx 6$ μm (upper wire in f), the wires exhibit a more complex spatial distribution characteristic of multipolar excitations.

No contrast is observed for sufficiently off-resonant excitation as evident by the lack of optical signal, Fig. 4.11b) and d), corresponding to several structural features seen in the topographies in a) and c). For wires orientated predominantly along the x-direction (wire section visible on left side of a), the longitudinal resonance can not be excited for s_{in}. Similarly, negligible contrast is observed for sub-micron Ag particles that exhibit plasmon resonance in the visible spectral region. The bent wire shown in c) does not exhibit any s-SNOM contrast although the driving field in the y-direction still has a component along the upper wire segment. This may be due to an associated spectral resonance shift and/or additional damping associated with the bend itself, thus emphasizing the sensitivity of the relationship between the wire geometry and its orientation with respect to the driving field.

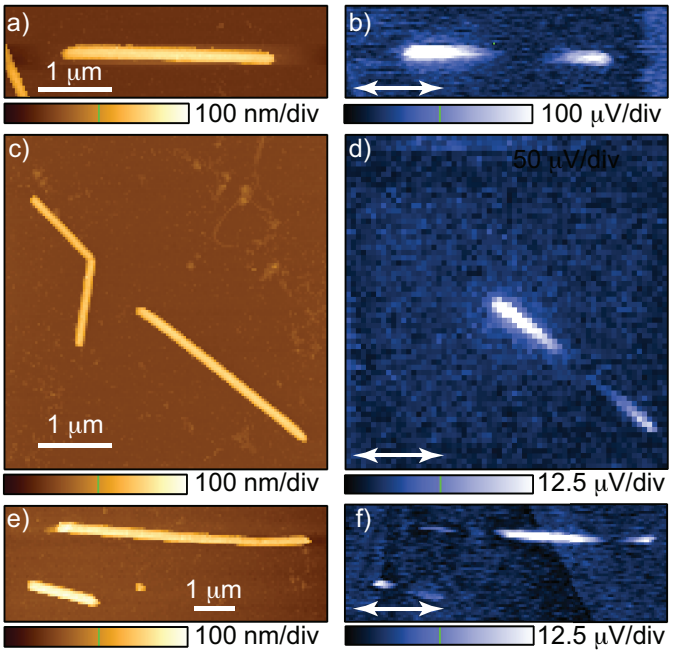

Figure 4.11: Topography (a,c, and e) and corresponding non-phase resolved near-field IR s-SNOM $|E_z|^2$ signal (b,d, and f) for $s_{\text{in}}p_{\text{out}}$ polarization configuration for crystalline Ag-wires of different lengths. The white arrows in panels b),d), and f) indicate the orientation of the excitation polarization. For lengths up to $L \approx 4$ μm the Ag wires exhibit a dipolar mode, with multipolar resonances supported for longer wire lengths (f).

Fig. 4.12a and b), displays corresponding AFM and s-SNOM data taken under the $p_{\text{in}}p_{\text{out}}$ configuration exhibiting self-homodyne interference contrast. The observed contrast arises from the constructive (left) and destructive (right) interference of the nanowire signal with the uncontrolled self-homodyne field provided by the far-field background as discussed above. Panels e) through h) show results for homodyne detection under controlled interferometric phase and amplitude reference conditions. Panels c) and d) display the topography of a wire of length, $l \approx 1.25$ μm exhibiting a dipolar resonance. Corresponding optical s-SNOM scans representing E_z are shown in e)- g) for relative phases of the homodyne signal of $\Phi = \pi$, $\pi/2$, and 0, respectively. Fig. 4.12h) shows the signal variation for a line scan along the center of the wire incrementally varying the phase between $\Phi = 0$ and π. The inversion of the signal contrast at the two nanowire ends varying the reference phase

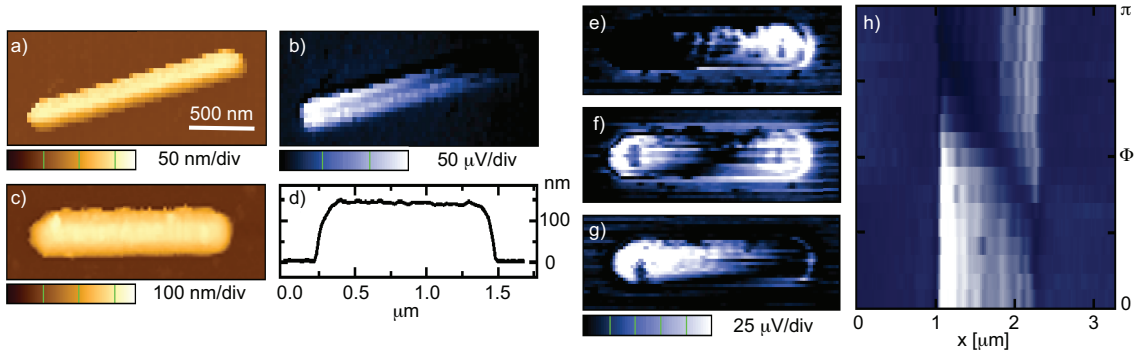

Figure 4.12: Topography a) and corresponding *s*-SNOM signal b) for a typical Ag wire under the influence of a self-homodyne field. The phase relation between the poles of a Ag wire is demonstrated by topography (c and d) with corresponding detected *s*-SNOM signal under interferometric homodyne amplification (e-h). Contrast arises from constructive and destructive interference of the reference field with out-of-phase field from the respective poles of the wire. E_z *s*-SNOM scans for discrete reference phase values of $\Phi = \pi$, $\pi/2$, and 0 (e,f, and g, respectively). Corresponding background subtracted *s*-SNOM line scans for continuous variation of Φ h).

is characteristic for the dipole excitation.

Based on observed spectral response and theory, the large SEIRA effect observed on structurally related micrometer sized metal nanowires was attributed to strong local-field enhancement at the poles [121]. The *s*-SNOM images in Fig. 4.11 and 4.12 agree with these predictions with the highest observed optical intensities occurring near the ends of the Ag wires as expected. Our measurements only provide a rough estimate of the local field enhancement with values of order 10-50 as deduced from comparison with the detected signal from the un-enhanced center of the wire and the estimate of an enhancement of unity around the noise level. This enhancement is consistent with a theoretical value of 45, calculated 1 nm above the surface for Ag wires at their dipole resonance in the 3.5 μm wavelength range [121].

Estimate of resonant length.

From studying Ag wires of different lengths, a dipolar field pattern is observed for wires between L ≈ 1 μm and L ≈ 4 μm. A resonant length of $L_{\text{dipole}} \simeq 3$ μm could be deduced for the $\lambda = 10.6$ μm wavelength excitation used. This length is considerably shorter than the first ideal classical antenna resonance at $L \approx \lambda/2 = 5.3$ μm. Despite high aspect ratios of 1:10 to 1:200, an inhomogeneous dielectric environment and still considerable damping (even at mid-IR frequencies) give rise to a departure from the ideal scattering behavior of perfectly conducting and infinitely thin metal wires in which the antenna resonances occur at lengths of $L \approx \frac{n\lambda}{2}$ for $n = 1, 2, 3, \ldots$ [140].

Within the low frequency limit, linear antenna resonances are dictated by both the approximation that the radius r is much smaller than the wavelength (i.e., $r \ll \lambda$) but is still much greater than the skin depth δ. In this spectral range, the optical properties of metals are largely frequency independent and characterized by both a large real conductivity σ_{Re} and low absorption coefficient $\alpha = 2/\delta$.

The extension of linear antenna structures to the infrared/visible spectral range typically results in structures in which the skin depth is comparable to the radius of the antenna, i.e., $\delta \sim r$. This is the case for our chemically synthesized Ag wires with radii down to $r \approx 25$ nm and skin depth $\delta \approx 30$ nm at $\lambda = 10.6$ μm [132]. Here, the electric field significantly penetrates into the antenna structure resulting in a deviation of the optical properties from that of classical antenna theory which is reflected in the modification of the half-dipole resonance length [18].

Recently, a modified classical waveguide theory for the TM modes of a cylindrical waveguide [133] which accounts for the reactance of the ends of the antennas was used to predict the effective wavelength scaling behavior for optical antennas [135]. This theory and other models, which incorporate DDA and boundary element methods [136,137], predict a scaling behavior that has been confirmed by infrared spectroscopy in lithographically grown structures [120, 141] and comparison of *s*-SNOM and numerical simulations of optical infrared antenna structures [142].

Using the modified waveguide theory [135] and assigning an effective real dielectric con-

stant equal to the geometric average of the dielectric constants for the SiO_2 substrate and air, $\epsilon_{\text{surr}} = \sqrt{\epsilon_{\text{air}} \cdot \epsilon_{\text{sub}}} \approx 2$, we derive an effective wavelength of $\lambda_{\text{eff}} \approx 6.7$ μm and half wavelength resonance of $L_{\text{dipole}} \approx 3.4$ μm for a typical Ag wire of radius of $r = 25$ nm for incident light $\lambda = 10.6$ μm. This result is in good agreement with our experimental findings of $L_{\text{dipole}} = 3$ μm which correspond to $\lambda_{\text{eff}} \approx 10.6$ μm$/(1.8 \pm 0.5) \approx 6 \pm 2$ μm.

Dephasing time and plasmon properties in the IR.

Planar SPPs in the visible are characterized by both a distinct dispersion relation with respect to the light line and a high degree of field localization near the surface resulting from a non-zero in-plane component of the electric field which permits the formation of a spatially and temporally varying charge distribution. These properties reflect the fact that the visible frequency range corresponds to the upper limit of the relaxation regime, $1/\tau \sim \omega < \omega_{\text{pl}}$ [18]. Unlike the low frequency limit, the optical properties of metals are marked by both real and imaginary conductivities σ_{Re} and σ_{Im}, respectively, as well as a related large absorption coefficient α. Visible frequencies, in particular, are distinguished by a low σ_{Im} and a negligible σ_{Re} which is reflected in the heavy loss and low propagation lengths for visible plasmon excitations [129, 130].

While the mid-IR and visible spectral ranges both fall into what is generally classified as the relaxation regime [18], these two spectral ranges are distinct in their optical material responses. Fig. 4.8 illustrates these inherent differences as manifested in σ_{Re} and σ_{Im} for a simple Drude description of the optical properties of silver [21, 22, 132]. At lower frequencies in the relaxation regime (the mid-IR spectral range) metals exhibit appreciable values of σ_{Re} and σ_{Im}. While α is expected to retain a relatively constant high value for frequencies throughout the entire relaxation regime ($\alpha \approx 7.7 \cdot 10^5,\ 9.0 \cdot 10^5,$ and $8.5 \cdot 10^5$ cm^{-1}, for $\lambda = 0.5,\ 10,$ and 30 μm, respectively), the enhanced conductivity relative to visible frequencies results in a reduction of loss and increase of the predicted propagation length l in the IR spectral range ($l \approx 16$ μm and 55 mm for an Ag/air interface at $\lambda = 0.5$ and 10 μm, respectively) [129, 130].

Of further physical importance for low-frequency plasmon properties is the relaxation

time τ of the metal which under the Drude model represents the mean time between electron scattering events. The relaxation time is of particular interest at mid-IR frequencies where the optical cycle time τ_{IR} becomes comparable to τ. As a result, the mid-IR spectral range represents the low frequency limit for the coherent plasmon excitation. This further highlights the interest in the variation of the carrier density in materials (e.g. semiconductors) to control the plasmon dephasing time τ [143].

4.5 Summary/Conclusions.

As revealed through the preceding chapter, surface plasmon polariton phenomena in noble metallic structures provide a means to enhance and localize electromagnetic fields to sub-wavelength dimensions. This capability provides a basis for the implementation of noble metallic structures in nano-optical applications. Specifically, localized surface plasmon resonances of noble metallic nano-structures provides a means of localizing electromagnetic fields at optical frequencies to nano-scale dimensions. Here, *s*-SNOM measurement techniques provide the capability to characterize the relationship between optical resonances of nano-structures with the associated near-field magnitude and distribution. We have here demonstrated the technique for Ag nano-prisms in the visible frequency range and Ag nano-rods in the mid-IR spectral range. The technique, however, may be extended to any nano-plasmonic system providing experimentalists with a means of correlating the dimensions and geometric details of single nano-structure with its intrinsic near-field optical response.

Chapter 5

THERMAL INFRARED NEAR-FIELD SPECTROSCOPY (TINS)

5.1 Introduction.

The study of thermal radiation has a long and rich history, most famously highlighted by Planck's description of the spectrum of a blackbody radiator which set the stage for the birth of quantum mechanics in the 20th century. Despite a long history of seminal contributions from Gustav Kirchhoff and Max Planck, research interest in thermal radiation has recently experienced a rebirth of interest. The primary focus of this interest lies, however, not in the description of thermal bodies in the far-field regime but rather in the near-field.

Recent theoretical models have predicted distinct spectral characteristics of the electromagnetic thermal near-field which fundamentally differ from the far-field regime both in magnitude and spectral distribution. Specifically, it has been predicted that the thermal near-fields exhibit strong spectral enhancement in the presence of surface resonances. In order to describe the properties of thermal near-fields, these models incorporate the microscopic source of the thermal radiation: the fluctuational microscopic current density distribution within the radiative body.

Combining scattering-Scanning Near-field Optical Microscopy (s-SNOM) with Fourier-transform spectroscopy using a heated atomic force microscope tip as both a local thermal source and scattering probe, for the first time the thermal near-field in the mid-infrared is spectroscopically characterized. Here, the spectrally distinct and orders of magnitude enhanced resonant spectral near-field energy density associated with vibrational, phonon, and phonon-polariton modes is observed. We describe this behavior and the associated distinct on- and off-resonance nanoscale field localization with model calculations of the near-field electro-magnetic local density of states (EM-LDOS). The results presented in this chapter provide a basis for intrinsic and extrinsic resonant manipulation of optical forces, control of nano-scale radiative heat transfer with optical antennas, and use of this

new technique of thermal infrared near-field spectroscopy (TINS) for broadband chemical nano-spectroscopy.

5.1.1 Historical development of the study of thermal radiation: far-field to the near-field.

The investigations of thermal radiation dates back hundreds of years, initially beginning with William Herschel's discovery of infrared light in his studies of the spectrum of the solar light in 1800 [144, 145]. The collaboration of Robert Bunsen and Gustav Kirchhoff in the mid-1800s led to further advances in the characterization and description of thermal light [146]; here, measuring the emission of the flames of various burning materials, Bunsen and Kirchhoff were able to correlate the thermal emission of various substances with the gaps in the solar spectrum. This observation led to the formulation of Kirchhoff's law for far-field thermal radiation which states, for a given material at thermal equilibrium with its surroundings the absorptivity is equal to the emissivity. Having established the relationship between absorption and emission, Kirchhoff further coined the term "blackbody" as a conceptual object with perfect absorption, and consequently, ideal thermal emission.

The measurement and description of the spectral distribution of thermal radiation was one of the pre-eminent challenges of physics in the late-1800s. A proposed model of the spectral distribution by German physicist Wilhelm Wien correctly described the spectrum at short-wavelengths, but was subsequently shown to be incorrect at long wavelengths [147]. This work was followed by the first measurement of thermal emission from a blackbody by Otto Lummer [148], and a model of thermal emission by Lord Rayleigh which converse converse to Wein's model, correctly predicted the correct spectral scaling at long wavelengths. It was at the turn of the century that Max Planck put forth a definitive model which would unify the Rayleigh-Jeans and Wein approximations [149]. This description was accomplished through the specification that the allowable energy states for thermal oscillators was not continuous, but rather had to assume discrete (quantized) values. It was this fundamental assumption which would lay the foundation for the development of quantum mechanics in the 20th century.

For over a century now, the laws of Kirchhoff [146] and Planck [149] have fully described

far-field thermal emission, the fundamental origin of which lies in the microscopic space-time fluctuation of charge carriers. However, recent studies of the electromagnetic thermal near-fields have emphasized fundamentally distinct spectral, spatial, and coherence properties at sub-wavelength dimensions for solid media [26, 150–153]. One of the most important and fascinating results of theoretical predictions [26, 152–154] is the *resonant enhancement* of the near-field spectral energy density when associated with either intrinsic electronic and vibrational excitations or extrinsic geometric resonances of the medium.

Despite its influence on and possibility for control of the above phenomena via resonant interaction, experimental investigations of the spectral distribution of the electromagnetic thermal near-field have remained difficult due to its purely evanescent character [155–158]. Specifically, while far-field thermal radiation is most often characterized by broadband blackbody-like emission, systems with characteristic surface resonances have been predicted to exhibit sharply peaked, near-monochromatic (vibrational lifetime limited) spectral energy density distribution in the near-field field regime [152]. In this chapter, the development and implementation of a new *s*-SNOM technique utilizing specially designed heated AFM probes will be discussed in order to, for the first time, characterize the spectral distribution of infrared thermal near-fields.

5.2 Far-field thermal radiation.

It is a fundamental property that all matter radiates when heated with a spectral intensity distribution which depends on the optical properties of the material, specifically the real and imaginary indices of refraction n and κ respectively (see chapter 2). The following subsections will introduce the concept of the electromagnetic density of states and how it relates to the derivation of Planck's formula for thermal emission from a blackbody radiator. These descriptions will be extended in later sections to the concept of the electromagnetic local density of states.

5.2.1 Derivation of the far-field electromagnetic density of states and energy density.

First consider a volume V consisting of a box with sides of length L. Inside this box, fields exist as transverse waves (normal modes) over varying frequencies. The frequencies of these

electromagnetic fields are related to the energy and momentum of the photon particles which make up these fields by the via the relations $E_{\rm ph} = \hbar\omega$ and $|\vec{p}_{\rm ph}| = \hbar|\vec{k}| = \hbar\omega/c$.

To determine the electromagnetic density of states it is necessary to count the number of modes which lie in a momentum interval of k to $k + dk$. Specifying the boundary condition that the electromagnetic waves have nodes at the box walls, the wavelengths must obey the relation $\lambda = nL/2$ where $n = 1, 2, 3....$. In accordance, the values of the wave-vectors are

$$k_x = n_x\frac{\pi}{L},\ k_y = n_y\frac{\pi}{L},\ k_z = n_z\frac{\pi}{L}. \tag{5.1}$$

The spacing of wavevector states in momentum space given above means that every mode in k-space occupies a momentum-space volume of

$$\delta V_k = \left(\frac{\pi}{L}\right)^3. \tag{5.2}$$

The number of modes below a given absolute momentum value $|\vec{k}|$ is expressed as the volume of a sphere of radius $|\vec{k}|$ in momentum space $V_k = 4/3\pi k^3$. Counting the number of modes in all directions within the momentum interval of k to $k + dk$ by we find that

$$dV_k = 4\pi k^2 dk. \tag{5.3}$$

Subsequently dividing by the momentum volume per mode yields the total number of modes in the momentum interval k to $k + dk$

$$\frac{dV_k}{\delta V_k} = \frac{L^3}{2\pi^2}k^2 dk. \tag{5.4}$$

Finally, we can divide by the total volume of the box $V = L^3$ to arrive at the density of modes, the total modes per unit volume in the momentum interval k to $k + dk$ [1]

$$D[k]dk = \frac{dV_k}{\delta V_k L^3} = \frac{k^2}{2\pi^2}dk. \tag{5.5}$$

For photons, D can be re-expressed in terms of the angular frequency of the electromagnetic waves using the relation $D[\omega] = D[k]\frac{dk}{d\omega}$ for $\omega = ck$. By further multiplying by a factor of two to account for the two possible polarizations of transverse waves this yields

$$D[\omega] = \frac{\omega^2}{\pi^2 c^3}. \tag{5.6}$$

[1]Note that we have here only derived the density of states for a 3D body. For 1D and 2D bodies, the density of states is $D_{\rm 1D}[k] = \frac{1}{\pi}$ and $D_{\rm 2D}[k] = \frac{k}{2\pi}$ respectively

This density of modes for electromagnetic radiation is known as the electromagnetic density of states.

As photons have a spin of 1, they obey the Bose-Einstein distribution function $F[\omega]$.

$$F[\omega, T] = \frac{1}{\left(\exp[\frac{\hbar\omega}{k_B T}] - 1\right)}. \tag{5.7}$$

Above, k_B represents the Boltzmann constant.

The product of the Bose-Einstein distribution function with the density of states and the electromagnetic wave energy defines the spectral energy density of a given frequency interval within the volume. This was the famous Planck distribution for far-field electromagnetic waves proposed by Planck in 1900,

$$u_{\text{ff}}[\omega, T]d\omega = E_{\text{ph}} \cdot F[\omega, T] \cdot D[\omega]d\omega \tag{5.8}$$

$$\rightarrow u_{\text{ff}}[\omega, T] = \frac{\omega^2}{\pi^2 c^3} \frac{\hbar\omega}{\left(\exp[\frac{\hbar\omega}{k_B T}] - 1\right)} = D[\omega] \cdot \Theta[\omega, T]. \tag{5.9}$$

Here, $\Theta[\omega, T]$ represents the mean energy of a thermal oscillator (photon). Fig. 5.1a) displays the spectral energy density distribution for a blackbody at temperatures of 300, 500, and 700 K respectively.

Considering an area element within the volume V, the radiant energy flux is related to the energy density and the speed of light $q_{\text{rad}} = u_{\text{ff}}c/4$. By definition, if a blackbody is placed in the volume, it will absorb all incoming radiant energy. To remain at thermal equilibrium, it must emit the same amount of energy. As a result the spectral emissive power of a blackbody ξ_{bb} is defined to be

$$\xi_{\text{bb}}[\omega, T] = \frac{\omega^2}{4\pi^2 c^2} \frac{\hbar\omega}{\left(\exp[\frac{\hbar\omega}{k_B T}] - 1\right)}. \tag{5.10}$$

5.2.2 Extending the description of thermal radiation from blackbodies to real materials.

The spectral emissive power of real materials is characterized by several parameters including an object's intrinsic properties, such as the real and imaginary indices of refraction, as well as extrinsic parameters such as size and shape. Unlike the broad featureless spectrum which composes blackbody thermal emission, thermal emission from real bodies reflects the

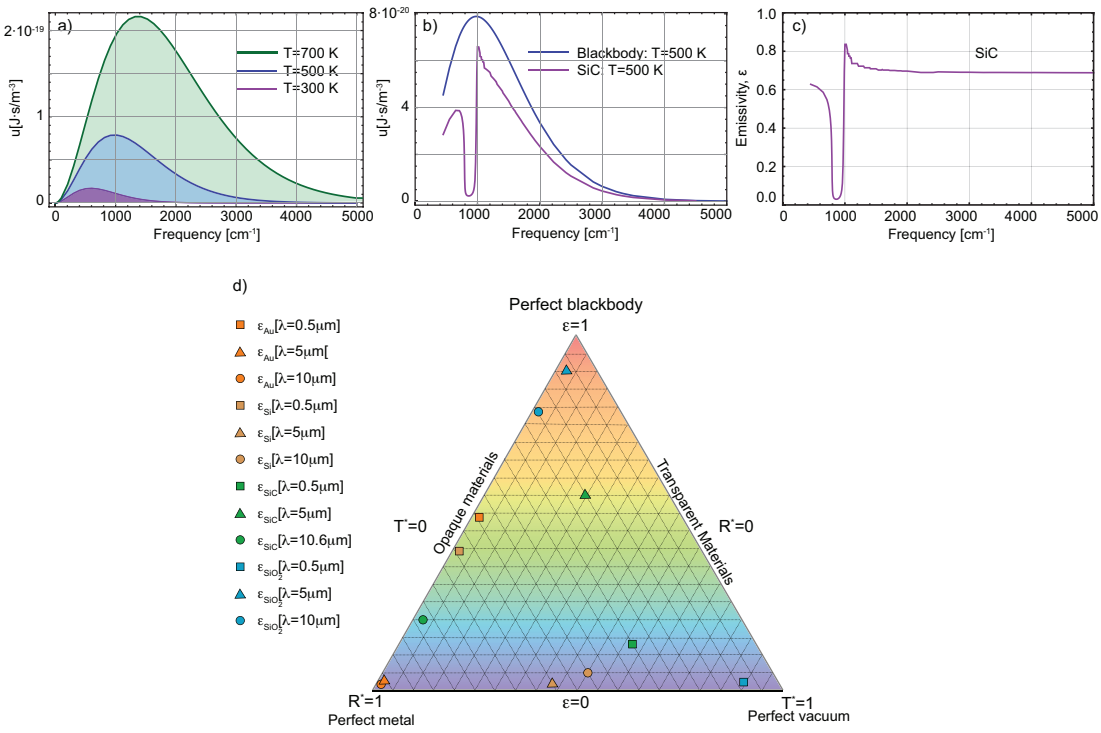

Figure 5.1: The spectral energy density associated with a blackbody described by Planck's Law is displayed in panel a). The difference between the spectral energy density associated with the thermal emission from an ideal blackbody and a real material (SiC) is shown in panel b). As determined by Kirchhoff's law, the thermal emission of SiC at most frequencies is very similar to an ideal blackbody. Strong deviations from black-body occur between 800 and 1000 cm^{-1} where SiC is highly reflective due to its Reststrahlen band. The emissivity of SiC as determined from panel b) is displayed in panel c). Panel d) displays the emissivity of a 1mm thick optical slab for several materials at assorted wavelengths. This panel illustrates that materials can deviate from perfect blackbody emissivity through finite transmissivity and reflectivity. The bottom two corners of the triangle represents materials with zero reflectivity which occurs either through full transmission (T=1, perfect vacuum) or full reflectivity (R=1, perfect metal).

material/object properties above. By characterizing this far-field thermal emission we can consequently gain information on the optical properties of a given material/object.

The emissivity of a given body is defined as the ratio of the spectral emissive power of that of a blackbody radiator

$$\varepsilon[\omega, T] = \frac{\xi_{\text{body}}[\omega, T]}{\xi_{\text{bb}}[\omega, T]}. \tag{5.11}$$

Kirchhoff's law states that, at thermal equilibrium the directional-spectral emissivity is equal to the directional-spectral absorptivity of a material. The only assumption here is that the material is at uniform temperature and that the fields within the enclosure are not strong enough to modify the intrinsic properties of the object via non-linear interaction.

The definition of directional absorptivity A for Kirchhoff's law is $A[\omega, \theta] = 1 - R[\omega, \theta] - T[\omega, \theta]$ with quantities $R[\omega, \theta]$ and $T[\omega, \theta]$ representing the directional reflectivity and transmissivity respectively, averaging over both s and p polarizations. It is often assumed that the directional emissivity $\varepsilon[\omega, \theta]$ is equivalent to $\varepsilon[\omega, \theta] = A[\omega, \theta] = 1 - R[\omega, \theta]$. The primary approximation here is that the total transmission through the object $T[\omega, \theta]$ is $\simeq 0$. This assumption implies that the object is semi-infinite or opaque; however, this requires that the characteristic size of the object l is much larger than the penetration depth of radiation δ ($l \gg \delta$). Fig. 5.1d) demonstrates a visualization of when this assumption is valid, simulating the calculated emission from a 1 mm thick semi-infinite slab for various materials and emission wavelengths. The left hand side of the triangle represents materials considered to be opaque while the right side represents those considered to be transparent. The top point of the triangle represents a perfect blackbody radiator. Conversely, the bottom edge represents an object which has no thermal emission; this arises as no absorption occurs either through perfect reflectivity (left corner), perfect transmission (right corner), or combination of reflection and transmission which results in zero absorption (bottom edge).

With this caveat in mind, for the further descriptions we will assume for simplicity that the materials are semi-infinite and opaque. Describing the directional emissivity as

$$\varepsilon[\omega, \theta] = 1 - R[\omega, \theta], \tag{5.12}$$

and the total emissivity for a given material can be expressed as

$$\varepsilon[\omega] = \frac{1}{\pi}\int_0^{2\pi}\int_0^{\pi/2}(1 - R[\omega,\theta])d\theta d\phi. \tag{5.13}$$

Fig.5.1b) gives examples of the spectral energy density $u_{\mathrm{ff,SiC}}$ associated with a SiC surface. It is evident that SiC behaves very much like a blackbody radiator except in the 800-1000 cm^{-1} spectral window. This deviation is due to the high reflectivity Reststrahlen band which occurs due to the presence of the LO and TO phonon modes for SiC (see following discussion further in chapter). The relationship of the emissivity and reflectivity is displayed in Fig. 5.1c).

5.3 Thermal radiation in the near-field regime.

5.3.1 Definition of electromagnetic local density of states.

The electromagnetic density of states $D[\omega]$ discussed in the previous section is a fundamental quantity for a homogeneous material from which many macroscopic quantities can be derived. With the introduction of spatial variation in the material properties, it is necessary to introduce the Electromagnetic Local Density of States (EM-LDOS) $\rho[\vec{r},\omega]$. Here, the distinction lies in the fact that the density of states $\rho[\vec{r},\omega]$ is now a function of the spatial coordinate $\vec{r}$. The following section will follow the definition of the EM-LDOS established by Joulain et al. [26, 153]

To derive an expression for the EM-LDOS, we begin by considering a system with temperature T in thermal equilibrium. Similar to Eqn. 5.9 where the spectral energy density $u_{\mathrm{ff}}[\omega,T]$ is defined in terms of the density of states $D[\omega]$, the *local* spectral energy density $u[\vec{r},\omega,T]$ may be defined in terms of the EM-LDOS $\rho[\vec{r},\omega]$,

$$u[\vec{r},\omega,T] = \rho[\vec{r},\omega]\cdot\frac{\hbar\omega}{\left(\exp[\frac{\hbar\omega}{k_BT}]-1\right)} = \rho[\vec{r},\omega]\cdot\Theta[\omega,T]. \tag{5.14}$$

In their derivation of the expressions for the EM-LDOS, Joulain et al. introduce the correlation functions $\mathcal{E}_{ij}$ and $\mathcal{H}_{ij}$ for the electric and magnetic fields respectively for a

stationary system.

$$\mathcal{E}_{ij}[\vec{r},\vec{r}',t-t'] = \frac{1}{2\pi}\int d\omega \mathcal{E}_{ij}[\vec{r},\vec{r}',\omega]\exp[-i\omega(t-t')] = \langle E_i[\vec{r},t]E_j^*[\vec{r}',t']\rangle \quad (5.15)$$

$$\mathcal{H}_{ij}[\vec{r},\vec{r}',t-t'] = \frac{1}{2\pi}\int d\omega \mathcal{H}_{ij}[\vec{r},\vec{r}',\omega]\exp[-i\omega(t-t')] = \langle H_i[\vec{r},t]H_j^*[\vec{r}',t']\rangle \quad (5.16)$$

These quantities are useful as the electromagnetic energy density is the sum of both the electric and magnetic energy contributions. The primary goal here is determine $u[\vec{r},\omega,T]$ through the relation,

$$u[\vec{r},\omega,T] = \frac{\epsilon}{2}\langle|E[\vec{r},\omega]|^2\rangle + \frac{\mu}{2}\langle|H[\vec{r},\omega]|^2\rangle. \quad (5.17)$$

In order to determine the magnitude of the electromagnetic fields above a medium, the microscopic source of the electromagnetic fields must be considered. This source is the fluctuational current density distribution arising from the random thermal movement of charged particles (electrons, ions, ect...) within the medium.

Working from the microscopic picture of a fluctuational current density distribution, two requirements exist in determining the external $u[\vec{r},\omega,T]$ associated with a given thermal body: 1) it is necessary to establish the relationship between a thermal current element within the material and the electromagnetic field induced outside the thermal body, and 2) the statistical properties of the fluctuational current distribution must be understood.

To satisfy the first requirement, the electric and magnetic fields outside the material associated with a given electric current element $\vec{j}[\vec{r}]$ or magnetic current density element $\vec{m}[\vec{r}]$ inside the material may be established using the Greens dyadic functions for the system geometry:

$$\vec{E}[\vec{r},\omega] = i\mu_0\omega\int \overleftrightarrow{G}^E[\vec{r},\vec{r}_b,\omega]\cdot\vec{j}[\vec{r}_b,\omega]d^3\vec{r}_b \quad (5.18)$$

$$\vec{H}[\vec{r},\omega] = \int \overleftrightarrow{G}^H[\vec{r},\vec{r}_b,\omega]\cdot\vec{m}[\vec{r}_b,\omega]d^3\vec{r}_b. \quad (5.19)$$

Here, the quantities $\overleftrightarrow{G}^E$ and $\overleftrightarrow{G}^H$ represent the Green dyadic function for the specific system geometry relating the current within the material to the field generated above the interface. The integral over $d^3\vec{r}_b$ represents the integral over the entire thermal body.

The second requirement is met via the application of the fluctuation-dissipation theorem which relates the power spectrum of the fluctuational current density to the loss mechanisms of the material. Here, the correlation function statistical fluctuations of the current density distribution can be related to imaginary part of the dielectric permittivity [26],

$$\langle j_i[\vec{r_1},\omega]j_j[\vec{r_2},\omega']\rangle = 4\pi\epsilon_0\omega\mathrm{Im}[\epsilon[\omega]]\cdot\Theta[\omega,T]\delta_{ij}\delta[\vec{r_1}-\vec{r_2}]\delta[\omega-\omega']. \tag{5.20}$$

Implementing both Green's dyadic (Eqn. 5.19)and the fluctuation-dissipation theorem (Eqn. 5.20), the expressions for the correlation functions may be derived [153]:

$$\mathcal{E}_{ij}(\vec{r},\vec{r}',\omega) = \Theta[\omega,T]\cdot\frac{\mu_0\omega}{2\pi}\mathrm{Im}\left[G^E_{ij}(\vec{r},\vec{r}',\omega)\right] \tag{5.21}$$

$$\mathcal{H}_{ij}(\vec{r},\vec{r}',\omega) = \Theta[\omega,T]\cdot\frac{\epsilon_0\omega}{2\pi}\mathrm{Im}\left[G^H_{ij}(\vec{r},\vec{r}',\omega)\right]. \tag{5.22}$$

Considering only positive frequencies, the spectral energy density $u[\vec{r},\omega,T]$ can be expressed in terms of the correlation functions and thus the dyadic Green's functions.

$$u[\vec{r},\omega,T] = 4\left(\left(\frac{\epsilon_0}{2}\right)\sum_{i=1,3}\mathcal{E}_{ii}[\vec{r},\vec{r},\omega]+\left(\frac{\mu_0}{2}\right)\sum_{i=1,3}\mathcal{H}_{ii}[\vec{r},\vec{r},\omega]\right) \tag{5.23}$$

$$\rightarrow u[\vec{r},\omega,T] = \Theta[\omega,T]\cdot\frac{\omega}{\pi c^2}\mathrm{Im}[\mathrm{Tr}[\overleftrightarrow{G}^E[\vec{r},\vec{r},\omega]+\overleftrightarrow{G}^H[\vec{r},\vec{r},\omega]]]. \tag{5.24}$$

Comparing with the definition for the EM-LDOS given by Eqn. 5.14, we arrive at a formula for the electromagnetic local density of states in term of the dyadic Green's function for the system,

$$\rho[\vec{r},\omega] = \frac{\omega}{\pi c^2}\mathrm{Im}[\mathrm{Tr}[\overleftrightarrow{G}^E[\vec{r},\vec{r},\omega]+\overleftrightarrow{G}^H[\vec{r},\vec{r},\omega]]]. \tag{5.25}$$

5.3.2 The EM-LDOS for a semi-infinite planar half space.

In this section, following the derivation of Joulain et al. [26,153], the EM-LDOS corresponding the planar geometry will be derived along with the associated spectral energy density. The system geometry in this case is defined by a material composing upper semi-infinite planar half space ($z > 0$) of complex dielectric permittivity ϵ_1 and a material composing lower semi-infinite planar half space ($z < 0$) of complex dielectric permittivity ϵ_2. Both the upper

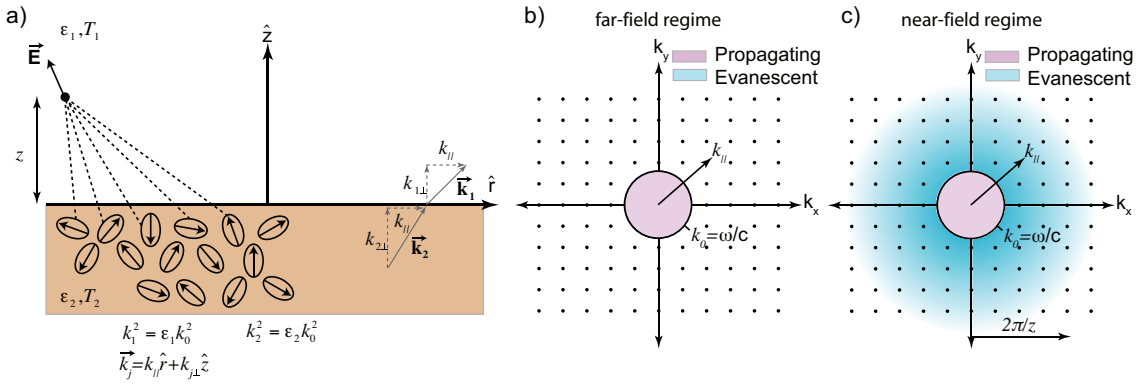

Figure 5.2: a) schematic depiction of the parameters of the description of the EM-LDOS associated with a semi-infinite planar half-space. The fluctuational currents within the surface are related to the induced field through the Greens Dyadic function for the system [159]. The wave-vector components in the parallel and perpendicular directions to the surface plane associated with these fields are displayed on the right side of panel a). A qualitative depiction of the contribution to the total EM-LDOS from the propagating far-field waves ($k_{||} < k_0$) and evanescent solutions ($k_{||} > k_0$) is provided for the far- and near-field regimes (panels b) and c) respectively).

and lower half spaces are assumed to be composed of linear, isotropic, and non-magnetic media and in general have frequency depended dielectric permittivities.

The Green's function for this system from ref [159] correlates the microscopic current density element at a given location in the lower half space with the s and p-polarized plane waves generated and accounts for their presence in upper half space by incorporating the Fresnel reflection coefficients of the planar surface separating the two half-spaces [159].

Combination of this Green's dyadic function with the fluctuation-dissipation theorem allows for the expression of the electromagnetic local density of states $\rho[z, \omega]$ as shown by Eqn. 5.26, at a given frequency ω and height above a material z, in terms of an integral over the parallel wavevector component $k_{||}$ from zero to infinity. The notation corresponding to the system geometry here follows that derived for surface waves in chapter 2 and is displayed schematically in Fig. 5.2.

$$\rho[z,\omega] = \frac{\rho_v[\omega]}{2}\Bigg\{\underbrace{\int_0^{\omega/c} \frac{k_\parallel}{k_0\,|k_{1,\perp}|}\frac{2-|r_{12}^s|^2-|r_{12}^p|^2}{2}dk_\parallel}_{\text{propagating}} + \underbrace{\int_{\omega/c}^{\infty} \frac{4k_\parallel^3}{k_0^3\,|k_{1,\perp}|}\frac{\mathrm{Im}[r_{12}^s]+\mathrm{Im}[r_{12}^p]}{2}e^{-2\mathrm{Im}[k_{1,\perp}]\cdot z}dk_\parallel}_{\text{evanescent}}\Bigg\}. \tag{5.26}$$

The equation above gives insight into the nature of the EM-LDOS as a function of height above a planar surface as it may expressed as a sum of evanescent and propagating contributions. Propagating contributions correspond to values of $k_\parallel$ which are below that of the free-space wavevector k_0; evanescent contributions thus correspond to values of $k_\parallel$ which are greater that of the free-space wavevector k_0.

The three unit vectors $\hat{x}$, $\hat{y}$, and $\hat{z}$ define a point in space as $\vec{r} = x\hat{x} + y\hat{y} + z\hat{z}$ and light wavevectors as $\vec{k} = k_x\hat{x} + k_y\hat{y} + k_z\hat{z}$. It is simpler to further express these vectors in terms of the in and out-of-plane contributions as $\vec{r} = \vec{R} + \vec{z}$ and $\vec{k} = \vec{k}_\parallel + \vec{k}_\perp$ where $\vec{R} = x\hat{x} + y\hat{y}$, $\vec{k}_\parallel = k_x\hat{x} + k_y\hat{y}$, and $\vec{k}_{\perp,i} = k_z\hat{z}$. Fig. 5.2a) shows the relationship of the wavevectors between both the upper and lower media.

Within Eqn. 5.26, $\rho_v = \omega^2/\pi^2c^3$ represents the vacuum density of states while k_0 represents the free-space wavevector ($k_0 = \omega/c$). The quantities r_{12}^s and r_{12}^p represent the Fresnel reflection factors of the medium for s and p polarizations expressed as the in and out-of-plane components of the wavevector of the light,

$$r_{12}^p = \frac{-\epsilon_1 k_{\perp,2} + \epsilon_2 k_{\perp,1}}{\epsilon_1 k_{\perp,2} + \epsilon_2 k_{\perp,1}} \tag{5.27}$$

$$r_{12}^s = \frac{k_{\perp,1} - k_{\perp,2}}{k_{\perp,1} + k_{\perp,2}}. \tag{5.28}$$

Finally $k_\parallel$ and $k_{n,\perp}$, in the upper and lower half-space ($n = 1$ and $n = 2$) may be related to one another by the dispersion relation for light $\epsilon_n\mu_n k_0^2 = k_{n,\perp}^2 + k_\parallel^2$ with $\mathrm{Im}[k_{n,\perp}] > 0$ and $k_0 = \omega/c$ [26].

In the following sections I will discuss how the height above a surface affects the magnitude of the EM-LDOS through integration of Eqn. 5.26. Both the far- and near-field regimes will be addressed.

The EM-LDOS in far-field regime.

The primary expectation for the calculation of the EM-LDOS using Eqn. 5.26 is that it should match the classical description of far-field thermal radiation given by Kirchhoff and Planck. It is evident that terms inside the first integral correspond to the $1 - R[\omega, \theta]$ given in Kirchhoff's law for opaque bodies in Eqn. 5.12.

In the far-field regime ($z \gg \lambda$), only in-plane wavevectors corresponding to propagating solutions in the first term of Eqn. 5.26 contribute to the EM-LDOS ($k_{\parallel} < k_0$, $k_{1,\perp} \in \mathbb{R}\mathrm{e}$). As a result, the far-field spectral energy density associated with Eqn. 5.26 reduces to the classical solution defined by the Kirchhoff's emissivity ε and the Planck distribution, $u_{\mathrm{ff}}[\omega, T] = \varepsilon[\omega] \cdot u_{\mathrm{bb}}[\omega, T]$ [160].

The EM-LDOS in the near-field regime.

While the far-field contribution to the EM-LDOS is still present for sub-wavelength distances from the surface $z < \lambda$, the contribution of the evanescent solution in Eqn. 5.26 ($k_{\parallel} > k_0$ for which $k_{1,\perp} \in \mathbb{I}\mathrm{m}$) approaching the near-field regime begins to become significant. In the quasi-static near-field limit ($z \ll \lambda$), the evanescent solutions are the dominant component of the EM-LDOS [26, 153]. These solutions are contained in the second integral term of Eqn. 5.26.

The relation $k_{\parallel} \gg \frac{\lambda}{4\pi z}$ gives the specific value of $k_{\parallel}$ for which the contribution to the total EM-LDOS becomes negligible. This implies that in near-field regime large values of $k_{\parallel}$ ($k_{\parallel} \gg k_0$) now make large contributions to the total EM-LDOS. In this limit of large $k_{\parallel}$ ($k_{\parallel} \to \infty$), the Fresnel reflection factors reduce to $r_{12}^{s} = 0$ and $r_{12}^{p} = \frac{\epsilon_2 - 1}{\epsilon_2 + 1}$. Here, the EM-LDOS may be approximated by the evanescent component described by the second integral term in Eqn. 5.26, which further simplifies to,

$$\rho_{\mathrm{evan}}[z, \omega] \simeq \frac{1}{\pi^2 \omega} \frac{\mathrm{Im}[\epsilon_2]}{|\epsilon_2 + 1|^2} \int_{\omega/c}^{\infty} k_{\parallel}^2 \exp\left[-2k_{\parallel} \cdot z\right] \cdot dk_{\parallel}. \tag{5.29}$$

The integration of Eqn. 5.29 simplifies to the formula for the quasi-static scaling of the EM-LDOS given by Eqn. 5.30

$$\rho_{\mathrm{evan}}(z, \omega) \simeq \frac{1}{4\pi^2 \omega z^3} \frac{\mathrm{Im}[\epsilon_2]}{|\epsilon_2 + 1|^2}. \tag{5.30}$$

In the near-field limit, this results in a spectral energy density which exhibits $\propto z^{-3}$ scaling and can be expressed as

$$u_{\text{evan}}[z,\omega,T] \simeq \Theta[\omega,T] \cdot \frac{1}{4\pi^2\omega z^3} \frac{\text{Im}[\epsilon_2]}{|\epsilon_2+1|^2}. \tag{5.31}$$

5.3.3 Simulation of the spectral distribution and magnitude of thermal near-fields above surfaces.

The experimental measurements in the following sections focus on the characterization of the thermal fields above three materials. First, polytetrafluoroethylene (PTFE) was chosen as an example of a molecular solid with its characteristic symmetric and anti-symmetric C–F vibrational stretch modes. Natural SiO_2 quartz and SiC as crystalline solids with collective phonon and phonon-polariton surface excitations.

Using the optical constants (n and κ) for each of these materials, the EM-LDOS and the associated spectral energy density $u[z,\omega,T]$ can be calculated for specific heights above the surface using Eqn. 5.26. Fig. 5.3 displays the changes observed in the magnitude and spectral distribution of $u[z,\omega,T]$ for z = 100, 10, 1, and 0.1 μm representing the transition from the far-field to the near-field regimes.

For PTFE (a) in the far-field regime (i,ii) calculation of the predicted EM-LDOS shows that it behaves very much like a blackbody radiator. Small variations in $u[z,\omega,T]$ are predicted associated with the C–F molecular resonances of PTFE located at 1158, 1210, and 1240 cm^{-1} (latter two spectrally not resolved) [161,162]. Transitioning to the near-field regime (iv), $u[z,\omega,T]$ can be approximated by Eqn. 5.31. Here, peaks occur associated with the peaks in the imaginary part of the permittivity for PTFE (Im[ϵ_{PTFE}]) associated with the previously mentioned molecular resonances.

The prediction of the far-field $u[z,\omega,T]$ associated with SiC (b) and quartz SiO_2 (c) surfaces, as expected, follows Kirchhoff's law. As shown by Fig. 5.3 (row i) both materials are predicted to exhibit black-body like spectral distributions, with deviations occurring where the materials exhibit heightened reflectivity. For SiC, this heightened reflectivity occurs in the Reststrahlen band (800-1000 cm^{-1}) associated with the LO and TO phonon modes of SiC (797 and 971 cm^{-1}, respectively). Similarly quartz SiO_2 exhibits heightened

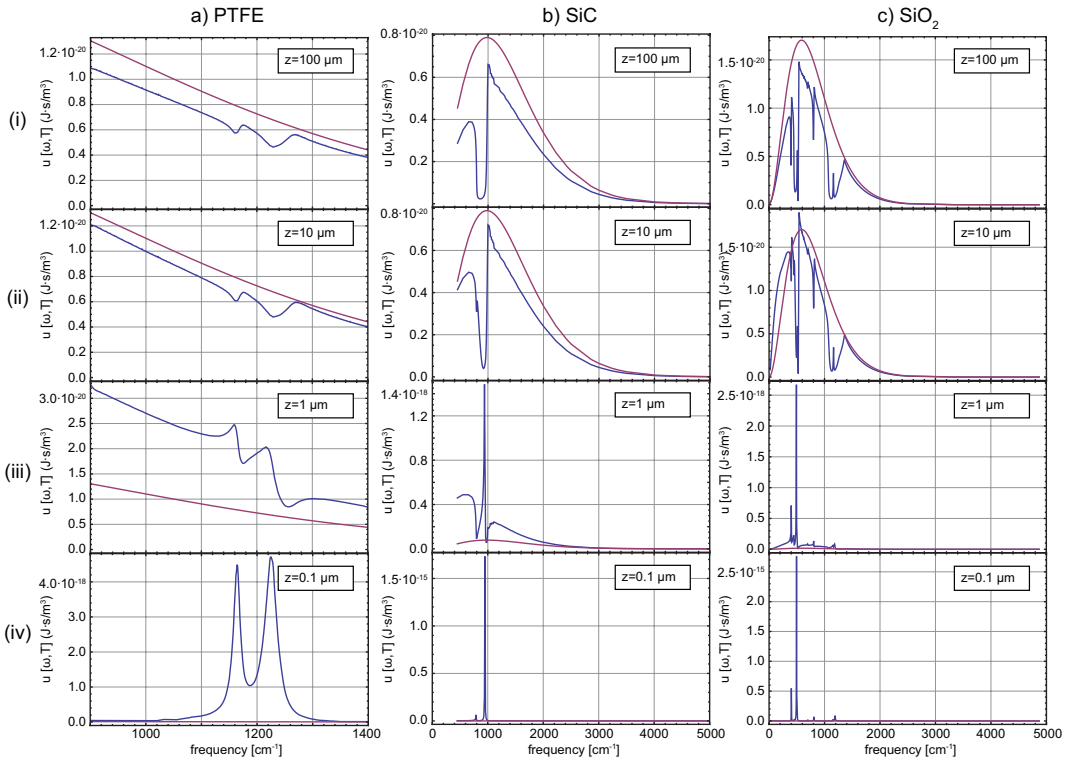

Figure 5.3: The changes in the spectral energy density $u[z,\omega,T]$ (blue-lines) above PTFE (a), SiC (b), SiO_2(c) surfaces at representative distances of z =100, 10, 1, and 0.1 μm (iv,iii,ii, and i respectively) display the transition from the radiative far-field regime to the near-field regime. The spectral energy density of a ideal blackbody radiator is shown (purple lines) as a reference. The temperature for the calculations above is $T = 300$ K.

reflectivity with its LO and TO modes ($1050 - 1250$ cm^{-1}) [163, 164].

In near-field regime both SiC and quartz SiO_2 meet the necessary conditions necessary for a surface phonon polariton wave (SPhP) (SPhP condition$\rightarrow$ $\mathrm{Re}[\epsilon_2] = -1$). With the spectral energy density in the near-field limit approximated by Eqn. 5.31 it is evident in Fig. 5.3 that these surface wave resonances result in the drastic enhancement in $u[z,\omega,T]$. For SiC the SPhP resonance condition is met at approximately $\omega_{\mathrm{SPhP}} = 950$ cm^{-1}. For quartz SiO_2, due to the presence of multiple phonon modes, the SPhP resonance condition is met at several locations. This is evidenced by the surface wave dispersion relation shown for quartz in chapter 2. Due the limitations on the spectral range of the detector used in

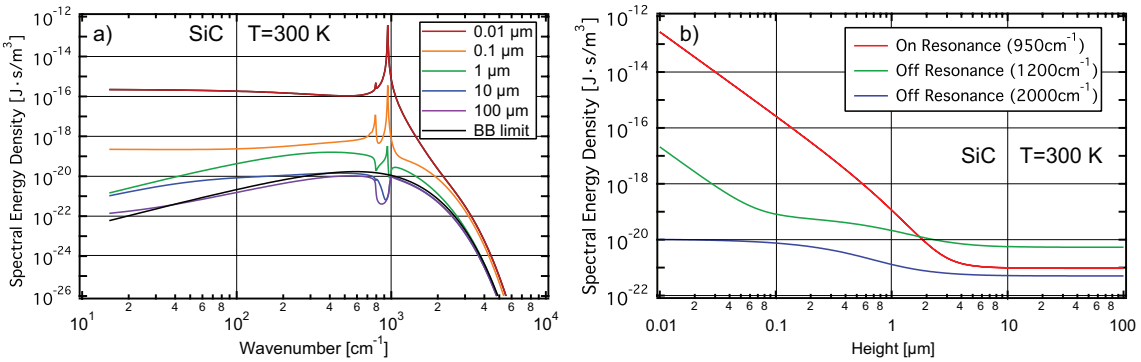

Figure 5.4: Using SiC as an example material, panel a) exhibits the changes in the magnitude and spectral distribution of the spectral energy density $u[z,\omega,T]$ as a function of height z. Panel b) shows the scaling of $u[z,\omega,T]$ for SiC three separate frequencies both on and off resonant. The temperature for the data in both panels is $T = 300$ K.

the following experimental section, for quartz SiO_2 we will focus on the surface waves which occur at $\simeq$1157 and 1190 cm^{-1}.

The variation of the spectral distribution of $u[z,\omega,T]$ with z is further displayed for SiC in Fig. 5.4a). The scaling of the $u[z,\omega,T]$ for differing frequencies is displayed in Fig. 5.4b). The on-resonant contribution ($\omega = 950$ cm^{-1}) is depicted by the red line while the scaling at off-resonant frequencies is depicted by the green and blue lines ($\omega = 1200$ cm^{-1} and $\omega = 2000$ cm^{-1} respectively).

While the model calculations predict drastic changes in the $u[z,\omega,T]$ in the near-field regime, the evanescent character of these fields has made experimental characterization difficult. Previous to this work, no spectrally sensitive measurement of the near-field EM-LDOS and $u[z,\omega,T]$ had been made. In the following sections, the implementation of *s*-SNOM techniques using heated AFM probes towards characterizing the spectral distribution of the EM-LDOS will be detailed.

5.4 Thermal Infrared Near-field Spectroscopy (TINS) using s-SNOM techniques with heated AFM tips.

As discussed above, recent studies of the electromagnetic thermal near-field have recently emphasized fundamentally distinct spectral, spatial, and coherence properties at sub-wavelength

dimensions for solid media [26, 152, 153]. The properties of thermal near-fields determine important near-surface phenomena including not only nano-scale radiative heat transfer [165,166] but also the Van der Waals/Casimir-Polder forces originating in the zero-point fluctuations or induced by the thermal fluctuations as first shown by Lifshitz and demonstrated by off-resonance interaction at a dielectric surface [167–170]. One of the most fascinating results of recent theoretical predictions [26,152–154] is the *resonant enhancement* of the near-field spectral energy density when associated with either intrinsic electronic and vibrational excitations or extrinsic geometric resonances of the medium. Despite its influence on and possibility for control of the above phenomena via resonant interaction, experimental investigations of the spectral distribution of the electromagnetic thermal near-field have remained difficult due to its purely evanescent character [150, 155–158, 171].

In the following section, I will demonstrate the generation, evanescent field scattering, and interferometric detection of thermal near-fields using a new scattering scanning near-field optical microscopy (*s*-SNOM) implementation with novel heated thermal atomic force microscope tips. With this technique of thermal infrared near-field spectroscopy (TINS), I will identify the enhanced and spectrally narrow evanescent fields associated with different molecular vibrational and surface phonon polariton modes.

5.4.1 Experimental apparatus for TINS.

The experimental layout is shown in Fig. 5.5. The system is based on an atomic force microscope (AFM, CP-Research, Veeco Inc.) operating in non-contact dynamic force mode and modified to allow for independent control of sample and tip temperature. The thermal evanescent fields induced via sample or tip heating [156, 157] are scattered by the AFM tip into detectable far-field radiation. This tip-scattered thermal radiation is collected using a Cassegrain-type reflective objective (NA=0.5, not shown) oriented at an angle of 60° with respect to the surface normal, directed through a Michelson interferometer, and detected by a mercury-cadmium-telluride (MCT) detector (Kolmar, Model KLD-0.25/DC/11.5) from $5.5-12$ μm; the detector spectral range is here limited by the detector bandgap at the long-wavelengths and the achievable temperature/detector sensitivity at shorter wavelengths.

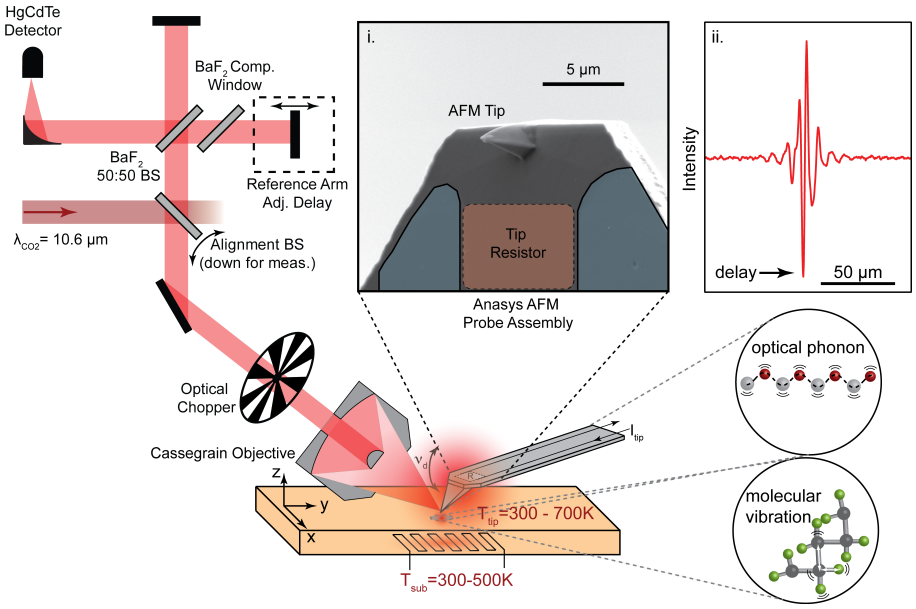

Figure 5.5: Experimental setup for thermal infrared near-field spectroscopy (TINS) measurements with thermal near-field radiation scattered by the tip and spectrally resolved via a Michelson-type FTIR interferometer (inset ii: typical interferogram). Both the surface or a specialized AFM tip (inset i) can be heated resistively with the tip in dynamic force feedback. The evanescent thermal near-field exhibits resonant enhancement via molecular or phonon resonances.

Discrimination of the near-field signal against the far-field emission/scattering is performed by lock-in filtering on the fundamental frequency of the AFM tip-dither frequency ν_d [15,46].

A resistive sample heater controls the sample temperature in the 300 - 500 K range with upper limit set by stable AFM scanning conditions. Specially designed AFM probes (Anasys Instruments, AN2-200) allow for resistive tip heating up to $\simeq$ 700 K (Fig. 5.5, inset ii). These probes have been further modified by focused-ion beam milling for free line of sight optical access to the tip-sample apex region.

The advantage of the use of heated AFM probes is that they allow for stable scanning conditions to be maintained with higher temperatures in the tip-sample gap region compared to either sample heating or active heating of both tip and sample. With the heated AFM tip in close proximity to the material surface, efficient localized heat transfer occurs via

ballistic thermal air conduction [172]. Using localized surface melting of polycarbonate samples allowed us to gauge the surface temperatures near the tip to be at least ~ 550 K with the AFM operating in non-contact force feedback mode. Note that for the purpose of our study discussed here, exact knowledge of the surface temperature is not critical. Surface temperature primarily affects the signal intensity and, only to a minor extent, the spectral characteristics of the near-field energy density distribution.

The spectral distribution of the scattered thermal light from the heated tip-sample gap region is reconstructed via interferometric FTIR detection. With the use of a dielectric tip material (Si) which is off-resonant and thus spectrally broadband in the vibrational spectral range of interest ($5.5 - 12$ μm), the tip-scattered light reflects the intrinsic vibrational/phonon resonances of the sample surface [45, 153].

5.4.2 Results of TINS characterization.

Fig. 5.6 (a-c, red lines, upper panels) shows the tip-scattered thermal near-field signal for SiC, SiO_2, and PTFE, respectively, using a heated tip at $\simeq 700$ K. For all three materials *peaked* near-field spectral signal distributions are observed associated with the respective molecular or surface phonon polariton (SPhP) resonances as discussed below. For comparison, the expected spectral energy density distribution $u[z, \omega, T]$ at 20 nm above the surface is calculated for the three materials using literature values for the respective complex dielectric function (a-c, black lines, upper panels) [23,173] following the exact procedure discussed in the appendix (i.e., not using the quasi-static approximation). The corresponding relative far-field thermal emission spectra from the three heated materials measured with the AFM tip retracted are shown (a-c, red lines, lower panels) normalized against emission from a Si surface. They exhibit a signal *decrease* near the respective resonances in accordance with Kirchhoff's law of thermal emission for opaque bodies (Fig. 5.6 a-c), black line, lower panels) [160].

As can be seen for SiC, a peaked near-field signal occurs near ~ 945 cm^{-1}; for SiO_2 it is observed between 1150 and 1205 cm^{-1}. These spectral peaks correspond to the SPhP resonance modes of the respective materials. The SPhP resonance condition is met in

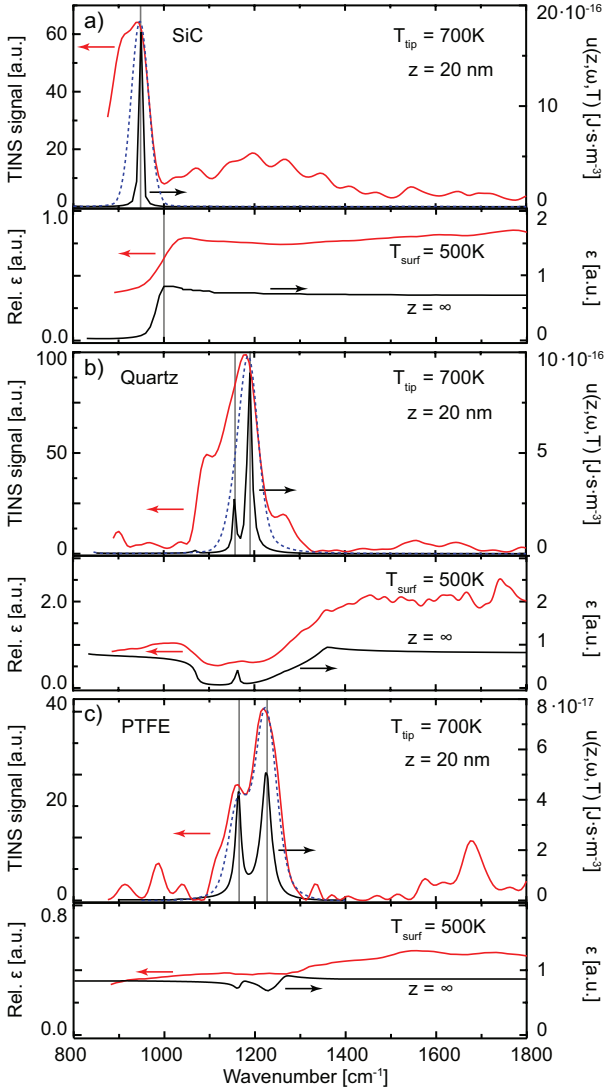

Figure 5.6: Tip-scattered enhanced thermal near-field signal (upper panels, red lines, a-c) for SiC, SiO_2, and PTFE, associated with the characteristic phonon-polariton, phonon, and vibrational resonances. The spectral energy density associated with the EM-LDOS (upper panels, black lines, a-c), calculated for $z = 20$ nm and $T = 500$ K, is concurrently displayed in the figure with the simulated spectral distribution of the TINS signal (blue dashed lines, a-c, arbitrary units). In contrast, far-field thermal emission from heated substrates (lower panels, red lines, a-c) exhibit signal decreases associated with elevated reflectivity on resonance in agreement with calculated far-field thermal emissivity given by Kirchhoff's law (lower panels, black lines, a-c).

SiC at $\simeq$ 950 cm^{-1} while for SiO_2 it is met both at $\simeq$1157 and 1190 cm^{-1}. As a non-dispersive molecular solid PTFE does not meet the conditions for surface wave excitation. Its distinct molecular resonances located at 1158, 1210, and 1240 cm^{-1} (latter two spectrally not resolved) are associated with the different C–F symmetric ω_S and antisymmetric ω_{AS} vibrational stretch modes [161, 162]. The measured signal magnitude is slightly weaker compared to that from polaritonic materials.

The observed resonant near-field characteristics are fundamentally distinct from the manifestation of these resonances in far-field emission, scattering, and reflection. SiC exhibits a reduction in far-field emissivity below $\sim$ 1000 cm^{-1} which marks the onset of the high reflectivity Reststrahlen band ($800 - 1000$ cm^{-1}). The measured emission from SiO_2 shows slight dips corresponding to enhanced reflectivity associated with the series of LO and TO Si-O phonon modes ($1050 - 1250$ cm^{-1}) [163,164]. The PTFE film further exhibits reduced emissivity in the vicinity of the C-F vibrational modes, albeit weaker, due to the lower vibrational density of states compared to that of the optical phonon modes in SiC or SiO_2.

In order to verify the near-field origin of the observed behavior, we measured a series of near-field spectra as a function of distance above the sample surface and observed *peaked* TINS signals associated with the expected resonances of the EM-LDOS up to a height of $\sim$ 1 μm above the sample surface. As an example the corresponding tip-sample distance dependence of the integrated combined ω_S and ω_{AS} modes for PTFE ($1100 - 1300$ cm^{-1}) is shown in Fig. 5.7 (red solid circles) A strong near-field confinement below $\sim$ 200 nm is found. The corresponding parameter free on-resonance model calculation of the distance dependence of the expected TINS signal derived from the spectral energy density above PTFE is shown as the solid line. [2]

In contrast, the off-resonant signal contribution (here integrated from 1400 - 1600 cm^{-1}) does not exhibit a discernible increase (blue open squares) within the uncertainty of the experiment. This behavior is also reproduced by the corresponding off-resonant calculation

[2]With the scattering power of the tip, $P_{\mathrm{scat}}[z,\omega,T] \propto u[z,\omega,T]$, we here model the distance dependence of the TINS signal occurring at a frequency of ν_d as proportional to the quantity $\partial u/\partial z$ as the signal in dynamic *s*-SNOM measurements are primarily sensitive to the gradient of the optical near-field (see ref. [174]).

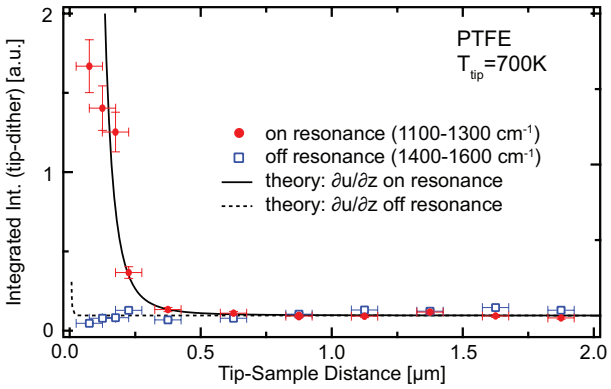

Figure 5.7: Distance dependence for the integrated spectral intensity on- (1100-1300 cm^{-1}) and off-resonance (1400-1600 cm^{-1}) for PTFE in comparison to corresponding model calculations (solid and dashed lines) exhibiting strong near-field localization.

(dashed line) which only exhibits a weak increase at very short distances (< 50 nm) [26,153].

In addition to characterizing the TINS tip-sample distance dependence for PTFE we have also acquired corresponding data for SiC as shown in Fig. 5.8. As expected from the spectral energy density $u[z, \omega, T]$, we observe an onset of signal increase associated with the SiC surface phonon polariton (SPhP) resonance located at $\omega \simeq 950$ cm^{-1} ($\lambda \simeq 10.5$ μm) at a height of $z \simeq 1.5$ μm corresponding to a $\sim \lambda/2\pi$.

We observe a less pronounced enhancement than expected from the $u \propto z^{-3}$ scaling as seen for PTFE. A possibility for this discrepancy is the differences in the visco-elastic damping of the cantilever in addition to variations in the heat transfer properties between the tip and surface.

5.4.3 Discussion of TINS measurements results.

The origin and consequences of the difference between the far- and near-field spectral behavior, its distance dependence, and its material specific resonant and non-resonant relationship with molecular vibrations, optical phonons, or surface polariton modes can be understood from an in-plane wavevector $k_{\|}$ dependent analysis of the spectral distribution of the EM-LDOS calculated using Eqn. 5.26 and displayed in Fig. 5.9.

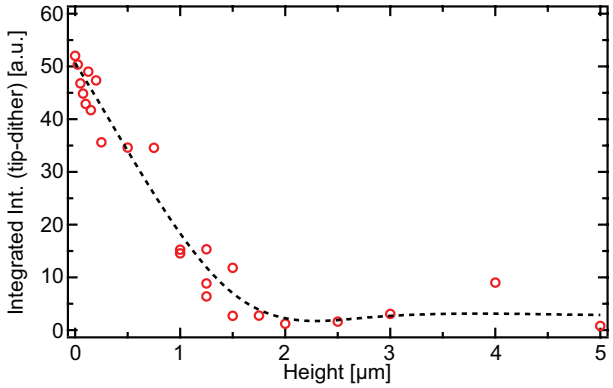

Figure 5.8: Distance dependence of the spectrally integrated resonant TINS signal (925-975 cm^{-1}). Onset of the signal increase is seen at a height of $z \simeq 1.5\ \mu m \simeq \lambda/2\pi$ as expected. An interpolation (black dashed line) of the approach data is provided as a guide to the eye.

In the far-field regime ($z \gg \lambda$, $k_{\|} < k_0$), materials generally act as broadband emitters with decreased emissivity associated with increased reflectivity. This corresponds to $k_{\|} < k_0$ for far-field emission with k_0 representing the free space wavevector (white dashed line). In the transition from the far- to the near-field (i, ii, iii), the contributions to the total EM-LDOS from states with large in-plane wavevector components $k_{\|}$ begins to become significant. Due to the large on-resonance contributions from the evanescent modes to the EM-LDOS, which increase with decreasing distance much faster than the off-resonance contributions, the initial onset of the near-field regime occurs at larger distances at resonant frequencies (as seen in the data in Fig. 5.7).

Under conditions for surface wave excitation ($\mathrm{Re}[\epsilon_2] < -1$), enhancement of the EM-LDOS associated with evanescent fields begins near $z \simeq \lambda$. Here, states with $k_{\|}$ satisfying the polariton dispersion relation $k_{\|} = \frac{\omega}{c}\sqrt{\frac{\epsilon_2}{\epsilon_2+1}}$ start to become the principle contribution to the EM-LDOS. In close proximity to the surface ($z \ll \lambda$), the EM-LDOS lies in the quasi-static regime where it is dominated by large in-plane wavevector states ($k_{\|} \gg k_0$) at frequencies where $\mathrm{Im}[\epsilon_2]$ is maximal or the surface polariton resonance condition $\mathrm{Re}[\epsilon_2] = -1$ is met as can be seen from Eqn. 5.30.

This behavior is shown specifically for materials without (Fig. 5.9a: PTFE) and with

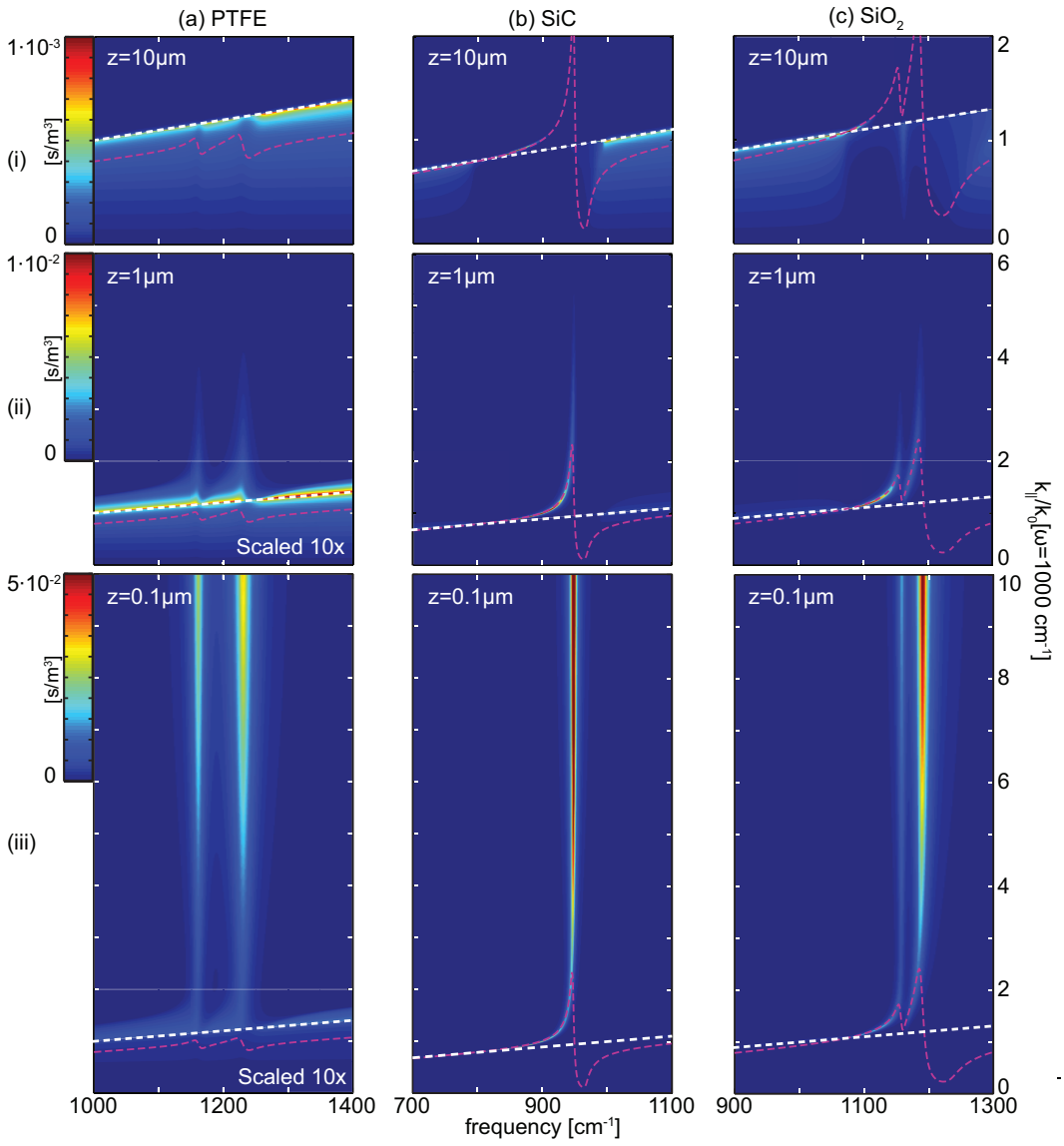

Figure 5.9: Calculated in-plane wavevector dependence of the local electromagnetic density of states (EM-LDOS) $\rho[z,\omega]$ above a surface for PTFE a), SiC b), and SiO_2 c) for the far-field (i), transitional (ii), and quasi-static near-field (iii) regimes represented by heights of 10, 1, and 0.1 μm respectively. The free-space light line dispersion (white dashed) marks the far (below) to near-field (above) transition while the material's surface wave dispersion relation (dashed magenta) indicates the driving surface resonances.

(Fig. 5.9b and c: SiC and quartz SiO_2) SPhP excitation. The three distances above the surface of 10, 1, and 0.1 μm in the plots represent the far-field, transitional, and electrostatic near-field regimes, respectively. In the far-field regime $\rho[10\ \mu\text{m}, \omega]$ is dominated by states below the light line (white dashed) where $k_{\|}$ corresponds to propagating modes. The near-field regime is characterized by $k_{\|}$ above the light line representing evanescent fields. The magenta lines show the $k_{\|}[\omega]$ which satisfy the SPhP dispersion relation.

PTFE represents a material with localized non-dispersive molecular excitations. In the far-field (i) it exhibits characteristic broadband emission with only slight dips in $\rho[z, \omega]$ on resonance. As it fails to meet the surface polariton dispersion criterion, near-field enhancement occurs where $\text{Im}[\epsilon_{\text{PTFE}}]$ is maximal on resonance (ii, iii). As a consequence, and in agreement with experiment, the spectral near-field line-widths correspond to the far-field absorption line-widths also defined by $\text{Im}[\epsilon_{\text{PTFE}}]$.

In contrast, for SiC (Fig. 5.9b) (with similar results for quartz SiO_2), the enhancement of $\rho[z, \omega]$ is governed by the dispersion relationship for the SPhP. As a consequence, the peak magnitude of $\rho[z, \omega]$ is over one order of magnitude larger for SiC compared to PTFE. For SiC, as seen at a distance of 10 μm (i), the characteristic gap in the far-field propagating states ($k_{\|} < k_0$) beginning at 1000 cm^{-1} is related to the high-reflectivity Reststrahlen band. In the transition regime at a distance of 1 μm (ii), an enhancement at energies below the SPhP resonance of 950 cm^{-1} following the surface wave dispersion relation develops. At short distances (iii) the distribution of EM-LDOS is governed by high wave-vector contributions located at the asymptote of the dispersion relation corresponding to the resonance condition for surface phonon-polariton excitation. This leads to the characteristic strong SPhP peak in the EM-LDOS responsible for the distinct spectral differences between the near-field and the far-field regime as observed in the experiment as well as the larger near-field response of SiC compared to PTFE.

To understand the detailed relationship between the tip-scattered thermal near-field signal and the underlying EM-LDOS, one has to consider that the detected near-field signal can be affected by the mutual optical polarization between the tip and the sample. Similar to conventional s-SNOM with external excitation illumination, here the radiating polarization in the tip is driven by the thermal evanescent field which in turn is affected by the resonant

dielectric properties of the sample. Modeling the tip as a small off-resonant polarizable sphere, its effective polarizability as a function of distance above the surface z and radius r is given by

$$\alpha_{\text{eff}} = \alpha \left(1 - \frac{\alpha\beta}{16\pi r^3 (1 + \frac{z}{r})^3}\right)^{-1}, \tag{5.32}$$

with $\beta = (\epsilon_2 - 1)/(\epsilon_2 + 1)$ relating the strength of the image dipole in the surface and $\alpha = 4\pi r^3 \cdot (\epsilon_{\text{sph}} - 1) \,/\, (\epsilon_{\text{sph}} + 2)$ representing the Clausius-Mossotti relation for the polarizability of a sphere with dielectric permittivity ϵ_{sph} [15,46]. The resulting optical polarization leads to a spectral distribution of the scattered power which can be expressed as the product of $u[z, \omega, T]$, the effective scattering cross-section of the sphere C_{eff}, and the speed of light c as,

$$P_{\text{scat}}[z, \omega, T] = C_{\text{eff}} \cdot c \cdot u[z, \omega, T_{\text{surf}}]. \tag{5.33}$$

Here, the effective scattering cross-section of the sphere C_{eff} is defined in terms of the effective polarizability as $C_{\text{eff}} = k^4 |\alpha_{\text{eff}}|^2/(6\pi)$ [175].

The resulting spectral distribution of the tip-scattered intensity induced by the near-field thermal spectral energy density for $T = 500$ K is plotted in Fig. 5.6 (blue dashed line) for all three materials convolved with the $\simeq 25$ cm^{-1} spectral resolution of our experiment. We find good general agreement between the experimentally observed results and the model for the scattered power by the tip given by Eqn. 5.33. The scattered near-field power derived from the relationships above also agrees well with the 30-100 pW of near-field scattering power observed in our measurements.

The experimental results on SiC are reminiscent of laser s-SNOM spectroscopic measurements which exhibit a signal peak at 920 cm^{-1} [48, 104]. As in s-SNOM, Eqn. 5.33 incorporates a optical phase related few cm^{-1} red shifts with line asymmetry due to the strong tip-sample coupling at short distances ($z \lesssim$ AFM tip apex radius) [15,48]. This effect is slightly more pronounced when considering details of tip geometry and higher-order mode coupling compared to the simple model above, but within the limits of the natural line width of molecular or phonon excitation. A 5-10 cm^{-1} red shift and spectral broadening is also expected from phonon softening and increased damping with temperature [171, 176–178]. We attribute these as the dominant effects, together with a higher defect density of the nat-

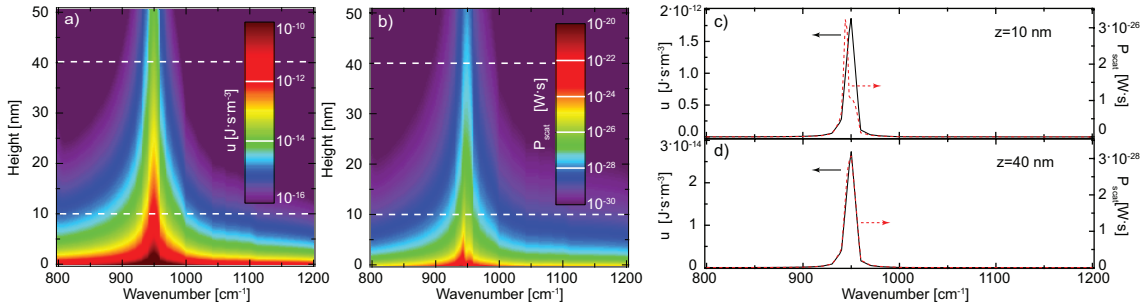

Figure 5.10: The height and spectral dependence of $u[z, \omega, 500\text{ K}]$ a) and $P_{\text{scat}}[z, \omega, 500\text{ K}]$ b) are displayed with logarithmic color scales as calculated using Eqns. 5.26 and 5.33 for a Si sphere of radius $a = 20$ nm. Panels c) and d) compare the spectral distributions of $u[z, \omega, 500\text{ K}]$ and $P_{\text{scat}}[z, \omega, 500\text{ K}]$ for heights of 10 and 40 nm, marked by the white dashed lines in panels a) and b), representing height-to-tip radius ratios of $z/a = 0.5$ and $z/a = 2$ respectively.

ural quartz measured, for the observed deviations from the model calculations. However, a detailed discrimination is not possible within the available spectral resolution and signal to noise ratio of our experiment.

For distances larger than the strong tip-sample coupling range of about the ~ 40 nm of the tip apex radius, TINS can thus serve as a measurement of the evanescent spectral energy distribution and resonances of the sample with the tip acting only as a weakly perturbing scatterer. The associated underlying near-field EM-LDOS, also for shorter distances, may be explicitly extracted using an appropriate models that incorporates the dynamic variation of coupling with the tip-dither motion, the role of far-field interference and surface reflection, details of the tip geometry affecting coupling and scattering, as well as contributions due to variations in the surface topography.

With knowledge of the EM-LDOS calculated using Eqn. 5.26, the spectral energy density above a specific surface material at a given temperature may be calculated by multiplying with the Planck distribution $u[z, \omega, T] = \rho[z, \omega] \cdot \Theta[\omega, T]$. Fig. 5.10a) displays the resulting $u[z, \omega, T]$ in the near-field regime above a SiC surface in the vicinity of the SPhP resonance frequency at 950 cm^{-1}. The associated scattering by the AFM-tip, modeled by the scattering of a small off-resonant polarizable sphere and calculated via Eqn. 5.33 for a 20 nm Si

sphere, is displayed in Fig. 5.10b). Line-traces displaying the spectral distribution $u[z, \omega, T]$ and the associated spectral scattering power P_{scat} of the tip-sphere at heights of 10 and 40 nm above the surface are displayed in panels c) and d) of 5.10 representing height to tip-radius ratios of 0.5 and 2 respectively.

At distances below the AFM tip-radius (panel c), the effect of mutual coupling between the tip and its image dipole leads to a slight ($\sim$ 5 cm^{-1}) redshift in the P_{scat}. Due to the narrow line-width of $u[z, \omega, T]$ associated with the SPhP resonance in the near-field limit, the magnitude of spectral shift in P_{scat} is constrained to the line-width of the peak in $u[z, \omega, T]$. Furthermore, the incorporation of surface reflection terms for the P_{scat} has only minimal effects on its spectral distribution. Finally, for heights greater than the tip-height (panel d), any effects due to mutual coupling with the surface are minimal, meaning that the scattering distribution of the non-resonant sphere directly reflects the intrinsic spectral distribution of $u[z, \omega, T]$.

5.4.4 TINS as a nano-spectroscopic technique.

Far-field thermal emission spectroscopy, with its limited sensitivity, has long been known as a useful technique for materials characterization especially where implementation of external light sources is not practical or even possible [179, 180]. Our work shows that the enhanced EM-LDOS in the thermal near-field associated with resonance modes enables infrared thermal near-field spectroscopy as a new scanning probe technique with IR vibrational contrast and spatial resolution determined by the EM-LDOS near-surface localization and/or tip apex radius.

The spatial resolution we achieve is demonstrated in Fig. 5.11 for a spectrally integrated TINS scan of a PTFE flake boundary of thickness $\sim$ 100 nm on a Si substrate. The line trace (f, laterally averaged over 6 lines in the high resolution scans c,d) indicates a spatial resolution of $\simeq$ 50 nm consistent with the tip apex radius. We interpret the enhanced signal at the PTFE step edge with elevated near-field coupling and scattering at the edge.

Using the spatial resolution data obtained from Fig. 5.11, the sensitivity of the TINS measurement can be estimated for PTFE. Here, for a density of $2.2 \cdot 10^6$ g/m^3 and a tip-apex

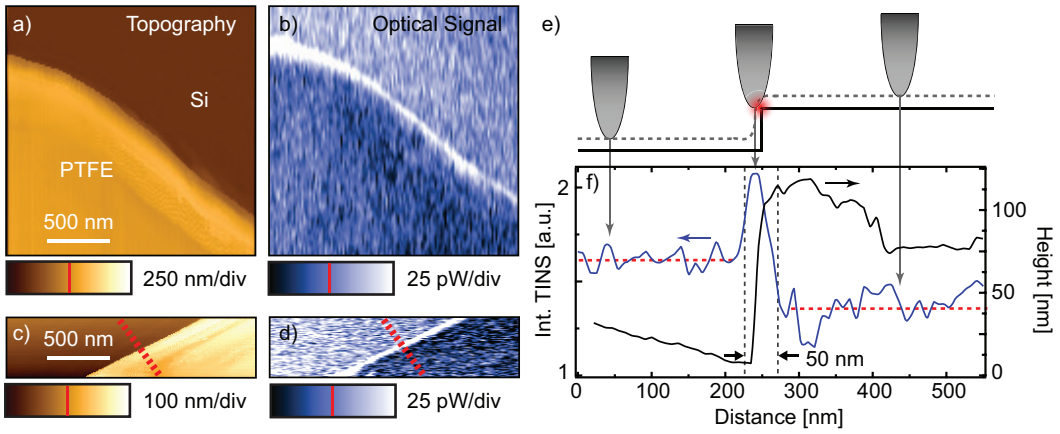

Figure 5.11: Topography a, c) and spectrally integrated TINS signal b,d) with contrast between a PTFE flake of thickness ~ 100 nm on a Si substrate. Panels c) and d) represent a higher resolution scan near the PTFE step edge with line-trace f) of topography and TINS signal (laterally averaged over 6 scan lines, along red dashed line in c). An increase in scattering with the tip at the PTFE step edge is observed as indicated schematically in e). The spatial resolution of $\simeq 50$ nm as indicated by the vertical grey dashed lines f) agrees with expectation related to tip apex radius.

localized sample volume of $\sim 1 \cdot 10^6$ nm^3, the number of sampled C-F groups amounts to $\sim 5 \cdot 10^7$, corresponding to ≈ 40 attomol of CF_2 groups. Modeling the statistical distribution of the PTFE CF_2 groups using the micro-canonical partition function for a harmonic oscillator $Z^* = 1/(1-\exp(-\hbar\omega/k_BT))$, an estimated $3-8\%$ fraction of vibrationally excited oscillators contributes to the signal for temperatures in the 500-700 K range. Assuming a minimal signal-to-noise ratio of ~ 10 necessary for spectral peak assignment the resulting sensitivity for spectroscopic contrast is as high as 3-5 attomol.

This sensitivity represents an increase in IR-spectroscopic sensitivity of at least 4 orders of magnitude over conventional far-field IR microscopy techniques where spatial resolution is constrained by the diffraction limit (~ 10 μm) [181] and non-enhanced far-field absorption. The sensitivity is comparable to conventional laser-based s-SNOM [106], and can be further improved utilizing IR optical antenna modes of specially engineered tips. This implementation of s-SNOM with a heated tip thus allows for broadband chemical nano-spectroscopy, complementary to the use of an external thermal light-source [44], yet with

higher sensitivity and the thermally driven vibrational optical dipoles providing their own intrinsic light source.

In summary, our spectroscopic characterization of the enhanced electromagnetic near-field spectral energy densities connect the previously well defined regime of broadband far-field thermal radiation to the prediction of intrinsic and extrinsic thermal near-field resonances and their wave-vector distribution. The results open the door for, e.g., tailoring heat management in microelectronic and thermophotovoltaic devices, optical antenna resonant control and switching of optical forces, enhanced IR and thermal sensing, and compact chemical nano-imaging and -spectroscopy instrumentation without the need for an external excitation source.

Chapter 6

S-SNOM CHARACTERIZATION OF CORRELATED ELECTRON SYSTEMS: VANADIUM DIOXIDE (VO_2) MICRO-CRYSTALS.

Some of the most profoundly interesting and potentially useful physical phenomena in condensed matter physics today occurs in a class of materials known as transition metal oxides. These materials exhibit a wide range of emergent properties including colossal magnetoresistance, metal-insulator transitions, multi-ferroicity, and high-temperature superconductivity. They are prized today for their value as magnets and as materials for electronics. Transition metal oxide systems are often characterized by competing nearly degenerate states with coupled charge, orbital, spin, and lattice degrees of freedom. Despite the obvious attractiveness of transition metal oxide systems for technological applications, the understanding of the complex physics which underlies these systems is largely incomplete. The lack of systematic knowledge of the relevant driving forces and parameters behind many of the exotic phases exhibited by these systems make material design and device development difficult. In the following chapter, I will introduce the implementation of *s*-Scanning Near-field Optical Microscopy (*s*-SNOM) for the characterization of the complex phases of these systems characterized by complex, correlated electron phenomena. In particular, I will focus on the utilization of infrared *s*-SNOM/Raman spectroscopy in mapping phase separation during the metal-insulator transition in vanadium dioxide (VO_2); additionally, I will discuss the ultrafast characterization the photo-induced phase transition in VO_2.

6.1 Introduction to correlated electron systems and phase separation.

The recognition of the importance of role of electron-correlation effects in condensed matter systems emerged with the development of the band theory description of metals and insulators in first half of the 20th century [182–186]. The "band structure" description for a given crystalline material represents the solution for the allowed energy and momentum states for non-interacting electrons within a periodic crystal lattice. The electronic states in this

description can be expressed in terms of Bloch states for which the energy eigenfunction for a periodic (crystalline) system may be written as the product of a plane wave envelope function and a periodic function. These solutions take the form of bands representing the energy-momentum dispersion relation for electronic states for a specific direction and crystal lattice symmetry.

Under this model, insulators are defined as materials with electron energy bands which are completely occupied with a large energy band-gap separating the filled valence and empty valence bands. As the valence electrons of a solid material completely fill a given band, no states are available to excite electrons under small energy perturbations characteristically prohibiting electronic conduction. Correspondingly, if the valence electrons only partially fill the band which they occupy, small energy perturbations may excite the highest energy electrons at the Fermi level to unoccupied states making the material a conductor. Semi-conductive materials are subsequently defined as those materials for which valence electrons fill an entire band, but for which unoccupied states are not far separated by a large energy gap.

It was recognized early on, however, that the description of electrons in terms of delocalized Bloch waves failed to incorporate electron-electron interactions [187] resulting the model's failure to correctly predict the electronic structure for certain materials. The first primary example was that of NiO for which conventional band theory predicts the material to be metallic, but which is found to be a transparent insulator [188, 189]. It was proposed that the insulating character of this material system was due to electron-electron interactions and it was later shown that the insulating properties were due to the presence of an anti-ferromagnetic sub-lattice [190–193]. In addition to NiO, many materials have been identified for which the band structure description fails to correctly predict the electronic properties of the system. This early example sets the stage for the broad definition of correlated electron systems.

The term "correlated electron systems" is often used to represent the class of materials for which the non-interacting band-structure model fails to correctly predict the electronic properties of the system [194]. The interactions present in correlated electron systems spans a wide variety of interaction mechanisms including electron-electron, -phonon, and -quasi-

particle interactions. Under this broad definition, Mott insulators are systems which are insulating by virtue of the electron-electron interactions in spite of the prediction by the band-structure model of a metallic state. For these systems Coulomb repulsion of electrons at differing crystal lattice sites is strong, consequently blocking electron motion at low temperatures/energies [195].

One of the defining properties of correlated electron systems is the measured value of the kinetic energy of mobile electrons K_{exp} is much lower than that predicted by the band structure model ($K_{\text{exp}}/K_{\text{band}} < 1$) [195–197]. This is a result of the competing interests of the mobility of the electrons and correlation effects which favor localization through the mutual Coulomb interaction between electrons; a higher correlation effect inhibits mobility, thus reducing the kinetic energy of electrons below that expected from band theory. In contrast, simple metal systems with non-interacting itinerant electrons exhibit kinetic energies in good agreement with band-structure model calculations ($K_{\text{exp}}/K_{\text{band}} \simeq 1$) [195–197].

Despite being the focus of research interest for nearly a century, many correlated electronic systems are still poorly understood. The description of correlated electron systems is one of the pre-eminent challenges of current condensed matter research. The transition metal compounds, in particular, represent a system class predisposed towards this type of strong correlative effect by the presence of d band electrons. Here, the d bands are characterized as occurring in a narrower energy bandwidth than comparable s orbital band and further must have states for up to ten electrons resulting in a high free electron density of levels related to the d band [24]. In addition, the d states are characterized by both spin and orbital degrees of freedom.

The energetic interplay of these degrees of freedom under the constraints imposed by the crystal lattice field make transition metal compounds ideal systems for correlated electron effects to occur. Transition metal oxides exhibit a wide range of emergent properties including colossal magneto-resistance (CMR) [198–200], metal-insulator transitions (MIT) [201], multi-ferroicity [202], and high-temperature superconductivity [203, 204]. Despite the obvious attractiveness of potentially using these phenomena for technological applications, the largely incomplete understanding of the underlying complex fundamental physics, and even lack of systematic knowledge of relevant driving forces and parameters behind many of these

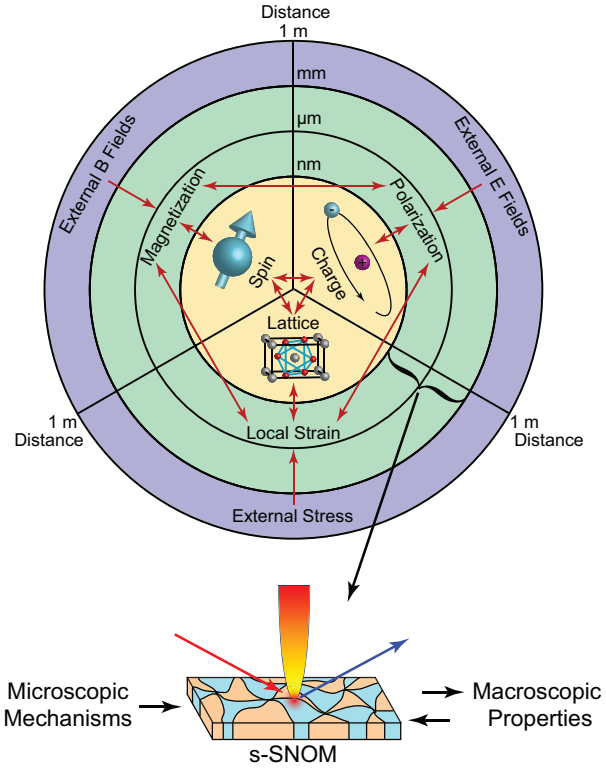

Figure 6.1: The role of coupled charge, spin, and lattice degrees of freedom in the formation of inhomogeneous mesoscopic domains ranging from the atomic scale, to macroscopic dimensions given by external fields. The interplay of these interactions (red arrows) can result in intrinsic phase coexistence on mesoscopic length scales (1 nm$<$ l$<$1 mm) which we can access spectroscopically on the nanoscale with scattering scanning near-field optical microscopy (s-SNOM) with $<$ 10 nm spatial resolution.

exotic phases, make material design and device applications difficult.

The strong electron correlation in transition metal oxides and related materials leads to unusually rich phase diagrams with distinct crystallographic, electronic, and magnetic phases with frustration and degenerate ground states. One resulting overarching phenomenon is that in many cases phase competition and coexistence of multiple phases exists near phase boundaries. It has become increasingly evident that this gives rise to structural and electronic inhomogeneities and nanoscale spatial phase separation with complex spatial architecture [205–210]. This phase co-existence over a wide range of length scales from

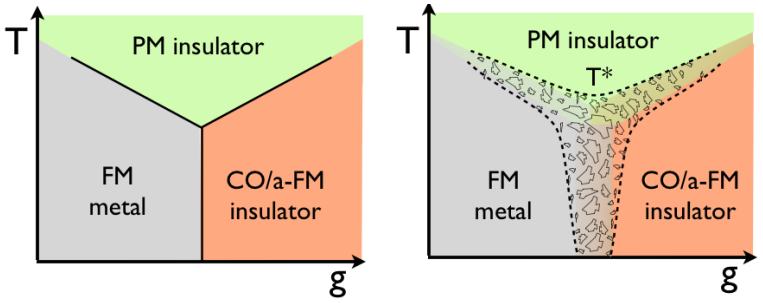

Figure 6.2: Schematics of an example phase diagram indicating the ideal macroscopic first order phase boundaries (left) and multi-phase coexistence and spatial separation scenario (right) with domain formation. The parameter g represents a generalized control parameter such as doping, strain, or external fields. After ref. [205]

nano- to microscale, is determined by both intrinsic and extrinsic factors. It can be static or dynamic, and is very sensitive to external stimuli via, e.g., electric and magnetic fields, strain, current, and temperature (Fig. 6.1).

While the transition between the distinct electronic, magnetic, and crystallographic phases of correlated electron materials is often predicted to be discontinuous (first order) it is often observed to occur over broad ranges of the independent system parameter (i.e. temperature, external strain, ect...). This is a result of the discontinuity in the thermodynamic free energy for a first order phase transition in an unconstrained system in thermal equilibrium. Here, the system should entirely exist in one phase or the other. However, the interplay of external parameters (temperature, pressure, electromagnetic fields, strain) with local conditions (strain, crystal boundaries, defects, ect) within these materials oftentimes favors the local existence of one or the other specific phases (Fig. 6.2).

Evidence of local phase separation on mesoscopic length scales and domain formation emerged indirectly from bulk characterization such as transport [211, 212] , x-ray and neutron diffraction [213, 214], and angle resolved photo-emission spectroscopy (ARPES) [215]. Here, macroscopic quantities expected to exhibit a discontinuous change at the phase transition temperature are broadened. This has been interpreted with the formation of an inhomogeneous phase distribution.

While the evidence of phase separation is often evident in macroscopic-scale characterization of these systems, the disadvantage of these measurement techniques is that they are unable to characterize the nature of the microscopic distribution of the constituent phases. As a consequence, bulk characterization techniques are only able to provide a measurement of the average of an inhomogeneous distribution of microscopic domains.

In an effort to gain information about the underlying spatial texture and domain formation, scanning tunneling microscopy (STM) [216–221], electron microscopy techniques (SEM, TEM) [222–226], photoelectron emission microscopy (PEEM) [227], magnetic force microscopy (MFM) [228–231], piezoresponse force microscopy [232], conductive AFM [208], as well as conventional optical microscopy techniques [207,233,234] have been applied. From the wide range of investigations it emerged that spatial phase separation and co-existence in strongly correlated electron systems spans > 5 orders of magnitudes in mesoscopic length scales ranging from the atomic to the 10s μm scale, yet of mostly unknown texture (stripes, patches, topology, and hierarchy). In these studies the fundamental questions of interest are, what factors are involved in the formation of phase inhomogeneities, how are those factors related to the distribution characteristic length scale of phase domains, and what are the intrinsic electronic properties of said domains?

While all the techniques mentioned above have their individual strengths, the indirect scattering/diffraction techniques face the challenge that for irregular domains fundamentally distinct textures and topologies could give nearly identical experimental signatures. The real space direct imaging techniques are often sensitive to only one order parameter, and/or applicable to only a limited number of perturbations. In general, electron microscopies are not applicable under magnetic or electric field and it is difficult to obtain contrast between metallic and insulating phases. STM and PEEM are not a priori bulk techniques, with concerns of perturbation from surface electronic states and sensitivity to surface contaminations. PFM and MFM can determine ferroelectric and magnetic domain order, respectively, yet not simultaneously, and are insensitive to antiferromagnetic order (which is prevailing in many multiferroics). Depending on the technique special sample preparation is often required. There is therefore a real lack of a technique that can image multiple order parameter simultaneously, operate under strong magnetic and electric fields,

over a wide range of temperatures, access many different orders of length scales, and can simultaneously probe ultrafast time scales.

In order to simultaneously gain access the mesoscopic length scales characteristic of phase inhomogeneities in correlated electron systems in addition to the energy levels of the relevant solid-state excitations (0.01-1eV) and temporal dynamics (1fs-1ns) it is necessary to characterize the material properties with high spatial resolution at frequencies in the optical regime. In far-field optical characterization the spatial resolution of conventional far-field microscopy techniques is constrained by the diffraction limit. As discussed in chapter 3, *scattering*-type scanning near-field optical microscopy (s-SNOM), as a combination of scanning probe microscopy with optical spectroscopy, can provide few- nanometer optical spatial resolution. It relies on the local field enhancement and its spatial confinement as provided by the optical antenna properties of ultra-sharp probe tips [39, 41, 235]. Scanning the tip in close proximity to the sample by means of atomic-force or scanning-tunneling feedback (AFM, STM), imaging contrast arises due to the local mutual near-field tip-sample polarization. As a consequence the scattered light from the tip-apex region contains spectroscopic information about the sample from a region later- ally confined by the dimensions of the tip apex radius, which in turn defines the spatial resolution (practically limited to about 5-10 nm) [14, 104, 236–238].

Through implementation of apertureless *s*-SNOM techniques, we may gather characterize the optical properties of these correlated electron systems below the diffraction limit to a resolution of $\simeq$ 10 nm. In recent years, *s*-SNOM measurement methods have utilized a variety of optical contrast methods including elastic light scattering, Raman spectroscopy, fluorescence, and nonlinear optical spectroscopy. In this chapter, I will discuss focus on the metal-insulator transition in vanadium dioxide (VO_2), and how implementation of *s*-SNOM characterization using IR elastic light scattering in combination with far-field optical techniques provides a more detailed analysis of the phase separation behavior and transition mechanisms of this correlated electron system.

6.2 Metal-Insulator Transitions (MIT).

In the description of metal-insulator transitions the fundamental mechanism by which a large change in the electronic properties occurs can typically be separated into one of two categories. The nature of the transition can be related to the physics of the insulting state. For the case of non-interacting electrons, the insulating state is accurately described through the band structure model and the transition to the metallic state is correlated with a change in the crystal lattice. Metal-insulator transitions related with electron-electron interactions can correspondingly be associated with the change in the magnitude of the electron-electron interactions in the material.

6.2.1 Peierls-type insulators.

The electrons within a metal-insulator transition fitting the Peierls-type model are approximated as non-interacting electrons. Under this model, the essential change which induces the MIT occurs when the specific volume of the crystal unit cell changes in such a manner that electronic bands constituting the band-structure no longer overlap. The formation of a band-gap through structural distortion prevents the electrons at the Fermi-level from entering the conduction band through small energy perturbations resulting in a transition to a semi-conducting/insulating state from the conductive state.

This type of transition from a metallic to insulating state through lattice distortion was first put forth by Rudolf Peierls [239] in which he showed that a 1D half filled metal is unstable against a structural distortion. Peierls considered a 1D chain of atoms with one electron per atom separated by distance a, at temperature $T = 0$, over which electrons at the Fermi energy with wavenumber $k_F = 2\pi/a$ could move freely.

If the evenly spaced lattice sites along the chain are slightly distorted following the function $\delta x[x] = \Delta \cos[2k_F x]$ the mean cost in elastic energy is proportional to $E_{el} \propto \Delta^2/4$. Peierls, however, showed that the reduction in electronic energy is $\propto \Delta^2 \ln[\Delta]$. This implies that small distortions are energetically favorable as the reduction in electronic energy is greater than the gain in elastic energy. One consequence of this lattice distortion is that electrons now experience a periodic potential $U[x] \propto \Delta \cos[2k_F x]$ resulting in the formation

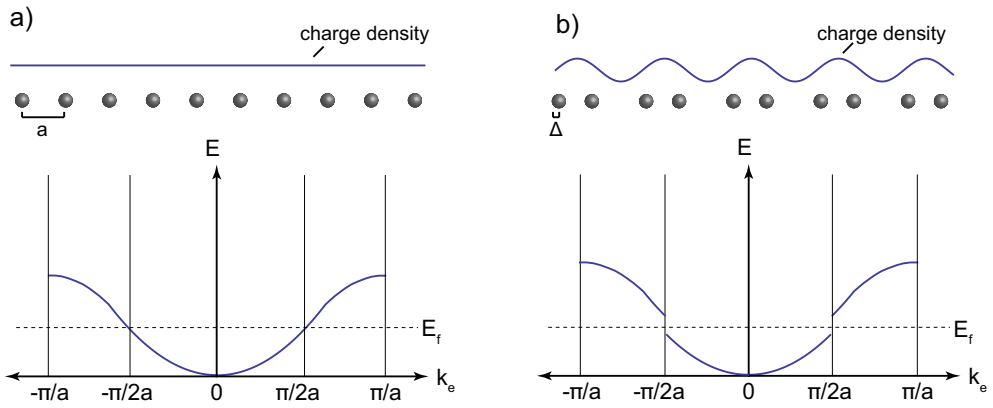

Figure 6.3: The charge density distribution and the electron energy dispersion for a linear 1D chain of atoms is pictured above for a equally spaced chain a) and a chain exhibiting Peierls distortion and the formation of a charge density wave b)

of a band gap at $\pm k_F$ and charge density waves within the 1D lattice. The lattice distortion and related change in the band structure is pictured in Fig. 6.3.

Extending the concept of a Peierls-type distortion to solid state systems in three dimensions, lattice deformations may also be induced through the interaction of the electrostatic crystal field with localized electrons [194]. For example, for transition metal atoms surrounded by oxygen octahedra a cubic crystal lattice symmetry would yield degeneracy in some of the d electronic orbitals. In this case, it may be energetically favorable to reduce the degeneracy and thus lower some electronic orbital energy levels through the distortion of the oxygen octahedra [194]. The observation of a change in electronic properties through such a lattice distortion which doubles the size of the unit cell characteristically defines a Peierls-type metal-insulator transition. For a Peierls insulator the interaction between electrons and lattice ions results in the static, periodic distortion of the whole crystal lattice structure generating the formation of charge density waves extending through the crystal lattice.

6.2.2 Mott-Hubbard insulators.

As discussed in the introduction, several materials exist as insulators due to correlated electron interactions despite being predicted as having metallic electronic structure from band model calculations. Specifically, under this picture a Mott-Hubbard type insulator can be defined as an insulator whose gap for single particle excitations at the Fermi level arises through electron-electron interactions. The effect of these correlations forces a quantum phase transition from a correlated metal to a Mott-Hubbard insulator in which the local magnetic moments do not display long range order [194, 240].

Mott first proposed how electron-electron interactions could suppress metallic behavior in favor of an insulating electronic phase [190]. Under his description when electron moves from one crystal lattice site to another, it leaves behind it a positively charged hole. The electron and hole attract each other with a force resulting from the potential $U \propto -e^2/r$, where e is the electron charge and r is the electron-hole separation. It was further reasoned that the presence of electron-hole pairs here would screen the field between the electron and a hole, reducing the potential to $U \propto -(e^2/r)\exp[-\delta_{eh}r]$, where δ_{eh} depends on the density of electron-hole pairs [190]. When the density of pairs becomes large enough, the potential U no longer can maintain bound states, allowing the system to conduct.

Specifically, in this description it is the Coulomb potential which is the critical interaction, with a large U causing electrons to be localized at each lattice site within the crystal. This description was formalized by Hubbard in the Mott-Hubbard Hamiltonian [241, 242]. In simple terms, within the Hubbard model electrons are allowed to travel between atomic sites on a crystal lattice and are described as having s orbitals [194, 240]. An additional term accounts for the Coulomb repulsion experienced by two electrons of opposite spin which share the same lattice site.

The Hubbard hamiltonian may be expressed as, [240–242]

$$H = \sum_{i,j} t_{i,j} a_{i,\sigma} a_{j,\sigma} + U \sum_{i} n_{i\uparrow} n_{i\downarrow}. \tag{6.1}$$

Here, the suffixes i and j refer to the nearest-neighbor sites on the lattice while σ refers to the spin direction. $n_{i,\sigma}$ represents the electron number operator for the spin state σ.

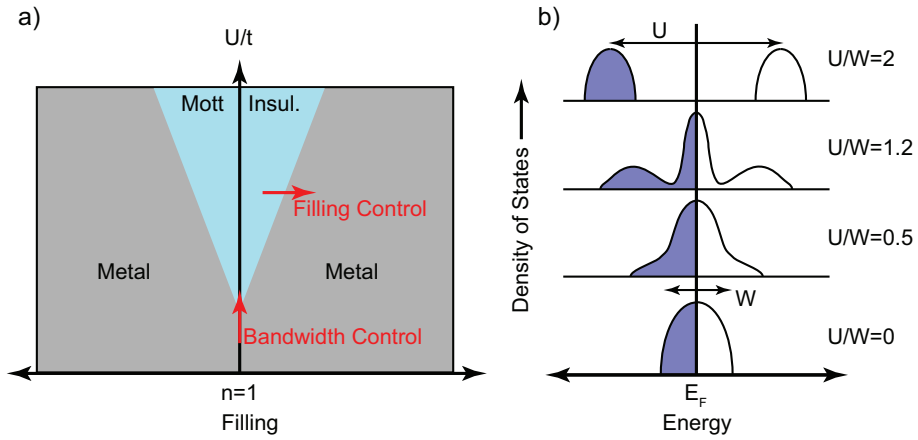

Figure 6.4: Panel a) displays the metal-insulator phase diagram based on the Hubbard model. The independent variables here are the strength of the Hubbard potential U and the filling level n. The red arrows indicate the two transition mechanisms which occur via bandwidth control and filling control. Panel b) displays the Hubbard model for the relationship between the density of states and the U for a bandwidth control type transition showing the transition from a metallic state for $U/W = 0$ to the fully insulating state at $U/W = 2$ [201, 243].

t_{ij} represents the hopping matrix which is responsible for the motion of electrons between different atoms which can be related to the bandwidth W via the relation $t = W/2z$ where z represents the coordination number of the system. Finally, U represents the intra-atomic correlation energy related to the Coulomb repulsion.

The most simple regime in the Hubbard Hamiltonian lies in the limit of $t_{ij} \gg U$. In this case, the interaction between electrons is neglected. This reduces the model to the band structure model with delocalized electrons.

Conversely, the opposite limit lies in $t_{ij} \ll U$ where the electron localization energy term is much larger than the kinetic energy for the hopping of delocalized electrons; as a result, the electrons are localized on their lattice sites. This interaction regime leads to the formation of the previously described "Mott" insulator in which the band theory predicts metallic behavior but where the electron-electron repulsion is dominant resulting in the formation of a band gap.

It is important to note that the Hubbard model in its most simple form makes some

drastic over-simplifications. Specifically, the model only considers electrons in the s orbit. The transition metal compounds in typical correlated electron materials, however, contain several electrons in the d-orbitals. The degeneracy of the d orbitals in the crystal-lattice and the interactions between the different orbital states adds to the complexity of these transition metal compounds.

In the simple Hubbard model presented above the two essential parameters are the strength of the electron-electron localization potential U and the band filling n. For the case of an empty band or full band ($n = 0$ or $n = 2$) the system is considered to be a band insulator. With no electron-electron localization, half filling ($n = 1$) of a band would predict a metallic state. However, increasing the electron localization potential U/t results in the formation of an insulating phase for $n = 1$. This transition at finite U is called a bandwidth-control metal-insulator transition and is of first-order [201, 240]. The vertical red arrow in panel a) of Fig. 6.4 represents the bandwidth control transition while panel b) displays the relationship of the electronic density of states for various ratios of U to the bandwidth W. For the case of a half filled band with s orbitals, the critical value of U for which the two bands separate is $W = 1.15U$ [240]. Experimentally the ratio of U to t may be traditionally controlled by application of strain or pressure which shortens the interatomic distance, decreasing the localization and increasing the transfer rate between lattice sites.

In addition to bandwidth control MIT, the filling of carriers can also lead to the metallic phase. This filling-control metal-insulator transition is not necessarily first-order [201]. The horizontal red arrow in panel a) of Fig. 6.4 represents the filling control transition pathway. Experimentally, filling-control transitions can be implemented through the doping of the carrier concentration either through substitution of chemical elements or through photo-doping.

6.3 The MIT in vanadium dioxide (VO_2).

The vanadium oxides (VO, V_2O_3, VO_2) are among the most famous of materials believed to undergo a Mott transition [201, 244, 245]. VO, VO_2, and V_2O_3 with cubic, monoclinic, and trigonal crystal structures in the insulating phase exhibit metal-insulator transitions

with orders of magnitude changes in conductivity at 114, 153, and 340 K, respectively [244]. Each of these oxides exhibits unique phase behavior as a function of temperature, pressure, and doping. The complexities associated with their phase transitions arise from the interplay of electron-lattice effects which emerge via crystallographic or unit cell volume changes [246, 247] at the phase transitions and electron-electron interactions via Coulomb repulsion [245, 248].

The MIT in bulk VO_2 was characterized in 1959 by Morin, in which the DC electrical conductivity was found to undergo a transition from a low-temperature semiconductor to a high-temperature metal at approximately 340 K [244]. Despite the relatively simple stoichiometry and structure of VO_2, as well as the fact that its MIT was discovered over 50 years ago, many questions regarding the nature of its MIT remain unresolved. The complex nature of the MIT, in addition to its easily accessible transition temperature above ambient room temperatures, has made VO_2 one of the most widely studied correlated electron materials. To date, the fundamental mechanism of the MIT is still debated as the observed properties of the transition exhibits both Peierls-like and Mott-like characteristics [245, 248–253].

Complicating the development of a fundamental description of the mechanism underlying the MIT is the fact that VO_2, in addition to the change in electronic properties across the MIT, also exhibits a change in crystal structure between the metallic and insulating phases. Furthermore, several different insulating phases exist, each with its own structural differences from the high temperature crystal structure. Fig. 6.5 displays the temperature-pressure phase diagram for VO_2 which exhibits a high temperature metallic phase (R) and three insulating phases (M1, M2, and T) which will be discussed in detail in the following section.

6.3.1 Crystal structures of the phases of vanadium dioxide.

The rutile phase (R):

The high temperature phase of VO_2 is characterized by a metallic electronic phase and a rutile (R) tetragonal crystal structure with space group $P4_2/mnm$ (D_{4h}^{14}, No. 136) [255].

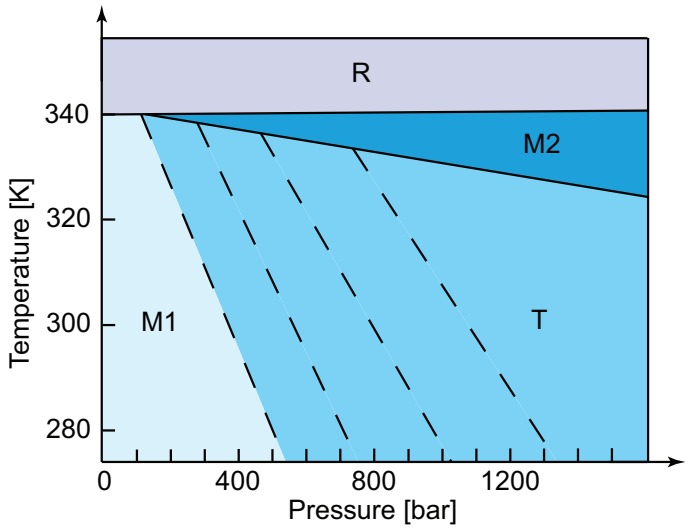

Figure 6.5: The temperature-stress phase diagram for VO_2 under uniaxial stress showing the presence of the R, M1, M2, and T phases as measured via nuclear magnetic resonance spectroscopy by Pouget et al in ref[[254]].

As shown in Fig. 6.6a) each of the vanadium atoms in the body-centered tetragonal lattice is surrounded by an oxygen octahedron.

The vanadium atomic sites in the tetragonal crystal structure can further be divided into to distinct sub-lattices denoted here as sub-lattice A and sub-lattice B. Sub-lattice A is composed of the vanadium sites at the center of the unit-cell which share an oxygen octahedra edge for an octahedron with the same orientation surrounding [110] its neighboring vanadium atoms along the c axis. Sub-lattice B is similarly composed of the corner vanadium atoms surrounded by 90° rotated oxygen octahedra $[1\bar{1}0]$ which are connected by a corner site to the octahedra surrounding the vanadium sites in sub-lattice A [256]. These sub-lattice chains are indicated in Fig. 6.6 by the red arrows parallel to the c_R axis.

The monoclinic 1 phase (M1):

The monoclinic M1 insulating phase occurs at temperatures below T_{MIT} at low pressures/levels of Cr doping [257] and is defined by a crystal structure with a space group of $P2_1/c$ (C_{2h}^5, No. 14) [258]. Here, the vanadium sites are shifted from the R crystal

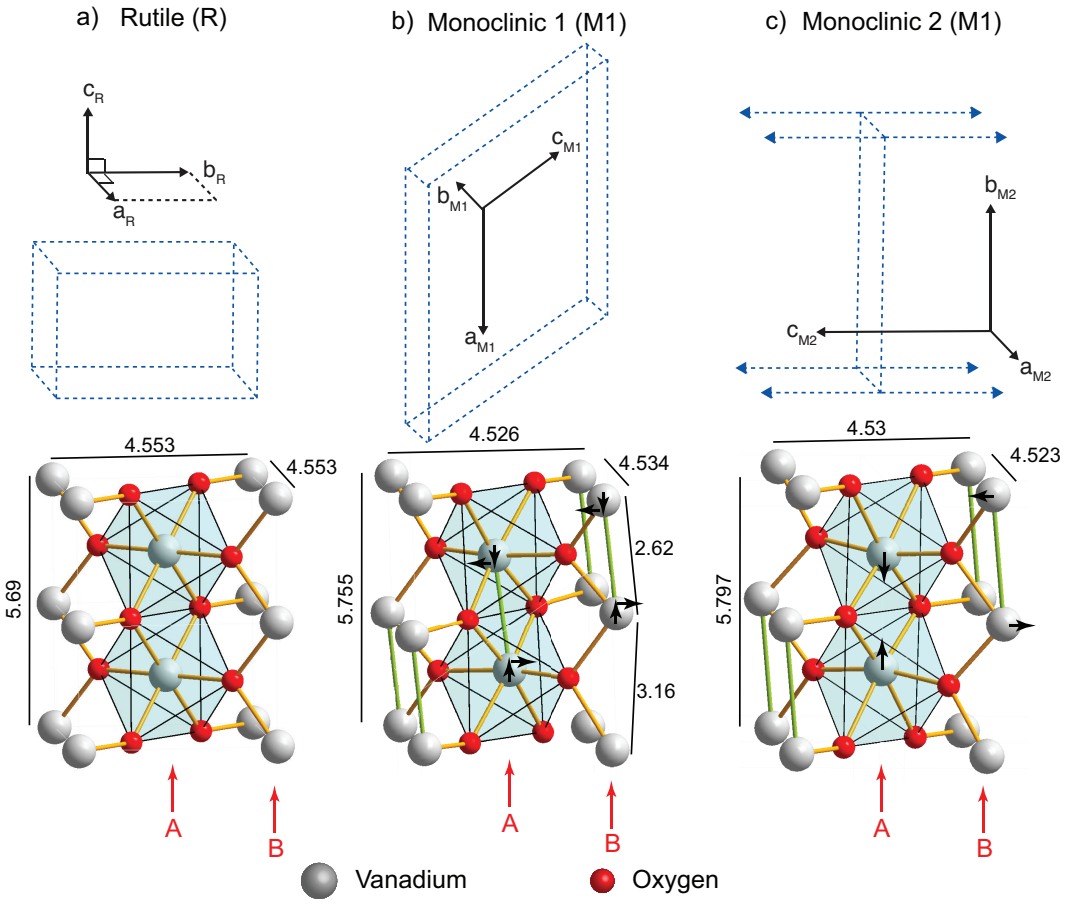

Figure 6.6: The crystal structures of the primary phases of VO_2 are displayed above with panels representing the a) metallic/tetragonal-rutile (R) phase, b) the semiconducting/monoclinic (M1) phase, and c) the semiconducting/monoclinic (M2) phase. The directions of the lattice vectors and the shape of the unit cell are given in the first row of panels, while a visualization of the crystal lattice is provided in the second row. The vanadium atom chain sub-lattices A and B are denoted by the red vertical arrows. The distortion motion from the rutile crystal structure to the M1 and M2 phases is represented by the black arrows for each of the respective insulating phases.

structure first through a pairing of vanadium atoms along the c_R axis and second from a characteristic in-plane displacement of the vanadium atoms which alternates along the c_R and a_R axes.

Fig. 6.6b) displays the M1 crystal structure with the green bonds between the vanadium lattice sites indicating the V-V pairing distortion and the black arrows representing the in-plane displacement on the two marked sub-lattices. Note that pairing and displacement of the vanadium atoms results in two distinct V-V separation distances of $\simeq 2.62$ and $\simeq 3.16$.

The basis vectors for the M1 unit cell symmetry are displayed in the upper panel of Fig. 6.6b). The approximate relationship of the basis vectors of the M1 phase to those of the rutile phase is given through the following lattice transformation,

$$\begin{pmatrix} \mathrm{a} \\ \mathrm{b} \\ \mathrm{c} \end{pmatrix}_{\mathrm{M1}} = \begin{pmatrix} 0 & 0 & -2 \\ -1 & 0 & 0 \\ 0 & 1 & 1 \end{pmatrix} \begin{pmatrix} \mathrm{a} \\ \mathrm{b} \\ \mathrm{c} \end{pmatrix}_{\mathrm{R.}} \tag{6.2}$$

In addition, the lattice constants of the M1 phase as compared to R are shorter by $\approx 0.6\%$ along the $\mathrm{a_R}$ axis, shorter by $\approx 0.4\%$ along the $\mathrm{b_R}$ axis, and longer by $\approx 1.0\%$ along the $\mathrm{c_R}$ axis [247, 255]. This results in a modification of the average unit cell volume from the R phase of -0.044% [247].

The monoclinic 2 phase (M2):

As shown in Fig. 6.5, the monoclinic M2 insulating phase of VO_2 occur at temperatures below T_{MIT} at elevated uniaxial stress along the $[110]_R$ direction [254] or through doping of Cr [246] or Al [259]. The crystal structure of the M2 occurs with a crystal symmetry of $C2/m$ (C_{2h}^3, No.12) [246].

The primary structural distinction of the M2 phase from that of the M1 phase is related to the two vanadium site sub-lattices. In the M1 crystal structure, the vanadium atoms in both sub-lattices undergo the pairing and in-plane displacement distortions. In contrast, for the M2 crystal structure these distortions do not occur equally for both sub-lattices. As shown in Fig. 6.6c), sub-lattice A pairs but does not show the in-plane zig-zag displacement. Sub-lattice B exhibits in-plane zig-zag displacement but does not exhibit pairing. This

unique distortion for each sub-lattice in V-V distances of $\simeq 2.54$ and $\simeq 3.26$ for sub-lattice A and $\simeq 2.93$ for sub-lattice B.

The basis vectors for the M2 unit cell symmetry are displayed in the upper panel of Fig. 6.6b). The approximate relationship of the basis vectors of the M2 phase to those of the rutile phase is given through the following lattice transformation. Note however that these basis vectors are dependent on the definition of the orientation of the crystal lattice and may change depending on the definition [256, 260]

$$\begin{pmatrix} \mathrm{a} \\ \mathrm{b} \\ \mathrm{c} \end{pmatrix}_{\mathrm{M2}} = \begin{pmatrix} 1 & 0 & 0 \\ 0 & 0 & 2 \\ 0 & -2 & 0 \end{pmatrix} \begin{pmatrix} \mathrm{a} \\ \mathrm{b} \\ \mathrm{c} \end{pmatrix}_{\mathrm{R.}} \tag{6.3}$$

In addition, the lattice constants of the M2 phase as compared to R are shorter by $\approx 0.4\%$ along the $\mathrm{a_R}$ axis, shorter by $\approx 0.7\%$ along the $\mathrm{b_R}$ axis, and longer by $\approx 1.7\%$ along the $\mathrm{c_R}$ axis [246, 247, 255]. This results in a modification of the average unit cell volume from the R phase of 0.6% [246].

Recent studies have identified the M2 phase via X-ray diffraction in ensembles of VO_2 single crystals [261] and via Raman spectroscopy in single surface bound/clamped crystals [262]. However, details of the nanoscale domain formation and phase behavior of the M1, M2, and R phases, together with their complex dependence on stress and temperature within these micro-crystallites are not yet fully understood. The results of our *s*-SNOM characterization of these structures will be discussed in section 6.4 of this chapter.

The triclinic phase (T):

The triclinic phase (T) has been found to be a transitional phase between the M1 and M2 insulating phases. The structure of this phase in moving from M2 to M1 corresponds with the progressive dimerization of sub-lattice B and a progressive tilting of sub-lattice A. These two gradual distortions leads to the equivalency of sub-lattice A and B with the vanadium atoms chains in the c_R direction in both sub-lattices being both dimerized and tilted.

6.3.2 Details of the band structure of VO_2.

Details of the band structure of VO_2 are important to the description of the correlated electronic effects in the material. A band structure illustration of the energy bands of VO_2 is displayed in Fig. 6.7 with the orientation of the $3d$ orbitals with respect to the unit cell of the rutile crystal structure displayed by panel a). Within the crystal lattice the fivefold degenerate d levels of an isolated V^{4+} ion are split by the crystal field. Here, the octahedral field of the six oxygen atoms provides a splitting in the a double degenerate upper state of e_g symmetry (d_{z^2} and $d_{x^2-y^2}$) and a triply degenerate lower state of t_{2g} symmetry (d_{xy}, d_{xz}, and d_{yz}) [249].

According to the band model proposed by Goodenough et al in ref [249], the $d_{x^2-y^2}$ lies in the plane of the four oxygens in the oxygen octahedral and lobes oriented towards the nearest vanadium atom neighbor in the c_R direction. It is this orbital which allows for V-V bonding along the c_R axis forming what is denoted as the $d_{\|}$ band. This $d_{\|}$, along with a π^* band (formed through the mixing of the d_{xz}, and d_{yz} states with the $2p$ oxygen orbitals) lie near the Fermi level of the metallic state as is shown by the band structure in Fig. 6.7b).

Under the band-structure description, the transition from the metallic to the insulating state is reflected in the band structure through two effects. First, the pairing of vanadium atoms along the c_R axis breaks the degeneracy of the $d_{\|}$ band resulting in the formation of bonding and anti-bonding orbital states. Secondly, the distortion results in a slight elevation of the π^* bands above the Fermi energy through the hybridization of the $3d-2p$ orbitals. These band structure modifications leave the lower half of the $d_{||}$ band full and below the Fermi energy.

6.3.3 The question of the mechanism of the metal-insulator transition in VO_2.

Since its discovery, the question of what the fundamental mechanism of the strong MIT in VO_2 has been a point of much experimental and theoretical interest and debate. The primary point of interest lies in whether the essential character of the insulating state is attributable to a Peierls type mechanism or a Mott-Hubbard type electron-electron interaction effect. In its basic form, the Peierls-type mechanism attributes the opening of the

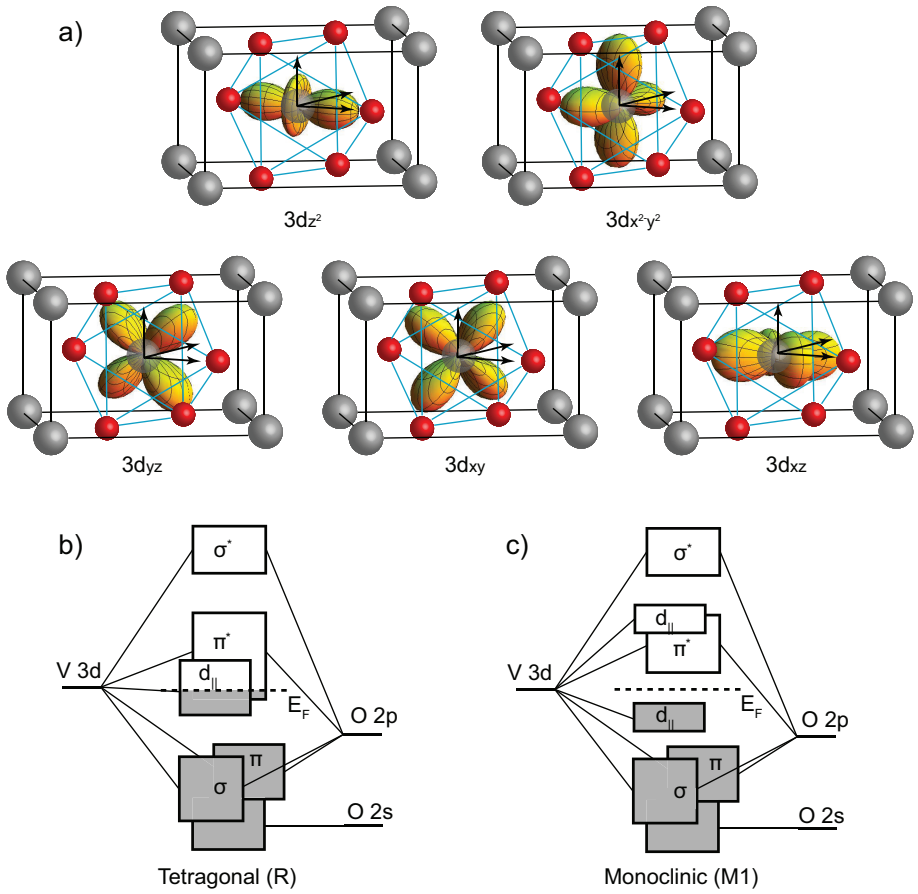

Figure 6.7: The relevant orientation of the $3d$ orbitals with respect to the rutile crystal structure is displayed in panel a). Panels b) and c) display the band-structure for the metallic/tetragonal (R) and insulating/monclinic (M1) crystal structures as derived by Goodenough et al. in ref[[249]]

bandgap in VO_2 to the pairing and tilting distortions of the crystal lattice between the insulating and metallic phases [249, 251, 252]. While band theory calculations correctly predict the upshifting of the $d_{\|}$ band in the transition from the insulating to the metallic state, they often underestimate the size of the gap [249] or even predict a semi-metallic state [256]. In the Mott description, the metal-insulator and structural transition are viewed as coupled and is attributed to the presence of strong electron-electron interactions [193, 250, 253].

6.3.4 VO_2 micro-crystals.

Due to changes in the lattice parameters associated with the MIT, bulk crystals suffer from strain-induced degradation in repeated cycling across T_{MIT} [263]. For related reasons, the MIT in polycrystalline VO_2 thin films is broadened over a wider temperature range [264–266] than in single crystals [244] as a result of a highly inhomogeneous macroscopic material response [267, 268] possibly the result of inevitable nonuniform local stress. This makes the interpretation of macroscopic measurements on polycrystalline samples difficult and calls for investigations of the properties of individual single crystals. The study of individual small VO_2 single crystals avoids averaging over an inhomogeneous ensemble [261] and eliminates the granular structure of polycrystalline films [267, 268] providing access to the correlation of the MIT with intrinsic crystallographic properties as well as the influence of stress (see Fig. 6.8).

In the investigations discussed below, we have characterized the MIT of small individual VO_2 crystals bound to an oxidized Si substrate. These micron-sized crystals are highly resistant to degradation on thermal cycling [229, 270, 271]. It has previously been shown that the substrate-induced stress from the elastic misfit in the fused crystal/substrate system results in the formation of periodic metallic and insulating domains during the MIT [229, 270]. The study of this system should provide important information relevant for the interpretation of measurements on disordered polycrystalline films.

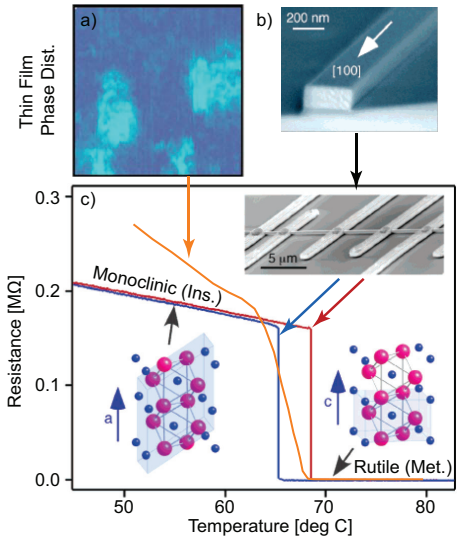

Figure 6.8: The conductivity (c) related to the MIT in VO_2 thin films and single crystal micro-beams are contrasted above using data from refs [269] and [229] respectively. Polycrystalline VO_2 thin films exhibit inhomogeneities and a percolative MIT transition (a) in contrast with free-standing single VO_2 micro-crystals (b) with a sudden first-order phase transition.

6.3.5 Micro-crystal synthesis.

The VO_2 crystals are grown by vapor phase transport as described previously [229, 272]. VO_2 (Sigma-Aldrich, $\geq 99.99\%$) powder placed upstream from an oxidized silicon substrate is heated to $\sim$ 1275°K in a tube furnace with 20 mbar of argon carrier gas for 30 min. The resulting single crystals that grow on the substrate have roughly rectangular cross-sections with thickness in the range of 25 to 200 nm, widths between 50 nm and several micrometers, and lengths up to hundreds of micrometers. As known from X-ray diffraction [272] and confirmed by our Raman measurements, the longitudinal axis corresponds to the $[100]_{M1} = [001]_R$ crystallographic c-axis direction of the metallic R phase.

6.3.6 Phase separation via domain formation on VO_2 micro-crystals.

Phase separation phenomena via the formation of micron-scale alternating metallic and insulating domains in these surface-adhered crystals, as readily observed by far-field microscopy,

involves the interplay of the mismatch of the thermal expansion coefficients between VO_2 and the substrate, the crystal volume change associated with the MIT, the free energies of the respective phases, and the energy associated with domain wall formation [229, 273].

As stated in the previous section, the microcrystals are grown at high temperatures ($\sim 1275°$K) in a tube furnace bonded to the surface substrate. As the system temperature is reduced the crystals experience tensile stress due to the higher thermal expansion coefficient of VO_2 compared with the Si/SiO_2 substrate. This stress is expected to be larger along the long axis of the crystal (c_R axis) due to the larger thermal expansion coefficient in the c_R direction [247].

Cooling from the high temperature metallic phase to the low temperature insulating phases, this tensile stress promotes the appearance of periodic insulating domains at temperatures above T_{MIT}, whose formation reduces the average stress along the crystal as their lattice constants are larger in the c_R direction compared to the R phase (6.6) [229].

This periodic domain formation can be qualitatively described by modeling the total energy E per unit length of the beam as [274]

$$E[\lambda] = \frac{\lambda \varepsilon_{mf}}{\pi^3} \sum_{j=0}^{\infty} \frac{1 - \exp[-2(2j+1)\pi t/\lambda]}{(2j+1)^3} + \frac{\gamma t}{\lambda} + \frac{(f_M + f_I)t}{2}. \tag{6.4}$$

Here, λ is the spatial period of the domain pattern, while $\varepsilon_{mf} = \left(\frac{Y(\Delta c/c)^2}{2(1-\nu^2)}\right)$ is the volume density of the elastic misfit energy. The quantity Y represents the Young's modulus, $\Delta c/c \simeq 0.011$ the elongation difference in the c_R direction between the insulating and metallic phase, ν the Poisson ratio, γ the domain wall energy per unit domain-wall area, and f_I and f_M the the free energy densities of the M and I phases respectively. With knowledge of the wire thickness, minimization of the energy may be modeled through the formation of periodic insulating and metallic domains [229].

Upon further cooling, the insulating domains grow in size until the metallic phase has completely disappeared, at which point the axial stress has become compressive (see analysis below). Micro-crystals released from the substrate exhibit no domain formation converting entirely to the insulating or metallic phase near T_{MIT} demonstrating that the phase separation is primarily induced via strain.

6.3.7 Raman analysis of crystallite phase.

Raman scattering experiments for phase identification are performed using a home-built micro-Raman setup in an epi-illumination and detection geometry using a NA = 0.8 objective (Olympus, 50x). For illumination we use a continuous wave HeNe laser ($\lambda = 632.8$ nm) with incident power of <0.01 mW to minimize sample heating. The scattered light is filtered with a long-pass filter with a cutoff corresponding to a Raman shift of $\sim$160 cm^{-1} and detected with an imaging spectrograph with a N_2(l)-cooled CCD (Acton Research).

Due to its symmetry group, the M1 phase is characterized by 18 Raman active modes with $9A_g$ and $9B_g$ modes [275]. Similarly, the M2 phase also exhibits 18 Raman active modes with a slightly different distribution with $10A_g$ and $8B_g$ modes [276]. The M1 and M2 Raman spectra differ primarily in shifts of the 607 cm^{-1} and 189 cm^{-1} M1 phonon frequencies to higher energies, the decrease of the 441 cm^{-1} mode frequency, and the splitting of the 221 cm^{-1} M1 mode. This, together with the spectrum of the R phase which is dominated by a featureless luminescence [277,278], allows for the unambiguous distinction between the M1, M2, and R phases.

Our group has characterized the uniaxial stress-temperature phase diagram for VO_2 by utilizing Raman spectroscopy to determine the insulating phase of VO_2 micro-crystals on bendable polycarbonate substrates. The characterization of the strain-phase relationship for VO_2 is vital, as the nature of the observed phase separation for substrate bound VO_2 micro-crystals is associated with the external stress applied by the substrate.

Fig. 6.9a) displays the characterization performed by Atkin et al. in our group on VO_2 micro-crystals attached to a bendable polycarbonate substrate [279]. Here, the amount of external strain on the crystallite may be controlled by adjusting the buckling of the substrate to which the micro-crystal is attached [1]. This control allows for all three insulating phases (M1, T, and M2) to be induced on a single micro-crystal for varying levels of strain. Fig. 6.9b) displays the characteristic Raman spectra of each of these phases while Fig. 6.9c) shows the fine differences between the three phases as evidenced by the $\omega_0 \simeq 600$ cm^{-1}

[1] Unlike the substrate bound micro-crystals, for the study of micro-crystals on bendable substrates the VO_2 micro-crystals are glued at their ends to the bendable polycarbonate surface.

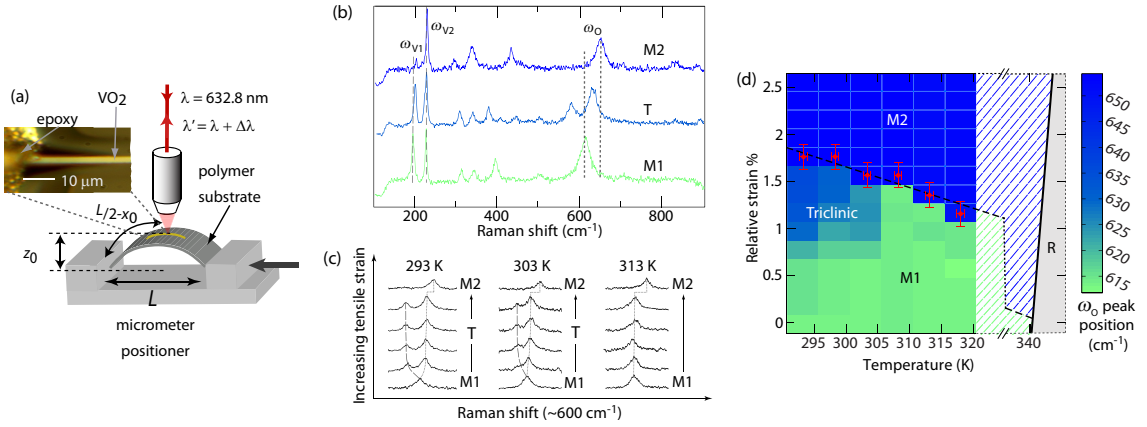

Figure 6.9: The panels above represents the experimental setup and data collected by Atkin et al. [279]. Panel a) displays the experimental configuration in which a VO_2 micro-crystal glued to a flexible polymer substrate. This micro-crystal is stressed via buckling up or down of the substrate, which is controlled by a micrometer stage. Panel b) shows examples of the characteristic M1,T, and M2 Raman spectra observed. Panel c) displays the shifting of related to the Raman mode located at ~ 600 cm^{-1} relating the intrinsic differences between the three insulating phases. Panel d) relates the uniaxial strain-temperature phase diagram of the insulating phases of VO_2 represented via the shift in peak position of the ω_0 phonon mode denoted in panel b).

peak. The resulting uniaxial strain-temperature phase diagram is displayed in Fig. 6.9d).

Fig. 6.10c) shows room temperature Raman spectra identifying free standing VO_2 crystals protruding from the edge of the substrate wafer to be in the M1 and M2 insulating phases [262,276–278,280]. We were also able to obtain the M2 phase for certain freestanding crystals, induced as a metastable state by the micron-size laser focus using slightly higher illumination intensities[2].

6.4 s-SNOM characterization of the metal-insulator transition in substrate bound VO_2 crystallites.

6.4.1 s-SNOM experimental details.

In order to investigate the fine spatial details of the phase separation on VO_2 micro-crystals as they are heated through the MIT, we implement high resolution s-SNOM mapping of the phase transition. Here, the IR *s*-SNOM experimental setup, as shown schematically in Fig. 6.10a), is based on a modified atomic force microscope (AFM, CP-Research, Veeco Inc.). A CO_2 laser with wavelength $\lambda \simeq 10.6$ μm is focused onto a Pt-coated AFM probe (Nanosensors, ATEC) with a Cassegrain objective (NA = 0.5) at an angle of 65° with respect to the surface normal (elliptical focus size of ≈ 30 μm in width, incident power $\simeq 5$ mW). The incident polarization is primarily oriented parallel with respect to the tip axis (6.10a). The tip-scattered near-field response is detected by a mercury-cadmium-telluride (MCT) detector (Kolmar, Model KLD-0.25/DC/11.5) and discriminated against the far-field background via lock-in detection on the second-harmonic of the cantilever dither oscillation frequency [46, 101].

Related with the large changes in DC conductivity, VO_2 also exhibits large changes in the its optical properties (permittivity, optical conductivity, reflectivity, ect.) [281–283] Optical excitation in the 6-12 μm mid-IR range, i.e., well above the optical phonon energies and below the interband transition, allows for optimal contrast between the insulating and metallic phases of the VO_2 [281, 283]. The image contrast due to the optical

[2]While the characteristic Raman peaks observed here agree well with previous measurements [276], the exact mechanism behind the metastable stabilization of these freestanding crystals which likely involves the localized heating/strain associated with the laser focus is difficult to characterize.

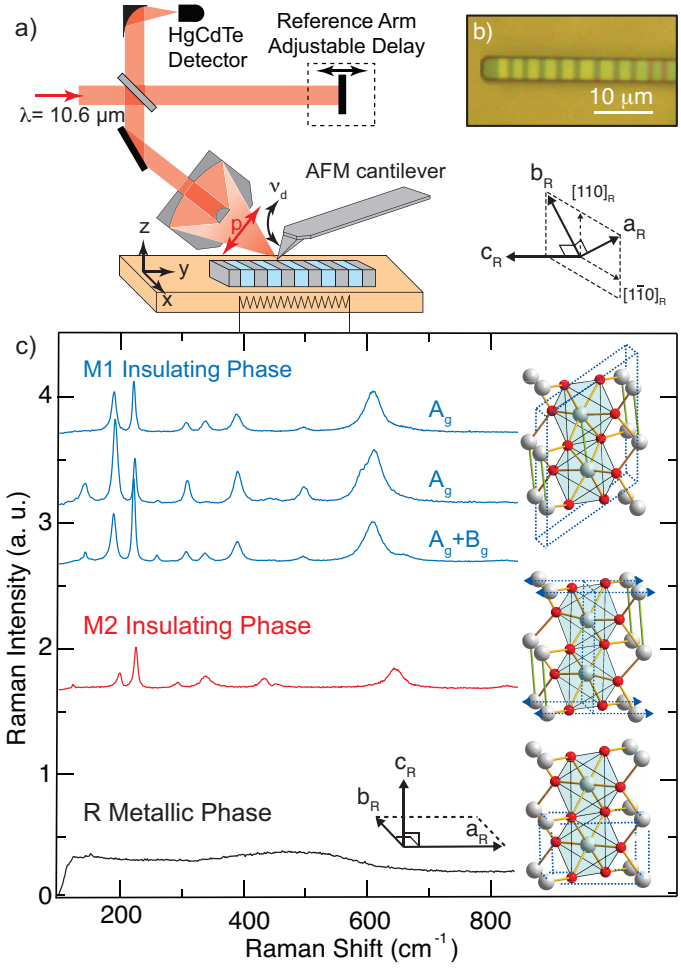

Figure 6.10: Schematic of the IR *s*-SNOM experiment (a) for characterization of domain formation of substrate bound VO_2 crystals (b). Raman spectra from freestanding VO_2 crystals (c) with lattice representations of the M1, M2, and R crystal structures centered around oxygen octahedra oriented along the $[1\bar{1}0]$ direction. The three Raman spectra for the M1 phase (top to bottom) were taken for illumination/detection polarization with respect to the longitudinal (c_R) axis of the crystal of parallel/parallel, perpendicular/perpendicular, and parallel/unpolarized yielding the A_g modes for the first two cases and a superposition of the A_g and B_g modes for unpolarized detection.

dipole-dipole coupling between tip and sample (as discussed in Chapter 3, Section 3.5) is determined by the local spatially varying dielectric function of the surface. Regions of the metallic phase, with comparatively large IR optical conductivity, provide a higher effective tip-sample polarizablility and thus a higher IR-*s*-SNOM signal compared to the dielectric insulating phases [15, 46, 284]. The typically observed *s*-SNOM spatial resolution of 10-20 nm is conventionally determined by the radius of curvature of the AFM tip [46].

Our room temperature Raman measurements of individual crystals bound to the substrate identify every crystal in a given macroscopic sample region as seemingly being in the M1, M2, or T insulating phase. It is interesting to note here, that the Raman peak shifts associated with the insulating phase are less clearly defined for the substrate bound rods as a result of the stress induced by the substrate. Most samples exhibited some degree of peak shifting and broadening from the ideal spectra observed in Fig. 6.10. We have found that deviations are typically associated with the triclinic phase [279].

In the following discussions on substrate bound rods we typically identify the phase as either M1 or M2. While a particular spectrum may not completely resemble a specific phase, the identification stems from the proximity of a given spectrum to either the M1 or the M2 phase or a clear mixture thereof. Even for substrate bound micro-crystals in which we observe topographic variations associated with the twinning of the crystal in the M2 phase (see discussion in following section) [285, 286], we still measure a Raman spectrum which does not perfectly match the M2 phase of non-substrate bound crystallite.

Lastly, crystals in M2 at room temperature were found to relax into the M1 phase after loosening from the surface by a buffered-oxide etch. This is indicative of the dominant role of stress in the phase behavior, although additional factors such as oxygen deficiency from the growth process cannot be completely ruled out.

6.5 Results of s-SNOM characterization.

Fig. 6.11 shows topography a) and simultaneously recorded *s*-SNOM data (b-d) following a VO_2 crystal initially identified to be in the M1 phase at room-temperature through the MIT. Such crystals convert from the low-temperature fully insulating state (b) through the sudden appearance of a first metallic domain (Fig. 6.11c), Fig. 6.13a: 341 K), to a roughly

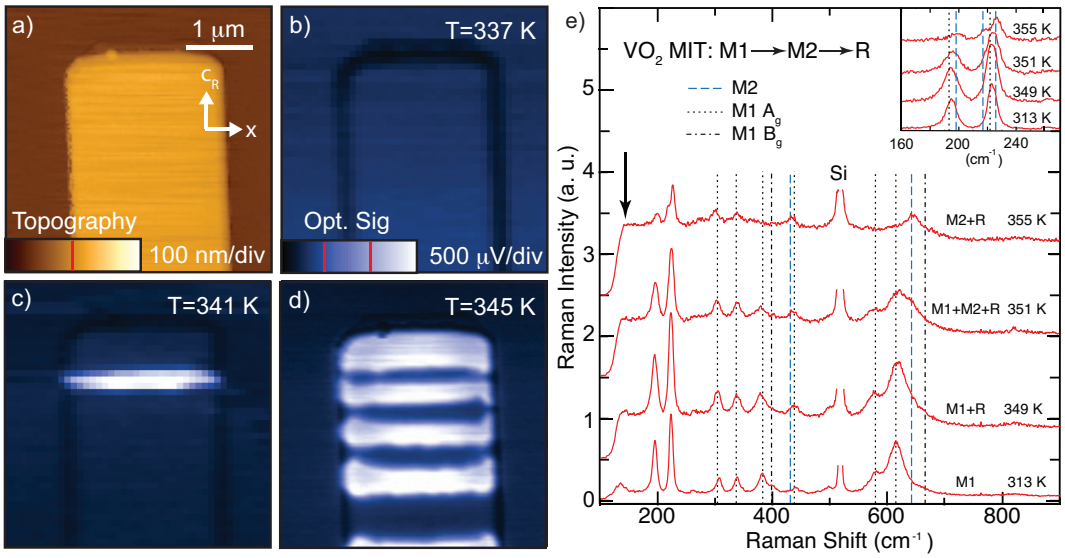

Figure 6.11: *s*-SNOM images (b-d) with corresponding topography (a) of a VO_2 crystal (h=35 nm) initially in the M1 insulating phase, and its metallic/insulating domain formation (c, d) as the crystal is heated through the MIT. The phases of the insulating domains are identified by Raman measurements (e) finding M1 + M2 + R (351 K) and M2 + R (355 K) intermediate phase coexistence regimes.

periodic set of insulating and metallic domains (Fig. 6.11d), Fig. 6.13a: 345 K), to the fully metallic state at temperatures of 370 - 390 K (Fig. 6.13a: $T > 370$ K).

The initial appearance of metallic domains is reflected in the Raman spectra by a sharp rise in the luminescence background (Fig. 6.11e), arrow). Up to $\sim$ 350 K the insulating domains of the regular domain pattern formed remain purely M1 phase. As the temperature is increased further and the insulating domains begin to shrink in size a conversion of M1 to M2 is observed as seen from the appearance of the characteristic M2 Raman modes (Fig. 6.11e), 351 K spectrum). Within a narrow temperature range of $\sim$ 5 K all insulating domains appear to shift to convert to M2 phase (Fig. 6.11e), 355 K) without a significant change in the total fraction of R. This M1$\rightarrow$M2 conversion occurs around 30 K below the temperature where the fully metallic state is reached.

Fig. 6.13a) shows the associated domain formation and spatial evolution in a repeated *s*-

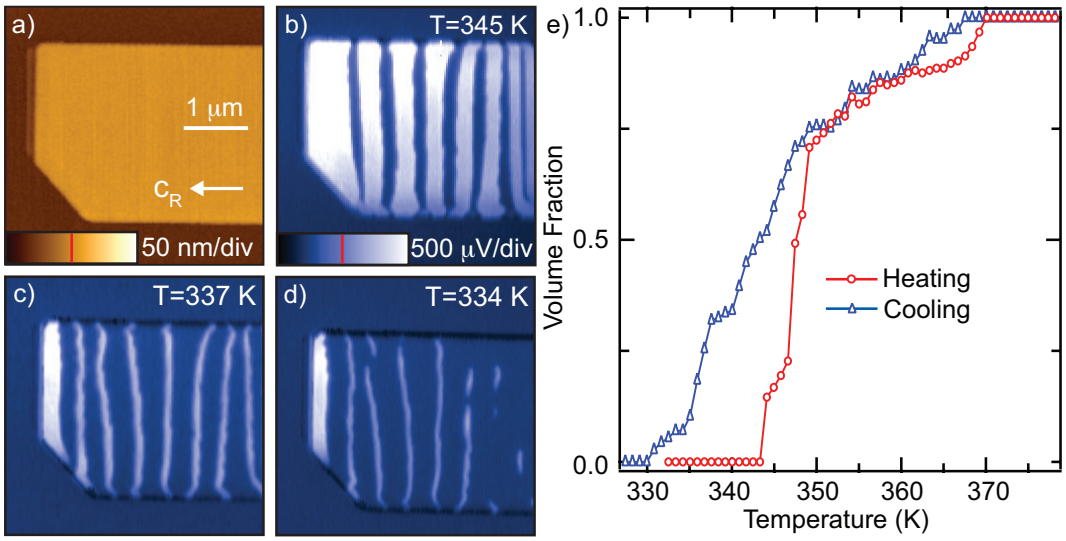

Figure 6.12: *s*-SNOM images (b-d) with corresponding topography (a) of a VO_2 crystal (h=25 nm) being cooled through the MIT. Periodic metallic and insulating domains exist slightly above T_{MIT} (b). As temperature is lowered, the size of the metallic domains decreases (c) resulting in the eventual break up and dissipation of metallic domains (d).

SNOM line-scan along the longitudinal (c_{R}) axis down the center of the crystal in Fig. 6.11a). The sudden appearance of the first metallic domain in the scan region is followed by a splitting, rearrangement, and subsequent formation of the alternating domain pattern indicating the intermediate superheating and discontinuous release of stress energy. With the enhanced spatial resolution of $\lesssim 30$ nm provided by *s*-SNOM, it can be seen that thin insulating domains persist up to $T > 375$ K. The increase in *s*-SNOM noise with increasing temperature is the result of tip/cantilever heating and related jitter in the force feedback.

The corresponding process of cooling through the MIT is spatially illustrated in Fig. 6.12. Here, cooling from the fully metallic phase at higher temperatures (b) *s*-SNOM measurements reveal the formation and coexistence of a well-defined alternating set of insulating and metallic domains. With cooling below T_{MIT}, the growth of insulating domains results in a mostly insulating crystal with metallic domains with more irregular domain boundaries (c). Further cooling results in the inevitable breakup of metallic domains (d) with the metallic stripes eventually breaking into smaller islands of metallic phase.

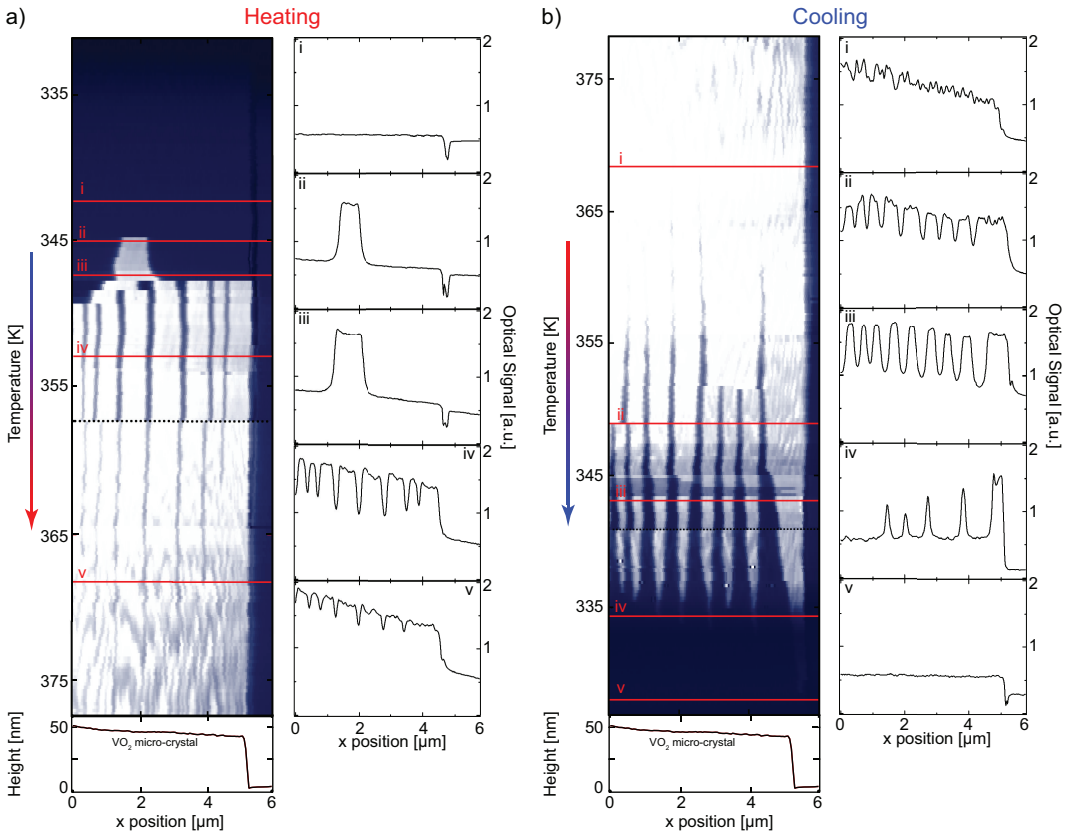

Figure 6.13: The dynamics of domain formation on an individual micro-crystal as a function of heating and cooling is pictured above. Here, the data pictured corresponds to a 6 μm long line scan down the center of the micro-crystal shown in Fig. 6.11a) as the surface temperature is slowly increased (a) and decreased (b). The line traces (i-v) show exhibit the optical contrast above the micro-crystal at various points along the MIT process.

The entirety of the cooling process is illustrated in Fig. 6.13b) which represents the corresponding cooling ramp to the *s*-SNOM heating ramp consisting of repeated line scans displayed of the micro-crystal displayed in Fig. 6.11. Here, topography of a line-scan down the center of a VO_2 crystal (e) which was found to be in the M1 phase at room temperature is correlated with IR *s*-SNOM signal over a wide temperature range. For this crystal the nucleation of insulating domains is observed between 365-370 K. The resulting growth of insulating domains through further cooling results in the eventual disappearance of metallic domains at approximately 330 K, The hysteresis curve of the fraction of metallic domains

for both the heating and cooling curves over the nearly 6 μm section of the crystal observed is given in Fig. 6.12e).

In contrast to the sudden formation of metallic domains during the heating cycle, upon cooling the MIT is a gradual process with a continuous shrinking of the metallic domains. The final disappearance of the last metallic domains beyond *s*-SNOM sensitivity and resolution of width as small as 50 nm is observed at temperatures as low as $T = 330$ K indicating a pronounced hysteresis at the low temperature side of the MIT. Unfortunately, in IR *s*-SNOM measurements it is difficult to distinguish between the M1 and M2 phases which appear to have only small differences in their dielectric properties in the infrared [3]. However, comparison of Raman and high spatial resolution *s*-SNOM results indicates that the M1→M2 transition occurs at a stage of the MIT where between 70% and 85% of the crystal is in R phase.

Fig. 6.14 shows Raman and *s*-SNOM results for crystals that are initially fully in the M2 phase at room temperature. On warming the first emergence of R domains is observed near 360 K, i.e., at temperatures higher than that found for crystals initially in the M1 phase at room temperature. As the temperature increases the periodic domain formation and their spatial evolution proceeds in a qualitatively similar fashion to the case above. However, as the Raman spectra indicate, the insulating phase in these crystals remains purely M2 throughout the entire transition and over the entire temperature range investigated with no trace of M1 appearing. With temperatures as high as 410 K, the purely metallic phase is found to be complete at temperatures higher (30 K) than in crystals originally in M1. Interestingly, at low temperatures before the appearance of the first metallic domains, two additional Raman modes at 362 cm^{-1} and 568 cm^{-1} can be discerned that are not attributable to either the M1 or M2 phases and whose amplitude decreases with temperature. These resonances may be due to stress or other interfacial effects.

Only for crystals initially in the M2 phase, an additional weak *s*-SNOM contrast was observed in the insulating phase in the form of periodic striation parallel to c_R (Fig. 6.14b). The contrast is only $\sim 3\%$ of the metal-insulator contrast. These signal variations, with

[3] complementary tip-enhanced Raman scattering (TERS) imaging suffered under the low phonon Raman cross sections of VO_2 [287]

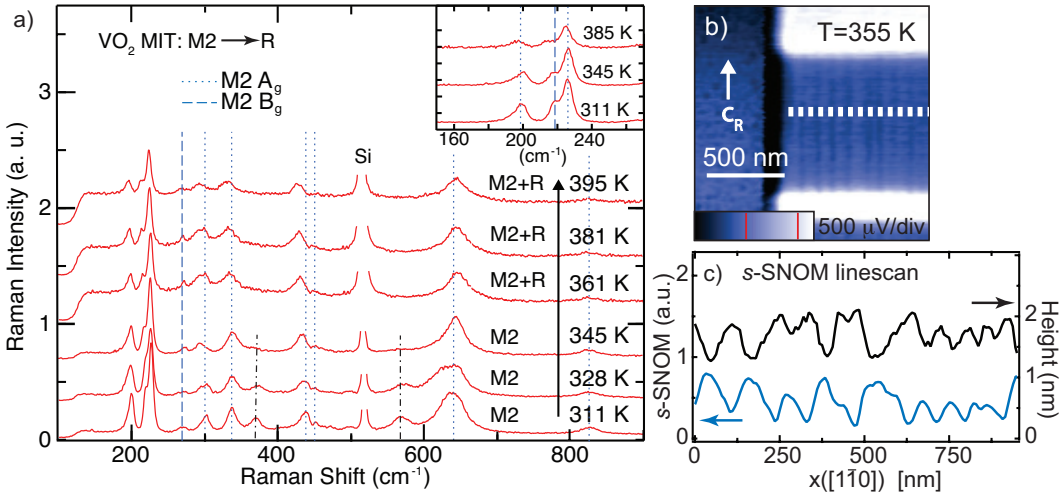

Figure 6.14: Sequence of Raman spectra on heating of a single VO_2 crystal initially in the M2 insulating phase at room temperature (a) with MIT proceeding via a M2 + R phase coexistence only. Periodic metallic domain formation (bright regions) and additional weaker sub-domain contrast pattern in the M2 insulating state (b) due to twinning (see text for details) [285, 286]. *s*-SNOM contrast correlated with $\sim$ 1nm topographic variations (c, line-scan along dashed line in b).

a period of $\approx$ 100 nm, are correlated with slight variations in surface topography of $\approx$ 1 nm (Fig. 6.14c). This observation can be attributed to polysynthetic twinning of the M2 phase of the VO_2 crystals as shown recently by micro X-ray diffraction measurements of strained crystals [271]. The resulting birefringence can give rise to a polarization modulation of the tip-scattered signal and thus slight variations in the *s*-SNOM contrast. The *s*-SNOM/topographic striation is found to be independent of temperature while the crystal remains in the insulating phase with the signal variations disappearing upon conversion to the metallic phase. The modulation pattern reappears after cooling and the emergence of the M2 phase. No change in the characteristic M2 Raman spectral signature associated with this M2 sub-domain patterning is found.

6.6 Model for the stress-domain/phase distribution for the MIT in VO_2 microcrystals.

From the results shown above and similar measurements of VO_2 crystals of different sizes and shapes, we conclude that crystals initially in the M1 phase at room temperature convert to the metallic phase via a sequence of a) formation of periodic metallic domains followed by b) the conversion of the M1 insulating domains into the M2 phase, and finally c) the growth and convergence of the metallic domains into the fully metallic phase of the crystal: $\mathrm{M1} \rightarrow \mathrm{M1} + \mathrm{R} \rightarrow \mathrm{M2} + \mathrm{R} \rightarrow \mathrm{R}$. Those crystals found initially in the M2 phase convert directly via the formation of periodic metallic domains and their gradual growth through heating into the fully metallic state: $\mathrm{M2} \rightarrow \mathrm{M2} + \mathrm{R} \rightarrow \mathrm{R}$.

While the actual three-dimensional stress field within these crystals is complicated and varying throughout the transition, the largest relative change in lattice constants between the three phases occurs along the c_R axis. Metallic stripes are always seen to form perpendicular to this axis even in wide crystals with small aspect ratios. We therefore consider a simple model to describe the phase/domain behavior which assumes the elastic energy to be governed primarily by the axial stress in the c_R direction σ, with σ_{ave} representing a spatial average over the crystal. The source of this axial stress is the strain mismatch δ of the differing constituent phases of the crystal with the substrate. It is important to note, that while σ_{ave} may be close to zero due to the alternating compressive and tensile stress, the respective elastic energy of the for all domains is nonzero.

However, σ_{ave} has physical significance as it is proportional to the net stress applied to the crystal via the substrate. The observation that these stressed VO_2 crystals form domains as they move through the MIT indicates that minimization of the elastic energy of the substrate outweighs internal energy gain within the crystal due to the elastic energy, free energy density, and domain wall formation required to create a periodic set of domains (see Fig. 6.15b). In the fully insulating or metallic state we assume that σ is nearly uniform along the crystal and equal to σ_{ave}. In the coexistence regime during the MIT, σ should vary along the c_R crystal axis as the structure alternates between insulating (more positive/compressive stress) and metallic (more negative/tensile stress) domains. This corresponds to a reduction

of the average stress, and therefore the total elastic energy of the crystal/substrate system.

Fig. 6.15a) shows a graphical representation of the phase and domain evolution of the VO_2 crystal with temperature with the associated average axial stress σ_{ave}. The stress-temperature correlation shown in this figure takes into account the combined knowledge from measurements of the spatial evolution of domains provided by *s*-SNOM, the observation of phase composition yielded by Raman measurements, previous characterization of the crystallographic phases [246, 247], and understanding of sample growth conditions. The solid (dashed) lines represent the behavior of σ_{ave} during cooling (heating).

As a result of the different thermal expansion coefficients ($\alpha_R > \alpha_{\text{Si}}$) during the initial cooling after fusion of the crystal to the substrate, at temperatures slightly above the MIT the crystal experiences tensile stress (Fig. 6.15a: region i, I). This tensile stress may be approximated through estimation of the strain mismatch of the crystal in the R phase, $\delta_R \approx (\alpha_{\text{R}} - \alpha_{\text{Si}}) \cdot (T - T_{\text{g})}$. Here, T_{g} represents the temperature at which the crystal grows on the substrate.

For all crystals (both those in M1 and those in M2 at room temperatures), on cooling towards the transition σ_{ave} can be reduced most effectively by introducing thin M2 domains [4]. This is consistent with the observation that the insulating phase at higher temperatures is initially M2. An associated consequence of the tensile strain is that the first appearance of insulating domains occurs well above T_{MIT}; indeed, we observe the appearance of insulating domains as high as $\simeq$400 K. Upon further cooling, M2 domains grow continuously with decreasing temperature, thus reducing σ_{ave} further (Fig. 6.15a: region ii, II).

For the crystals in the M1 phase at room temperature, on cooling to a temperature of $\sim$ 350 K, at which $\sim$ 25% of the crystal is in the insulating phase, the remaining insulating domains convert from the M2 to M1 phase within a 4-5 K temperature range. *s*-SNOM measurements indicate only a $\sim$ 4% change in the volume fraction of the crystal occupied by the R phase within this temperature window over which the M2$\rightarrow$M1 conversion occurs for typical crystals. This conversion of the insulating regions can be understood in terms of

[4] A fully rigorous treatment of the MIT of substrate bound crystals must account for several energy contributions and the interplay of strain inhomogeneities, domain wall energy, interfacial effects, and the free energy densities of the individual phases.

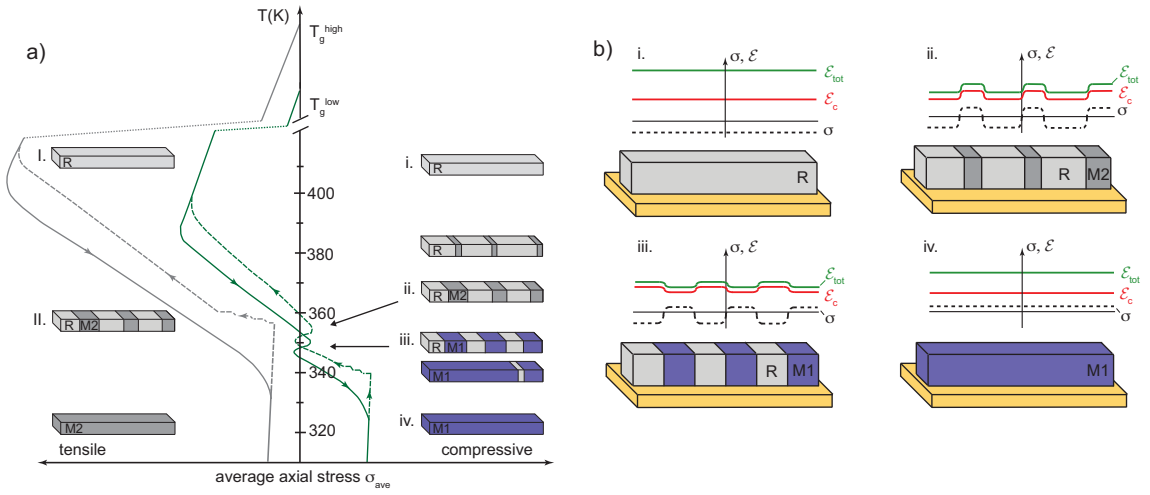

Figure 6.15: Schematic of the MIT domain evolution of VO_2 crystals as a function of temperature and its relationship with the average external axial stress. Dashed/solid lines indicate heating/cooling curves, respectively. Relationship (b) between the domain configuration with stress σ within individual domains (dashed line), the associated elastic energy density of the crystal $\mathcal{E}_c$ (solid red line), and the elastic energy of the crystal/substrate system $\mathcal{E}_{tot}$ for a crystal stabilized in the M1 phase at room temperature at stages i-iv during the MIT.

the continuous growth of the M2 domains, with σ eventually becoming locally compressive. Compressive stress for the M1 phase is consistent with the previously reported compressive stress value of 0.4% [270]. With compressive stress the M1 phase, with its shorter axial lattice constant and lower free energy, becomes more favorable than the M2.

After the complete conversion of M2 to M1, further cooling results in the steady growth of the insulating domains until the fully insulating state is reached (Fig. 6.15a: region iii). The persistence of R domains below the bulk transition temperature is consistent with compressive stress favoring the R phase with its shorter lattice constant. The compressive stress is also revealed by the fact that crystals are found to buckle when released from the substrate for transport devices with their ends fixed by evaporated electrodes [270].

Upon heating (dashed green line) these crystals exhibit the first emergence of R domains near the bulk transition temperature (Fig. 6.11f: 340-350 K). The initial discrete appearance of almost micron-size R domains should result in a step-wise reduction of the average

compressive stress as indicated. The formation of periodic R domains and their gradual widening may make the stress in the adjacent insulator tensile, promoting the conversion of the insulating domains from M1 to M2 at $\sim$ 350 K (Fig. 6.11g: 351,355 K) with a hysteresis of $\sim$ 5 K relative to the cooling case. This conversion is followed by the steady growth of the R domains (Fig. 6.11f: 350-370 K) resulting finally in a fully metallic crystal under tensile stress. The hysteresis observed at the beginning and end of the MIT is asymmetric, with a less than 5 K offset between disappearance and first reappearance of insulating M2 domains at higher temperature, but a $>$ 10 K between the discrete appearance of metallic domains on warming versus the gradual disappearance of metallic domains on cooling.

For a crystal found stabilized in M1 at room temperature, 6.15b illustrates the relationship between the stress experienced by domains of different phase within a crystal with both the elastic energy density of the crystal $\mathcal{E}_c$ and the elastic energy density of the crystal/substrate system $\mathcal{E}_{tot}$ at various stages of the MIT. Here, upon cooling the formation of domains (i$\rightarrow$ii) results in a release of the substrate stress and thus a reduction in $\mathcal{E}_{tot}$. Growth of the insulating domains eventually results in a conversion of insulating M2 domains to M1 in order to lower the stress applied by the substrate (ii$\rightarrow$iii). Finally, further cooling leads to the formation of a fully insulating wire (iii$\rightarrow$iv) under compressive stress as dictated by the substrate. Here again, the substrate related stress results in an overall increase in $\mathcal{E}_{tot}$.

Fig. 6.16a) shows the temperature dependence of the approximate volume fraction of the different phases during heating and cooling (dashed and solid lines, respectively), derived from analysis of the *s*-SNOM images and the Raman phase identification. While the details vary somewhat between different crystals the general behavior is reproducible. The corresponding volume fraction plot for the set of crystals in M2 at room temperature is shown in Fig. 6.16b). For these crystals, the temperature at which the first M2 domains appear is higher compared to crystals stabilized in the M1 phase at room temperature. This suggests that a higher initial tensile stress differentiates these crystals from the M1 crystals. Such higher built in tensile stress for M2 at temperatures slightly above T_{MIT}, with respect to their M1 counterparts, could result from a higher growth/fusing temperature T_{g}. This would be consistent with the observation that upon warming, R domains appear at tem-

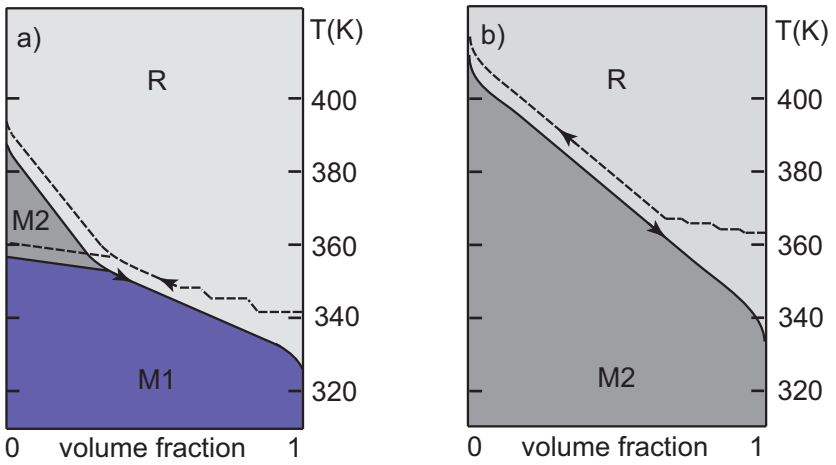

Figure 6.16: Associated temperature dependence of crystal volume fraction in the M1, M2, and R phases for a crystallite initially in the M1 at room-temperature (a). Corresponding diagram for crystals found in the M2 phase at room-temperature (b).

peratures 10-20K higher than T_{MIT} (Fig. 6.14a: up to 361 K). This furthermore fits with our observation that crystals grown further upstream (higher T_{g}) within the temperature gradient in the furnace tend to be in the M2 phase at room temperature. That the details of crystal growth may affect the phase of VO_2 at room temperature underscores the importance of the role of stress in the MIT and is consistent with previous studies which have linked M2 stabilization to small system perturbations [246, 254, 257, 261].

6.7 Conclusions on s-SNOM characterization of the MIT in VO_2 micro-crystals.

Our results offer a cautionary note for interpreting measurements of VO_2 samples in general and polycrystalline thin films in particular. In the latter nanoscale heterogeneities with crystallites of different sizes, individual local stress conditions, and random distribution of the crystallographic orientations obscure the intrinsic properties of the individual phases in macroscopic measurements. Indeed, a stochastic behavior in such films was observed [288], and previous *s*-SNOM studies on polycrystalline films revealed a complex correlation between the MIT and, e.g., film morphology, topography, and grain boundaries [267, 268].

Our work identifies an even more complex combination of multiple nanoscale phase and

domain heterogeneities than previously assumed [229] even in small, perfect single crystals adhering to substrates or to each other, as a result of elastic effects. Not only do we see the expected mixture of metallic and insulating domains, with new morphological details revealed by sensitive high resolution *s*-SNOM probing, but we also observe an unexpected pervasive presence of the M2 insulating phase, and its competition with M1, within single crystals – an observation consistent with the known ready stabilization of M2 by doping and moderate stress [246, 254, 261]. From these results we conclude that M2 should be present over a certain temperature range around the MIT, at least transiently, in polycrystalline thin films, given the unavoidable local stress due to the MIT of individual crystallites, as well as most likely in bulk VO_2 samples. If this conclusion proves correct, the possibility of a transient M2 insulating phase involved in the MIT should be considered for samples with undefined crystallographic orientation. This consideration may apply not only for static measurements like the one performed here, but also for ultrafast measurements where the transition has been found to depend not only on photo-doping but atomic motion of the unit cell as well [289]. We note that although Raman signatures of M2 were not recognized in earlier studies of thin films, their observation would have been difficult due to the obscuring presence of V_2O_5 Raman lines in that case [278].

Studying small single crystals offers the opportunity for a new methodical approach to the MIT in VO_2. In addition to their excellent homogeneous form and resistance to degradation, it is possible to apply a uniform and controlled stress after release from the substrate [270,271]. The combination of nano-optical, ultrafast, and electrical measurements should then allow precise determination of the properties of each of the multiple individual homogeneous phases and their conversion by stress, and clarification of the possibly key role of the intermediate M2 phase [253, 256] as well as other aspects of the mechanism behind the MIT in this archetypal strongly correlated material.

In conclusion, our results underscore the general importance of understanding the implications of any inhomogeneous variation in the local stress distribution on the properties of complex systems with phase transitions with associated lattice changes in general and VO_2 in particular. The insight provided by the combination of different optical spectroscopies with s-SNOM highlights the potential of new nano-optical techniques to isolate and probe

the intrinsic optical response of individual nanoscale domains desired for the characterization of the wide range of correlated electron systems.

6.8 Characterization of the ultrafast photo-induced MIT in VO_2 micro-crystals.

6.8.1 Photo-induced phase transitions.

In section 6.2 of this chapter, the concept of a metal-insulator transition induced by either structural changes to the crystal lattice or changes in the chemical composition was introduced. Yet another means of inducing a phase transition from an insulating to metallic state which further allows for access to the ultrafast dynamics of the phase transition process is via photo-doping using ultrafast (sub-100 fs) intense pulsed laser light. Here, for visible laser pulses whose wavelength is greater than the bandgap energy of the material for most semiconducting materials, light interacts mostly with electrons, photo-exciting them to states across the bandgap and above the Fermi energy.

For the photo-excitation process on insulating/semiconducting materials, at time $t = 0$ the energy of the light pulse pump pulse hits sample and excites electrons into a highly non-equilibrium state of specific momentum. Initially, the momentum distribution of excited carriers is randomized through electron scattering on the $\simeq 10$ fs timescale. Carrier-carrier scattering results in Coulomb thermalization and the formation of a Fermi-Dirac distribution for electrons with a well-defined temperature T_e [290]. The timescale of electron thermalization lies typically in the 10 to 1000 fs range, after which the system ends up in a state where the electrons and the lattice have different temperatures, as described by the two-temperature-model [290].

Energy relaxation subsequently occurs, on the several picosecond timescale as the excess energy from the hot electrons is transferred from the electrons to the lattice by means of electron-phonon scattering [290]. This process results in a phonon distribution of a Bose-Einstein distribution with temperature T_{ph}. Finally, electron-hole recombination occurs on long timescales $\propto 1$ ns, typically through many body processes and radiative recombination [290]. Unlike insulators and semiconductors, whose bandgap is typically larger than most phonon energies, in metals the electron-hole recombination at the Fermi level can occur

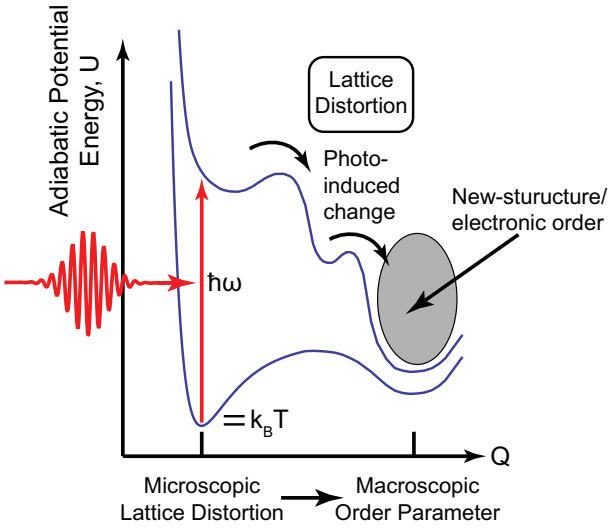

Figure 6.17: Following refs [195, 292] a qualitative model for the process of photo-induced structural phase transitions is depicted above The axes here represent the potential energy of the system and the structural normal coordinate of the system. Photo-excitation from an ultrafast pulse excites carriers in the ground state initiating a structural change which drives an electronic phase transition to a state different from that of the ground-state.

simply via phonon emission [291].

Rather than simply inducing a transient excited state, ultrafast optical excitation can induce in certain cases new quasi-stable material phases [292]. The process by which a system reaches a new macroscopic phase that has electronic/optical/structural properties which are characteristically different that its initial phase through the interaction with pulsed light excitation is known as a photo-induced phase transition [195, 292]. For the case of a photo-induced metal-insulator phase transition, the transition process can occur via several differing mechanisms corresponding the means by which the material in question is initially insulating.

One such transition pathway is a photo-induced structural phase transition. When an electron in an insulating crystal is photo-excited, a local lattice distortion is induced around the site of the localized electron. For a large change in the charge distribution, the resulting distortion causes motion in the crystal lattice surrounding the electrons which can cause

the formation of a new equilibrium position for the excited states. This process is called the lattice relaxation of an optical excitation, and the resultant lattice changes may be referred to as a photo-induced structural change. This process is illustrated schematically in Fig. 6.17.

For materials classified as "Peierls" type insulator, a transition to the metallic state can be induced by removing distortion of the nuclear structure associated with modulation of the charge density in the crystal. As discussed in subsection 6.2.1 a "Peierls" type insulator is one in which a periodic lattice distortion which doubles the unit-cell size results in a reduction of electronic energy and the formation of a band-gap. Here, ultrafast optical excitation induces lattice motion which modifies the structural distortion thus allowing the conduction of electrons [293]. Photo-induced phase transitions of this type may even be induced through the direct coherent excitation of the IR active vibrational modes of the material associated with the structural distortion related to the charge density wave [294].

Materials classified as "Mott" type insulators, those whose insulating character is attributable to electron localization via Coulomb repulsion, can exhibit a photo-induced MIT through simple electron-electron interactions. Similar to the carrier doping of the crystal via chemical doping, ultrafast optical excitation may excite electrons across the bandgap until a critical amount of charge carriers in the valence band is reached. When the critical carrier density is reached, under the Mott-Hubbard Hamiltonian model the band-gap collapses and the system acts as a metal. As the collapse of the band-gap is only dependent on the carrier density within the valence band, this transition may occur on fast timescales, even as the electron and lattice temperatures are reaching equilibrium [292, 295].

6.8.2 Ultrafast characterization of the photo-induced phase transition on single VO_2 microcrystals.

Several previous ultrafast spectroscopic investigations have addressed the MIT in VO_2 using visible [289,296–300], THz [301], and electron diffraction [302] excitation and probe methods. These studies have given insight into the nature of the photo-induced MIT in VO_2 by providing information on the dynamics of the transient response of VO_2 to photo-excitation.

Through observation of the role of the coherent phonon response to optical excitation as well as the transition time necessary to form a metallic state through photo-doping, evidence may be gained as to the specific role of the both lattice and correlated electron effects in the photo-induced MIT transition in VO_2.

Recent studies have demonstrated evidence of lattice structural elements involved in the MIT process through the presence of phonon oscillations after the MIT transition [301], the finding of a 80fs "phonon bottle-neck" in the time necessary to transition from the metallic phase to the insulating state, and the finding of a threshold fluence ($\sim$ 7 mJ/cm^2) for photo-inducing the MIT [289,297] . The observation of this "phonon bottle-neck" was made through the noting that fastest possible transition time for VO_2 is $\simeq$ 80 fs, which correlates with the time necessary for the dimerized/paired V-V chains to tilt in order to allow the formation of a metallic state. This measurement was used as evidence of a structurally driven phase transition mechanism, as although the $d_{\|}$ band was highly depleted it was still viewed as necessary for the vanadium atoms to shift their positions in order to allow the metallic state [297].

It should be noted, however, these previous investigations were carried out on polycrystalline or bulk samples. As discussed in section 6.3.4, these systems suffer from poorly defined crystal orientation and local stress resulting in a percolative phase transition when heated [267]. Without a well defined stress, the nature of the insulating phase for these samples can be complex.

Indeed, most studies only describe the photo-induced phase transition process in terms a transition from the insulating to metallic state without taking into consideration the nature of the insulating phase. The nature of the initial insulating phase of the VO_2 has important implications. As discussed in section 6.3.1, the M2 insulating phase lies structurally between the M1 insulating phase and the metallic R phase. This structural composition implies that the insulating character of the M2 could have more predominant contribution from electron-electron interactions.

As a consequence, for VO_2 it is highly desirable to characterize the transient dynamics of the photo-induced phase transition on system which has a well-defined crystallographic orientation in which the identity of the insulating phase is well know; in these aspects VO_2

micro-crystals represent an ideal system. In the following sections, our preliminary characterization of the transient response of VO_2 micro-crystals to ultrafast optical excitation will be presented and discussed in the context of previous measurements.

6.8.3 Experimental setup for degenerate pump-probe characterization of single VO_2 micro-crystals.

An important consideration in the implementation of pump-probe techniques is the utilization of significantly short pulses with repetition rates high enough to allow for noise reduction but slow enough to allow for the system to recover to is resting state before the arrival of the next excitation pulse. For the photo-induced metal insulator transition, it has been shown that VO_2 does not relax quickly into the insulating state after photo-excitation even after several nanoseconds [302]. For pump-probe measurement of the photo-induced MIT, an ultrafast light source with repetition rates on the several μs timescale are thus highly desirable.

In accordance, for our experiments we utilize ultrafast pulses with a full width half max duration of $\simeq$ 45 fs with an adjustable repetition rate between 50 and 450 kHz which are generated by a Ti:Sapph. regenerative amplifier (KM Labs, Wyvern). The information of the pulse-shape and duration are fully measured using second-harmonic generation Frequency Resolved Optical Gating (FROG) characterization.

A beam-splitter divides each ultrafast pulse into a pump and probe pulse with a power ratio of 19:1 respectively. Both pulses are focused onto a single substrate bound VO_2 micro-crystal with pump and probe focal diameters of 25 and 15 μm respectively. The parabolic mirror used to focus the pump and probe pulses onto the micro-crystal is also used to collect the reflected components of both beams. Using spatial and polarization filtering, the reflected component of the probe pulse is separated from the pump pulse and focused onto a Si photodiode.

By chopping the pump and probe beams at mutually prime frequencies ω_{pump} and ω_{probe} the both the total reflectivity and the pump induced change in reflectivity may be measured. This is achieved through the implementation of lock-in filtering. Applying lock-in filtering

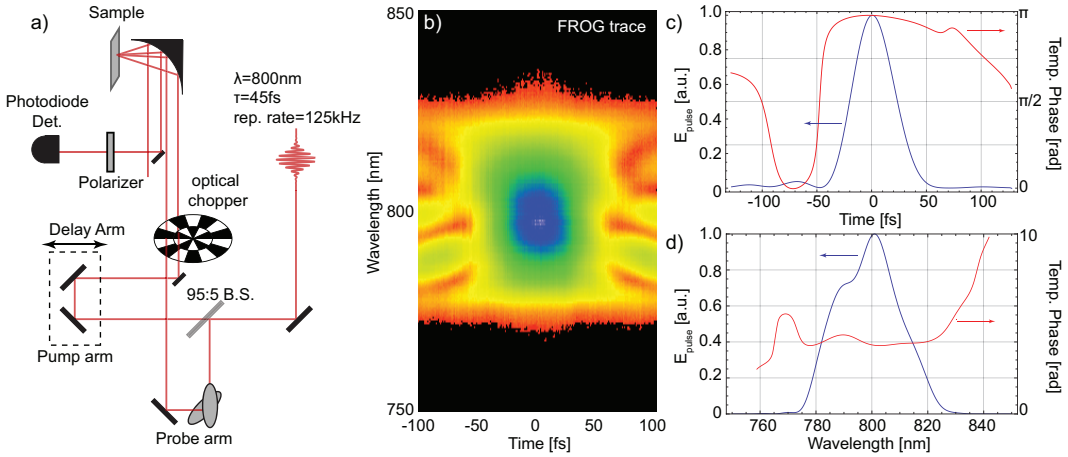

Figure 6.18: a) beam path diagram for degenerate pump-probe microscopy. b) the frequency resolved optical gating (FROG) trace measurement for the ultrafast ($\sim$ 45 fs) pulses generated by the Wyvern Ti:Sapph. regenerative amplifier. Panels c) and d) display the FROG reconstructions of the electric field and phase in both the temporal and spectral domains respectively.

on ω_{probe} the magnitude of the reflected light $R[t]$ is measured. By implementing lock-in filtering to detect the component of the signal at the difference frequency $\omega_{\text{det}} = \omega_{\text{pump}} - \omega_{\text{probe}}$ the pump-induced change in the reflectivity can be measured. In the experiments shown here, the pump and probe frequencies are $\omega_{\text{pump}} = 505$ and $\omega_{\text{probe}} = 707$. Thus lock-in filtering of the signal at $\omega_{\text{det}} = 202$ provides the pump-induced change in the reflectivity.

6.8.4 Reconstruction of the response function of a system for pump-probe characterization.

A response function for a system defines the relationship between a system input signal $S[t]$ and measured output observable $G[t]$ as a function of the present (t) and past (τ) values of the input. The relationship between signal input and output observable for a linear response function $X[t - t']$ can be expressed as

$$G[t] = \int_{-\infty}^{t} X[t - \tau]S[\tau]d\tau. \tag{6.5}$$

This relates to pump-probe characterization as the measured quantity G, whether the

transient reflectivity or transmission, over all t represents the convolution of the response function of the system with excitation signal.

$$G[t] = (X * S)[t] = \int_{-\infty}^{\infty} X[t-\tau]S[\tau]d\tau. \tag{6.6}$$

By the convolution theorem, the Fourier transform $\mathcal{F}$ of the convolution of the input signal and the response function is the product the individual Fourier transforms $X[\omega]$ and $S[\omega]$.

$$G[\omega] = \mathcal{F}((X * S)[t])[\omega] = \mathcal{F}(X[t])[\omega] \cdot \mathcal{F}(S[t])[\omega] = X[\omega] \cdot S[\omega] \tag{6.7}$$

If in addition to the measured transient response of the system $G[t]$, the input signal $S[t]$ is also well characterized, a reconstruction of the response function of the system may be made. For the case of our measurements, the observable signal $G[t]$ represents the measured transient reflectivity of the signal while the intensity of the ultrafast pulse represents the input signal.

Modeling the expected signal, the real transient reflectivity to the pump pulse alone $R[t]$ can be expressed as the convolution of the excitation signal $S[t]$ and the intrinsic response function $X[t]$, $R[t] = (X * S)[t]$. However, $R[t]$ is not the quantity experimentally observed. The measured transient reflectivity $R'[t]$ is actually the convolution of $R[t]$ with probe signal whose temporal profile is also S[t]. Consequently, for the pump probe measurements presented here, the relationship between the observed signal with the response function of the system can be expressed as

$$R'[t] = (R * S)[t] = ((X * S) * S)[t]. \tag{6.8}$$

By the convolution theorem, the relationship of the Fourier transform of R' to the Fourier transform of S and X] can be expressed as

$$\begin{aligned} R'[\omega] =& (X * S)[\omega] \cdot S[\omega] \\ =& X[\omega] \cdot S[\omega] \cdot S[\omega] \\ =& X[\omega] \cdot S^2[\omega]. \end{aligned} \tag{6.9}$$

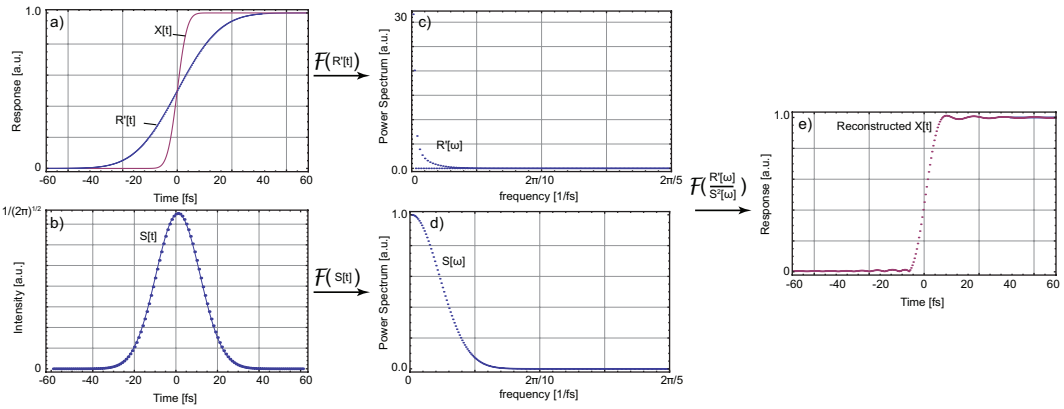

Figure 6.19: The method for reconstructing a response function $X[t]$ using a well characterized output signal $R'[t]$ and known input signal $S[t]$ is modeled above. Panel a) shows a sharp(10 fs) response function $X[t]$ (red line) compared with an the actually measured transient signal $R'[t]$ (blue line). Panel b) shows the a gaussian model pulse $S[t]$ which is used to both excite and probe the response $X[t]$ resulting in the measured quantity $R'[t]$. Panels c) and d) respectively show the Fourier transforms $S[\omega]$ and $R'[\omega]$. Finally, panel e) illustrates the reconstructed response function which compares favorably with the response function initially shown in panel a).

The response function of the system is thus

$$X[t] = \mathcal{F}\left(\frac{R'[\omega]}{S^2[\omega]}\right). \tag{6.10}$$

Fig. 6.19 demonstrates the observed signal and response function reconstruction for a very short response function ($\tau_{\mathrm{R}} \simeq 10$ fs) probed by pulses of longer duration ($\tau_{\mathrm{p}} \simeq 30$ fs). Panel a) displays a comparison of the observed signal $R'[t]$ with the real response function for the system $X[t]$. With knowledge of the pump and probe pulse profile (panel b) the approximate response function may be reconstructed (panel e).

6.8.5 Preliminary results of pump-probe microscopy measurements.

As described in section 6.8.3, degenerate pump-probe measurements were performed at room temperature on single VO_2 micro-crystals for several differing values of the pump fluence both above and below the photo-induced MIT threshold.

Below the fluence threshold, the measured transient reflectivity exhibits a modulation due to coherent lattice excitations. At short time-scales ($t < 100$ fs) a sharp change in the reflectivity is observed as the pump pulse excites electrons from the $d_{\|}$ band across the band gap (see band structure diagram from ref. [249] in Fig. 6.7). A picosecond timescale decay is observed which is correlates with the energy relaxation of these excited electrons through optical phonon emission [290].

Superimposed upon the slow change in transient reflectivity associated with the energy relaxation of the electrons are high frequency modulations in of the reflectivity associated with coherent phonon excitation. Analysis of the structural motions the which the frequencies of these coherent phonons represent and how those motions correlate with the pump fluence may yield insight into the changes of the lattice symmetry of the VO_2 micro-crystals associated with the photo-induced MIT.

Fig. 6.20a) and b) displays the measured transient reflectivity from a VO_2 micro-crystal in the triclinic phase for fluences below the photo-induced MIT fluence threshold (Fluence$\simeq$ 1.5 mJ/cm^2). Here the decay of the transient reflectivity associated with the energy relaxation of the excited electrons is fitted with using the function:

$$\frac{-\Delta R}{R}[t] = \frac{1}{2}\left(1 + \mathrm{erf}[t/\tau_p]\right) \cdot \left(A \exp[-t/\tau_e] + B(1 - \exp[-t/\tau_e]) \cdot \exp[-t/\tau_s]\right). \qquad (6.11)$$

In the fit above, the approximate duration of the pump pulse is represented by τ_p which accounts for the sharp change in the reflectivity as the pump pulse interacts with the sample. The quantities A and B represent the magnitude of the short and long timescale timescale reflectivity changes respectively. Finally, τ_e and τ_s represent the decay constants of the fast electronic decay through energy relaxation and the slow time decay (tens of picoseconds) of the system back to its equilibrium state.

It is notable that some distinct differences are observed between the values of A and B which depends on the orientation of the VO_2 micro-crystal with respect to the polarization of the probe pulse. Fig. 6.20a) shows the measured transient reflectivity change with the polarization of the probe beam parallel to the c_R axis of the micro-crystal. For this probe polarization/crystal orientation geometry for $t > 2$ ps, the magnitude of the transient

reflectivity is characterized by magnitude of the long-time scale response, B. The magnitude of B for this experimental geometry is generally $\simeq A/5$.

In contrast, Fig. 6.20a) shows the measured transient reflectivity change with the polarization of the probe beam perpendicular to the c_R axis of the micro-crystal. For this probe polarization/crystal orientation geometry, the magnitude of the transient reflectivity at long time-scales is nearly equivalent to the equilibrium value for $t < 0$.

The differences observed in the long time-scale reflectivity response is an indication of a strong anisotropy in the optical conductivity of the crystal. As indicated by Fig. 6.20a) and b), the excited electrons exhibit a much higher reflectivity response in the c_R direction as opposed the the $(a_R - b_R)/\sqrt{2}$ direction.

Subtracting the fit of the exponential decay due to the energy relaxation of the excited electrons and the long time-scale response, we are able to isolate the high frequency modulations attributable to the excitation of coherent phonon vibrational modes. Here, pump pulse generates coherent phonon oscillations whose frequencies are recovered via Fourier transform and displayed in the insets of Fig. 6.20a) and b). For the measurement shown, two strong modes at 200 and 225 cm^{-1} are observed in addition to side peaks at 125 and 300 cm^{-1}. These modes are observed to decrease in magnitude and broaden as the pump fluence is increased (data not shown), but still remains below the fluence threshold for the photo-induced MIT. All four modes lie in rough agreement with the A_g Raman modes observed by ref [280].

For fluences above the threshold necessary for the photo-induced MIT, a large change in reflectivity ($\frac{-\Delta R}{R} \simeq 0.05$) is observed which remains for long time scales (¿100 ps). Of particular interest is the time-scale which the system transitions from the insulating equilibrium state to the photo-induced metallic state. As discussed previously, it has been previously observed that an 80 fs "phonon-bottleneck" is the fundamental limit on the transition time of the MIT in VO_2. As shown in Fig. 6.20c) our results correspond relatively closely with this observation. Here, an exponential fit of the MIT indicates that transition time is approximately 85 ± 5 fs. However, as discussed in section 6.8.4 by accounting for the duration of the probe pulse we can reconstruct the intrinsic response function of the system as shown in Fig. 6.20d). This response function reconstruction indicates a slightly

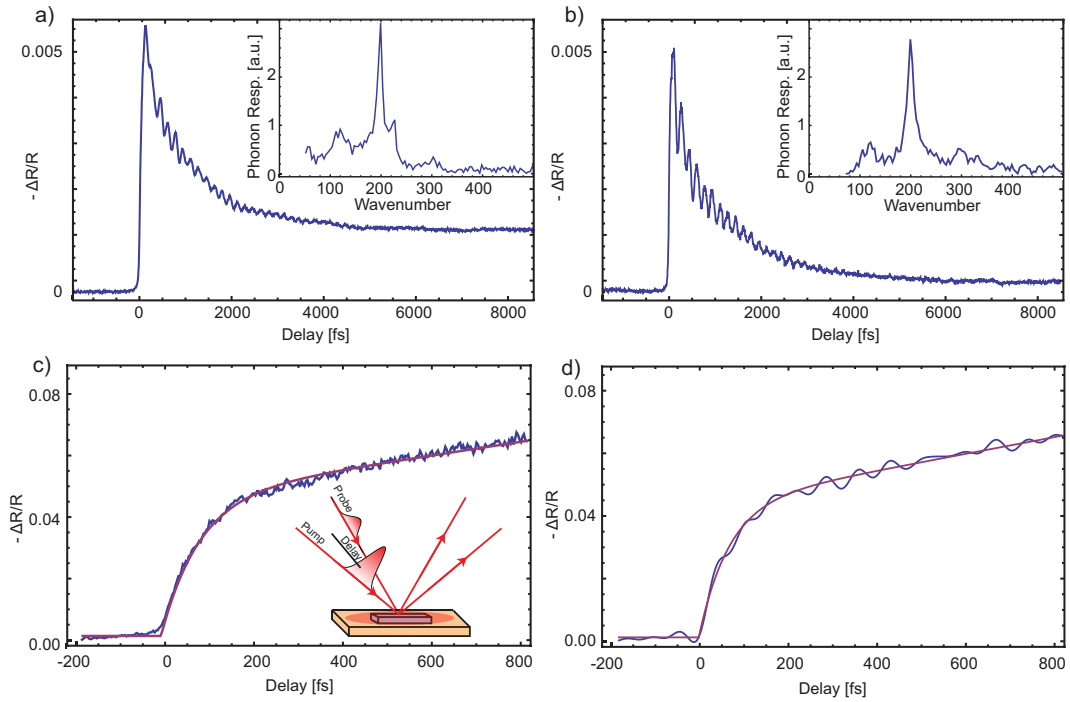

Figure 6.20: Panels a) and b) display the observed transient reflectivity for pump probe measurements below the transition photo-induced MIT fluence threshold respectively (Fluence $\simeq$ 1.5 mJ/cm^2). Panel a) represents a measurement with the probe polarization parallel to the c_R axis while panel b) displays the similar measurement with the probe polarization perpendicular to the c_R axis of the micro-crystal. Panels c) and d) represent a single measurment of the photo-induced MIT above the fluence threshold (Fluence $\simeq$ 8 mJ/cm^2). Panel c) represent the actual raw data, while d) represents the reconstructed response function. Exponential fits of to the data in c) and d) yield transition times of 85 and 67 fs $\pm$5 fs respectively.

faster transition time of $67 \pm 5fs$.

6.8.6 Outlook.

As demonstrated by the preliminary results in the preceding section detailing the characterization of the photo-induced MIT on VO_2 micro-crystals, the details of the ultrafast response of individual micro-crystals may vary from that demonstrated by previous characterizations on larger samples. We hope that further measurements on micro-crystals in

the purely M1 or M2 crystal phases will reveal insight into the complex coupling and roles of the lattice and electronic structure. Future measurements on comparing the ultrafast response at both higher and lower temperatures may further reveal details of this coupling. Specifically, the observation of the photo-induced MIT transition time at low temperatures where the phonon motion correlated with the V-V tilting and dimerization is frozen out could provide important information on the role of the lattice in the phase transition. In addition, measurement of the ultrafast response on a micro-crystal with adjustable strain could allow for the comparison of the ultrafast response of the various insulating phases on a single crystal.

BIBLIOGRAPHY

[1] R. Feynman: *P. Engineering and Science* (1960) 22

[2] V. Parsegian: *Van der Waals forces*: Cambridge University Press (2006)

[3] M. Born, E. Wolf: *Principles of Optics:*: Cambridge University Press (1999)

[4] E. Hecht: *Optics*: Pearson Education, Inc. (2002)

[5] J. Weiner: *Rep. Prog. Phys.* **72** (2009) 064401

[6] J. Goldstein, D. Newbury, D. Joy, C. Lyman, E. P., E. Lifshin, L. Sawyer, J. Michael: *Scanning Electron Microscopy and X-ray Microanalysis*: Springer, 3rd edn. (2003)

[7] D. Williams, C. Carter: *Transmission Electron Microscopy*: Springer (2009)

[8] J. Kaastra, F. Paerels (eds.): *High resolution X-Ray spectroscopy: past, present, and future*: Springer (2010)

[9] M. Ernst, H. Hug, R. Bennewitz: *Scanning probe microscopy: the lab on a tip*: Springer (2004)

[10] P. Eaton, P. West: *Atomic Force Microscopy*: Oxford University Press (2010)

[11] G. Binnig, H. Rohrer, C. Gerber, E. Weibel: *Phys. Rev. Lett.* **50** (1983) 120

[12] G. Binnig, C. F. Quate, C. Gerber: *Phys. Rev. Lett.* **56** (1986) 930

[13] G. Binnig, H. Rohrer: *Rev. Mod. Phys.* **59** (1987) 615

[14] L. Novotny, B. Hecht: *Principles of Nano-Optics*: Cambridge University Press (2006)

[15] M. B. Raschke, C. Lienau: *Appl. Phys. Lett.* **83** (2003) 5089

[16] G. Pollack, D. Stump: *Electromagnetism*: Addison & Wesley (2002)

[17] J. Jackson: *Classical Electrodynamics*: Wiley & Sons, 3rd edn. (1998)

[18] M. Dressel, G. Gruner: *Electrodynamics of Solids*: Cambridge University Press (2002)

[19] G. Fowles: *Introduction to Modern Optics*: Dover, 2nd edn. (1989)

[20] P. Drude: *Ann. Phys.* **306** (1900) 566

[21] M. A. Ordal, L. L. Long, R. J. Bell, S. E. Bell, R. R. Bell, R. W. Alexander, C. A. Ward: *Appl. Opt.* **22** (1983) 1099

[22] P. B. Johnson, R. W. Christy: *Phys. Rev. B* **6** (1972) 4370

[23] E. Palik (ed.): *Handbook of Optical Constants of Solids*, vol. 1: Academic Press (1985)

[24] N. Ashcroft, N. Mermin: *Solid State Physics*: Thompson Learning (1976)

[25] H. Ehrenreich, H. R. Philipp: *Phys. Rev.* **128** (1962) 1622

[26] K. Joulain, J. Mulet, F. Marquier, R. Carminati, J.-J. Greffet: *Surf. Sci. Rep.* **57** (2005) 59

[27] E. T. Arakawa, M. W. Williams, R. N. Hamm, R. H. Ritchie: *Phys. Rev. Lett.* **31** (1973) 1127

[28] A. Boardman (ed.): *Electromagnetic Surface Modes*: Wiley & Sons (1982)

[29] J. Le Gall, M. Olivier, J.-J. Greffet: *Phys. Rev. B* **55** (1997) 10105

[30] B. Sernelius: *Surface Modes in Physics*: Wiley & Sons, 1rst edn. (2001)

[31] L. Rayleigh: *Phil. Mag.* **5** (1896) 167

[32] E. Synge: *Phil. Mag* **6** (1928) 1

[33] D. W. Pohl, W. Denk, M. Lanz: *App. Phys. Lett.* **44** (1984) 651

[34] R. C. Reddick, R. J. Warmack, T. L. Ferrell: *Phys. Rev. B* **39** (1989) 767

[35] D. Courjon, J.-M. Vigoureux, M. Spajer, K. Sarayeddine, S. Leblanc: *Appl. Opt.* **29** (1990) 3734

[36] E. Betzig, J. K. Trautman, T. D. Harris, J. S. Weiner, R. L. Kostelak: *Science* **251** (1991) 1468

[37] E. Betzig, P. L. Finn, J. S. Weiner: *App. Phys. Lett.* **60** (1992) 2484

[38] H. A. Bethe: *Phys. Rev.* **66** (1944) 163

[39] M. Specht, J. D. Pedarnig, W. M. Heckl, T. W. Hnsch: *Phys. Rev. Lett.* **68** (1992) 476

[40] R. Hollander de, N. van Hulst, R. Kooyman: *Ultramicroscopy* **57** (1995) 263

[41] Y. Inouye, S. Kawata: *Opt. Lett.* **19** (1994) 159

[42] F. Zenhausern, Y. Martin, H. K. Wickramasinghe: *Science* **269** (1995) 1083

[43] F. J. Giessibl: *Rev. Mod. Phys.* **75** (2003) 949

[44] F. Huth, M. Schnell, J. Wittborn, N. Ocelic, R. Hillenbrand: *Nat Mater* **10** (2011) 352

[45] N. Behr, M. B. Raschke: *J. Phys. Chem. C* **112** (2008) 3766

[46] R. Hillenbrand, F. Keilmann: *Phil. Trans. R. Soc. Lond. A* **362** (2004) 787

[47] R. Esteban, R. Vogelgesang, K. Kern: *Phys. Rev. B* **75** (2007) 195410

[48] A. Cvitkovic, N. Ocelic, R. Hillenbrand: *Opt. Express* **15** (2007) 8550

[49] C. F. Bohren, D. R. Huffman: *Absorption and scattering of light by small particles*: John Wiley, New York (1998)

[50] R. W. Rendell, D. J. Scalapino, B. Mühlschlegel: *Phys. Rev. Lett.* **41** (1978) 1746

[51] R. W. Rendell, D. J. Scalapino: *Phys. Rev. B* **24** (1981) 3276

[52] J. Renger, S. Grafström, L. M. Eng, R. Hillenbrand: *Phys. Rev. B* **71** (2005) 075410

[53] R. Esteban, R. Vogelgesang, K. Kern: *Nanotech.* **17** (2006) 475

[54] N. Calander: *J. Appl. Phys.* **92** (2002) 4878

[55] N. Ocelic, A. Huber, R. Hillenbrand: *Appl. Phys. Lett.* **89** (2006) 101124

[56] C. Talley, J. Jackson, C. Oubre, N. Grady, C. Hollars, S. Lane, T. Huser, P. Nordlander, N. Halas: *Nano Lett.* **5** (2005) 1569

[57] Y. Cao, R. Jin, C. Mirkin: *Science* **297** (2002) 1536

[58] J. Chen, B. J. Wiley, Y. Xia: *Langmuir* **23** (2007) 4120

[59] F. Tam, G. Goodrich, B. Johnson, N. Halas: *Nano Lett.* **7** (2007) 496

[60] A. McFarland, R. VanDuyne: *Nano Lett.* **3** (2003) 1057

[61] A. Haes, R. Van Duyne: *Anal. Bioanal. Chem.* **379** (2004) 920

[62] D. Stuart, J. Yuen, N. Shah, O. Lyandres, C. Yonzon, M. Glucksberg, J. Walsh, R. VanDuyne: *Anal. Chem.* **78** (2006) 7211

[63] J. Chen, F. Saeki, B. Wiley, H. Cang, M. Cobb, Z.-Y. Li, L. Au, H. Zhang, M. Kimmey, X. Li, Y. Xia: *Nano Lett.* **5** (2005) 473

[64] H. Cang, T. Sun, Z.-Y. Li, J. Chen, B. J. Wiley, Y. Xia, X. Li: *Opt. Lett.* **30** (2005) 3048

[65] A. W. H. Lin, N. A. Lewinski, J. L. West, N. J. Halas, R. A. Drezek: *J. Biomed. Opt.* **10** (2005) 064035

[66] D. O'Neal, L. Hirsch, N. Halas, J. Payne, J. West: *Cancer Letters* **209** (2004) 171

[67] A. Gobin, M. Lee, N. Halas, W. James, R. Drezek, J. West: *Nano Lett.* **7** (2007) 1929

[68] E. Ozbay: *Science* **311** (2006) 189

[69] J. Vasseur, A. Akjouj, L. Dobrzynski, B. Djafari-Rouhani, E. El Boudouti: *Surf. Sci. Rep.* **54** (2004) 1

[70] I. I. Smolyaninov, Y.-J. Hung, C. C. Davis: *Appl. Phys. Lett.* **87** (2005) 241106

[71] S. Maier, P. Kik, H. Atwater, S. Meltzer, E. Harel, B. Koel, A. Requicha: *Nature Mater.* **2** (2003) 229

[72] U. Kreibig, M. Vollmer: *Optical Properties of Metal Clusters*, vol. 25 of *Springer Series in Materials Science*: Springer, Berlin (1995)

[73] R. Jin, Y. Cao, E. Hao, G. Metraux, G. Schatz, C. Mirkin: *Nature* **425** (2003) 487

[74] J. Washio, Y. Xiong, Y. Xia: *Adv. Mater.* **18** (2006) 1745

[75] L. Sherry, R. Jin, C. Mirkin, G. Schatz, R. VanDuyne: *Nano Lett.* **6** (2006) 2060

[76] K. Kelly, E. Coronado, L. Zhao, G. Schatz: *J. Phys. Chem. B* **107** (2003) 668

[77] K. Shuford, M. Ratner, G. Schatz: *J. Chem. Phys.* **123** (2005) 114713

[78] P. Schuck, D. Fromm, A. Sundaramurthy, G. Kino, W. Moerner: *Phys. Rev. Lett.* **94** (2005) 017402

[79] E. Cubukcu, E. Kort, K. Crozier, F. Capasso: *Appl. Phys. Lett.* **89** (2006) 093120

[80] J. Merlein, M. Kahl, A. Zuschlag, A. Sell, A. Halm, J. Boneberg, P. Leiderer, A. Leitenstorfer, R. Bratschitsch: *Nat. Photonics* **2** (2008) 230

[81] J. W. Mitchell, R. G. Goodrich: *Phys. Rev. B* **32** (1985) 4969

[82] P. Rai-Choudhury (ed.): *Handbook of Microlithography, Microsmachining, and Microfabrication. Volume 1: Microlithography*, vol. 1: Society of Photo-Optical Instrumentation Engineers (1997)

[83] Y. Sun, Y. Xia: *Science* **298** (2002) 2176

[84] S. Chen, D. Carroll: *Nano Lett.* **2** (2002) 1003

[85] T. Sau, C. Murphy: *Langmuir* **20** (2004) 6414

[86] H. Wang, D. Brandl, P. Nordlander, N. Halas: *Acc. of Chem. Res.* **40** (2007) 53

[87] H. Ditlbacher, A. Hohenau, D. Wagner, U. Kreibig, M. Rogers, F. Hofer, F. Aussenegg, J. Krenn: *Phys. Rev. Lett.* **95** (2005) 257403

[88] T. Jensen, M. Malinsky, C. Haynes, R. Van Duyne: *J. Phys. Chem. B* **104** (2000) 10549

[89] J. R. Krenn, G. Schider, W. Rechberger, B. Lamprecht, A. Leitner, F. R. Aussenegg, J. C. Weeber: *Appl. Phys. Lett.* **77** (2000) 3379

[90] J. Mock, D. Smith, S. Schultz: *Nano Lett.* **3** (2003) 485

[91] L. Sherry, S.-H. Chang, G. Schatz, R. VanDuyne, B. Wiley, Y. Xia: *Nano Lett.* **5** (2005) 2034

[92] A. Murray, W. Barnes: *Adv. Mater.* **19** (2007) 3771

[93] B. Wiley, Y. Sun, Y. Xia: *Acc. Chem. Res.* **40** (2007) 1067

[94] N. Félidj, J. Grand, G. Laurent, J. Aubard, G. Lévi, A. Hohenau, N. Galler, F. R. Aussenegg, J. R. Krenn: *The Journal of Chemical Physics* **128** (2008) 094702

[95] J. Kottmann, O. Martin, D. Smith, S. Schultz: *Opt. Express* **6** (2000) 213

[96] G. Schatz, R. Duyne: *Electromagnetic mechanism of surface enhanced spectroscopy*: Reproduced from: Handbook of Vibrational Spectroscopy (2002)

[97] E. Hao, G. Schatz: *J. Chem. Phys.* (2004) 357

[98] B. J. Wiley, S. H. Im, Z.-Y. Li, J. McLellan, A. Siekkinen, Y. Xia: *J. Phys. Chem. B* **110** (2006) 15666

[99] C. Haynes, R. Van Duyne: *J. Phys. Chem. B* **105** (2001) 5599

[100] Z. Wang: *J. Phys. Chem. B* **104** (2000) 1153

[101] M. Rang, A. C. Jones, F. Zhou, Z. Y. Li, B. J. Wiley, Y. N. Xia, M. B. Raschke: *Nano Lett.* **8** (2008) 3357

[102] R. Esteban, R. Vogelgesang, J. Dorfmuller, A. Dmitriev, C. Rockstuhl, C. Etrich, K. Kern: *Nano Lett.* **8** (2008) 3155

[103] A. García-Etxarri, I. Romero, F. J. García de Abajo, R. Hillenbrand, J. Aizpurua: *Phys. Rev. B* **79** (2009) 125439

[104] R. Hillenbrand, T. Taubner, F. Keilmann: *Nature* **418** (2002) 159

[105] A. Cvitkovic, N. Ocelic, J. Aizpurua, R. Guckenberger, R. Hillenbrand: *Phys. Rev. Lett.* **97** (2006) 060801

[106] M. Raschke, L. Molina, T. Elsaesser, D. Kim, W. Knoll, K. Hinrichs: *ChemPhysChem* **6** (2005) 2197

[107] C. C. Neacsu, J. Dreyer, N. Behr, M. B. Raschke: *Phys. Rev. B* **73** (2006) 193406

[108] K. G. Lee, H. W. Kihm, J. E. Kihm, W. J. Choi, H. Kim, C. Ropers, D. J. Park, Y. C. Yoon, S. B. Choi, D. H. Woo, J. Kim, B. Lee, Q. H. Park, C. Lienau, D. S. Kim: *Nat. Photonics* **1** (2007) 243

[109] K. Lee, H. Kihm, K. Ahn, J. Ahm, Y. Suh, C. Lienau, D. Kim: *Opt. Express* **15** (2007) 14993

[110] R. Hillenbrand, F. Keilmann, P. Hanarp, D. S. Sutherland, J. Aizpurua: *Appl. Phys. Lett.* **83** (2003) 368

[111] R. Ossikovski, Q. Nguyen, G. Picardi: *Phys. Rev. B* **75** (2007) 045412

[112] R. Hillenbrand, F. Keilmann: *Appl. Phys. B* **73** (2001) 239

[113] M. Achermann, K. L. Shuford, G. C. Schatz, D. H. Dahanayaka, L. A. Bumm, V. I. Klimov: *Opt. Lett.* **32** (2007) 2254

[114] B. T. Draine, P. J. Flatau: *J. Opt. Soc. Am. A* **11** (1994) 1491

[115] J. Millstone, S. Park, K. Shuford, L. Qin, G. Schatz, C. Mirkin: *J. Am. Chem. Soc.* **127** (2005) 5312

[116] C. L. Leverette, S. A. Jacobs, S. Shanmukh, S. B. Chaney, R. A. Dluhy, Y. P. Zhao: *App. Spectrosc.* **60** (2006) 906

[117] S. J. Huo, X. K. Xue, Q. X. Li, S. F. Xu, W. B. Cai: *J. Phys. Chem. B* **110** (2006) 25721

[118] S. Lal, N. K. Grady, J. Kundu, C. S. Levin, J. B. Lassiter, N. J. Halas: *Chem. Soc. Rev.* **37** (2008) 898

[119] F. Le, D. W. Brandl, Y. A. Urzhumov, H. Wang, J. Kundu, N. J. Halas, J. Aizpurua, P. Nordlander: *Acs Nano* **2** (2008) 707

[120] F. Neubrech, T. Kolb, R. Lovrincic, G. Fahsold, A. Pucci, J. Aizpurua, T. W. Cornelius, M. E. Toimil-Molares, R. Neumann, S. Karim: *Appl. Phys. Lett.* **89** (2006) 253104

[121] F. Neubrech, A. Pucci, T. W. Cornelius, S. Karim, A. Garcia-Etxarri, J. Aizpurua: *Phys. Rev. Lett.* **101** (2008) 157403

[122] J.-J. Greffet: *Science* **308** (2005) 1561

[123] N. F. Yu, J. Fan, Q. J. Wang, C. Pflugl, L. Diehl, T. Edamura, M. Yamanishi, H. Kan, F. Capasso: *Nat. Photonics* **2** (2008) 564

[124] A. Alu, N. Engheta: *Nature Photonics* **2** (2008) 307

[125] L. Tang, S. E. Kocabas, S. Latif, A. K. Okyay, D.-S. Ly-Gagnon, K. C. Saraswat, D. A. B. Miller: *Nat. Photonics* **2** (2008) 226

[126] P. Krenz, J. Alda, G. Boreman: *Infrared Physics & Technology* **51** (2008) 340

[127] C. Fumeaux, M. A. Gritz, I. Codreanu, W. L. Schaich, F. J. González, G. D. Boreman: *Infrared Phys. Technol.* **41** (2000) 271

[128] A. Bouhelier, R. Bachelot, G. Lerondel, S. Kostcheev, P. Royer, G. P. Wiederrecht: *Phys. Rev. Lett.* **95** (2005) 267405

[129] H. Raether: *Surface Plasmons on Smooth and Rough Surfaces and on Gratings*: Springer, Berlin (1988)

[130] S. Maier: *Plasmonics: Fundamentals and Applications*: Springer (2007)

[131] J. Saxler, J. G. Rivas, C. Janke, H. P. M. Pellemans, P. H. Bolivar, H. Kurz: *Phys. Rev. B* **69** (2004) 155427

[132] H. Bennett, B. J.M.: *Optical Properties and Electronic Structure of Metals and Alloys*: North-Holland, New York (1966)

[133] J. Stratton: *Electromagnetic Theory*: McGraw-Hill Book Company, Inc. (1941)

[134] M. I. Stockman: *Phys. Rev. Lett.* **93** (2004) 137404

[135] L. Novotny: *Phys. Rev. Lett.* **98** (2007) 266802

[136] E. R. Encina, E. A. Coronado: *J. Phys. Chem. C* **111** (2007) 16796

[137] G. Bryant, F. GarciadeAbajo, J. Aizpurua: *Nano Lett.* **8** (2008) 631

[138] K. E. Korte, S. E. Skrabalak, Y. Xia: *J. Mater. Chem.* **18** (2008) 437

[139] B. Wiley, Y. G. Sun, Y. N. Xia: *Langmuir* **21** (2005) 8077

[140] C. Balanis: *Antenna Theory: Analysis and Design*: John Wiley & Sons, Inc., second edn. (1997)

[141] F. Neubrech, D. Weber, R. Lovrincic, A. Pucci, M. Lopes, T. Toury, M. L. de La Chapelle: *Appl. Phys. Lett.* **93** (2008) 163105

[142] R. L. Olmon, P. M. Krenz, A. C. Jones, G. D. Boreman, M. B. Raschke: *Opt. Express* **16** (2008) 20295

[143] J. Gomez-Rivas, M. Kuttge, H. Kurz, P. Haring Bolivar, J. Sanchez-Gil: *App. Phys. Lett.* **88** (2006) 082106

[144] Z. Zhang: *Micro/Nanoscale Heat Transfer*: McGraw Hill (2007)

[145] F. Herschel: *Phil. T. R. Soc. Lond.* **90** (1800) 437

[146] G. Kirchhoff: *Monatsber. preuss Akad.* (1859) 783

[147] W. Wien: *Sitzungsber. preuss. Akad.* (1893) 55

[148] O. Lummer, P. E.: *Verh. phys. Ges.* **1** (1899) 23

[149] M. Planck: *Verh. Phys. Ges.* **2** (1900) 237

[150] C. M. Hargreaves: *Physics Lett. A* **30** (1969) 491

[151] D. Polder, M. Van Hove: *Phys. Rev. B* **4** (1971) 3303

[152] A. V. Shchegrov, K. Joulain, R. Carminati, J.-J. Greffet: *Phys. Rev. Lett.* **85** (2000) 1548

[153] K. Joulain, R. Carminati, J.-P. Mulet, J.-J. Greffet: *Phys. Rev. B* **68** (2003) 245405

[154] J. Pendry: *J. Phys-Condens. Mat.* **11** (1999) 6621

[155] E. Rousseau, A. Siria, G. Jourdan, S. Volz, F. Comin, J. Chevrier, J.-J. Greffet: *Nat. Photonics* **3** (2009) 514

[156] Y. Kajihara, K. Kosaka, S. Komiyama: *Rev. Sci. Instrum.* **81** (2010) 033706

[157] Y. D. Wilde, F. Formanek, R. Carminati, B. Gralek, P. Lemoine, K. Joulain, J. Mulet, Y. Chen, J. Greffet: *Nature* **444** (2006) 740

[158] A. Kittel, U. F. Wischnath, J. Welker, O. Huth, F. Ruting, S.-A. Biehs: *Appl. Phys. Lett.* **93** (2008) 193109

[159] J. Sipe: *J. Opt. Soc. Am. B* **4** (1987) 481

[160] H. O. McMahon: *J. Opt. Soc. Am.* **40** (1950) 376

[161] C. Y. Liang, S. Krimm: *J. Chem. Phys.* **25** (1956) 563

[162] R. E. Moynihan: *J. Am. Chem. Soc.* **81** (1959) 1045

[163] W. G. Spitzer, D. A. Kleinman: *Phys. Rev.* **121** (1961) 1324

[164] J. F. Scott, S. P. S. Porto: *Phys. Rev.* **161** (1967) 903

[165] C. Fu, Z. Zhang: *Int. J. Heat Mass Tran.* **49** (2006) 1703

[166] S. Shen, A. Narayanaswamy, G. Chen: *Nano Lett.* **9** (2009) 2909

[167] H. B. G. Casimir, D. Polder: *Phys. Rev.* **73** (1948) 360

[168] E. Lifshitz: *Dokl. Akad. Nauk SSSR* **100** (1955) 879

[169] M. Antezza, L. P. Pitaevskii, S. Stringari: *Phys. Rev. Lett.* **95** (2005) 113202

[170] J. M. Obrecht, R. J. Wild, M. Antezza, L. P. Pitaevskii, S. Stringari, E. A. Cornell: *Phys. Rev. Lett.* **98** (2007) 063201

[171] F. Gervais, B. Piriou: *Phys. Rev. B* **11** (1975) 3944

[172] P.-O. Chapuis, J.-J. Greffet, K. Joulain, S. Volz: *Nanotech.* **17** (2006) 2978

[173] E. H. Korte, A. Rseler: *Anal. Bioanal. Chem.* **382** (2005) 1987

[174] R. L. Olmon, M. Rang, P. M. Krenz, B. A. Lail, L. V. Saraf, G. D. Boreman, M. B. Raschke: *Phys. Rev. Lett.* **105** (2010) 167403

[175] C. Bohren, D. Huffman: *Absorption and Scattering of Light by Small Particles*: Wiley & Sons (1983)

[176] J. A. Schuller, T. Taubner, M. L. Brongersma: *Nat. Photon.* **3** (2009) 658

[177] C. R. Otey, W. T. Lau, S. Fan: *Phys. Rev. Lett.* **104** (2010) 154301

[178] A. K. Hafeli, E. Rephaeli, S. Fan, D. G. Cahill, T. E. Tiwald: *J. Appl. Phys.* **110** (2011) 043517

[179] J. Barr: *Infrared Phys.* **9** (1969) 97

[180] S. Chiang, R. G. Tobin, P. L. Richards, P. A. Thiel: *Phys. Rev. Lett.* **52** (1984) 648

[181] H. A. Bechtel, M. C. Martin, T. E. May, P. Lerch: *Rev. Sci. Instrum.* **80** (2009) 126106

[182] H. Bethe: *Annalen der Physik* **87** (1928) 55

[183] A. Sommerfeld: *Zeitschrift fr Physik A Hadrons and Nuclei* **47** (1928) 1

[184] F. Bloch: *Zeitschrift fr Physik A Hadrons and Nuclei* **57** (1929) 545

[185] A. H. Wilson: *Proc. R Soc. Lond. A* **134** (1931) 277

[186] A. H. Wilson: *Proc. R Soc. Lond. A* **133** (1931) 458

[187] E. Wigner: *Phys. Rev.* **46** (1934) 1002

[188] J. H. de Boer, E. J. W. Verwey: *Proc. Phys. Soc.* **49** (1937) 59

[189] N. F. Mott, R. Peierls: *Proc. Phys. Soc.* **49** (1937) 72

[190] N. F. Mott: *Proc. Phys. Soc. A* **62** (1949) 416

[191] J. C. Slater: *Phys. Rev.* **82** (1951) 538

[192] N. Mott: *The Beginnings of solid state physics: a symposium held 30 April-2 May 1979, organized by Sir Nevill Mott*: Royal Society (1980)

[193] N. Mott: *Phil. Mag.* **6** (1961) 287

[194] F. Gebhard: *The Mott Metal-Insulator Transition: Models and Methods*: Springer (1997)

[195] D. N. Basov, R. D. Averitt, D. van der Marel, M. Dressel, K. Haule: *Rev. Mod. Phys.* **83** (2011) 471

[196] S. Dordevic, D. Basov: *Ann. Phys (Leipzig)* **15** (2006) 545

[197] D. N. Basov, A. V. Chubukov: *Nat Phys.* **7** (2011) 272

[198] S. Jin, T. H. Tiefel, M. McCormack, R. A. Fastnacht, R. Ramesh, L. H. Chen: *Science* **264** (1994) 413

[199] Y. Tokura, N. Nagaosa: *Science* **288** (2000) 462

[200] T. Chatterji: *Colossal Magnetoresistive Manganites*: Kluwer Academic Publishers (2004)

[201] M. Imada, A. Fujimori, Y. Tokura: *Rev. Mod. Phys.* **70** (1998) 1039

[202] M. Fiebig, V. V. Pavlov, R. V. Pisarev: *J. Opt. Soc. Am. B* **22** (2005) 96

[203] J. G. Bednorz, K. A. Mueller: *Z. Physik B* **64** (1986) 189: 0722-3277

[204] K. M. Shen, J. S. Davis: *Mat. Today* **11** (2008) 14

[205] E. Dagotto: *Science* **309** (2005) 257

[206] E. Dagotto, T. Hotta, A. Moreo: *Phys. Rep.* **344** (2001) 1

[207] M. Fiebig, T. Lottermoser, D. Frohlich, A. V. Goltsev, R. V. Pisarev: *Nature* **419** (2002) 818

[208] T. Choi, Y. Horibe, H. T. Yi, Y. J. Choi, W. Wu, S.-W. Cheong: *Nat. Mater.* **9** (2010) 253

[209] N. Mathur, P. Littlewood: *Sol. State Comm.* **119** (2001) 271

[210] A. Moreo, S. Yunoki, E. Dagotto: *Science* **283** (1999) 2034

[211] Y. Tokunaga, M. Tokunaga, T. Tamegai: *Phys. Rev. B* **71** (2005) 012408

[212] T. Z. Ward, Z. Gai, H. W. Guo, L. F. Yin, J. Shen: *Phys. Rev. B* **83** (2011) 125125

[213] P. M. Woodward, D. E. Cox, T. Vogt, C. N. R. Rao, A. K. Cheetham: *Chem. Mater.* **11** (1999) 3528

[214] C. Ritter, R. Mahendiran, M. R. Ibarra, L. Morellon, A. Maignan, B. Raveau, C. N. R. Rao: *Phys. Rev. B* **61** (2000) R9229

[215] Z. Sun, J. F. Douglas, A. V. Fedorov, Y.-D. Chuang, H. Zheng, J. F. Mitchell, D. S. Dessau: *Nat Phys* **3** (2007) 248

[216] M. Fth, S. Freisem, A. A. Menovsky, Y. Tomioka, J. Aarts, J. A. Mydosh: *Science* **285** (1999) 1540

[217] S. H. Pan, J. P. O'Neal, R. L. Badzey, C. Chamon, H. Ding, J. R. Engelbrecht, Z. Wang, H. Eisaki, S. Uchida, A. K. Gupta, K.-W. Ng, E. W. Hudson, K. M. Lang, J. C. Davis: *Nature* **413** (2001) 282

[218] O. Fischer, M. Kugler, I. Maggio-Aprile, C. Berthod, C. Renner: *Scanning tunneling spectroscopy of high-temperature superconductors* (2007)

[219] K. McElroy, J. Lee, J. A. Slezak, D.-H. Lee, H. Eisaki, S. Uchida, J. C. Davis: *Science* **309** (2005) 1048

[220] C. V. Parker, P. Aynajian, E. H. da Silva Neto, A. Pushp, S. Ono, J. Wen, Z. Xu, G. Gu, A. Yazdani: *Nature* **468** (2010) 677

[221] A. Mesaros, K. Fujita, H. Eisaki, S. Uchida, J. C. Davis, S. Sachdev, J. Zaanen, M. J. Lawler, E.-A. Kim: *Science* **333** (2011) 426

[222] M. Uehara, S. Mori, C. H. Chen, S.-W. Cheong: *Nature* **399** (1999) 560

[223] J. Xu, Y. Matsui, T. Kimura, Y. Tokura: *Physica C* **357-360, Part 1** (2001) 401

[224] T. Asaka, S. Yamada, S. Tsutsumi, C. Tsuruta, K. Kimoto, T. Arima, Y. Matsui: *Phys. Rev. Lett.* **88** (2002) 097201

[225] J. C. Loudon, N. D. Mathur, P. A. Midgley: *Nature* **420** (2002) 797

[226] J. Tao, D. Niebieskikwiat, M. Varela, W. Luo, M. A. Schofield, Y. Zhu, M. B. Salamon, J. M. Zuo, S. T. Pantelides, S. J. Pennycook: *Phys. Rev. Lett.* **103** (2009) 097202

[227] T. Taniuchi, H. Kumigashira, M. Oshima, T. Wakita, T. Yokoya, M. Kubota, K. Ono, H. Akinaga, M. Lippmaa, M. Kawasaki, H. Koinuma: *Appl. Phys. Lett.* **89** (2006) 112505

[228] L. Zhang, C. Israel, A. Biswas, R. L. Greene, A. de Lozanne: *Science* **298** (2002) 805

[229] J. Wu, Q. Gu, B. Guiton, N. deLeon, L. Ouyang, H. Park: *Nano Lett.* **6** (2006) 2313

[230] D. Serrate, P. Ferriani, Y. Yoshida, S.-W. Hla, M. Menzel, K. von Bergmann, S. Heinze, A. Kubetzka, R. Wiesendanger: *Nat. Nano.* **5** (2010) 350

[231] J. H. Lee, L. Fang, E. Vlahos, X. Ke, Y. W. Jung, L. F. Kourkoutis, J.-W. Kim, P. J. Ryan, T. Heeg, M. Roeckerath, V. Goian, M. Bernhagen, R. Uecker, P. C. Hammel, K. M. Rabe, S. Kamba, J. Schubert, J. W. Freeland, D. A. Muller, C. J. Fennie, P. Schiffer, V. Gopalan, E. Johnston-Halperin, D. G. Schlom: *Nature* **466** (2010) 954

[232] E. B. Lochocki, S. Park, N. Lee, S.-W. Cheong, W. Wu: *Appl. Phys. Lett.* **99** (2011) 232901

[233] P. W. Kolb, D. B. Romero, H. D. Drew, Y. Moritomo, A. B. Souchkov, S. B. Ogale: *Phys. Rev. B* **70** (2004) 224415

[234] V. Podzorov, B. G. Kim, V. Kiryukhin, M. E. Gershenson, S.-W. Cheong: *Phys. Rev. B* **64** (2001) 140406

[235] F. Zenhausern, M. P. O. Boyle, H. K. Wickramasinghe: *Applied Physics Letters* **65** (1994) 1623

[236] W. Denk, D. W. Pohl: *Near-field optics: micoscopy with nanometer-size fields* (1991)

[237] E. J. Sanchez, L. Novotny, X. S. Xie: *Phys. Rev. Lett.* **82** (1999) 4014

[238] T. Taubner, R. Hillenbrand, F. Keilmann: *Nanoscale polymer recognition by spectral signature in scattering infrared near-field microscopy* (2004)

[239] R. Peierls: *More Surprises in Theoretical Physics*: Princeton University Press (1991)

[240] N. Mott: *Metal Insulator Transitions*: Taylor and Francis (1990)

[241] J. Hubbard: *Proc. R. Soc. Lon. A* **281** (1964) 401

[242] J. Hubbard: *Proc. R. Soc. Lon. A* **277** (1964) 237

[243] G. Kotliar, D. Vollhardt: *Physics Today* **57** (2004) 53

[244] F. J. Morin: *Phys. Rev. Lett.* **3** (1959) 34

[245] N. Mott: *Rev. Mod. Phys.* **40** (1968) 677

[246] M. Marezio, D. B. McWhan, J. P. Remeika, P. D. Dernier: *Phys. Rev. B* **5** (1972) 2541

[247] D. Kucharczyk, T. Niklewski: *J. Appl. Crystallogr.* **12** (1979) 370

[248] A. Zylbersztejn, N. F. Mott: *Phys. Rev. B* **11** (1975) 4383

[249] J. B. Goodenough: *J. Solid State Chem.* **3** (1971) 490

[250] D. Paquet, P. Leroux-Hugon: *Phys. Rev. B* **22** (1980) 5284

[251] R. M. Wentzcovitch, W. W. Schulz, P. B. Allen: *Phys. Rev. Lett.* **72** (1994) 3389

[252] R. M. Wentzcovitch, W. W. Schulz, P. B. Allen: *Phys. Rev. Lett.* **73** (1994) 3043

[253] T. M. Rice, H. Launois, J. P. Pouget: *Phys. Rev. Lett.* **73** (1994) 3042

[254] J. P. Pouget, H. Launois, J. P. D'Haenens, P. Merenda, T. M. Rice: *Phys. Rev. Lett.* **35** (1975) 873

[255] D. B. McWhan, M. Marezio, J. P. Remeika, P. D. Dernier: *Phys. Rev. B* **10** (1974) 490

[256] V. Eyert: *Ann. Phys* **11** (2002) 650

[257] J. P. Pouget, H. Launois, T. M. Rice, P. Dernier, A. Gossard, G. Villeneuve, P. Hagenmuller: *Phys. Rev. B* **10** (1974) 1801

[258] J. Longo, P. Kierkega: *Acta. Chem. Scand.* **24** (1970) 420

[259] M. Ghedira, H. Vincent, M. Marezio, J. Launay: *J. Sol. State Chem.* **22** (1977) 423

[260] A. Tselev, I. A. Lukyanchuk, I. N. Ivanov, J. D. Budai, J. Z. Tischler, E. Strelcov, A. Kolmakov, S. V. Kalinin: *Nano Lett.* **10** (2010) 4409

[261] J. I. Sohn, H. J. Joo, D. Ahn, H. H. Lee, A. E. Porter, K. Kim, D. J. Kang, M. E. Welland: *Nano Lett.* **9** (2009) 3392

[262] J. Y. Chou, J. L. Lensch-Falk, E. R. Hemesath, L. J. Lauhon: *J. Appl. Phys.* **105** (2009) 034310

[263] D. Maurer, A. Leue: *Mat. Sci. and Eng. A-Struct.* **370** (2004) 440 : 13th International Conference on Internal Friction and Ultrasonic Attenuation in Solids

[264] E. E. Chain: *Appl. Optics* **30** (1991) 2782

[265] H. S. Choi, J. S. Ahn, J. H. Jung, T. W. Noh, D. H. Kim: *Phys. Rev. B* **54** (1996) 4621

[266] Y. Chang, C. Koo, J. Yang, Y. Kim, D. Kim, J. Lee, T. Noh, H.-T. Kim, B. Chae: *Thin Solid Films* **486** (2005) 46 : WOE-11, 2004

[267] M. Qazilbash, M. Brehm, B.-G. Chae, P.-C. Ho, G. Andreev, B.-J. Kim, S. Yun, A. Balatsky, M. Maple, F. Keilmann, H.-T. Kim, D. Basov: *Science* **318** (2007) 1750

[268] A. Frenzel, M. M. Qazilbash, M. Brehm, B.-G. Chae, B.-J. Kim, H.-T. Kim, A. V. Balatsky, F. Keilmann, D. N. Basov: *Phys. Rev. B* **80** (2009) 115115

[269] M. M. Qazilbash, Z. Q. Li, V. Podzorov, M. Brehm, F. Keilmann, B. G. Chae, H. T. Kim, D. N. Basov: *Appl. Phys. Lett.* **92** (2008) 241906

[270] J. Wei, Z. Wang, W. Chen, D. H. Cobden: *Nat Nano* **4** (2009) 420

[271] J. Cao, E. Ertekin, V. Srinivasan, W. Fan, S. Huang, H. Zheng, J. W. L., Yim, D. R., Khanal, D. F., Ogletree, J. C., Grossman, J. Wu: *Nat. Nano* **4** (2009) 732

[272] B. Guiton, Q. Gu, A. Prieto, M. Gudiksen, H. Park: *J. Am. Chem. Soc.* **127** (2005) 498

[273] N. Sridhar, J. Rickman, D. Srolovitz: *Acta Mater.* **44** (1996) 4097

[274] S. K. Streiffer, J. A. Eastman, D. D. Fong, C. Thompson, A. Munkholm, M. V. Ramana Murty, O. Auciello, G. R. Bai, G. B. Stephenson: *Phys. Rev. Lett.* **89** (2002) 067601

[275] H. Kuzmany: *Solid State Spectroscopy*: Springer (1998)

[276] C. Marini, E. Arcangeletti, D. Di Castro, L. Baldassare, A. Perucchi, S. Lupi, L. Malavasi, L. Boeri, E. Pomjakushina, K. Conder, P. Postorino: *Phys. Rev. B* **77** (2008) 235111

[277] R. Srivastava, L. L. Chase: *Phys. Rev. Lett.* **27** (1971) 727

[278] G. I. Petrov, V. V. Yakovlev, J. Squier: *Appl. Phys. Lett.* **81** (2002) 1023

[279] J. M. Atkin, S. Berweger, E. K. Chavez, M. B. Raschke, J. Cao, W. Fan, J. Wu (2011)

[280] P. Schilbe: *Physica B* **316-317** (2002) 600

[281] A. S. Barker, H. W. Verleur, H. J. Guggenheim: *Phys. Rev. Lett.* **17** (1966) 1286

[282] H. W. Verleur, J. Barker, A. S., C. N. Berglund: *Phys. Rev.* **172** (1968) 788

[283] M. M. Qazilbash, K. S. Burch, D. Whisler, D. Shrekenhamer, B. G. Chae, H. T. Kim, D. N. Basov: *Phys. Rev. B* **74** (2006) 205118

[284] V. Gozhenko, L. Grechko, K. Whites: *Phys. Rev. B* **68** (2003) 125422

[285] A. C. Jones, S. Berweger, J. Wei, D. Cobden, M. B. Raschke: *Nano Letters* **10** (2010) 1574

[286] J. Cao, Y. Gu, W. Fan, L. Q. Chen, D. F. Ogletree, K. Chen, N. Tamura, M. Kunz, C. Barrett, J. Seidel, J. Wu: *Nano Lett.* **10** (2010) 2667

[287] S. Berweger, C. C. Neacsu, Y. Mao, H. Zhou, S. S. Wong, M. B. Raschke: *Nat. Nano.* **4** (2009) 496

[288] A. Sharoni, J. G. Ramirez, I. K. Schuller: *Phys. Rev. Lett.* **101** (2008) 026404

[289] A. Cavalleri, M. Rini, R. Schoenlein: *J. Phys. Soc. Jpn.* **75** (2006)

[290] A. Othonos: *J. Appl. Phys.* **83** (1998) 1789

[291] J. Hohlfeld, S.-S. Wellershoff, J. Gdde, U. Conrad, V. Jhnke, E. Matthias: *Chem. Phys.* **251** (2000) 237

[292] K. Nasu: *Rep. Prog. Phys.* **67** (2004) 1607

[293] C. M. Varma, A. L. Simons: *Phys. Rev. Lett.* **51** (1983) 138

[294] M. Rini, R. Tobey, N. Dean, J. Itatani, Y. Tomioka, Y. Tokura, R. W. Schoenlein, A. Cavalleri: *Nature* **449** (2007) 72

[295] L. Perfetti, P. A. Loukakos, M. Lisowski, U. Bovensiepen, M. Wolf, H. Berger, S. Biermann, A. Georges: *New Journal of Physics* **10** (2008) 053019

[296] A. Cavalleri, C. Tóth, C. W. Siders, J. A. Squier, F. Ráksi, P. Forget, J. C. Kieffer: *Phys. Rev. Lett.* **87** (2001) 237401

[297] A. Cavalleri, T. Dekorsy, H. H. W. Chong, J. C. Kieffer, R. W. Schoenlein: *Phys. Rev. B* **70** (2004) 161102

[298] M. Rini, A. Cavalleri, R. W. Schoenlein, R. Lpez, L. C. Feldman, R. F. Haglund, Jr., L. A. Boatner, T. E. Haynes: *Opt. Lett.* **30** (2005) 558

[299] H.-T. Kim, Y. W. Lee, B.-J. Kim, B.-G. Chae, S. J. Yun, K.-Y. Kang, K.-J. Han, K.-J. Yee, Y.-S. Lim: *Phys. Rev. Lett.* **97** (2006) 266401

[300] M. Rini, Z. Hao, R. W. Schoenlein, C. Giannetti, F. Parmigiani, S. Fourmaux, J. C. Kieffer, A. Fujimori, M. Onoda, S. Wall, A. Cavalleri: *Appl. Phys. Lett.* **92** (2008) 181904

[301] C. Kubler, H. Ehrke, R. Huber, R. Lopez, A. Halabica, J. R. F. Haglund, A. Leitenstorfer: *Phys. Rev. Lett.* **99** (2007) 116401

[302] P. Baum, D.-S. Yang, A. H. Zewail: *Science* **318** (2007) 788